# ROOM-TEMPERATURE FABRICATION OF ELECTROCERAMIC COMPOSITES

Nina Kuzmić

**Doctoral Dissertation**
**Jožef Stefan International Postgraduate School**
**Ljubljana, Slovenia**

**Supervisor:** Assoc. Prof. Dr. Srečo Davor Škapin, Jožef Stefan Institute, Ljubljana, Slovenia
**Co-Supervisor:** Assoc. Prof. Dr. Matjaž Spreitzer, Jožef Stefan Institute, Ljubljana, Slovenia
**Co-Supervisor:** Prof. Dr. Heli Jantunen, University of Oulu, Oulu, Finland

**Evaluation Board:**
Asst. Prof. Dr. Mojca Otoničar, Chair, Jožef Stefan Institute, Ljubljana, Slovenia
Assoc. Prof. Dr. Andraž Kocjan, Member, Jožef Stefan Institute, Ljubljana, Slovenia
Prof. Dr. Rick Ubic, Member, Boise State University, Idaho, United States of America

MEDNARODNA PODIPLOMSKA ŠOLA JOŽEFA STEFANA
JOŽEF STEFAN INTERNATIONAL POSTGRADUATE SCHOOL


Nina Kuzmić

# ROOM-TEMPERATURE FABRICATION OF ELECTROCERAMIC COMPOSITES

**Doctoral Dissertation**

# PRIDOBIVANJE ELEKTROKERAMIČNIH KOMPOZITOV PRI SOBNI TEMPERATURI

**Doktorska disertacija**

**Supervisor:** Assoc. Prof. Dr. Srečo Davor Škapin

**Co-Supervisor:** Assoc. Prof. Dr. Matjaž Spreitzer

**Co-Supervisor:** Prof. Dr. Heli Jantunen

Ljubljana, Slovenia, September 2024

*To my family,*
*to my dear Samo,*
*and to my friends,*
*thank you for your endless support and encouragement.*

# Acknowledgments

I want to express my deep gratitude to the supervisors Srečo, Mikko, Heli, and Matjaž for their unwavering moral support, knowledge transfer, and valuable consultations throughout my journey toward a PhD degree. Each of you was there for a unique reason, guiding me to evaluate my work, to learn critically, and, most importantly, to be consistent and patient. A special thanks to Dr. Mikko Nelo, who introduced me to experimental methods, guided me during my two working visits to Oulu at the Microelectronic Research Unit, and was always available to discuss my research ideas and challenges. I extend my gratitude to David Fabijan, JSI, for his invaluable assistance with measurements and simulations and overall support throughout my doctoral studies. Thanks to my other colleagues at the K9 department for their helpful research advice and constructive discussions, which helped me complete this work. The enjoyable coffee breaks and social moments we spent together meant a lot. Special thanks to Petruša, Uroš, Tjaša, Alja, Lea, Martina, and Mario for their help and support. In addition, I would like to thank Eva Terbovšek and Nina Martinc for providing external support in sample synthesis and processing. Many thanks to Abdullah Jabr from the University of Leoben for sharing insights and knowledge on mechanical properties and conducting mechanical tests on ceramics and ceramic composites. Thanks to Dr. Nina Daneu and Tina Radošević for conducting the TEM and SEM analysis. Thanks to Mitja Lasič for his help formatting my thesis's final version.

However, this was only possible with the funding I received from the Slovenian Research and Innovation Agency, PR-09775. In addition, I would like to thank the JECS Trust board for awarding me with a scholarship (2019225) during my two-month stay in Oulu, Finland. Last but not least, thanks to the Jožef Stefan Postgraduate School for their help with all scholastic duties, opportunities, and social activities I attended during my PhD. Thanks to Sergeja, Maša, and Tadeja for solving problems endlessly.

I will forever be grateful to my family and friends for their help, love, and support throughout my studies. Although not all of them come from scientific backgrounds, they patiently listened to my research updates and struggles along the way.

Thank you all for your endless insistence that I can achieve anything I set my mind.

# Abstract

In the scope of this thesis, I focused on $SrTiO_3$ (ST)-based dielectric ceramic composites as a lead-free perovskite material, which holds great potential for use in various electronic components. Such materials are large-scale and fabricated under high energy requirements, indicating an increasing need for a more environmentally friendly processing method. In this relation, Room Temperature Fabrication (RTF) offers a potential solution to reduce processing temperatures by using water-soluble inorganic compounds such as $Li_2MoO_4$ (LMO), which can be cured and densified at room temperature, resulting in the form of pure ceramic or ceramic composites.

In my doctoral research, I optimized the RTF processing parameters on the LMO-ST composite system to improve the dielectric performance. By using LMO or such inorganic salts as the binding phase between ST ceramic particles, an "upside-down" form of the composite was synthesized, where a high loading of functional ceramic filler and a small amount of binder in the form of a solid and saturated aqueous solution were combined. Densification occurs as the binder deposits on the surface of ST filler particles during pressing and drying.

Furthermore, I varied the composition (LMO binder content), which converted the upside-down composites to traditional 0-3 composites. In addition, alternative binders such as $Na_2MoO_4$, $Na_2WO_4$, $Na_2SiO_3$, and $MgSO_4$ were found to be suitable candidates for RTF systems, which resulted in a relative density of 81-87 %, relative permittivity of 65-130, and dielectric loss tangent values of 0.002-0.05 at 1 MHz and corresponding resonant frequencies in the microwave range (4-6 GHz). In the light of comparison, I utilized $BaTiO_3$ (BT) ceramics in the ceramic-binder upside-down composites and investigated the dielectric properties.

During the research course, all composite materials underwent characterization through microstructural imaging, mechanical testing (B3B), X-ray diffraction, Thermo-gravimetrical analysis, and Fourier-transform infrared analysis.

Additionally, I investigated the influence of residual porosity on the dielectric properties through theoretical modeling, i.e., rules of the mixture. The negative effect of residual porosity was partially mitigated by impregnation with Titanium isopropoxide (TTIP). In addition, OOF2 simulations were used to simulate the polarization and density of electric fields in such composites from the SEM images, and the experimentally observed phenomena were further explained.

Overall, this study's results brought meaningful progress in the field of RTF, which entails almost infinite possibilities of combining different materials for various applications and paves the way to more sustainable electronic production.

# Povzetek

V svoji doktorski disertaciji sem se osredotočila na raziskovanje dielektrično keramičnih kompozitov na osnovi stroncij titanata, $SrTiO_3$ (krajše ST), ki sodi med perovskitne materiale brez svinca in ima velik potencial za uporabo v različnih elektronskih komponentah. Zaradi visoke energetske porabe pri visokotonažni industrijski proizvodnji tovrstnih materialov za elektroniko potrebujemo okolju prijaznejši proizvodni pristop. Kot odgovor na to nudi metoda zgoščevanja pri sobni temperaturi (angleško "Room-temperature fabrication – RTF") potencialno rešitev za znižanje procesnih temperatur z uporabo vodotopnih anorganskih spojin, kot je $Li_2MoO_4$ (LMO). Takšne materiale je mogoče strjevati pri sobni temperaturi, bodisi v obliki enofazne keramike bodisi keramičnih kompozitov.

V svoji doktorski raziskavi sem preučevala vpliv in optimizacijo različnih procesnih parametrov zgoščevanja pri sobni temperaturi (RTF) na LMO-ST in podobnih kompozitnih sistemih. Z uporabo anorganskih soli kot veziva med ST keramičnimi delci sem pripravila »upside-down« obliko kompozitov. V takšnih "narobe obrnjenih" kompozitih spajamo visok delež funkcionalnega keramičnega polnila in majhno količino veziva, tako v obliki prahu kot nasičene vodne raztopine. Vezivo se med stiskanjem in sušenjem odlaga na površini ST delcev, kar na koncu privede do zgoščene tablete.

Spreminjala sem tudi sestavo (delež LMO), kar je vodilo do pretvorbe v t. i. tradicionalne 0-3 kompozite. Poleg tega sem raziskovala tudi druga veziva, kot so $Na_2MoO_4$, $Na_2WO_4$, $Na_2SiO_3$ in $MgSO_4$, ki jih lahko uporabimo namesto LMO. Uporaba le-teh privede do relativne gostote od 81 do 87 % in drugih uporabnih lastnosti, kot npr. dielektrična konstanta med 65 in 130 ter dielektrične izgube med 0,002 in 0,05, ki so bile izmerjene pri 1 MHz in ustreznih resonančnih frekvencah v mikrovalovnem območju (4–6 GHz). Za primerjavo dielektričnih lastnosti sem pripravila tudi kompozite z alternativnim keramičnim polnilom, $BaTiO_3$ (BT). V raziskavah sem uporabila različne metode karakterizacije, npr. mikrostrukturno analizo, mehanske teste (B3B), rentgensko difrakcijo, termogravimetrično analizo in infrardečo analizo Fourierove transformacije.

Dodatno sem raziskovala vpliv poroznosti na dielektrične lastnosti z uporabo matematičnih mešalnih pravil. Negativni učinek poroznosti sem delno omilila z uporabo impregnacije s titanovim izopropoksidom. Za simulacijo polarizacije in električnega polja v takšnih kompozitih iz slik elektronske vrstične mikroskopije sem uporabila program OOF2, ki omogoča razlago eksperimentalno opaženih pojavov. Rezultati te študije prinašajo pomemben napredek na področju RTF, ki vključuje skoraj neskončne možnosti kombiniranja različnih materialov za veliko različnih aplikacij in utira pot k bolj trajnostni proizvodnji elektronike.

# Contents

# List of Figures

# List of Tables

# Abbreviations

| | | |
|---|---|---|
| **JSI** | **...** | "Jožef Stefan" Institute |
| **IPS** | ... | International Postgraduate School |
| **RTF** | ... | Room temperature fabrication |
| **RTD** | ... | Room temperature densification |
| **RT** | ... | Room temperature |
| **RH** | ... | relative humidity |
| **ST** | ... | $SrTiO_3$, strontium titanate |
| **BT** | ... | $BaTiO_3$, barium titanate |
| **BST** | ... | $Ba_{1-x}Sr_xTiO_3$, barium strontium titanate |
| **PZT** | ... | $PbTi_{1-x}Zr_xO_3$, lead zirconium titanate |
| **LMO** | ... | $Li_2MoO_4$, lithium molybdate |
| **NMO** | ... | $Na_2MoO_4$, sodium molybdate |
| **NWO** | ... | $Na_2WO_4$, sodium tungstate |
| **NSiO** | ... | $Na_2SiO_3$, sodium silicate |
| **MSO** | ... | $MgSO_4$, magnesium sulfate |
| **TTIP** | ... | titanium(IV) isopropoxide |
| **ATTH** | ... | amorphous titania–titanium tetra hydroxide |
| **ss** | ... | saturated solution |
| **CS** | ... | Cold sintering |
| **HP** | ... | Hot-pressing |
| **HIP** | ... | Hot-isostatic pressing |
| **HHP** | ... | Hydrothermal hot-pressing |
| **HA** | ... | Heat-assisted (pressing) |
| **RF** | ... | Radiofrequency range |
| **EF** | ... | Electric field |
| **LCR** | ... | Inductance (l), Capacitance (C), and Resistance (R) meter |
| **MLCC** | ... | Multilayer ceramic capacitors |
| **AC** | ... | Alternating current |
| **IoT** | ... | Internet of Things |

| | | |
|---|---|---|
| **5G, 6G** | ... | fifth generation of wireless cellular technology, sixth-generation wireless |
| **DR** | ... | Dielectric resonator |
| **Q** | ... | Quality factor |
| **$TE_{01\delta}$** | ... | Transverse electric mode |
| **SEM** | ... | Scanning electron microscope |
| **TEM** | ... | Transmission electron microscope |
| **ROM** | ... | Rules of Mixtures |
| **MG** | ... | Maxwell Garnet |
| **NIST** | ... | National Institute of Standards and Technology |
| **CTCMS** | ... | Centre for Computational and Theoretical Materials Science |
| **OOF2, OOFEM** | ... | Object-oriented finite element analysis |
| **B3B** | ... | The Ball on Three Balls (mechanical test) |
| **FTIR** | ... | Fourier transformed Infrared Spectroscopy |
| **DRIFT** | ... | Diffuse Reflectance Infrared Fourier Transform Spectroscopy |
| **TG-MS** | ... | Thermogravimetric analysis/Mass spectroscopy |
| **XRD** | ... | X-ray diffraction |
| **CA** | ... | Contact angle |
| **QWED** | ... | Quick Wave Software for electromagnetic design and simulations |
| **GIMP** | ... | GNU Image Manipulation Program |
| **ICDD** | ... | The International Centre for Diffraction Data |
| **N/A** | ... | not applicable/available |

# Symbols

| | | |
|---|---|---|
| $\boldsymbol{\rho}$ | ... | density |
| $\boldsymbol{\rho}$ | ... | free space charge |
| $\boldsymbol{\varepsilon_r}$ | ... | relative permittivity, dielectric constant |
| $\boldsymbol{tan\ \delta}$ | ... | dielectric losses |
| $\boldsymbol{D}$ | ... | dipole moment |
| $\boldsymbol{E}$ | ... | electric field |
| $\boldsymbol{W}$ | ... | energy density of the electric field |
| $\boldsymbol{P}$ | ... | polarization |
| $\boldsymbol{Q}$ | ... | charge |
| $\boldsymbol{Q}$ | ... | quality factor |
| $\boldsymbol{f}$ | ... | frequency |
| $\boldsymbol{C}$ | ... | capacitance |
| $\boldsymbol{U}$ | ... | voltage |
| $\boldsymbol{A}$ | ... | area (of a dielectric) |
| $\boldsymbol{\tau_f}$ **or** $\boldsymbol{TCF}$ | ... | temperature coefficient of resonant frequency |
| $\boldsymbol{\Delta f}$ | ... | bandwidth |
| $\boldsymbol{T_c}$ | ... | the Curie temperature |
| $\boldsymbol{T_s}$ and $\boldsymbol{T_m}$ | ... | the sintering temperature, the melting temperature |
| $\boldsymbol{t}$ | ... | the Goldschmidt tolerance factor |
| $\boldsymbol{t}$ | ... | time |
| $\boldsymbol{r_A}$,$\boldsymbol{r_B}$ | ... | the radius of the A-cation, the radius of the B-cation |
| $\boldsymbol{r_X}$ | ... | the radius of the X anion |
| $\boldsymbol{\Delta L/L_0}$ | ... | sintering rate (or linear shrinkage) |
| $\boldsymbol{\gamma}$ | ... | surface energy |
| $\boldsymbol{a^3}$ | ... | the atomic volume of diffusing vacancy |
| $\boldsymbol{D^*}$ | ... | self-diffusion coefficient |
| $\boldsymbol{K}$ | ... | geometry-dependent constant |
| $\boldsymbol{k}$ | ... | the Boltzmann constant |

| | | |
|---|---|---|
| $d$ | ... | diameter |
| $h$ | ... | thickness |
| $\nu_c$ or $\nu_b$ | ... | the Poisson's ratio of composite or binder |
| $\sigma_{max}$ | ... | the maximum stress occurring at the center of the specimen |
| $F_{max}$ | ... | the maximum fracture load |
| $f$ | ... | a dimensionless factor that depends on the Poisson's ratio and the loading and specimen geometry |
| $\alpha$ | ... | the scale parameter (disc geometry) |
| $\beta$ | ... | the shape parameter (support geometry) |
| $R_a$, $R_b$ | ... | a supporting radius ($R_a$), which is related to the radius of the balls ($R_b$) |
| $P$ | ... | the probability of failure at a certain stress $\sigma$ |
| $m$ | ... | the Weibull modulus |
| $\Phi$, $p$, $P$ | ... | porosity |
| $x$ | ... | width of a pellet |
| $\theta$ | ... | contact angle |

# Chapter 1

# Literature Review and Theoretical Background

## 1.1 Green Energy Requirements

Energy is one of the most critical and debated topics in the 21st century. The rising demand to reduce reliance on energy derived from coal, petroleum, and natural gas is driving the need for environmentally friendly and clean energy alternatives. The crude production of fossil fuels has extended over a million years, and it cannot keep pace with daily depletion. The main drawback of fossil fuels lies in their accompanying emission of $CO_2$ and other pollutants, as well as damaging mining and digging techniques, which substantially affect natural ecosystems and threaten human health. New, alternative, non-polluting energy sources must be implemented to safeguard our environment and way of living. Green energy, derived from sources such as the sun, wind, water, heat, and vibration, is often strongly influenced by seasonal conditions. Efficient storage solutions are crucial after energy harvesting to ensure its potential use as a reliable energy source. This results in the high demand for devices that effectively store produced electrical energy. The concept of energy storage traces back to ancient times. It is very natural, i.e., making fire using wood and charcoal, biomass energy storage carriers of solar energy. Modern energy storage materials play a vital role in the versatile utilization of renewable energy. They have been the subject of significant attention, ranging from intensive research and development to their successful integration into industrial applications [1]. Commercial energy storage devices are generally divided into short- and long-term (battery). Capacitors and batteries represent the typical energy storage devices that differ in the capacity for storing energy and delivery of power. Energy can be stored under an electric or magnetic field. Two factors defining an energy storage device's capabilities and practical applications are energy density and power density, which are both materials-dependent. High energy density (10-300 Wh/kg) and moderate power density (<500 W/kg) are typical for batteries due to the slow movement of the charge carriers. On the other hand, capacitors usually possess high power density (~$10^4$ – $10^8$ W/kg) and low energy density (<30 Wh/kg) [2]. Capacitors and resonators are the primary fields of interest in terms of application tackled in this doctoral study. There are different types, such as double-layer, ultra-capacitors, supercapacitors, electrolytic capacitors, and multilayer ceramic capacitors (MLCCs) [3]. Capacitors belong to the category of passive electronic devices, which are widely utilized in electronics. More than 1 trillion MLCCs based on barium titanate are produced yearly [4]. The main demands for future electroceramics are high energy density (W>10 J $cm^{-3}$), a more comprehensive temperature stability range (–50 °C to 250 °C), high power density, fatigue resistance, lifetime reliability, and low manufacturing cost. Generally, the energy storage properties of

electroceramics are strongly related to microstructural characteristics such as density, grain and particle size, and secondary phases. Energy density can be optimized with an insulator's increased intrinsic band gap and higher density [2].

## 1.2 State-of-the-art in Electroceramics

### 1.2.1 Dielectric behavior of ceramics

Electroceramics are a class of advanced ceramic materials extensively used in the technical sector due to their unique properties. These properties include dielectric, piezoelectric, ferroelectric, pyroelectric, and thermoelectric properties, as well as electromechanical coupling and magnetic, electrocaloric, optical, mechanical, and catalytic properties [5],[6]. In microelectronics circuitry, many electronic components are integrated into a small space. A small component requires low power and hence not only facilitates the miniaturization of electronic devices but also reduces fabrication and processing costs for a wide range of electronic applications, many of them depicted in Figure 1.1 [7].

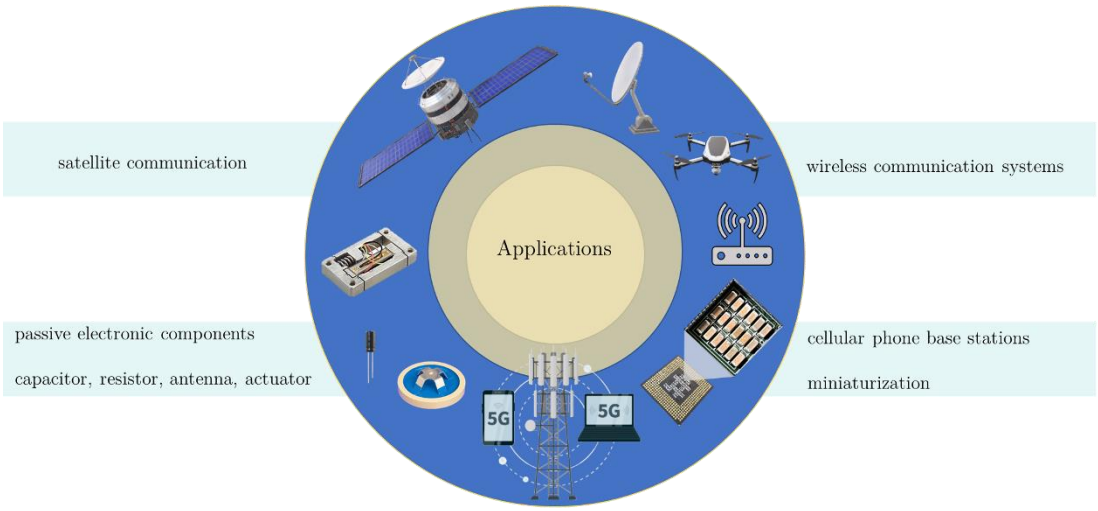


Figure 1.1: Applicative potential of dielectric ceramics.

A dielectric material is an electrically insulating material. One of the main characteristics is an electric dipole structure, which corresponds to the separation of positive and negative electrically charged centers on a molecular and atomic scale. The dipole moment is a vector pointing from negative to positive charge, which orients and interacts with the applied external electric field. The phenomenon of electric dipole alignment under an external electric field is so-called polarization. Polarization is directly proportional to the material's ability to store energy in the electric dipoles. Dielectric materials typically exhibit at least one of the four types of polarization: electronic, ionic, and orientation, as well as space charge polarization. The polarization and capacitance of materials are generally represented by a property called relative permittivity ($\varepsilon_r$ ). Relative permittivity, also known as the dielectric constant, is defined by the ratio of electric field strength, $E$, to electric flux density, $D$, as represented by the following equation (1.1).

$$\varepsilon_r = \frac{D}{\varepsilon_0 E} = \frac{C}{C_0} \tag{1.1}$$

It can also be expressed as the ratio of capacitance between capacitors of equal dimensions, where $C$ represents the capacitance of a capacitor filled with the material of interest, and $C_0$ is the capacitance of the reference/empty capacitor. Capacitance is defined as the quantity of charge stored on the plate divided by the voltage applied across a capacitor. As such, an increase in $\varepsilon_r$ represents an equal relative increase in charge stored in a capacitor at a given voltage and, thus, an increase in energy storage. It is a function of polarization and strongly depends on the field frequency range (radio frequency range (RF): usually 20 Hz – 1 MHz). In particular, $\varepsilon_r$ of a material defines how fast the electrical signal travels through it. Another facet of characterizing the dielectric properties of ceramics involves determining the quantity of electrical energy absorbed by a dielectric material when subjected to an electric field. Materials do not behave ideally and thus lose energy due to dissipation or scattering. The latter effect occurs as the electromagnetic wave propagates through a particle, interacts with the atoms, and deviates from the original direction. This scattering causes the wave to lose some of its energy. Depending on the type of material it interacts with, and the wavelength of the incoming wave, various phenomena like reflection, refraction/transmission, diffraction, or absorption can occur as a result [8]. Another factor that affects the overall energy loss is scattering caused by the oscillation of dipoles. The magnitude of dissipation is expressed as dielectric loss tangent ($tan\ \delta$). It can be affected by various factors such as electrical conduction, dielectric relaxation, dielectric resonance, non-linear processes, and crystal structure, which define the interaction with AC electric field. Furthermore, imperfections and impurities in crystal lattice, microstructural defects, porosity, cracks, random grain orientation, grain boundaries, dislocations, etc., can result in dielectric losses.

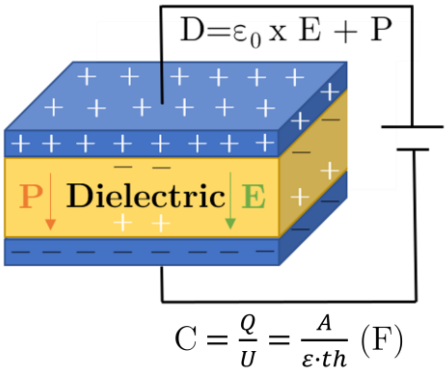


Figure 1.2: Dielectric in electric field.Adapted from [2].

Experimentally, the dielectric properties of a material, $\varepsilon_r$, and tan $\delta$ at radio- frequencies can be determined by the parallel plate capacitor method using an LCR meter. Due to the extensive motion of electrons, irreversible degradation of material or dielectric breakdown can occur at a high external electric field (RF). Dielectric strength corresponds to the magnitude of an EF, resulting in a breakdown [9].

The primary reason for dielectric materials to find applications in capacitors is their ability to interact with external electric fields. In the scope of this work, I focused on a parallel-plate capacitor consisting of one plate that becomes positively charged and the other that is negatively charged in the presence of applied voltage.

Most known and commercially used dielectric materials used for electronic or energy-storage applications are either lead-based ceramics (relaxor ferroelectrics as $Pb(Mg_{1/3}Nb_{2/3})O_3$–$PbTiO_3$, and antiferroelectrics as $PbZrO_3$, (Pb, La)(Zr, Ti)$O_3$, or lead-free ceramics based on $BaTiO_3$ (BT), $SrTiO_3$ (ST), $K_{0.5}Na_{0.5}NbO_3$, $Na_{0.5}Bi_{0.5}TiO_3$, $AgNbO_3$,

$NaNbO_3$ etc., which exhibit high energy density and high energy conversion efficiency [7]. Lead-free ceramics have gained a foothold in recent years due to the toxicity of lead/lead oxide-based compounds. As reported in the literature, a wide range of applicative properties with BT-based ceramics can be achieved by doping or substituting oxides with $Al_2O_3$, $La_2O_3$, MgO, $Nb_2O_5$, $Mn_2O_3$, $SiO_2$ and utilizing different sintering techniques and sintering aids. ST-based ceramics are well-known for being incipient ferroelectrics, demonstrating remarkable properties such as a high relative permittivity ($\varepsilon_r \sim 300$) and low dielectric loss ($< 1$ %) at room temperature (RT). Common approaches utilized to optimize the energy storage properties of ST-ceramics are doping with Ba-, Mg-, Ce-, Bi- on the A site or Mn, Sn- on the B site and using various sintering aids and sintering techniques. Other members of lead-free ceramics are $K_{0.5}Na_{0.5}NbO_3$-based ceramics and $Na_{0.5}Bi_{0.5}TiO_3$—based ceramics [2].

#### 1.2.1.1 Microwave dielectric properties

In the Internet of Things (IoT) era, we are facing increasing demand for improving wireless technologies such as faster Internet access, higher data rates, larger network capacity, lower battery consumption, etc. In response, fifth and sixth-generation (5G, 6G) cellular network technologies are emerging and require components with lower power consumption, which corresponds to dielectric loss $< 0.001$, shorter delay times, or latency when sending data, which is strongly related to the relative permittivity of materials [10], [11],[12]. Microwave materials encompass dielectric resonators (DR), filters, electromagnetic interference shielding materials, tunable dielectrics, polymer-ceramic and all ceramic composites, etc. DR operates in a micro- and milli-frequency range and can be integrated into various devices such as oscillators, bandpass and band-stop filters, and dielectric resonator antenna. Traditionally, DRs are fabricated with high-temperature solid-state synthesis. In this study, I present an alternative approach to fabricate DR materials at low temperatures.

In the microwave frequency range, the most common measure of the power loss is described by the quality factor, $Q$, which is in the case of materials with perovskite structure mostly simplified to be inversely related to $tan\ \delta$. This relation is true and can be applied when conduction, radiation, and external loss are negligible. $Q$ factor can be expressed in the following Equation (1.2).

$$Q = 2\pi \frac{maximum\ energy\ stored\ per\ cycle}{average\ energy\ dissipated\ per\ cycle} \tag{1.2}$$

Experimentally, microwave materials are characterized by their dielectric properties through transmission and reflection methods. For instance, the resonant cavity $TE_{01\delta}$ mode method appears to be the most accurate measurement technique suitable for high $\varepsilon_r$ materials, but it is applicable only in a narrow frequency band. Using $TE_{01\delta}$ mode, the effect of conductor and radiation losses are easily bypassed, as the sample is isolated using low-loss single-crystal quartz or Teflon spacer inside the cavity, represented in Figure 1.3 a). To prevent perturbation of the electromagnetic field, the cavity size should be large enough (typically 3–5 times larger than the test sample). The loaded $Q$ factor ($Q_L$) can be identified from the shape of the resonance peak (Figure 1.3 b)). The bandwidth (also marked as $\Delta f$) describes the width of the resonance curve read 3 dB down from the peak, while the peak frequency corresponds to the resonant frequency, f. The $Q$ factor is derived from the f divided by $\Delta f$ (Equation (1.3)).

$$Q_L = \frac{f}{\Delta f} \tag{1.3}$$

In the composite system containing two or more dielectric materials, the $Q$ factor appears as a sum of dielectric losses in all particular dielectric regions. The total loss of the system or the loaded Q-factor is thus described by the equation (1.4):

$$\frac{1}{Q_L} = \frac{1}{Q_d} + \frac{1}{Q_c} + \frac{1}{Q_r} + \frac{1}{Q_{ext}} \tag{1.4}$$

$Q_L$ factor hence represents the energy dissipation within the entire measurement system, which encompasses the sample material and the measuring instrument. *It* is associated with the sum of other $Q$-factors, each describing a different source of losses i.e. ($1/Q_{\mathrm{d}}$ as dielectric losses, $1/Q_{\mathrm{c}}$ as losses due to conductivity, $1/Q_{\mathrm{r}}$ as the radiation loss, $1/Q_{\mathrm{ext}}$ as the external losses). Moreover, there are external losses are coming from the external coupling between the resonator and feed. The radiation loss is neglected because most resonant cavities are shielded and cause no radiation effect. The desired quantity for most applications is the unloaded quality factor $Q_{\mathrm{u}}$, which is defined by the energy dissipation associated with the material itself [9].

$Q_{\mathrm{u}}$ represented in Equation (1.5) can not be measured directly but can be estimated from the $Q_L$ measurements.

$$\frac{1}{Q_u} = \frac{1}{Q_d} + \frac{1}{Q_c} + \frac{1}{Q_r} \tag{1.5}$$

$Q_{\mathrm{u}}$ can be also calculated by considering the voltage reflection coefficient $\beta$, and return loss, RL, which is further described in the equation (1.6)[13]:

$$Q_u = Q_L\,(1+\beta) = Q_L\left(1 - 10^{-\frac{RL}{20}}\right) \tag{1.6}$$

Where $\beta$ is a coupling factor defined by Equation (1.7),

$$\beta = \frac{1}{\frac{D}{d}-1} = \frac{1}{\Gamma} \cong \frac{1}{S_{11}} \tag{1.7}$$

Where D is the diameter of the Polar/Smith chart, defined by Kajfez (D = 2 Units), that is, d is the diameter of the touching circle between $S_{\mathrm{v}}$ and $S_{\mathrm{T}}$ [13], [14].

Experimentally, $Q_L$ is estimated from the shape of the resonance peak, where the bandwidth is defined as the width at −3 dB. The resonant frequency (at the peak) is divided by this width according to the equation (1.3).

QWED software computations based on Krupka method [15] are further used to obtain $\varepsilon_{\mathrm{r}}$ and $tan\ \delta$.

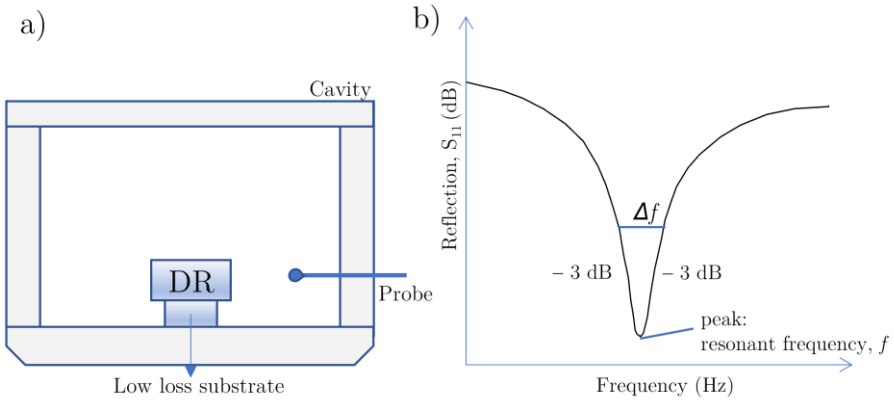


Figure 1.3: a) A microwave cavity measurement setup. b) The $TE_{01\delta}$ resonant peak (reflection mode). Adapted from [9].

From an applicative point of view, DR should exhibit high $Q$ values, high relative permittivity, and low-temperature coefficient of resonant frequency($\tau_f$) in the microwave range. The resonant frequency is mainly influenced by the physical dimensions of the ceramic resonator and the dielectric constant of the material. In fact, resonant frequency tends to decrease with the increase in relative permittivity of the material. Functional properties of materials suitable for DR application can be measured using different techniques, mainly size-, shape- and material property-dependent. Miniaturization of devices is possible by employing high $\varepsilon_r$ because the wavelength in the dielectric material is inversely proportional to the square root of material permittivity. When microwaves penetrate a dielectric material, they experience a reduction in their speed, approximately proportional to the square root of the material's permittivity. Consequently, this leads to a corresponding decrease in wavelength while the frequency remains unchanged. Ionic and electronic polarization mechanisms contribute strongly to the net dipole moments in the microwave frequency range [9],[16],[17].

## 1.3 Perovskite Ceramics

Perovskite materials exhibit a versatile and vast application potential, from future low-cost solar cells to next-generation electronic components [18], [19]. Such materials have diverse properties anywhere between ferroelectricity and superconductivity [20]. Perovskite structure was first observed in the 1920s in the mineral calcium titanate $CaTiO_3$, with the general formula $ABX_3$ and a three-dimensional network of the corner-sharing $BX_6$ octahedra. The perovskite structure can accommodate most metallic ions in the periodic table and various anions. The most commonly found materials exhibiting perovskite structure are oxides and fluorides. However, heavier halides and oxynitrides are also possible. The first breakthrough of perovskites came during the 1940s due to their exceptional ferroelectric properties [21]. The first reported use was a capacitor made from $BaTiO_3$ ceramics.

Perovskite materials can form different crystal structures based on the size and interaction of the A cation and the $BX_6$ octahedra. Perovskite structure consists of a large cation, A, similar to an anion, and a smaller cation, B. Two different-sized cations, A and B in $ABX_3$, allow many possible cations charge combinations, which enable a wide range of compositions [22], [23]. In structures, where sites are occupied by more than one species,

the effective ionic size is determined as a weighted average. If there are stoichiometric vacancies, they are assumed to have a size of 0 [24].

Due to A and B cations being different in size, structural distortions can occur. The dominance of certain types of perovskite structures is directly related to the inherent ability of octahedral tilt distortion with respect to the size mismatch between the A and B cations. The presence and magnitude of octahedral tilt distortion not only affects the crystal structure but also has a great influence on many physical properties [23]. Goldschmidt tolerance factor ($t$) is an empirical index, which is defined by the size (the ionic radius) of A-, B-, and X- ions of the atoms using the following formula (Equation (1.2)):

$$t = \frac{r_A + r_X}{\sqrt{2}(r_B + r_X)} \tag{1.2}$$

here $r_A$ is the radius of the A cation, $r_B$ is the radius of the B cation, and $r_X$ is the radius of the anion, as reported by Shannon [25]. Based on $t$-values varying between 0.8 and 1.1 for perovskite-structured materials, one can predict the preferential formation and stability of the perovskite structure. The lowest $t_0$ reported for oxide perovskites is 0.8465.[24],[26]. Structural changes, which are temperature and pressure-dependent, cause ferroelectricity – the most practically exploited and unique property of perovskites. The most known perovskite materials are titanates such as $PbTi_{1-x}Zr_xO_3$ (PZT), $BaTiO_3$ (BT), $Ba_{1-x}Sr_xTiO_3$ (BST), and $SrTiO_3$ (ST), with their specialty being the non-centrosymmetric structure in a specific temperature range [20], [22].

### 1.3.1 Strontium titanate, $SrTiO_3$

Strontium titanate (ST) is a typical ferroelectric material with a perovskite structure $(Pm\bar{3}m)$ presented in Figure 1.4, which exhibits beneficial functional properties for their application to microelectronics. ST possesses an ideal perovskite structure. Ideal perovskites are usually cubic but may be ordered or distorted, resulting in tetragonal, orthorhombic, rhombohedral, or hexagonal structures varying as a function of composition. In a cubic structure, the large cation (at cube corner position (0, 0, 0)) connects the anions in a close-packed arrangement with coordination number 12, where smaller cations occupy 1b (½,½,½) sites. The bond distance Ti-O is 1.953 Å, while Sr is equidistant from 12 oxygens, which means that Sr-O distance is half of the diagonal of any cell face (2.76 Å) [27]. Either cation or anion vacancies, as well as cation and anion substitutions, are the origin of defects in perovskites. By adjusting the composition, the optimization of properties in perovskite-related materials can be achieved.

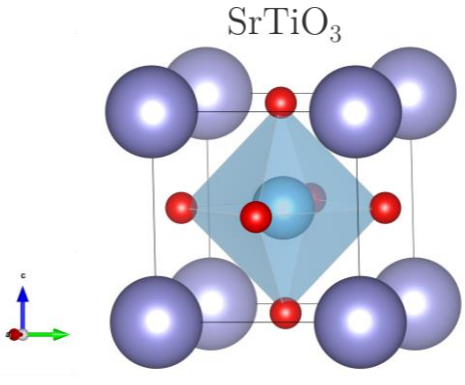


Figure 1.4: The schematic of $ABO_3$ perovskite structure of ST.

### 1.3.2 Barium titanate, $BaTiO_3$

In ferroelectric $BaTiO_3$ (BT), as a typical member of the perovskite family, each Ba ion is enclosed by 12 oxygen ions, forming a face-centered tetragonal lattice ($P4mm$) at RT (Figure 1.5 b)). Titanium ions occupy octahedral interstitial positions surrounded by six oxygen ions. Titanium ions have a +4 charge and a consequent high degree of polarization. $Ti^{4+}$ ions, in comparison with $Ba^{2+}$ ions, are too small to remain stable in an octahedral position, which results in the spontaneous polarization of $Ti^{4+}$ ions. In the applied electric field, $Ti^{4+}$ ions can relocate from random to aligned positions, contributing to high polarization and producing a high dielectric constant. BT is tetragonal at room temperature, $a = 3.995$ Å, $c = 4.034$ Å [27]. The cubic ($Pm\bar{3}m$) structure of BT is shown in Figure 1.5 a). The structure of ST is analogical to BT above $T_c$.

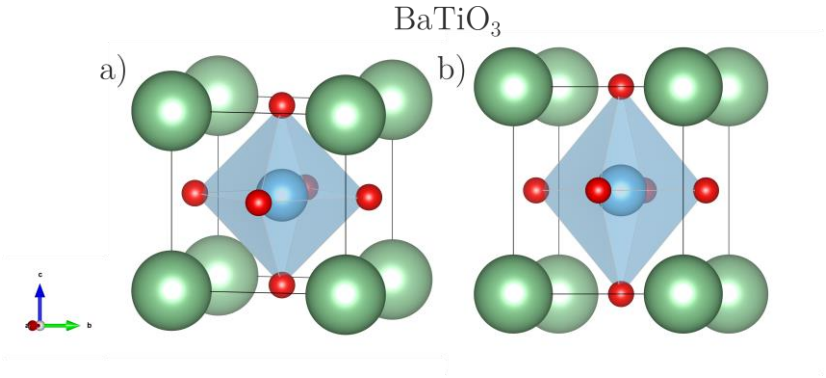


Figure 1.5: The schematics of $ABO_3$ perovskite structure of BT:a) cubic structure; b) tetragonal structure.

Temperature can substantially affect crystal structure and, thus, polarization characteristics of BT-like materials. BT can occur as a cubic structure above Curie temperature ($T_c$), which changes upon cooling to tetragonal (120 °C), where there is sufficient thermal vibration causing random orientation of Ti ions. A permanent dipole is formed when the octahedral site is altered with $Ti^{4+}$ ion in an off-center position. The Curie temperature is a temperature where phase transition and change of spontaneous polarization to permanent dipole occur. Temperature strongly depends on stoichiometry and grain size. Therefore, tailored polarization characteristics can be achieved by crystal chemical modifications [28].

#### 1.3.2.1 Ferroelectricity and piezoelectricity in BT and ST

As perovskite materials have exceptional electrical properties, it is essential to point out ferroelectricity and piezoelectricity. Spontaneous polarization, which occurs due to the positioning of ions within the unit cell, is typical for ferroelectrics. Above Curie temperature, the ions within the unit cell acquire symmetric positions in a perovskite structure. On the other hand, in piezoelectrics, electric polarization is induced due to mechanical stress, which results in their use as transducers between electrical and mechanical energies. For example, the piezoelectricity of PZT is a consequence of the off-center displacement of cations and anions in opposite directions (with respect to the cubic structure). In PZT, this causes a permanent polarization that can be changed under applied load or by a temperature change (pyroelectric effect) [21], [7], [29]. Piezoelectrics undergo spontaneous polarization only when exposed to an external stress (direct piezoelectric effect). On the other hand, piezoelectric materials will deform under the applied field (converse piezoelectric effect) [30]. However, it is important to note that not all

piezoelectrics are also pyroelectrics. In pyroelectrics, the magnitude of polarization can be changed with temperature.

The ferroelectric behavior of ceramics (ST, BT) strongly depends on their crystal structure. To achieve ferroelectric behavior, a material should exhibit a non-centrosymmetric crystal structure. Ferroelectricity in the perovskite structures of ST and BT occurs due to limited atomic displacements in $TiO_6$ octahedra, resulting in a consequent net polarization and formation of dipole moments. In BT, Ti ions in adjacent unit cells experience a similar displacement in the same direction, which, when exposed to external EF, move through the center of the octahedral site in the direction of one of the corner oxygen. Such reversibility of the structure results in high polarizability and permittivity [27]. Furthermore, an increased strength of external EF results in increased induced polarization and stored charge. The relation between polarization behavior and voltage is not linear and follows a form called a hysteresis loop. A hysteresis is formed when electric polarization follows EF with a delay up further to the transition point of saturation. Polarization in such materials can be reversed by applying an electric field [31]. BT exhibits ferroelectricity in tetragonal, orthorhombic, and rhombohedral structures [32]. Above the Curie temperature 120 °C), BT behaves as a paraelectric [28]. In comparison to BT, ST is a paraelectric at RT. It is also considered incipient ferroelectric, which means that a small amount of energy and/or dopants are required to transfer ST to a ferroelectric phase. The tetragonal distortion of the cubic structure in ST occurs at −168 °C [33]. However, under strain forces (application of EF), ST converts to a ferroelectric phase (T ~ −269 °C). Furthermore, sufficient concentration of dopants also results in ferroelectric phase transition in ST [34], [35]. In such transformation, ferroelectricity is induced by the dopant ions' off-center position and the dipoles' interaction. The ST crystal lattice possesses a very high polarizability. Dopants or impurities (concentration ~ $10^{-2}$-$10^{-3}$), as displacements in ST lattice, can initiate a ferroelectric state due to the interaction of dipole moments formed or elastic strains (uniaxial compression at only 1 kbar) that appear in the proximity of a dopant ion [36],[37],[38]. The ferroelectric order of ST can be further stabilized with $^{18}O$ isotope substitution [39].

Most ceramics applications are used at low operating temperatures. In practical use, dopants have been introduced to the main ceramic components, such as ST and BT, to lower the phase transition temperature and widen the relative permittivity range of the capacitor. One of the simplest ways is to substitute some Sr atoms for Ba atoms. ST exhibits the maximal relative permittivity at about −253 °C. Doping can lead to a possible maximum of permittivity in a temperature range between −253 °C–122 °C. The ratio between Sr and Ba in $Ba_{1-x}$ $Sr_xTiO_3$ (BST) determines the maximum permittivity. At temperatures above $T_c$, materials are in a paraelectric state, where no spontaneous polarization occurs [38], [40].

### 1.3.3 Structural defects

The overall performance and reliability of ceramics are determined by microstructural features such as (grain size and shape, porosity, grain boundaries, phase assemblage, etc) and chemical composition [41]. In addition, the influence of intragranular, planar (2D), linear (1D- dislocations), and point defects (0D) should not be neglected. Schottky and Frenkel defects are intrinsic point defect structures that can occur at RT due to entropy in a crystal, though their number increases with temperature. Point defects are strongly related to crystal structure, composition, temperature, and doping (extrinsic defects). In addition, their concentration can critically influence the properties of electroceramics. Schottky defects occur as cation and anion vacancies. Frenkel defects are linked defect pairs consisting of the vacancy and interstitial. Thus, they are formed when an atom is

moved from its lattice site onto an interstitial site (on both cation and anion sublattices). This type of defect is not common in perovskite structures. On the other hand, linear dislocations are less common in electroceramics; they are induced mainly by stress (wear) or high temperatures. Planar defects occur with a large probability due to translation (stacking faults), orientation, and inversion. An important example of planar defects is grain boundaries, which are open structures exposed to the segregation of impurities. The atom transport rate across and along interfaces at grain boundaries can be varied in such a way as to increase the densification rate, promote rapid grain growth in microstructure, and tailor properties. In addition, 3D defects refer to porosity (secondary grain growth). Such extrinsic factors that increase dielectric losses of electroceramics can be successfully reduced by proper material processing [9],[42]. Schottky defects in ST mostly consist of nominally charged Sr, Ti, and O vacancies and are referred to as the most stable ST-based defect structure. Such defects occur under various chemical conditions and composition changes, i.e., the SrO excess results in the formation of oxygen vacancies and a strontium–titanium anti-site defect. The point defects, such as oxygen vacancies and cation anti-site defects, are strongly related to the functionality of ST [43].

## 1.4 Connectivity Patterns in Ceramic Composites

Progressing interest in particulate composites gained a foothold in recent years as these multi-phase systems often yield an advantageous blend of properties of individual diverse materials. There are different types of composites, such as ceramic–ceramic, ceramic–polymer, and metal-polymer. In this work, I focused on ceramic-ceramic composites. A composite is a system where materials with significantly different physical or chemical properties are mixed to achieve advanced properties. When combining materials, it is vital to choose constituent phases with the desired properties and couple them in the most optimal way. A comprehensive understanding of the three-dimensional microstructure of such multi-component materials is strongly related to the interconnectivity between their individual constituents and can greatly influence overall effective performance. Connectivity can be attributed to the interfacial relationship of the major filler phase with the surrounding two phases, such as binder and air in pores, which affects mechanical and electric fluxes between the phases. Indeed, physical properties can change considerably depending on the manner of connection formation. The degree of connectivity is commonly determined by the number of dimensions (out of the standard three orthogonal spatial directions) in which each phase is self-connected [44]. Each phase in a composite system can be self-connected in zero, one, two, or three dimensions. There are 10 possible connectivity patterns for a two-phase and 20 possible connectivity patterns for a three-phase composite system. The number of connectivity patterns is defined as $(n + 3)!/3!n!$, where $n$ represents the number of phases [8], [44]. The most common is a 0-3 connectivity pattern, where 0-dimensional isolated filler particles are randomly distributed in 3 dimensions of the continuous host matrix. Such connectivity pattern is mostly utilized in ceramic-polymer composites [45].

The 2-2 connectivity pattern, often used in tape-casting, consists of alternating layers of the two phases. In the 3-2 connectivity, one phase is three-dimensionally connected, and the other phase is two. The 3-3 connectivity pattern is the most challenging and interesting, where the two phases form interpenetrating 3-dimensional networks. It is commonly found in living systems, such as corals [44]. The 0–3, 1–3, and 2–2 connectivity patterns are the most researched as such composites are easy to prepare and low-cost [8]. Nelo et al. introduced the term upside-down 0-3 composite, which relies on maintaining the high loading of ceramic filler with a small amount of the corresponding binder. In such a

composite system, the matrix is formed from a ceramic filler, hence the term "upside-down"[46]. In this doctoral study, the primary binder used was $Li_2MoO_4$ and ceramic filler $SrTiO_3$. Both upside-down and conventional 0-3 types of composite are represented in Figure 1.6. Increasing filler content is beneficial in terms of the dielectric performance of the composite.

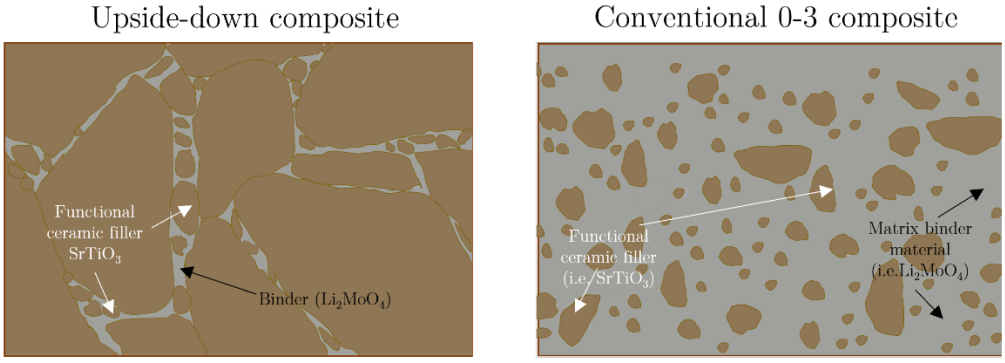


Figure 1.6: Schematics of upside-down 0-3 (left) and 0-3 composite (right).

## 1.5 Binders in Ceramic Composites

### 1.5.1 Lithium molybdate (LMO)

The crystal structure of lithium molybdate is composed of a three-dimensional arrangement, where corner-linked $LiO_4$ and $MoO_4$ tetrahedra are slightly distorted. $Li_2MoO_4$ (LMO) can be synthesized at RT by combining $MoO_3$ and LiOH x $H_2O$, resulting in a highly crystalline ternary phase [47]. LMO has a density of 2.66 g/cm$^3$ [48]. LMO exhibits a broad applicative spectrum, i.e., it can be used as a corrosion inhibitor [49], an effective catalyst for the oxidation of methane [50], or in the form of LMO composites with carbon nanofibers as an anode material for lithium-ion batteries [51]. LMO ceramics sintered at 540 °C for 2 h resulted in a relative density of 95.63 % and excellent microwave dielectric properties ($\varepsilon$ = 5.58, $Q_f$ = 49,328 GHz, *TCF or* $\tau_f$ = -168 ppm/°C at f = 10.17 GHz) [52]. LMO combined with $BaFe_{12}O_{19}$ was successfully cold-sintered at 120 °C and exhibited dielectric properties of $5.6 \leq \varepsilon \leq 5.8$, $Q$ =16,000-22,000 GHz at ~6 GHz [53].

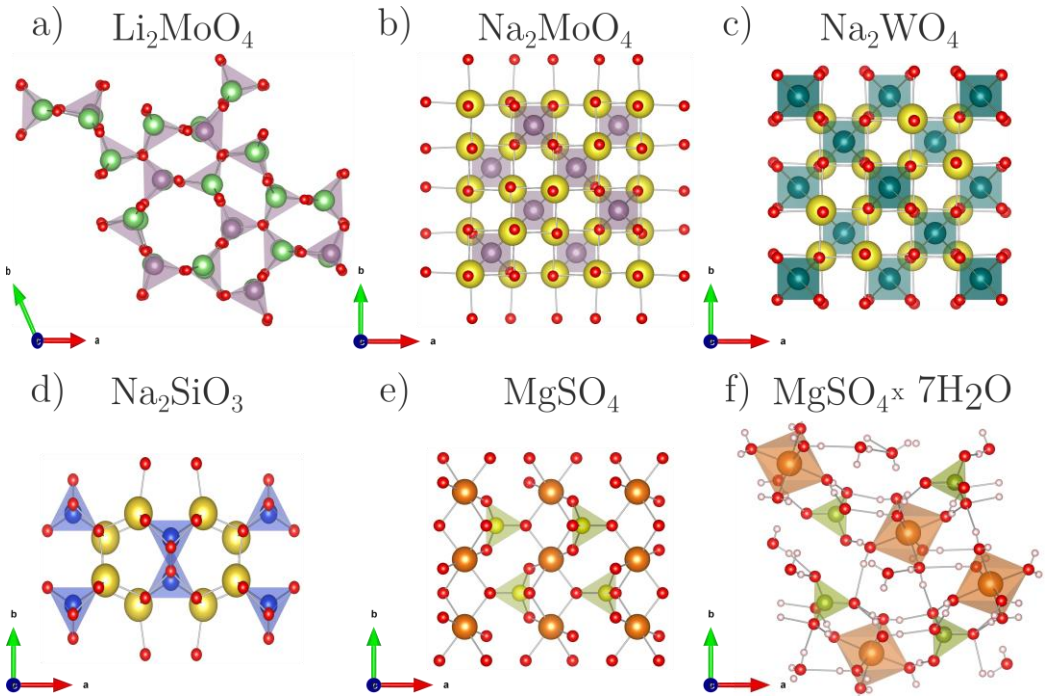


Figure 1.7: Crystal structures of binders. a) $Li_2MoO_4$, b) $Na_2MoO_4$, c) $Na_2WO_4$, d) $Na_2SiO_3$, e) $MgSO_4$, f) $MgSO_4$ x $7H_2O$.

### 1.5.2 Sodium molybdate (NMO)

$Na_2MoO_4$ (NMO) is a white, crystalline salt, which can exist in either anhydrous or dihydrate, $Na_2MoO_4 \cdot 2H_2O$ form and exhibits a density of 3.78 g/cm$^3$, a solubility of 65.3 g/100 mL of water (25 °C) [48]. NMO has a spinel-type structure with a network formed by a molybdenum oxygen polyhedron and sodium oxygen polyhedron (Figure 1.7 b)). As reported, NMO can be synthesized at 400 °C and exhibit interesting dielectric properties ($\varepsilon_r \sim 4.1$, $Q \times f \sim 35{,}000$ GHz, *TCF or* $\tau_f = -76$ ppm/°C, $\rho$=90 %) when sintered at 660 °C for 4 h [54]. Commercially, it can be used as fertilizer [55], corrosion inhibitor [56], heterogeneous catalyst for methanolysis [57]. Similarly, $Na_2MoO_7$ has been successfully cold-sintered at 200 °C, 350 MPa for 1 h, resulting in an orthorhombic crystal structure [58].

### 1.5.3 Sodium tungstate (NWO)

$Na_2WO_4$ (NWO) crystallizes in the rhombohedral crystal structure. In the presence of water, it tends to form orthorhombic di-hydrates. It has a density of 4.18 g/cm$^3$ and a solubility of 74.2 g/100 mL of water (25 °C). Figure 1.7 c) shows the crystal structure of NWO with $Na^+$ ions on the 16 c sites in octahedral coordination and $W^{+6}$ ions on the 8b sites in tetrahedral coordination [46]. NWO is suitable for use as a microwave dielectric ceramic prepared with cold sintering at a lower sintering temperature, which makes it a promising candidate for RTF [59]–[61]. Besides, it is used as a fire retardant in fabrics and for the fabrication of coated electrodes for electro-catalysis [62]. For microwave dielectric properties, NWO has been cold-sintered under two different conditions. The first is at 120 °C under a pressure of 120 MPa for 1 h, including additional drying at 100-300 °C. The second is at 240 °C with a heating rate of 10 °C min$^{-1}$, pressing at 400 MPa for 1 h, and additionally dried at 200°C for 12 h. Both sets of synthesis conditions resulted in promising

microwave dielectric properties with relative permittivity of ~5.80, $Q \times f =$ 22,000-70,000 GHz, and *TCF or* $\tau_f = -70$ ppm/K [59], [60].

### 1.5.4 Sodium silicate (NSiO)

$Na_2SiO_3$ (NSiO) is a white crystalline hygroscopic solid that produces an alkaline solution when dissolved in water. It exhibits a density of 2.61 g/cm$^3$ and can dissolve up to 22.2 g/100 mL of water at a temperature of 25 °C [63], [64]. The structure of NSiO is a chain silicate, shown in Figure 1.7 d), where the chains are linked through sodium atoms that are surrounded by five oxygen anions shaped like distorted trigonal bipyramids [65]. It has remarkable physical and chemical properties [66]. It can be used for hardening building materials, as a soil stabilizer [67], to control the corrosion of domestic water piping [68], as a corrosion inhibitor in cosmetics, as a chelating agent, as a buffering and pH adjuster, and is generally regarded as a safe food ingredient [69]. In general, the physical properties of sodium silicates control their binding power. NSiO is hardened in the ceramics industry as carbon dioxide gas is passed through it [67]. The main potential of NSiO for industrial and research applications lies in its exceptional properties across a wide range of temperatures and frequencies [70].

### 1.5.5 Magnesium sulfate (MSO)

$MgSO_4$ (MSO) is an anhydrous inorganic salt (density 2.66 g/cm$^3$, solubility 269 g/100 mL at 0 °C)[48], commercially mostly applied in the heptahydrate form $MgSO_4 \cdot 7H_2O$ (density 1.68 g/cm$^3$; solubility 71 g/100 mL d$H_2O$ at 20 °C), known as Epsom salt. According to the literature, MSO is used as a bath salt, in medicine for various purposes [63], [64] in the food industry, for wood impregnation, as a fire-retardant [71], as a fertilizer in agriculture [72] and ultimately for thermochemical storage systems [73]. Orbital measurements indicate that MSO is widespread across the Martian surface [74]. MSO naturally occurs in stable mineral deposits exclusively in hydrated forms, specifically as epsomite, hexahydrate, and kieserite, which contain seven (51 wt % water), six (47 wt % water), and one (13 wt % water) moles of bound crystal water. Rare, metastable MSO minerals are pentahydrate ($MgSO_4 \cdot 5H_2O$, 43 wt % water), starkeyite ($MgSO_4 \cdot 4H_2O$, 37 wt % water) and sanderite ($MgSO_4 \cdot 2H_2O$, 23 wt % water). Other hydration states (n = 12, 3, 1.25) are not identified as minerals but can be synthetically produced [75]. $MgSO_4 \cdot 7H_2O$ exists in two modifications, α-form, and β-form, occurring above and below 800 °C, respectively [76]. The hydration state of MSO salts depends on the relative humidity (RH) and temperature, which is depicted in a phase diagram [77]. Higher temperature and lower RH result in a lower hydration state. All hydration forms of MSO salts consist of $SO_4$ tetrahedra and Mg (O, $H_2O)_6$ octahedra, while some involve extra-polyhedral water (water that is not in octahedral coordination with Mg). Epsomite easily undergoes a transformation into hexahydrate by a loss of its extra-polyhedral water. This transition is reversible and takes place at approximately 50-55 % relative humidity (RH) at 25 °C. Kieserite is more stable at lower RH and higher temperatures; in thermogravimetric analysis, it is present up to 397 °C, compared with 177 °C for hexahydrate. However, as humidity increases, kieserite converts into hexahydrate or epsomite. Nevertheless, these phases do not easily revert back to kieserite upon desiccation [74], [75]. Structures of anhydrous MSO and MSO heptahydrate are depicted in Figure 1.7 e), f).

## 1.6 Ceramic Processing

### 1.6.1 Conventional high-temperature solid-state sintering

Materials manufacturing processes are often highly energy intensive and based on high temperatures, leading to an increase in carbon footprint. For instance, in manufacturing ceramic tiles, 83 % of the total $CO_2$ emissions are a consequence of firing and drying [78]. Ceramics can be produced using various techniques, with some of these methods dating back to ancient civilizations. Firing of the green body is performed to produce the desired microstructure. During solid-state sintering, a material system is heated to a sintering temperature ($T_s$), which is 0.5-0.95 of the melting temperatures ($T_m$). In such a way, the starting powder remains in a non-melted state. The bonding of particles and reduction of porosity during the sintering process takes place through atomic diffusion in the solid state. The sintering process is divided into three stages (Figure 1.8). In the first stage, the rearrangement of particles and the neck formation at the particle contacts take place. The second stage, called densification, involves the neck and grain growth, which is accompanied by shrinkage and porosity removal. The grain boundaries move as the grains grow at the expense of adjacent grains as long as the pores are interconnected. In the last stage, the porosity is partially to completely removed by vacancy diffusion along the grain boundaries. It is essential to control grain growth to achieve maximum removal of porosity. If the grains grow too fast, the grain boundaries move faster than the pores, leaving them isolated inside the grains. The main driving force of sintering is the reduction of surface free energy of the consolidated particles, which can be achieved by the atom diffusion process leading to densification or by coarsening of the microstructure. The reduction of surface area minimizes surface-free energy [79],[80]. The model of the mechanism of transport of material in sintering is presented in Equation (1.3):

$$\frac{\Delta L}{L_0} = \left(\frac{K\gamma a^3 D^* t}{kTd^n}\right)^m \tag{1.3}$$

where $\Delta L/L_0$ represents the sintering rate (or linear shrinkage), γ is the surface energy, $a^3$ is the atomic volume of diffusing vacancy, $D^*$ is the self-diffusion coefficient, $k$ is the Boltzmann constant, $T$ is the temperature, $d$ is the particle diameter, $t$ is the time, $K$ is geometry-dependent constant. The exponent $n$ is generally close to 3, while the exponent $m$ is in the range of 0.3–0.5 [79]. From Equation (1.3), it is obvious that the particle diameter affects the sintering rate the most.

Diffusion is either surface- or volume-kind and involves the transport of atoms or vacancies along a surface, grain boundary, or through lattice dislocations in the material. The sintering process yields a successfully formed microstructure composed of crystalline grains separated from each other by grain boundaries. In order to achieve a higher density of the body, the coarsening process should be suppressed. Density can be negatively affected by non-optimized processing conditions (sintering temperature and time, heating rate, and sintering atmosphere) and the presence of inhomogeneities. In addition, the sintering atmosphere should be carefully selected regarding gas composition, resulting in oxidation-reduction conditions.

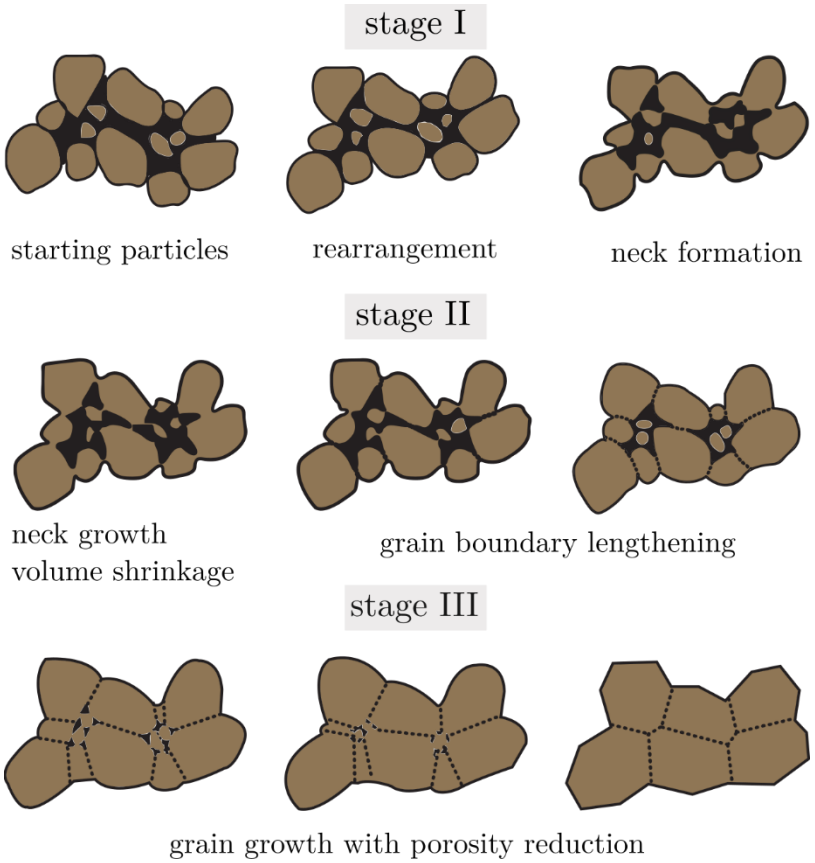


Figure 1.8: Sintering process (adapted from [60].)

High-temperature, large-scale fabrication of materials may result in several unwanted possible consequences, such as overfiring, warpage, excessive grain growth, incomplete burn-off of binders, decomposition, and polymorphic transformation upon cooling [81]. These phenomena could potentially lead to undesirable porosity and unreacted carbon residue, which might, on the one hand, increase production costs and, on the other hand, deteriorate the electrical and mechanical properties of the fabricated ceramics.

### 1.6.2 Hot-pressing

The main difference between conventional sintering and hot-pressing (HP) is the assistance of pressure during heating. By increasing the contacts between particles and optimizing the rearrangement of particles, the process of densification is accelerated, resulting in an overall improvement in packing efficiency. Simultaneous pressing can improve densification by a factor of 20, leading to several benefits such as reduced densification time and temperature, minimized residual porosity and grain growth, and less sintering aid needed. The process takes place in the furnace, which has a high-temperature die and an in-line press to employ and control the load. Generally, applied pressure ranges between 6.9-34.5 MPa. HP is typically performed at half of the melting temperature of the material, which is still lower compared to the conventional sintering temperature. HP is influenced by three mechanisms: plastic deformation, grain rearrangement (grain sliding), and stress-enhanced diffusion [82]. Hot-pressing can be conducted under uniaxial pressure or isostatic pressure (HIP). By latter, pressing from multiple directions is possible but demands a water-cooled autoclave attached. In this way, a preform made with a cold-pressing is needed. The main benefits of HIP are net-shape forming, elimination of die-wall friction effects, and preferred

orientation, which together lead to a higher mechanical strength [79]. HIP is often used as a post-sintering treatment to remove final porosity [83]. One version of hot-pressing is also hydrothermal hot-pressing (HHP), which employs hydrothermal conditions(<500 °C) and mimics the lithification geological process [84].

### 1.6.3 Low-temperature densification methods

In conventional solid-state sintering, densification occurs in a multistage process that involves diffusion of ions, grain growth, and elimination of pores between grains, which is accompanied by shrinkage of the ceramic body. Two prerequisites must be met for sintering: a transport mechanism for the material and its activation by an explicit energy source. Indeed, the latter is the main difference with new low-temperature alternatives for the fabrication of ceramics and ceramic composites. Sintering usually demands high temperatures to overcome diffusion activation energy. Furthermore, it is difficult to control the shrinkage of the material during sintering, so it can greatly affect the size and shape of the final product [79].

In nature, densification is a lifelong process observed in the formation of the earth's crust. Lithification, respectively, is the process by which sediment is compacted, cemented, and converted into sedimentary rock. Sediment consists of solid particles and voids between particles. The reduction in volume occurs by compacting the particles and thereby reducing the number of pores. Cementation takes place when minerals crystallize in the pores, thus effectively binding the sediment (see Figure 1.9). As described, clear similarities can be seen with new geologically inspired low-temperature consolidation methods based on high-pressure conditions and liquid phase assistance, which enables particle rearrangement, compaction, and crystallization from the liquid phase, which, in the end, results in dense materials [85]. A comparison between low and high-temperature consolidation methods is shown in Figure 1.9.

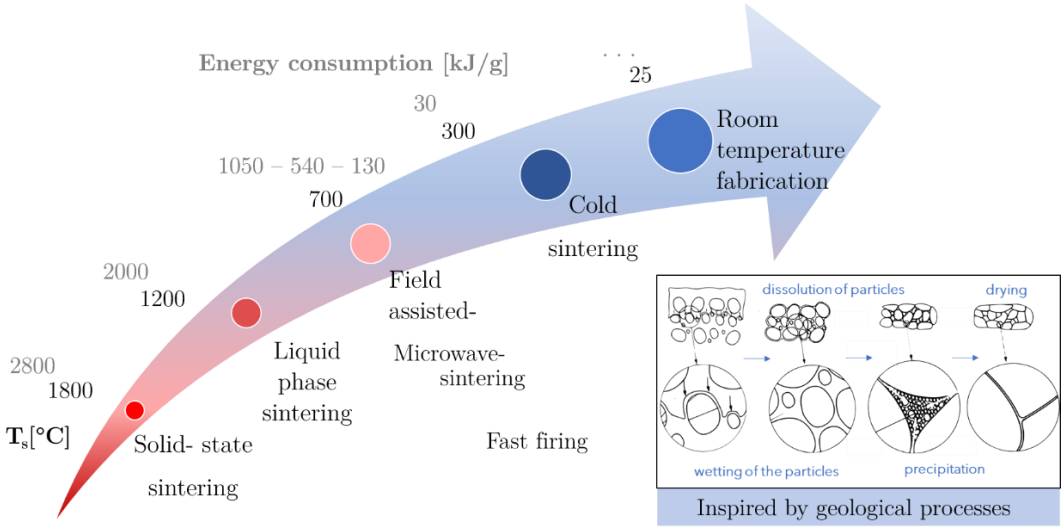


Figure 1.9: Ceramics processing. A tendency towards lower temperature and reduced energy consumption during the consolidation of ceramic materials. (Adapted from [86], [87],[88].)

Cold sintering (CS) was developed as an upgrade of hot pressing (following the Coble creep model) [89]. It has emerged as a highly efficient technique for compacting ceramics and composite materials at reduced temperatures ($0.1 \leq T_s/\ T_m \leq 0.2$). CS employs two

phases: a powder from which a ceramic body is formed and a transient solvent that enables mass transport. A mixture undergoes simultaneous heating and uniaxial pressing to induce dissolution and precipitation processes [90]. This consolidation process applies similar low-temperature metamorphic conditions ($T$= 150 °C – 350 °C, $p$= 200-800 MPa), which are common in geological processes such as diagenetic lithification, bulk rock deformation, and compaction of sediments [64],[70]. Pressure solution creep encompasses non-equilibrium chemo-mechanical enhanced dissolution (especially at grain-to-grain contacts), grain boundary diffusion towards open pore surfaces assisted by a liquid film, and precipitation in the pores, all driven by established chemical potential gradients [92]. CS relies on the pressure solution as the main densification mechanism but can include Ostwald ripening, coalescence, and epitaxial growth [58]. Dissolution-precipitation depends on surface area and interfacial energy. Chemical potential gradients are formed as a consequence of compressive and tensile stresses and established in areas with enhanced dissolution in the liquid phase and a high potential for contacting particle surfaces with low chemical potential. In CS, the establishment of congruent dissolution along with large solubility in a low-temperature aqueous environment is desired. The dissolution-precipitation mechanism is hindered with materials such as perovskites and spinels, where incongruent or limited solubility in water prevails [93]. This appears due to the atoms/ions being strongly bonded by the close-packed structures. Incongruent dissolution can produce second phases or an amorphous layer covering the lattice sites for nucleation, hindering the mass transport between aqueous and crystalline phases, which all negatively affect dielectric properties. This can be mitigated by adjusting the pH of a liquid phase accordingly [94]. The main goal of the CS process is to accelerate the kinetics by selecting nanoparticle-sized materials along with suitable experimental processing parameters [89]. Nanoparticles exhibit a high surface-to-volume ratio in comparison to coarse particles. Therefore, more lattice sites for nucleation are provided amidst precipitation.

Several studies report successful densification to high relative densities (>90 %) of different ceramic and composite materials at temperatures far below the conventional sintering temperatures [53], [58], [60], [95]–[98]. By employing CS, it was determined on a laboratory scale that the energy consumption for consolidating BT powder could be reduced significantly, from 2800 MJ/kg for conventional sintering to 30 MJ/kg, a decrease of two orders of magnitude [87]. Cold-sintered BT-PVDF composites (prepared at 190 °C, 350 MPa + 120 °C, 12h) exhibited a relative density of 94.8 %, relative permittivity of 71, and dielectric losses of 0.04 at 1 GHz [99]. Furthermore, ST can be cold-sintered at 180 °C but requires heating in air at 950 °C to reach average densities of 97 % and relative permittivity of 100 at 1 MHz [95]. However, in order to achieve sufficient dielectric properties, in many cases, additional post-heat treatment is carried out as the next step after CS.

At the hand of post-annealing (~700-900 °C) recrystallization from the amorphous phase, epitaxial growth of NP, precipitation, and the evolution of particle structure into a polygonal configuration take place [93]. In addition, the evolution and successful decomposition of impurities can be achieved by additional heat treatment phases [100].

## 1.7 Room Temperature Fabrication

Room temperature densification (RTD), or more general room temperature fabrication (RTF), was developed by Hanna Kähäri and other scientists from the Microelectronics research unit in Oulu, Finland. The first proof-of-concept of the method was based on

the compression (130 MPa) of the $Li_2MoO_4$ (LMO) powder (size below 180 μm) mixed with a small amount of distilled water. They measured the dielectric properties of as-prepared samples dried at RT and 120 °C and compared them to the measured values of control samples (conventionally sintered at 540 °C). Densification at RT was enabled due to the solubility of LMO in water at RT. The driving force for consolidation in RTF is pressure [101].

When RTF is applied in bulk ceramic upside-down composites, the high loading of filler material (for example, ST, BT, etc.) with required functional properties is combined with the corresponding binder (inorganic aqueous-soluble salt, i.e., LMO, partly in the form, of a saturated aqueous solution. The process depends on the water solubility of the inorganic binder. The RTF steps (sieving, mixing, ultrasound treatment, pressing, and drying) are illustrated in Figure 1.10. In fact, the effect of pressure on solubility is also very important and can impede both dissolution and crystallization [102]. During RTF of upside-down composites, the binder crystallizes on the surface of and in between the filler particles, thus physically binding them together. Densification of ceramics occurs at ambient temperature during pressing of the ceramic body, followed by drying at 110 °C. Drying is the last processing step, where the residual water evaporates, and the dissolved binder crystallizes between the solid particles, resulting in a dense final product. The temperature and duration of drying can be modified in such a way as to achieve sufficient evaporation of residual water in a specific time range. The method is based on soft solution processing, which combines mixing, molding with steel dies, pressing, and drying. The first prerequisite for efficient densification of such composites is the pretreatment of the filler component in order to obtain suitable particle size distribution (bimodal, polymodal), resulting in high packing density. Next, a binder in a liquid phase and a solid powder are used to ease the rearrangement of the particles during pressing. Another way to enhance the densification process is to coat filler particles with a binder, which resulted positively in the case of PZT-ceramics fabrication [103].

The RTF and CS processes share certain similarities—both use a liquid phase that can partially solubilize the powdered material and compaction under pressure, leading to particle rearrangement and the reprecipitation or recrystallization of the solid material. But there are some noticeable differences. In CS, densification occurs under pressure and simultaneous heating; the starting powder is predominantly nanosized, which may result in grain growth. However, also microsized powders can be used in CS [90],[104]. Compared to conventional sintering and CS, RTF does not induce grain growth and overall shrinkage of the sample. Therefore, it is considered as a net-shape technology. Moreover, as the pH of the liquid phase is often non-neutral in CS, particularly for incongruent dissolving materials, post-annealing is sometimes required at high temperatures [93].

This novel and innovative technique of ceramics densification is beneficial since as-prepared ceramics exhibit well-developed electrical characteristics without the need for their sintering at high temperatures, thus considerably reducing ceramics fabrication costs.

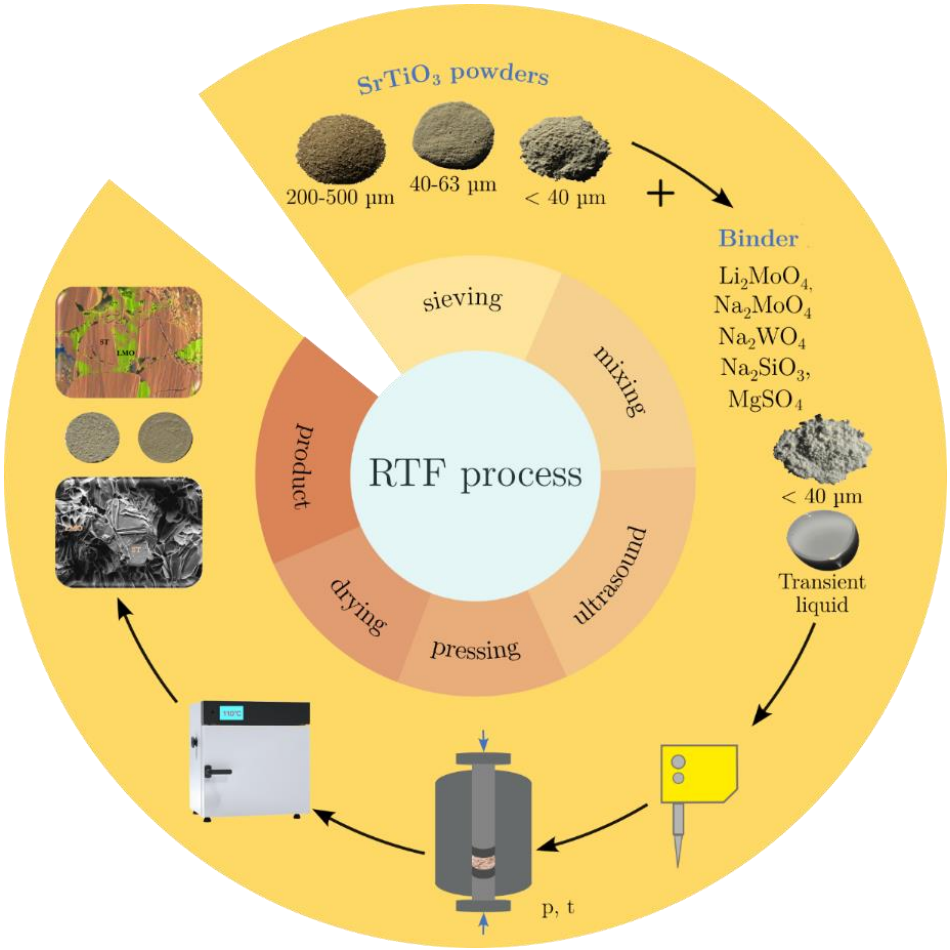


Figure 1.10: Schematic representation of the RTF process.

### 1.7.1 Crystallization from solution

Crystallization is defined as a process of producing crystalline substances and takes place from melts, solutions, and vapors. A crystal is a homogeneous solid particle in many characteristic forms that appear due to solidification under optimal conditions. Crystalline substances are classified as metal crystals, ionic crystals, valence crystals, semi-conductor crystals, and molecular crystals. Ionic crystals are common in salts and appear as a combination of highly electropositive and electronegative elements. Upon dissolution as a pre-step to crystallization, bonds between solid and solvent are weakened, and solute ions tend to have a higher attraction to water molecules than to each other. The basic concept in crystallization is solubility and “supersolubility”. Solubility represents the maximum concentration of a solute in a solution at equilibrium, indicating the point at which the solution becomes saturated, which is the degree to which the solute can dissolve. Solubility is, however, solute-, solvent- and temperature-dependent. Crystallization, however, can be brought about in different ways, i.e., through evaporation of a solvent until supersaturation, or as a result of decreased temperature, which causes reduced solubility, or simply due to a change like a system (adding another type of solvent,). Crystallization is a two-step process that involves nucleation and concurrent crystal growth. Supersaturation is the driving force of both processes and resembles a state of disequilibrium. A solid compound's chemical potential equals a dissolved compound's chemical potential at equilibrium. Dissolved solute molecules begin to form agglomerates,

and upon nucleation, smaller particles grow spontaneously within a metastable mother solution. The concentration gradient from the solution to the appearing crystals is the driving force of crystallization [105].

## 1.8 Rules of Mixtures in Composites

The properties of electroceramics can be tailored to suit the needs of various applications by employing a composite approach. A composite system can comprise n phases with different dielectric permittivity. The properties of such a composite system are influenced by the constituent phases, where the more prevalent matrix phase plays a significant role in determining the overall properties of the composite. Rules of mixtures are equations used to predict or calculate the effective properties of heterogeneous mixtures. The equations are based on the properties and volume fractions of the materials' constituents. Many of the mixing equations depend on general mixing models, either parallel or series. These rely on the assumption that the way permittivity is affected by inclusions in a medium is similar to how a dielectric material is affected in a capacitor when exposed to an applied electric field.

Various models for dielectric mixtures have been proposed and investigated to elucidate and predict the effect of each phase on the composite dielectric properties. Mixing equations are generally divided into two subgroups: symmetric equations for statistical mixtures or asymmetric equations for matrix-inclusion composite type [106]. Lichtenecker and Maxwell Garnett's (MG) theoretical models are two of the most commonly used for estimating and predicting functional properties of composites [8], [107], [108]. MG is known as a mean-field method and considers permittivity of the matrix and inclusions asymmetrically (Equations (1.11-1.14) [8]. It was adapted for spheres by Wagner and oriented/randomly oriented ellipsoids by Sillars/Fricke [106],[17],[18]. As reported, the MG model can only be used when the composite contains a low filler volume fraction [111]. The Bruggeman symmetric mixing rule (Equation 1.16) calculates the effective permittivity, assuming that spherical inclusions are evenly distributed in the surrounding matrix. Effective medium theories revolved around the polarizabilities of ellipsoidal inclusions surrounded by an effective medium. Among them, the Lichtenecker logarithmic mixing rule has shown good agreement with experimental values in many studies on ceramic-polymer composites (Equations (1.4-1.9)) [111]–[114]. Furthermore, it is possible to adjust an empirical factor, denoted as $k$, to fit the material more accurately based on the nature of the fillers and matrix (Table 1.1). Commonly, a value of 0.3 is used for $k$ [8]. Effective-medium-theory considers the particle shape but with limited accuracy [115]. The Looyenga equation (Equation (1.15)), based on the symmetric integration method for spherical particles, is not applicable if the permittivity difference among constituents is too large [106].

Table 1.1: A list of equations of rules of mixtures used for mathematical evaluation of relative permittivity in LMO-ST composites.

| Equation Number | Mathematical model | | Ref. |
|---|---|---|---|
| (1.4) | **Lichtenecker** | $\varepsilon^k = \sum_{i=1}^{N} f_i\, \varepsilon_i^k; k \neq 0$ | [116] |
| (1.5) | | $\varepsilon_L{}^k = f_1 \varepsilon_1{}^k + f_2 \varepsilon_2{}^k$; -1<k<1 | |
| (1.6) | | $\ln \varepsilon_L = f_1 \ln \varepsilon_1 + f_2 \ln \varepsilon_2\,; k = 0$ | |
| (1.7) | **Lichtenecker geological** | $\varepsilon^k = (1-p)\varepsilon_s{}^k + (p - f_w)\varepsilon_a{}^k + f_w \varepsilon_w{}^k$ | [117] |
| (1.8) | | $\ln\, \varepsilon = (1-p) ln\, \varepsilon_s + (p - f_w) ln\, \varepsilon_a + f_w ln\, \varepsilon_w$ | |
| (1.9) | **Reformulated Lichtenecker** | $\ln \varepsilon_{composite} = (1-f_{LMO}-f_{air}) ln\, \varepsilon_{ST} + f_{LMO} ln\, \varepsilon_{LMO} + f_{air}\, ln\, \varepsilon_{air}$ | [118], this work |
| (1.10) | **Fitting function** | $g(k) = \begin{cases} \left(f_1 \varepsilon_1{}^k + f_2 \varepsilon_2{}^k + f_3 \varepsilon_3{}^k\right)^{1/k}, k \neq 0. \\ e^{f_1 \log \varepsilon_1 + f_2 \log \varepsilon_2 + f_3 \log \varepsilon_3}, k = 0. \end{cases}$ | |
| (1.11) | **Maxwell-Garnett** | $\varepsilon = \varepsilon_1 \left( \frac{1 + 2V_2 \left( \frac{\varepsilon_2 - \varepsilon_1}{\varepsilon_2 + 2\varepsilon_1} \right)}{1 - V_2 \left( \frac{\varepsilon_2 - \varepsilon_1}{\varepsilon_2 + 2\varepsilon_1} \right)} \right)$ | [119] |
| (1.12) | | $\varepsilon_{composite} = \varepsilon_{ST} \left[ \frac{1 + 2(f_{LMO} - f_{air}) \left( \frac{\varepsilon_{LMO} - \varepsilon_{ST}}{\varepsilon_{LMO} + 2\varepsilon_{ST}} \right)}{(1 - (f_{LMO} - f_{air}) \frac{(\varepsilon_{LMO} - \varepsilon_{ST})}{((\varepsilon_{LMO} + 2\varepsilon_{ST}))}} \right]$ | [118], this work |
| (1.13) | | $\varepsilon = \varepsilon_1 + 3 f_2 \varepsilon_1 \left[ \frac{\varepsilon_2 - \varepsilon_1}{\varepsilon_2 + 2\varepsilon_1 - f_2(\varepsilon_2 - \varepsilon_1)} \right]$ | [120] |
| (1.14) | | $\varepsilon_1 = \varepsilon_{experimental}(1 + 1.5P)$ | |
| (1.15) | **Looyenga** | $\varepsilon^{1/3} = f_1 \varepsilon_1^{1/3} + f_2 \varepsilon_2^{1/3}$ | [106] |
| (1.16) | **Bruggeman** | $\frac{\varepsilon_1 - \varepsilon}{\varepsilon_1 + 2\varepsilon} \cdot f_1 + \frac{\varepsilon_2 - \varepsilon}{\varepsilon_2 + 2\varepsilon} \cdot (1 - f_1) = 0$ | [9] |

In calculations based on mixing equations, only the bulk ceramic constituents with a total volume fraction of 1 are often considered. However, it is essential to note that the remaining pores in the system can also play a significant role. Porosity appears as a constituent in composites and can be either unwanted or engineered, typically caused by processing conditions. It is often necessary to apply porosity correction in the mixing equations, as porosity reduces the relative permittivity of materials [120]. The relative permittivity of composite mixtures can have an additional contribution due to the accumulation of space charges at the boundary [29], [121]. As demonstrated, many different mixing rules are available for composite mixtures, and the fitting model must be chosen accordingly for each material system.

## 1.9 Object-oriented Finite Element Analysis (OOF2 Simulations)

Object-oriented finite element analysis (OOF2) is public-domain software developed by the National Institute of Standards and Technology (NIST) to perform linear elasticity and

thermal conductivity simulations [112]. OOF2 calculations on arbitrary two-dimensional microstructures are used to obtain approximate solutions to initial and boundary-value equations.

At its most basic level, OOF2 is constructed to analyze how boundary conditions influence the local fields in microstructures. Figure 1.11 provides a brief overview of OOF2's solver characteristics. OOF2 can solve any problem in which the divergence of some generalized flux is a generalized external force. Flux is a linear combination of fields and gradients of force. Common forces include displacement, voltage, and temperature, and typical fluxes include stress, polarization, and heat flux. OOF2 thus allows users to study the thermal, electrical, and stress fields in a microstructure, along with couplings such as piezoelectricity, pyroelectricity, and thermal expansion. OOF2 uses different sources such as mass and force density, free charge, and heat source. OOF2 can simulate various material properties and processes, including heat and mass diffusion, thermoelasticity, relative permittivity, thermal conductivity, and thermal capacity. An upgrade of OOF2 enables using nonlinear models that can simulate plasticity and ferroelectricity [122].

There is a principal object hierarchy in OOF2, where Microstructures contain Images and Skeletons, which in turn contain Meshes. For clarity, all OOF2 elements are written with the capital initial. Steps in the OOF2 simulation are depicted in Figure 1.12. Before its use in OOF2, a microstructure image must be segmented; each material in the image must be assigned a unique color. Tools such as ImageJ or GIMP can be used for this task. Such an image can be imported into OOF2, which forms the basis of a Microstructure. Microstructure is the fundamental object in OOF2 and consists of Pixel selection, Pixel groups, and a Material map, which assigns Materials to Pixels. A Pixel represents the smallest component of the Microstructure processed by OOF2 and consists of data arrays that describe a material. A set of Pixels in the Microstructure can be assigned to a Pixel group according to their colors and contrast. Each group is designated to specific material properties to differentiate between pixels when creating the Skeleton. Meshes are created based on the Skeleton.

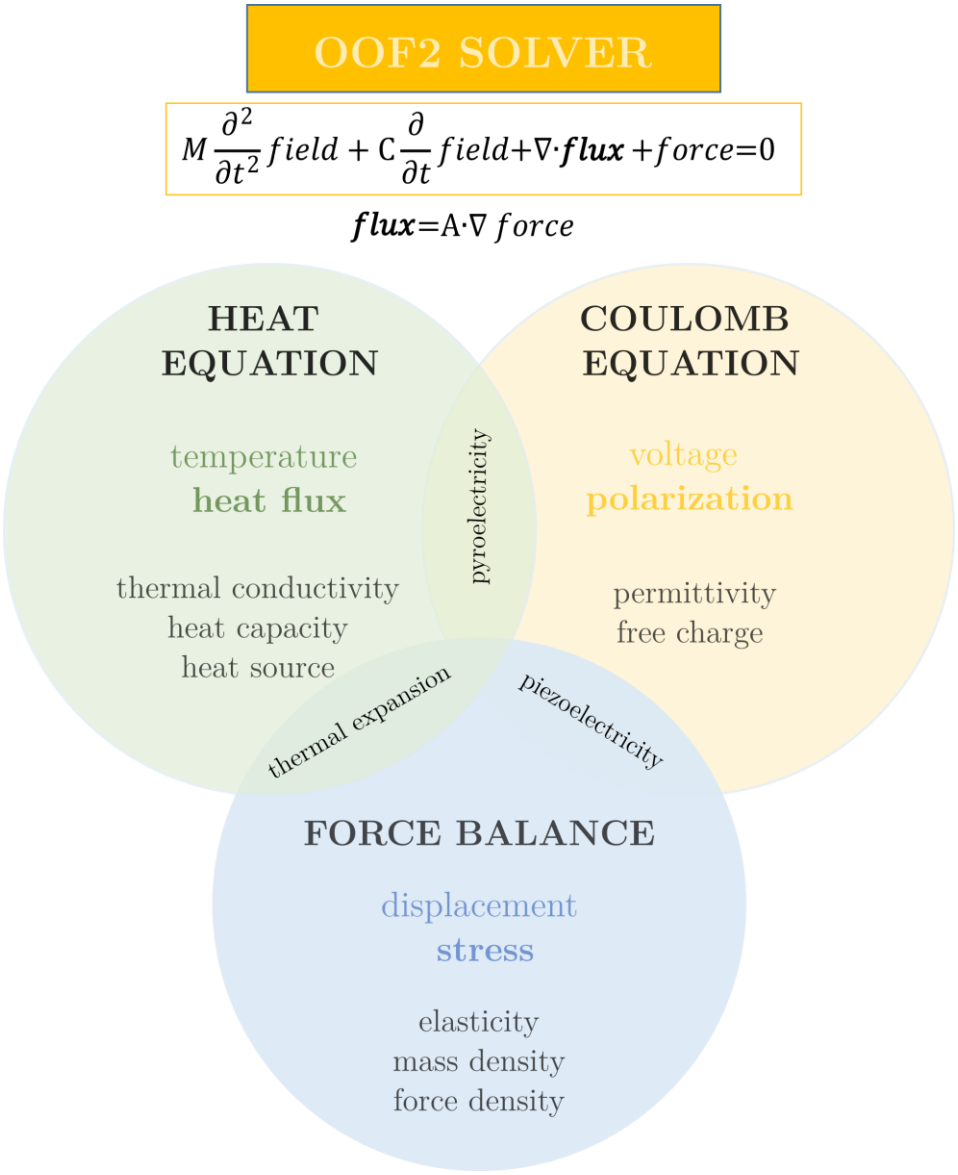


Figure 1.11: OOF2 solver characteristics.

The Skeleton is a pre-step to the finite element solution. While Microstructure consists of many Skeletons, which represent different discretizations, one Skeleton, in turn, produces many Meshes, which serve as options for various physics and solution methods to be implemented on a single geometry. Mesh is created upon the Skeleton's triangular/ quadrilateral elements, which contain Materials properties from pixelized Microstructure. The Skeletons should have a high average homogeneity over their Elements to ensure valid operation. The homogeneity of an Element is defined as the ratio of its dominant Pixel type versus its total Pixel count. To define boundary conditions before solving equations on a Mesh, one must first select Skeleton boundaries. When edge and point boundaries are selected, one can apply Dirichlet, Floating, and Neumann boundary conditions [123]–[126], [127].

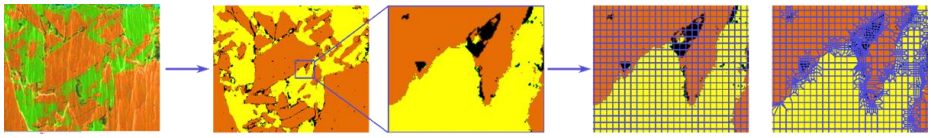

Figure 1.12: OOF2 analysis. Graphically represented steps from the real microstructure to a constructed material map or skeleton.

OOF2 internally does not use units. However, if the input data is in consistent units, the output data will follow. Some examples are displayed in Table 1.2. Both unit formats are equally valid and will lead to the same result for the same structure. In our case, it is assumed that the space charge is always 0. OOF2 is based on the Gauss law equation (1.17):

$$\nabla D - \rho = 0 \tag{1.17}$$

Table 1.2: OOF2 data and units.

| Data | Quantity/ parameter | Type | Unit format 1 | Unit format 2 | | |
|---|---|---|---|---|---|---|
| Input | Distance (width, height), [x,y] | Scalar | m | µm | | |
| | voltage [U] | Scalar field | V | mV | | |
| | permittivity [ε] | Scalar field | F/m=C /Vm | pF/µm | | |
| | free space charge* [ρ] | Scalar field | C/m³ | µC/µm³ | | |
| Data | Quantity | Type | Unit format 1 | Unit format 2 | Equation | Equation number |
| Output | electric field [E] | vector field | V/m | mV/µm= V/mm | $E = -\frac{\partial U}{\partial x}$ | (1.18) |
| | polarization [P] | vector field | C/m² | pF mV/µm²= fC/µm² | $P = \varepsilon \cdot E$ | (1.19) |
| | energy density [W] | Scalar field | CV/m³ =J/m³ | fC mV/µm³=aJ/µ m³ | $W = P \cdot \frac{E}{2}$ | (1.20) |

The relative permittivity among electric material properties assigned to the Microstructure in OOF2 defines the total polarization flux $P$, which depends linearly and isotopically on the gradient of the voltage field. The average energy density ($W$) is further calculated as the important output parameter following Equation (1.21)

$$W = \frac{\sum_{i=0}^{N} W_i}{N} \tag{1.21}$$

and represents the average energy density for all elements of the structure.
If the case of an ideal capacitor (single dielectric of area $A$ and thickness $h$) is applied, $W$ is calculated as:

$$W = \frac{1}{2}\varepsilon\frac{U^2}{h^2} \tag{1.22}$$

Considering this, the equivalent average absolute permittivity of our structure is derived by Equation (1.23):

$$\varepsilon = \frac{2h^2}{U^2}\sum_{i=0}^{N}\frac{W_i}{N} \tag{1.23}$$

The OOF2 software offers a unique advantage by combining real microstructural data, such as particle size, shape, spatial position, and actual orientation, with fundamental material parameters, including electric properties, elastic modulus, and Poisson's ratio of constitutive phases. This combination provides a better understanding of the overall material behavior [125].

## 1.10 Mechanical Strength of Ceramics

In general, mechanical characterization is performed by tensile testing, as in real-life cases, specimens genuinely break due to tensile stresses rather than compression. Tensile stresses will lead to fracture and usually emerge from either specimen misalignments or elastic property mismatches. Contrarily, the compression strength values of ceramics are generally ten or more times greater than the tensile strength values.

Biaxial tensile strength testing has been a longstanding practice, with many different test setups reported in the literature, e.g., ring-on-ring, punch-on-ring, ball-on-ring, piston-on-three balls, and ball-on-three balls test (B3B) [128], [129],[130].

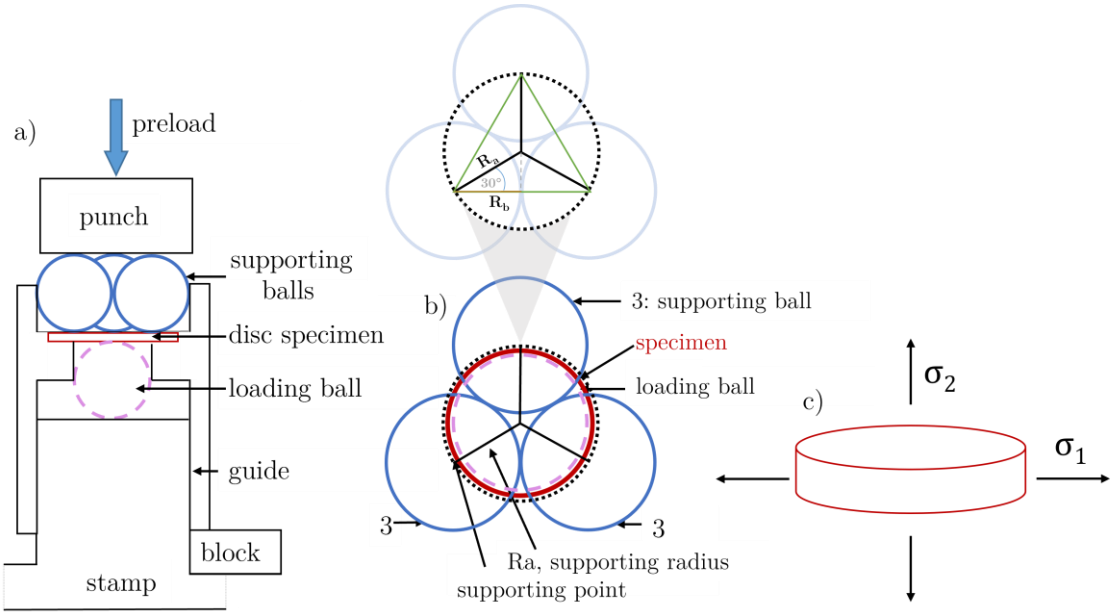


Figure 1.13: Schematic representation of biaxial B3B testing of a ceramic disc.a) the fixture, b) the closer view to the ball on three balls testing situation, c) Biaxial tension in a two-dimensional view; Adapted from [131],[132].

The Ball on Three Balls, B3B-test is a biaxial bending strength test, where a disc-shaped plate is symmetrically supported by three balls at the upper plane and loaded by a fourth ball in the center of the bottom plane (Figure 1.13) [128],[131]. The maximum tensile stress occurs in the center of the top plane of the specimen on the opposite side of the loading ball and is given by Equation (1.24),

$$\sigma_{max} = f(\alpha, \beta, \nu) \cdot \frac{F_{max}}{h^2} \tag{1.24}$$

$$\alpha = \frac{t}{R}, \ \beta = \frac{R_a}{R} \tag{1.25}$$

$$R_a = \frac{2R_b}{\sqrt{3}} \tag{1.26}$$

where $F_{\max}$ represents the maximum fracture load, $h$ is the thickness, and $R$ is the radius of the disc specimen. In contrast, $f$ is a dimensionless factor related to the geometry of the sample. More precisely, $\alpha$ is the scale parameter (disc geometry), $\beta$ is the shape parameter (support geometry) with the $R_a$, which is a supporting radius, which is related to the radius $R_b$ of the balls (Equations (1.25)). The radii $R_b$ of the supporting balls and the $R_b$ of the loading ball are the same. The correlation between both radii is described in Equation (1.26). Further, $\nu$ is the material's Poisson's ratio, inherent to the specimen [131], [133]. The Poisson ratio is the transverse strain divided by the longitudinal strain in the elastic loading direction. In simpler terms, it illustrates a material's ability to undergo deformation perpendicular to the loading direction. Generally, except ductile or high-temperature ceramics, regular ceramics exhibit relatively low Poisson ratios ($\leq 0.3$), corresponding to their brittle behavior [134],[135].

The most sensitive parameter is the thickness of the specimen, which must fit into the space beneath the loading ball. A 1 % error in thickness determination leads to approximately 2 % error in calculated stress [131].

The strength data of brittle materials often shows considerable variability in the measured results; therefore, the strength values must be statistically evaluated. The Weibull statistics-probability-based function is usually applied in ceramics to achieve this. Waloddi Weibull was the first to describe the statistical evaluation of brittle fracture in 1939 [136], [137],[138] based on "the weakest-link theory"[139]. Weibull statistics indicate a particular type of defect distribution, which explains that the largest defect is the limiting factor in determining fracture-related mechanical properties. In addition, Weibull assumed that each elemental part of the bulk material carries an individual property (or local strength). Thus, the probability of failure of each element is integrated over the entire specimen. The cumulative probability function of a two-parameter Weibull distribution is presented in Equation (1.27),

$$P = 1 - \exp\left[-\left(\frac{\sigma}{\sigma_0}\right)^m\right] \tag{1.27}$$

where $P$ means a probability of failure at a certain stress $\sigma$; $\sigma_0$ is the characteristic strength corresponding to the stress at which the probability of failure is 63 %, and $m$ is the Weibull modulus, which gives the distribution shape (shape parameter) [134],[137],[140]. Probability of failure, $P$ plotted against the logarithm of $\sigma_f$ gives a line of slope $m$, Weibull modulus. The slope can be estimated graphically or using the least squares or maximum likelihood method [138].

Based on the experimental data, there is usually a higher probability of failure with higher load amplitude and larger specimen sizes. The strength in brittle materials is mainly controlled and defined by the size of the major flaw in the specimen. Correspondingly, the

size of the specimen can significantly affect the mean strength, i.e., the strength of small specimens will be higher than that of larger specimens [141]. The Weibull theory further interpreted the effect of size on strength.

[131]. This is beneficial since many electronic components are rectangular. According to the literature, B3B testing has been applied to miniaturized electroceramic components [142] and metal castings [140].

Compared to uniaxial conventional bending testing, B3B testing of ceramics offers certain advantages, such as simplified preparation of test specimens, well-defined geometry of the load transfer from the jig to the specimen, high tolerance to measurement oscillations and geometrical inaccuracies, which is achieved by testing the center of the specimen that prevents the effect of edge finishing defects. Imperfect alignment and the edge effect of the specimen, which can be critical factors in other bending tests, become irrelevant in the B3B test. With this upgrade, it is possible to test as-sintered samples, which may appear to have slightly curved surfaces [129].

However, the relation between the volume under tensile load and the specimen volume is often a shortcoming of the B3B test. If the sample is small, microstructural defects may not be found in the sample volume. This absence of defects makes it difficult to localize the fracture, which means that the Weibull distribution is no longer valid [142]. Another constraint in B3B testing is that a Poisson's ratio value is required in all analytical Equations for fracture stress, which might not always be independently accessible from the literature [130].

## 1.11 Fractography

By its definition, brittle fractures happen with little or no plastic deformation and are generally caused by unavoidable microscopic flaws that appear during processing. The brittleness of ceramics results from the strong ionic or covalent bonding between the metallic and non-metallic elements [134].

Fractography is a valuable tool for identifying the cause of failure in brittle materials or even providing quantitative data about the loading conditions during testing. In fact, to a large extent, it is simply pattern recognition. Often, under mechanical loading, we wonder why our piece of ceramics or any other material broke even though we wouldn't expect it to, and thus, what the cause of the break was. In response, fractographic analysis can give us feedback on whether the strength test was performed correctly, whether the specimen was properly aligned, and ultimately where the fracture originates.

Fractographic analysis includes a few steps. First, the specimen must be reassembled– like solving a puzzle. Then, the tested specimen's fragments (size, shape) must be visually inspected to determine the breakage pattern. Then, the reconstructed sample is inspected under an optical microscope, and finally, the fracture surfaces are examined under a scanning electron microscope. Both halves of the fracture surface should be carefully inspected, as each provides information about the fracture origin. Branching patterns can explain the direction of crack propagation. Typically, a pair of branches pointing in opposite directions limits the origin of the fracture, as shown in Figure 1.14. The fracture begins as a single crack that propagates and splits into two or branches forward into multiple propagating cracks. Latter happens if the stresses are high enough or directed toward crack propagation.

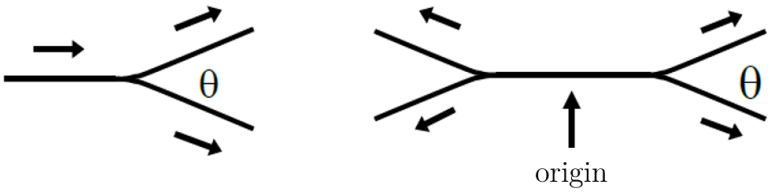


Figure 1.14: Crack branching [100].

Flaws and crack propagation in the specimens are often related to the processing and microstructure. Flaws can be either surface-, volume- or even edge-distributed. Different types of flaws can appear in the microstructure, such as large grains, grain boundaries, compositional inhomogeneity, porosity, inclusions, etc. Large grains may occur due to compositional variability or exaggerated local grain growth. They are easily recognized by optical inspection, as they reflect differently from the surrounding matrix. Crack propagation can be trans-granular (through grains) or inter-granular (along grain boundaries). Sometimes, side-by-side flaws can link and form a strength-limiting flaw. Surface voids, among the possible vulnerable fracture areas, are cavities that appear on the surface of a specimen after reacting with the processing environment. However, not all flaws in the microstructure will induce a fracture, as the limiting ones have to be oriented perpendicularly to the principle tensile stress. Besides, as Griffith's law states, there is a critical size of the crack that will propagate at a given applied stress. This means that small cracks are more stable and do not propagate that easily, as their energy generally rises with length. In contrast, larger cracks are less stable and propagate because their energy decreases with increasing length [143].

Another essential aspect to remember is to avoid contamination of the fracture surface before the sputtering for the SEM analysis, as impurities can mask flaws and obstruct the pattern identification process [132].

# Chapter 2

# Objective and Outline of This Work

## 2.1 Aim

The main focus of this dissertation was to investigate the densification and the resulting functional properties of ceramic composites, prepared at room temperature using LMO and alternatives as a binder and ST as the filler.

The aim of the first part of this thesis was to study the fabrication process, the microstructure, and the dielectric properties of the upside-down LMO-ST composites by exploring physical factors that affect each processing step. Furthermore, I aimed to experimentally investigate the effect of composition on the microstructure and dielectric properties. An important approach implemented was to compensate for the observed residual porosity in LMO-ST composites by impregnating the composite with titanium(IV) isopropoxide (TTIP).

In the second part of this thesis, my goal was to describe the dielectric properties of LMO-ST composites as a function of composition by using mathematical mixing rules and Object-oriented finite element simulation software (OOF2). In addition, the effect of binder coating on ST filler particles would be simulated using OOF2 and then compared to experimental results. Therefore, I aimed to explain the composite material's response to an electric field better.

In addition, I aimed to focus on finding new binders as an alternative to LMO and investigating their binding potential in ceramic composites fabricated at room temperature.

In the final section of my thesis, I aimed to analyze the mechanical properties of ceramics and ceramic composites using the ball-on-three-balls-bending (B3B) test.

The following is a list of leading questions which were addressed in the doctoral dissertation:

- How do physical parameters, such as particle size, applied pressure, and drying time, affect the densification and dielectric properties of LMO-ST composites?
- How does the change in composition (LMO-ST proportion) affect densification and dielectric properties?
- How does residual porosity affect dielectric properties?
- Is it possible to improve relative density and dielectric properties through impregnation?
- Can any trends be identified through theoretical analysis based on the rules of mixture and OOF2 simulations?
- Which are the optimal alternatives to LMO binder?
- What are the mechanical properties of LMO-ST and ST-alternative binder composites?
- Which approach of mechanical characterization is the most reliable and consistent in testing such materials?

## 2.2 Hypotheses

Hypothesis 1: **The optimization of the RTF process, including the use of larger particle-size filler powders, higher applied pressure, and longer drying time exposure, increases relative permittivity.**

Many studies have focused on selecting the best combination of composite constituents to obtain dense structures [144], [145]. The Furnas and Dinger-Funk packing models are based on the appropriate proportioning of different particle sizes to achieve improved packing density of mixtures [146], [147]. It is possible to achieve higher packing density using non-uniform particles. Smaller particles fill the gaps between the larger ones, resulting in denser structures. Pressure is expected to facilitate densification, and hence, by increasing the pressure, a denser composite structure will appear as a result. In addition, when exposing samples to a temperature above 100°C, adsorbed moisture and remaining water from processing are removed.

Hypothesis 2: **Higher binder (LMO) content increases relative density but decreases relative permittivity.**

On the one hand, smaller and softer LMO particles are expected to fill the pores and compress more under pressure than the harder ST phase. On the other hand, the LMO binder represents a low relative permittivity material, which, when combined with a high relative permittivity material (ST), would result in a decreased dielectric performance of the composite. For this reason, I tackled this research dilemma experimentally.

Hypothesis 3: **Residual porosity decreases the dielectric properties of binder-ST ceramic composites, which can be proved by using mathematical rules for mixtures.**

It is generally known that porosity is one of the main drawbacks to the relative permittivity of materials. Particularly when the pores are filled with adsorbed moisture or residual water, this can negatively affect the overall loss within a dielectric material. Using the rules of mixture, one can predict or mathematically estimate the effect of porosity, as has been utilized in many studies [9].

Hypothesis 4: **OOF2 simulations can characterize the electric field and polarization within the binder-ST composite and help us further understand local field phenomena within the composites.**

In RTF of binder-ST composites, a complex multiphase system can respond unusually to the applied electric field in reality. As reported in the literature [125], object-oriented finite element analysis (OOF2) can solve the Coulomb Equation and build the data about the polarization and energy density from the actual microstructure of binder-filler composites. It is, therefore, expected that simulations can assist in understanding the properties and functionality of such composites.

Hypothesis 5: **Impregnation with titanium (IV) isopropoxide (TTIP) improves the relative density and dielectric properties of LMO-ST composites.**
The residual porosity in composites and ceramics made at room temperature is expected to be approximately 15 % [46], [103], [148]. The dielectric constant of classically sintered

ST ceramics and RT-fabricated LMO-ST ceramic composites differ mainly due to the much larger porosity (sintered ST exhibits 1-2 % porosity). I believe the overall dielectric properties of RT-fabricated pellets can be improved by introducing an impregnation process with a liquid medium that solidifies after drying and has a relative permittivity greater than 1 (air). For instance, titanium (IV) isopropoxide transforms into titanium dioxide after hydrolysis, polycondensation, and heating at a sufficient temperature [149].

Hypothesis 6: **The characteristic mechanical strength of sintered ST and binder ceramics surpasses that of RTF binder ceramics and binder-ST composites.**

A critical aspect of using ceramic materials in electronics to ensure their smooth operation and long life is their mechanical stability when subjected to loads during operation. Processing conditions can play a big role in this and significantly impact the final functional properties of such electroceramic passive elements.
Multiphase binder-filler composites prepared at room temperature are composed of materials with significantly different inherent mechanical properties. It was, therefore, expected that their response to loading stresses would be very complex and somewhat lower compared to sintered ceramics. As mentioned above, such materials are more porous, which is generally known to have a significant effect on the final mechanical properties.
To the best of my knowledge, there has been no literature study to date that examines the mechanical strength of RTF ceramics and composites, which motivated me to conduct such research.

## 2.3 Thesis Outline

The doctoral thesis is divided as follows: in **Chapter 1** introduction to the theoretical background of the research topic and the existing literature review is provided. In **Chapter 2** the aim, goals, and hypotheses of the thesis are presented. In **Chapter 3,** the materials and methods used to conduct the experimental investigation are presented. The experimental results and discussion are divided into **Chapters 4–9**. In **Chapter 4**, the optimization of the RTF method on LMO-ST composites and the effect of various processing parameters on dielectric properties and microstructure are presented. In **Chapter 5,** the experimental and mathematical evaluation of the effect of varied composition (LMO-ST proportion) on dielectric properties is outlined. In **Chapter 6**, the OOF2 simulations on real and engineered microstructures were used to provide a deeper insight into the electrical properties of composites. In **Chapter 7**, impregnation with titanium(IV) isopropoxide (TTIP) was used to reduce overall porosity in LMO-ST. In **Chapter 8**, the focus is shifted to replacing the extensively researched binder, LMO, with innovative inorganic alternatives. The performance of these new binders was investigated, with particular emphasis on their density and dielectric properties in radio and microwave frequency ranges. The experimental work was extended to employing BT as the filler phase and comparing the results with binder-ST composites. In **Chapter 9**, results on the mechanical characterization of binder-ST composites are presented, and compared to the mechanical strength of single-phase binder ceramics and ST ceramics.

# Chapter 3

# Materials and Methods

## 3.1 Synthesis of ST- and BT-binder Ceramic Composites

The composite samples for RTF experiments were fabricated using a two-stage process. At first, ST ceramic pellets were prepared by combining high-purity $SrCO_3$ and $TiO_2$ powders (both chemicals ≥ 99.9 %, Sigma - Aldrich Co., United States), which were used for subsequent composites. c Binders were used in two forms: as a powder, sieved <40 µm, and as binding aqueous phase–saturated solution. The composition was mostly kept constant, wherein a high loading of ST filler (93.5 wt %, 85 vol %) was combined with a selected binder (6.5 wt %, 15 vol %). However, a chapter with varied LMO binder (from 1, 6.5, 10, 20, 30, 40, 50, 60, 80, and 100 wt %) content is an exception.

The RTF process encompasses sieving, mixing, ultrasound treatment, pressing, and drying. Precisely, ST fractions and the desired amount of LMO were weighed using an analytical balance (AG104, Mettler Toledo) and mixed by shaking for 1 min in a 25-mL glass vial. Subsequently, a saturated aqueous solution of a binder (0.2 mL/per 0.666 g of dry composite mixture) was added to the mixture and well mixed, then transferred into a steel dye with a diameter of 10 mm. Once the mixture was placed into the die, ultrasonic treatment (UP100H ultrasonic processor with MS1 sonotrode – 100 W, 30 kHz, Hielscher Ultrasonics GmbH) was implemented to enhance mixing, particle wetting and enable a denser distribution within the mixture. Next, the binder-ST mixture underwent uniaxial pressing (Manual Lab press from P/O/Weber, Germany) at RT, wherein a varied pressure ranging from 60 MPa to 1 GPa and pressing times between 1 to 60 min were applied. Subsequently, the pressed pellets were weighed and dried for 3 to 20 h at 110 °C. An equivalent outcome in terms of relative density and dielectric properties was achieved when composite samples were dried at RT in a desiccator for 24 h. Furthermore, during my visits to Finland, binder-ST composites were hot-pressed at 110°C for 1 h. In this study, processing parameters were thoroughly inspected and optimized somewhat to regulate the energy consumption within this fabrication process. After drying, composite pellets were reweighed, and the water content of 2-3 wt % and total binder content of 9 wt % were estimated from the mass difference and the binder solubility value. The dimensions, including the width and height of the pellets, were measured with a caliper, from where the relative density of the composite samples was calculated. The RTF process scheme is presented in Figure 1.8.

### 3.1.1 Synthesis of ceramic compounds ST, BT; binders NMO, NWO, NSiO

To synthesize ST ceramics, a precise stoichiometric ratio (1:1) of $SrCO_3$ and $TiO_2$ powders was thoroughly mixed in a planetary mill (Retsch) with the addition of ethanol as a mixing medium (30 min, 250 rpm). Following the milling, the ethanol was evaporated at 80 °C. The resulting powder was then uniaxially compacted into pellets ($d$=12 mm, $p$=250 MPa) and calcined at 1100 °C for 20 h (heating rate 5 °C $min^{-1}$). Calcined pellets were crushed and again homogenized with milling in ethanol. Dried powder was pressed into pellets and sintered at 1400 °C for 20 h (heating rate 5 °C $min^{-1}$). Both calcination and sintering were performed in an air atmosphere. Subsequently, a detailed characterization of the sintered ST ceramics was performed, focusing on their microstructural and dielectric properties. To prepare the sintered ST for use in composites, it was crushed in agate mortar and then sieved into various size fractions ranging from <40 µm up to 500 µm. For this, a stack of steel sieves with different mesh sizes (500, 200, 150, 63, and 40 µm; 200 µm in diameter, ISO3310 Endecotts Limited) fixed in a Sieve Shaker (Octagon 200 Sieve shaker, 230 V, 50 Hz, Endecotts Limited) was used. The Na-based salts were prepared via a solid-state reaction, as shown in Figure 3.1. For the synthesis of a particular binder, both reactants were well mixed in an appropriate stoichiometric ratio in a mortar. The binders $Na_2MoO_4$, $Na_2WO_4$, and $Na_2SiO_3$ were synthesized from sodium hydroxide (NaOH, 98 %, Fisher Scientific), molybdenum oxide ($MoO_3$, 99.5 % Thermo Scientific), tungsten oxide ($WO_3$, 99.9 %, Fluka), and silicon dioxide ($SiO_2$, 99.999 %, Alfa Aesar) following the reactions and conditions depicted in Fig. 3.1. The synthesis conditions for NWO and NSiO were optimized in this study based on the existing literature [22, 28]. The powders were homogenized by ball milling (Retsch, Germany) in ethanol (250 rpm, 30 min) before calcination. The dried powder mixture was pressed into pellets and calcined at elevated temperatures. After synthesis, the binder pellets were crushed using a mortar and pestle.

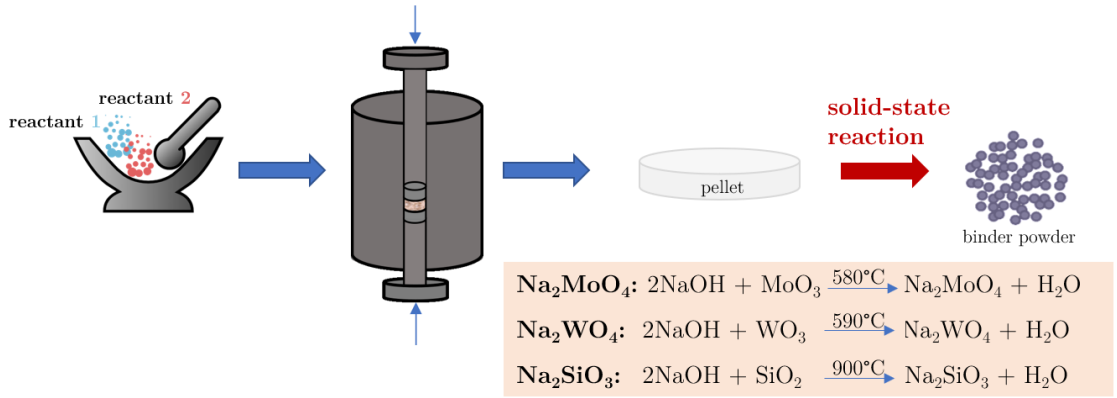


Figure 3.1: Solid-state synthesis of the NMO, NWO, and NSiO binders.

## 3.2 Density Measurements

The densities of the LMO-ST composites were determined using two methods: geometrically measuring the dimensions and weight of the samples after drying and using the He pycnometer method. Whereas the pycnometric density ($\rho_{py}$ or $\rho_{apparent}$) of the samples was measured using a gas pycnometer (Ultrapyc 5000 Foam, helium).

The subsequent equations (3.1-3.7) were used to compute the geometric, theoretical, apparent densities, total and open porosity, and the fraction of open porosity:

$$\rho_{geo} = \frac{m}{\pi x r^2} \tag{3.1}$$

$$\rho_{th} = f_1\rho_1 + f_2\rho_2 \tag{3.2}$$

$$\rho_{py} = \frac{(\rho_{geo}\cdot\rho_{th})}{\Phi_{closed}\cdot\rho_{th}+\rho_{geo}} \tag{3.3}$$

$$\Phi_{total} = 1 - \frac{\rho_{geo}}{\rho_{th}} \tag{3.4}$$

$$\Phi_{open} = 1 - \frac{\rho_{geo}}{\rho_{py}} \tag{3.5}$$

$$\Phi_{closed} = \Phi_{total} - \Phi_{open} \tag{3.6}$$

$$\%\ of\ \Phi_{open} = \frac{\Phi_{open}}{\Phi_{total}} \tag{3.7}$$

Where ρ is the density ($\rho_1$, $\rho_2$ for components 1 and 2, $\rho_{py}$ for pycnometric density), $m$ is the mass, $x$ is the width of the pellet, $r$ is the radius of the pellet, and $f$ stands for the volume fraction ($f_1$, $f_2$ for components 1 and 2), Φ is the porosity.

The geometrical density of each sample pellet was calculated from the mass and dimensions. Theoretical density was assumed from the starting volume fractions of solid binder and solid filler. Relative density equals the quotient of geometrical and theoretical density (Equation (3.8)). In addition, the binder content coming from the saturated solution was calculated (Equation (3.9)) and added to the total mass of the binder (Equations (3.11), (3.12), (3.14)). Total filler content was calculated with Equation (3.13). Water content was calculated from the mass difference between the weighed pellet before drying (after pressing) and after drying (Equation (3.10)). The theoretical density of the pellet and relative density were corrected by including the volume of the dissolved binder (equation 3.15). Fractions of air and filler were calculated by Equations (3.17) and (3.18).

$$\rho_{relative} = \frac{\rho_{geometrical}}{\rho_{theoretical}} \tag{3.8}$$

$$m_{\text{dissolved binder}} = \text{water content}(\%)\cdot m_{before\ drying}\cdot solubility\ of\ the\ binder \tag{3.9}$$

$$\text{water content}\ (\%) = \Delta\text{mass} = \frac{m_{before\ drying} - m_{after\ drying}}{m_{before\ drying}}\cdot 100 \tag{3.10}$$

The sample pellet is weighed after pressing (before drying) and after drying.

Total mass of the binder:

$$m_{\text{binder, total}} = \left(wt\ \%\ of\ the\ binder\cdot m_{before\ drying}\right) + m_{\text{dissolved binder}} \tag{3.11}$$

$$Total\ binder\ content\ (wt\ \%) = \frac{\frac{total\ binder\ content\ (wt\ \%)\cdot m_{after\ drying}}{\rho_{binder}}}{\frac{total\ binder\ content\ (wt\ \%)\cdot m_{after\ drying}}{\rho_{binder}} + \frac{total\ filler\ content\ (wt\ \%)\cdot m_{after\ drying}}{\rho_{filler}}} \tag{3.12}$$

$$total\ filler\ content\ (wt\%) = 1 - total\ binder\ content\ (wt\ \%) \tag{3.13}$$

$$total\ binder\ content\ (vol\%) = \frac{m_{\text{binder,total}}}{m_{after\ drying}} \tag{3.14}$$

$$\rho_{theoretical,\ corrected} = (\ total\ binder\ content\ (vol\ \%) \cdot \rho_{binder}) + ((1 - total\ binder\ content\ (vol\ \%)) \cdot \rho_{filler} \quad (3.15)$$

$$\rho_{relative,\ corrected} = \frac{\rho_{geometrical}}{\rho_{theoretical,\ corrected}} \quad (3.16)$$

$$vol\ \%\ of\ air = 1 - \rho_{relative,\ corrected} \quad (3.17)$$

$$vol\ \%\ of\ filler = 1 - vol\ \%\ of\ binder - vol\ \%\ of\ air \quad (3.18)$$

## 3.3 Coating

In this work, only ST ceramic particles were coated with LMO binder. A precise description of a coating procedure with LMO can be found here [103] and is presented in Figure 3.2. The required mass of LMO powder (6.5 wt %/15 vol %) was weighed and mixed with a few drops of deionized water, and then 1,2-butanediol (> 98 %, Fluka) was added to the LMO slurry. ST powder in all size fractions (40-500 µm) was added. Concurrent mixing and heating to 150 °C were applied. First, water from the LMO-ST solution evaporated. Then, 1,2-butanediol solvent was added, which caused the evaporation of water and precipitation of LMO on the surface of ST particles due to its higher boiling point of 192 °C.

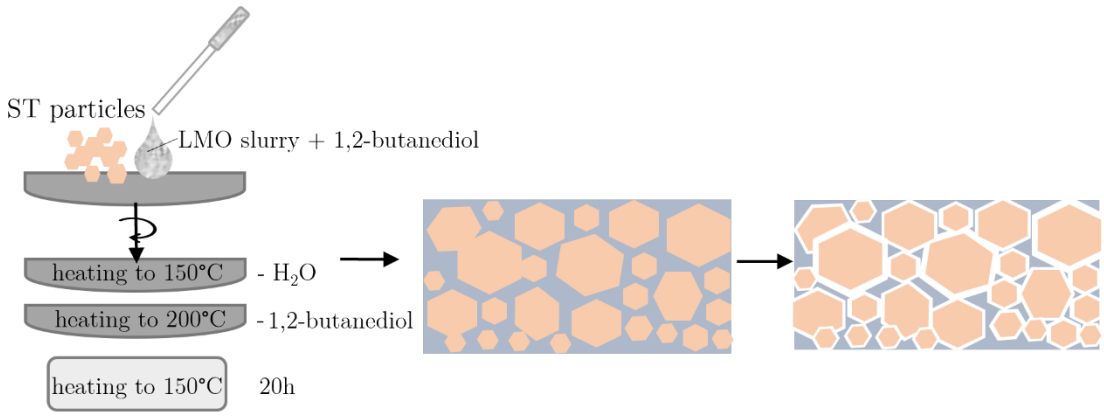


Figure 3.2: The schematics of the coating procedure.

Finally, the temperature was increased to 200 °C to evaporate the remaining 1,2-butanediol. A thick paste of ST and LMO was formed and post-heated at 150 °C in the laboratory oven for 20 h. The coated ST particles were then wetted with LMO saturated solution, transferred to a steel die, sonicated for 30 s, pressed at 250 MPa for 5 min, and dried for 6 h at 110 °C in the laboratory oven. Afterward, dimensions were measured using a caliper, and silver paste was applied to the top and bottom sides of the pellet as required for dielectric measurements.

## 3.4 Impregnation

Impregnation was performed only on the LMO-ST samples with a 6.5 wt % (15 vol %) LMO composition. As-prepared LMO-ST samples were immersed in TTIP solution in a 10 mL glass vial. Impregnation involves four steps: deaeration, filling the pores under high

pressure, hydrolysis under water vapor, and drying (Figure 3.3). First, the vials were transferred to the desiccator coupled with a cold trap (liquid nitrogen) and a vacuum pump. This step was utilized to remove air from the pores of the pellets. For this purpose, the pressure was lowered to about 100 mbar for 10 min. Subsequently, the vials containing the pellets were subjected to a high pressure of up to 3 bar for 3 min. Thus, the pores in the composites were filled with TTIP. The samples were then subjected to water vapor for 10 min to prompt hydrolysis of TTIP. Subsequently, the samples were dried in air at 110 °C for 4 h. The entire impregnation process with all 4 steps, shown in Figure 3.3, was repeated one or three times for two different sets of experiments. Moreover, two other drying procedures were tested. The impregnated samples were dried in a vacuum oven at room temperature for 4 h or fired at 400 °C for 4 h. After drying, the density and dielectric properties of the pellets were measured. The impregnation process is simple and feasible for a larger batch of samples, making it easily scalable for industry [149].

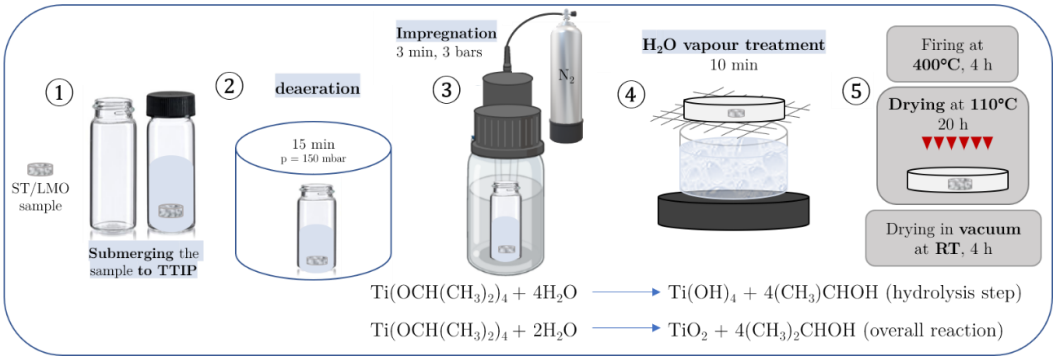


Figure 3.3: Schematic representation of the impregnation process using TTIPto compensate residual porosity in LMO-ST composites.

## 3.5 X-ray Diffraction Analysis

The crystal structure of all composite constituents and composites was examined at room temperature using X-ray diffraction (XRD, AXS D4 Endeavor, Bruker Instruments).

## 3.6 Scanning Electron Microscopy-Energy Dispersive Spectroscopy (SEM-EDS)

A scanning electron microscope FESEM Ultra plus (Carl Zeiss, Germany) with an energy-dispersive spectrometer (EDS, Inca 400, Oxford Instruments) was used to perform a microstructural analysis. Prior to the SEM examination, to avoid the buildup of electrons on the surface of the specimen, known as sample charging, a thin film of 4-5 nm thick Pt layer using PECS (GATAN Inc.) was deposited. For SEM-EDS analysis, cross-sections of the pellets were prepared using an ion beam cross-section polisher (Jeol IB-19520CCP, Jeol Ltd., Japan). FESEM–EDS, Carl Zeiss SMT AG was used for SEM imaging of binder-ST samples in Oulu. For SEM imaging of fractured samples in Leoben, Thermo Scientific™ Apreo 2 SEM was used.

## 3.7 Fourier-Transform Infrared Spectroscopy (FTIR)

The nature of the bonds in the prepared binder-ST and impregnated composite pellets was investigated using a diffuse reflectance infrared Fourier-transform spectrometer (DRIFT; PerkinElmer Spectrum 100, Waltham MA, USA). Spectra were measured in the wavenumber range 400-4000 $cm^{-1}$. Sample preparation for DRIFT was carried out by mixing 5 mg of the investigated material with 70 mg of KBr.

## 3.8 Thermogravimetric Characterization

For thermogravimetric analysis, heat treatment of samples was performed from 40 °C to 800 °C using a thermogravimetric analyzer coupled with a mass spectrometer (TG-MS; NETZSCH STA 449 C/6/G Jupiter, 403 C Aëoloss QMS 403). Mass loss and released gases were evaluated on ~150 mg of powder for each sample (as-prepared binder-ST, pure binders, pure ST, impregnated- LMO-ST samples) in $Al_2O_3$ crucibles. A heating rate of 10 K $min^{-1}$ in an operating atmosphere, consisting of 20 % oxygen and 80 % argon, with a total flow rate of 50 mL $min^{-1}$, was utilized for the measurements.

## 3.9 Surface Wettability

The intermolecular interactions of the different binders with ST were investigated by measuring their surface wettability using a contact angle meter, Theta Lite (Biolin Scientific, Gothenburg, Sweden). Polishing of the ST surface was performed using grinding paper (grits 1200, 2000, and 4000), cleaned with water and acetone, exposed to ultrasound, and dried in a drying oven at 110 °C to prevent water adsorption at the surface. All ST surfaces were treated equally to avoid the effect of surface roughness on the contact angle (CA) measurements. Droplets (3 µL) of a saturation solution of each binder were placed on the polished ST surface. Ten subsequent images were taken of the droplets at one-second intervals to observe any changes in the droplet shape. The images were analyzed using the Attension theta 4.1.0 Software to obtain the corresponding contact angles. The arithmetic mean of the left and right contact angles was considered for the final contact angle measurement. At least six replicates saturated solution droplets were deposited on the ST pellet to obtain the average value and standard deviation.

## 3.10 Dielectric Measurements

Prior to dielectric measurements, silver paste (DuPont 5064H, DuPont Microcircuits Material, United States) was applied to the top and bottom surfaces of the pellet. The applied paste on both sites was then dried at 110 °C. Subsequently, relative permittivity and dielectric losses were measured using an Agilent 4284A Precision LCR meter with a custom sample holder, with open/short circuit calibration. The entire setup was placed inside a desiccator during the measurements. A custom-made setup was constructed after the effect of moisture on composites was observed. All dielectric assessments were carried out within the frequency range of 20 Hz to 1MHz, with an amplitude of 1 V. Dielectric properties of ceramic composites were measured using the $TE_{01\delta}$ resonant cavity method. Pure binders were characterized using the N1501A coaxial probe method (Keysight). The temperature coefficient of the resonant frequency of the binder-ST composites was measured on three parallel samples of each composition at five different temperatures (from 27.5 °C to 65 °C, each step 10 °C; cooled down to 27.5 °C and remeasured) using $TE_{01\delta}$

resonant cavity method (Vector network analyzer, E8361C, Agilent) coupled with thermal chamber Ultra 2000 (Kambič) setup.

## 3.11 Microstructural Simulation Using OOF2

The OOFEM analysis was performed on the SEM-EDS images of polished cross-sections of LMO-ST composites to investigate the microstructure-property relationship. The OOF2 was used for the approximate relative permittivity in composite samples. The software requires a microstructural image that is transformed into a binary image and serves as the input data. Microstructure is divided into pixel groups and assigned to materials properties. The simulation of the microstructure subjected to an applied electric field was conducted. Using OOF2, the distribution of polarization and energy of the electric field for the entire Microstructure was evaluated. Simulation was performed on different sample compositions of LMO (10 %, 20 %, 30 %, 50 %, 85 %)-ST composites. With OOF2 simulations, the effect of binder content, coating of ST ceramic particles, and electric field penetration through the composite material was demonstrated. The Ubuntu Linux system was used to run OOF2.

## 3.12 Mechanical Measurements – Ball on Three Ball Test (B3B) and Fractography Analysis

The characteristic strength of ceramics and ceramic composites was measured under biaxial bending using the ball-on-three-balls (B3B) test [131]. The measuring setup is depicted in Figure 3.4. The experiments were conducted under ambient conditions (~25 °C and ~30 % RH) utilizing a Zwick 010 testing machine (manufactured by Zwick GmbH & Co. KG in Ulm, Germany). Depending on the sample type, a 10 kN load cell was employed with a 0.5 mm $min^{-1}$ displacement rate and a 2-5 N preload. All samples measured 10 mm in diameter and exhibited thickness variations ranging from 0.8 mm to 2.0 mm. A B3B testing fixture included four balls measuring 6.35 mm in size, which had to be precisely aligned in the test jig. The use of a manifold guide can ensure a good alignment. The fixture is placed in the universal testing machine, and some load is applied. When preload was detected, the guide was carefully removed. The friction between the fixture and balls keeps the supporting balls and the specimen in place while the loading ball is fixed in its position. Next, the loading was increased until the specimen was fractured. The characteristic strength ($\sigma$) values were obtained by fitting the measured data in agreement with the two-parameter Weibull statistics using the maximum likelihood method. After the B3B mechanical testing, sample fractures for each sample were reassembled under a stereomicroscope to identify the origin of the fracture (Smartzoom 5 digital microscope, Carl Zeiss Microscopy LLC., United States). Fractography analysis and fracture pattern identification were conducted by microstructure imaging using a scanning electron microscope (Thermo Scientific™ Apreo 2 SEM). Before SEM imaging, samples were gold coated using an Agar sputter coater.

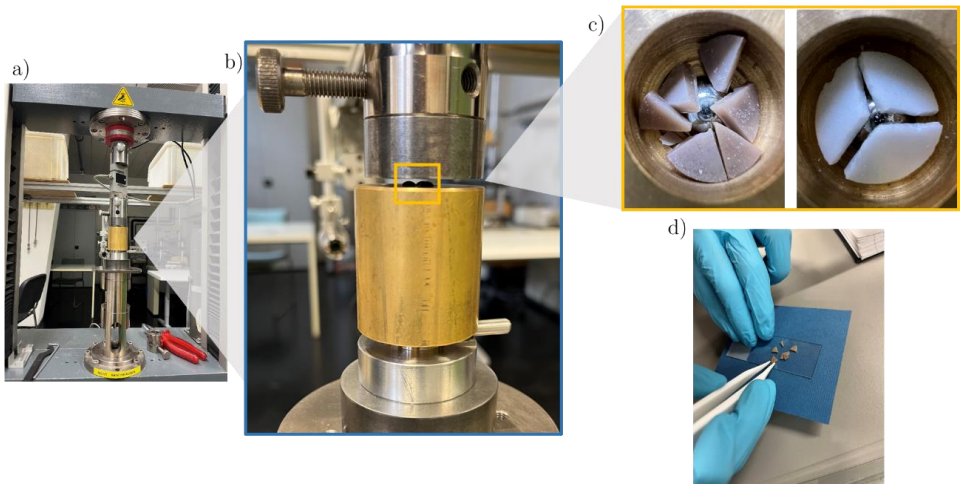


Figure 3.4: The B3B biaxial testing setup. a, b) measuring setup; c) fractured samples in fixtures; d) reassembling sample fragments for fractography analysis.

# Chapter 4

# The Optimization of RTF Process – the Effect of Processing Parameters on Density and Dielectric Properties

This chapter provides an overview of the process of "Room temperature fabrication (RTF)" of ceramic upside-down lithium molybdate-strontium titanate (LMO-ST) composites. RTF is a promising alternative to the time- and energy-consuming high-temperature sintering of electroceramics, which involves mixing the initial phases, molding with a steel dye, pressing, and drying. By the cause of densification, LMO-ST composites, based on a high ratio of filler ST coupled with the corresponding LMO binder, are fabricated. Part of the binder is admixed to the ceramic particles, and an additional part is added as a saturated aqueous solution, which crystallizes during pressing and drying, leading to its deposition on the surface of the filler particles.

Investigating various processing aspects and corresponding microstructural and structural analyses provided a more profound understanding of the method. Optimizing processing conditions such as particle size distribution, pressure, pressing time, ultrasonic treatment, and drying time improved the functional properties of the LMO-ST composites.

The results of this chapter were published in the manuscript entitled: Dielectric Properties of Upside-Down $SrTiO_3/Li_2MoO_4$ Composites Fabricated at Room Temperature

**Published in the journal** Frontiers in Materials, April 22, 2021;
https://doi.org/10.3389/fmats.2021.669421.

## 4.1 Results and Discussion

This chapter presents the results of the study in which I attempted to optimize the RTF method for the LMO-ST composites. For this purpose, the influence of different processing parameters on the dielectric properties of the prepared composite samples was evaluated. The composition of 93.5 wt % of ST and 6.5 wt % of LMO (which equals 15 vol % of LMO/85 vol % of ST) was used. The experimental results in terms of relative density and relative permittivity are presented with a corresponding error bar of 2 % calculated from the accuracy of the measured sample dimensions and LCR meter. Moreover, the error value of the dielectric losses was estimated to be only 0.004 % and, therefore, was not further reported. Further in this thesis, the relative density error values are not shown next to the data, as they remained consistent up to 2 % for different samples. The temperature dependence of the relative permittivity in the temperature range from 20 to 80 °C at 1 MHz was investigated. The results showed that a typical value of the temperature coefficient ranges from 0.13 % to 0.15 %, which agrees well with the literature data for ST ceramics [150],[151]. The two-component composites described in this chapter comprise functional ST ceramics and the LMO binding phase. The ST ceramic used as filler in these composites exhibited a relative permittivity ($\varepsilon_r$) of 296 and dielectric losses (tan $\delta$) of 0.0015 at 1 MHz. LMO served as a binding phase and exhibited relative permittivity of 5 and dielectric losses of 0.0005 at 1 MHz.

### 4.1.1 Microstructural characterization of ST, LMO, and LMO-ST composites

Preliminary characterization of the as-prepared ST ceramic revealed that calcination and sintering resulted in a very dense ceramic with a high relative density of over 98 % and an average grain size of 1.5 μm (Figure 4.1).

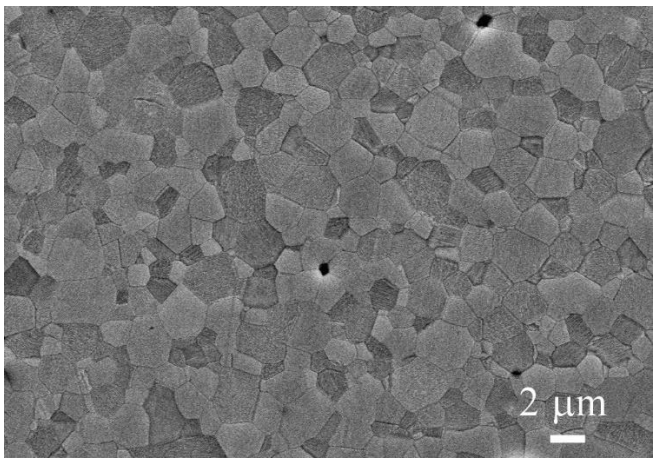


Figure 4.1: SEM micrograph of conventionally sintered ST at 1400 °C for 20 h.

Figure 4.2 shows the microstructures of the prepared composites. The SEM micrographs and EDS mapping show a 0–3 composite microstructure in which the roles of the binder LMO and ST filler are flipped due to the compositional proportion. Hence, the term "upside-down" comes. In Figures 4.2 a–c, the green-colored regions are associated with LMO, while the orange-colored areas belong to the ST particles. The LMO phase is distributed among the larger ST particles (Figure 4.2 a), and smaller ST particles are embedded in the LMO phase (Figure 4.2 b). Moreover, Figures 4.2 a–c show that the

samples have residual porosity, which is consistent with the results of the density measurements. Prepared cross-sections showed a typical curtaining pattern on the surface due to ion beam treatment by the cross-section polisher (Figures 4.2 a–c). The LMO phase, which incorporates smaller ST particles, fills the voids between larger ST particles. The contact between the LMO phase and the ST particles is predominantly tight, but porosity and loose contacts can be observed in certain places. The addition of LMO in both dry (powder) and wet (ss) forms was expected to create a continuous thin layer (coating) of the binder on the surface of ST particles. This was, however, not confirmed by the SEM analysis. One possible reason is that a significant amount of the saturated LMO solution was removed from the composite mixture during pressing. As a result, the LMO film was successfully precipitated only in certain areas in the sample pellet, such as voids between ST particles.

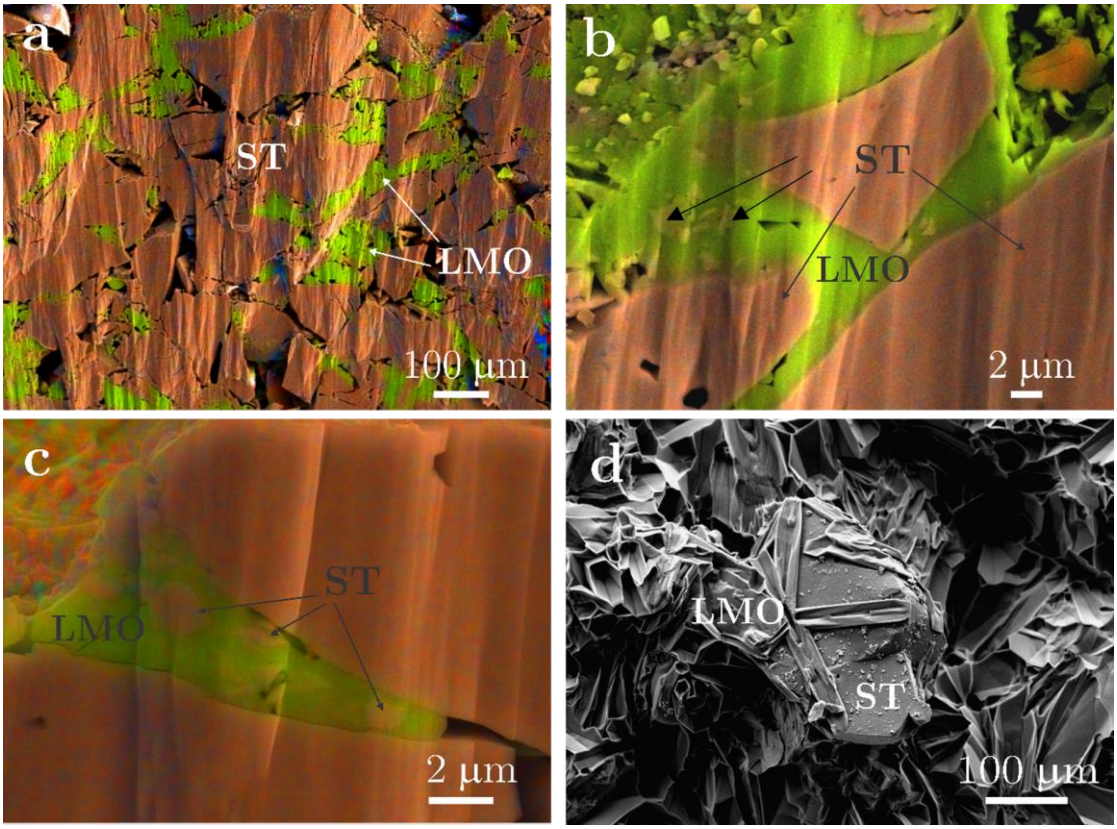


Figure 4.2: EDS mappings of the cross-section (a–c). (b, c) Expanded view of the LMO-ST contact showing good adhesion and bonding of LMO (green color) on the surface of larger and smaller ST particles (orange color). (d) SEM micrograph of the surface of the prepared samples.

The SEM micrographs of the surface of as-prepared LMO-ST pellets demonstrate that LMO is concentrated at the bottom and top of the pellet after the densification process. This behavior can be attributed to the pressing phase and pressure gradient. The liquid LMO-rich phase is pressed out at the top and bottom of the steel dye. When the pellets undergo drying as post-processing, water evaporation, and extensive LMO crystallization occur in this area. As a result, I obtained a surface, as seen in the micrograph in Figure 4.2 d.

### 4.1.2 XRD Analysis of LMO, ST, and LMO-ST composites

Figure 4.3 shows the XRD patterns of the representative LMO-ST composite sample and both initial components (LMO, ST). The pattern of the composite sample exhibits the characteristic XRD reflections of ST (ICDD No. 35-0734) and LMO (ICDD No. 12-0763), confirming that the components do not react. The intensity of reflections belonging to the LMO phase is weaker than ST reflections due to the low total LMO phase content (~9 wt %). However, the most intense LMO reflections are observed at 20°, 21.1°, 24.9°, 26.8°, and 27.6° 2Θ values.

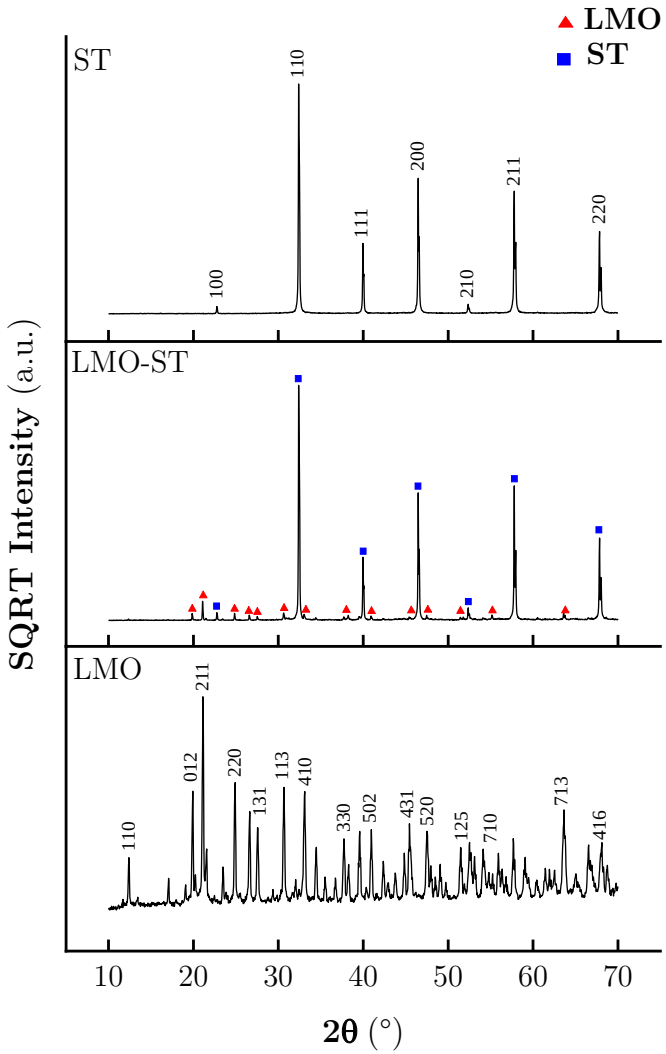


Figure 4.3: X-ray diffraction patterns of LMO-ST composite, ST sintered at 1400 °C, and commercial LMO.

### 4.1.3 The Effect of Particle Size Distribution on Dielectric Properties of LMO-ST Composites

As a first step in investigating different processing parameters for RTF of LMO-ST composites, I examined the effects of particle size and the proportion of various fractions. One essential physical property of as-prepared composites is the packing density, which ideally should be as high as possible, as indicated in previous works [101]. The packing density is strongly related to the distribution of larger to smaller particles and their volume fractions. Thus, it tends to decrease when the ratio of larger to smaller particles decreases. The Furnas model can predict the packing mechanism so that smaller particles fill the interstices between larger packed particles, leading to lower porosity [152]. According to the literature, wide particle size distribution contributes positively to higher relative density values [103]. For this purpose, the size of ST particles was varied to inspect the effect of particle size distribution on the density and dielectric properties. In contrast, the size of LMO particles was constantly ranging below 40 µm. For this section, I maintained constant processing conditions: 0.5 min of ultrasonic treatment, 5 min of pressing at 250 MPa, and 20 h of drying to prepare LMO-ST composites. The average relative density, average relative permittivity, and dielectric losses, measured from a series of three samples prepared under the same experimental conditions, are presented in Table 4.1. I prepared five samples that consisted of different-sized ST particles. Using smaller particles (mixture 1) resulted in the lowest relative density of 76 %, while higher relative density values of 81 % and 84 % were obtained with LMO-ST mixtures 2 and 3, respectively, consisting of larger particles. Following the Furnas model for randomly dispersed spheres, the initial particle size distribution was changed from single to triple modal ($d_1$, 1/7 of $d_1$, 1/49 of $d_1$) and mixed in the ratio of fractions 75/14/11. Theoretically, in this way, a maximum packing density of 95 % can be achieved [153]. LMO-ST mixtures 4 and 5 implemented this idea with a relative density of 83–84 %. There was a noticeable increase in density when the particle size of ST was increased from 40 µm to 200-500 µm. This increase may be due to the smaller particles being less able to be wetted and compressed. Cabiscol et al. showed that if the primary particle is sufficiently small, the inter-particle cohesion force will dominate over the external forces, which results in stable structures at low bulk density. In addition, smaller particles are more cohesive and tend to agglomerate [154]. However, the density did not improve when changing from mixture 3 to mixture 5.

Table 4.1: The effect of ST particle size fractions on the relative density and dielectric properties of LMO-ST composites fabricated at RT and measured at 1 MHz.

| **LMO-ST mixture number** | **Particle size range (µm)** | **Relative density, ρ** | **Relative permittivity, $\varepsilon_r$** | **Dielectric losses, *tan* δ** |
|---|---|---|---|---|
| 1 | <40 | 76±2% | 46±1 | 0.005 |
| 2 | 150-200 | 81±2% | 65±1 | 0.003 |
| 3 | 200-500 | 84±2% | 70±1 | 0.002 |
| 4 | 75 %150-200 + 25 %<40 | 83±2% | 67±1 | 0.003 |
| 5 | 75 % 200-500 + 14 % 63-40 + 11 %<40 | 84±2% | 73±1 | 0.005 |

*$\rho$, $\varepsilon_r$, tan $\delta$ average values were calculated on 3 parallel samples.*

Regarding dielectric properties, the ceramic prepared from smaller particles (mixture 1) exhibited the lowest relative permittivity of 46 with the corresponding dielectric losses of 0.005. This could be due to the higher porosity in the case of sample mixture 1. According to the results, pellets consisting of larger particles (mixture 3) exhibited a relative permittivity of 70 and dielectric losses of 0.002, compared to sample mixture 2, where a lower relative permittivity of 65 and dielectric losses of 0.003 were achieved. Thus, the improved relative permittivity of LMO-ST composites was observed with the increasing size of the initial ST particles. Generally, by increasing the relative permittivity of the samples, their dielectric losses were also increasing. Compared to mixture 2, mixture 4 shows a slightly improved relative permittivity of 67. Similarly, mixture 5 outperformed mixture 3 by having a relative permittivity of 73, corresponding to increased dielectric losses of 0.005. Although I did not detect a large difference in density between mixtures 3 and 5, the difference in $\varepsilon_r$ can be further explained by the OOF2 results. The small ST particles filling the empty space between the larger particles are expected to increase the polarization in the composites compared to if there was only air, which is expected to happen when we only have large ST particles. Mixture 1, which consists of only small particles, results in higher porosity, which is the main factor for the lower relative permeability. The implementation of only smaller particles in composite mixtures resulted in more interfaces having either air around them or a thin layer of precipitated LMO from a saturated solution. According to the OOF2 simulations (shown in Chapter 6), the LMO and air disrupt the path of the electric field, reducing the polarization through the composites.

Based on these results, the LMO-ST mixture 5 was selected as having the optimal particle size distribution and was thus used in further experiments.

### 4.1.4 The Effect of Ultrasonic Treatment on Dielectric Properties of LMO-ST Composites.

After initial experiments on the effects of particle size distribution on packing density and dielectric properties, I further investigated the effect of ultrasonic treatment time.
If particles are not well-mixed and agglomerated, undispersed zones of a compound can form, which negatively affects the binding process. As previously reported, ultrasonic irradiation in liquid-solid systems provides more uniform mixing [155] and improves the crystallization process of the LMO binder on the ST filler particles. In addition, the ultrasonic field causes bubbles to collapse near the particle surface, increasing the overall mass transfer. In the absence of a sufficient mass transfer, high supersaturation subsequently occurs, leading to aggregation of the LMO [156].

In this section, LMO-ST samples were prepared from mixture 5, which consisted of ST particles <40 µm, 40–63 µm, and 200–500 µm. The moisturized sample mixture was subjected to ultrasonic treatment using the ultrasonic processor. The ultrasound duration varied between 0, 0.5, 1, 2, and 5 min. Other operating conditions were constantly set: 5 min of pressing at 250 MPa and 20 h of drying, respectively.

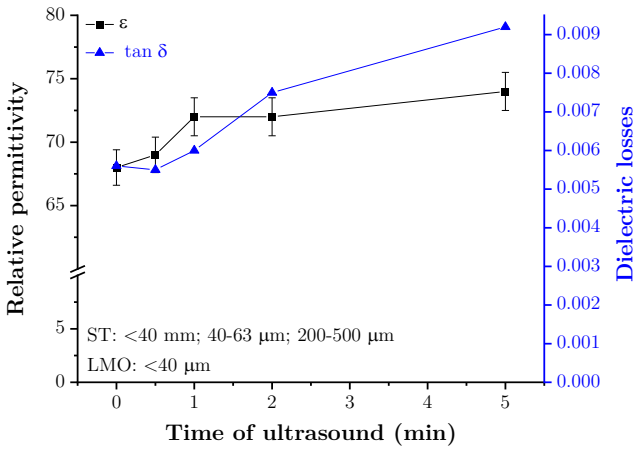


Figure 4.4: The effect of ultrasound duration on the dielectric properties of LMO-ST composites fabricated at RT.

After applying ultrasound treatment, a constant relative density of 83 was obtained from the dimensions of the samples. Results on relative permittivity and dielectric losses are shown in Figure 4.4. It can be seen that the duration of ultrasonic treatment of the initial mixture affects the dielectric properties of the LMO-ST composites. The highest measured relative permittivity was obtained after the composite system was treated with ultrasound for 5 min, while the lowest dielectric losses were obtained after 0.5 min. As shown, the relative permittivity increased by 10 % with the increase in ultrasonic treatment duration, but dielectric losses doubled. From a practical point of view, I aimed to facilitate the fabrication process, so the ultrasonic treatment was set to a constant 0.5 min in further experiments.

### 4.1.5 The Effect of Humidity on Dielectric Properties of LMO-ST Composites

During the preliminary experimental work, I observed substantial variations in dielectric properties from batch to batch. Therefore, the experimental focus in this section was placed on the effect of ambient humidity on the dielectric properties of LMO-ST composites. In line with this, previous work on dielectric ceramics reported that the operating environment and humidity strongly influence dielectric losses [157].

In the case of LMO-ST composites, moisture sensitivity could be attributed to a slight hygroscopicity of $Li_2MoO_4$ [158]. Accordingly, optimization of the measurement setup was necessary. Dielectric measurements were performed in a desiccator to create humidity-controlled conditions. During the RTF of LMO-ST composites, the following operating conditions were constantly set: 0.5 min of ultrasonic treatment, 5 min of pressing at 250 MPa, and 20 h of drying.

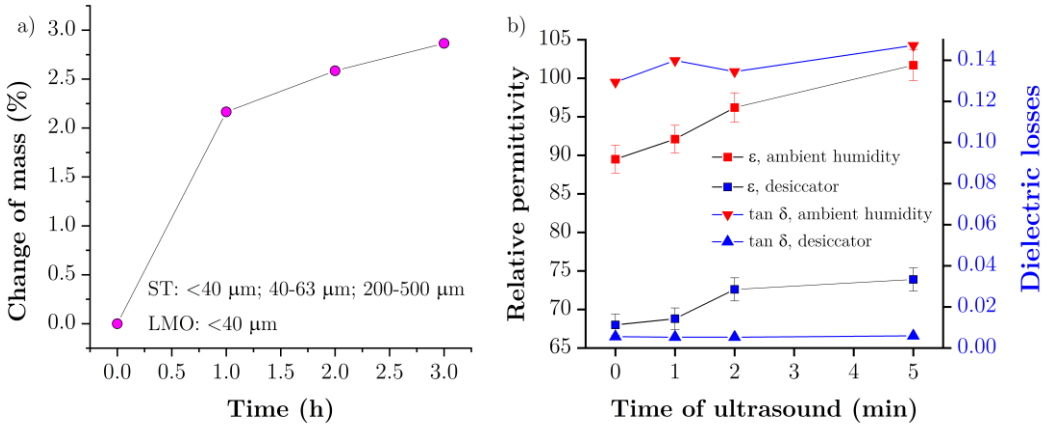


Figure 4.5: LMO-ST composites exposed to different conditions. (a) LMO-ST samples were exposed to 100 % humidity, and the change in mass over time was observed. (b) The effect of ultrasound duration on the dielectric properties of LMO-ST composites was measured under two different conditions: ambient humidity (60 % RH) and in a desiccator.

Figure 4.5 a) shows that water adsorption on LMO-ST composites exposed to 100 %relative humidity increases steadily with time. Figure 4.5 b) shows the effect of ambient humidity on the dielectric properties of the samples. One set of the samples was exposed to ambient conditions of approximately 60 % relative humidity, and the other set was placed in a desiccator immediately after drying. The results of both sets show a significant difference in the relative permittivity and dielectric losses. For example, the relative permittivity under moisture-free conditions ranges from 68 to 74, compared to relative permittivity values reaching 102 under ambient conditions. In addition, dielectric losses were increased from 0.005 to 0.147 for the same change. From these results, it can be concluded that ambient humidity immensely affects the dielectric properties of the LMO-ST composites. Relative permittivity increases due to the presence of physically adsorbed water, which has a relative permittivity of 80 at 1 MHz and RT (higher than LMO or air permittivity) [159]. Adsorbed-free water apparently increases both relative permittivity and dielectric losses. Consequently, the pellets should be stored in a desiccator at constant low humidity or impregnated with silicone electronic coating [158].

### 4.1.6 The Effect of Drying on Dielectric Properties of LMO-ST Composites

The post-processing step of drying was carried out at 110 °C alongside RTF to speed up the evaporation process and guarantee that all residual water was removed completely. I aimed to improve the drying efficiency and investigate how reduced drying time impacts the final properties of the LMO-ST composites. Sample pellets were pressed at room temperature and dried for 3, 6, 10, and 20 h. The weight and dimensions of the pellets were measured immediately after drying. Interestingly, the calculated relative density of 83 % was found to be constant across all samples, implying that it was not dependent on the variations in drying time.

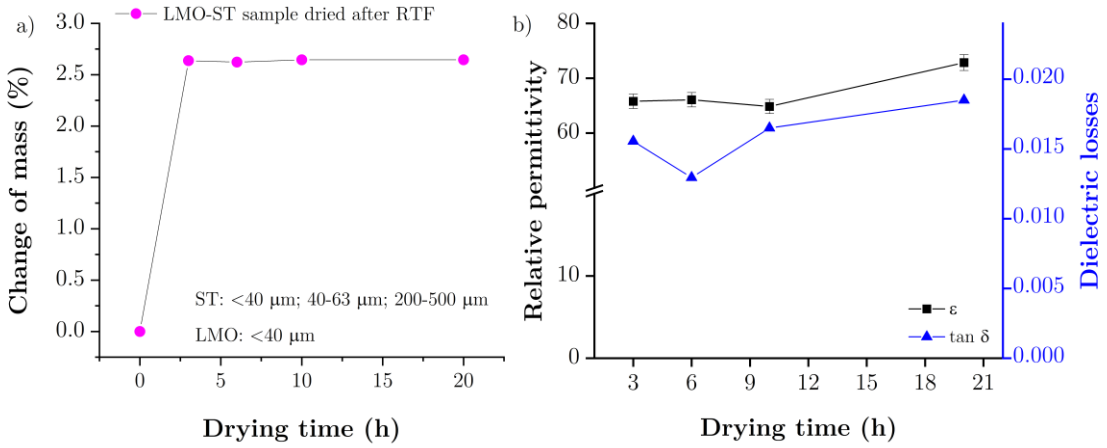


Figure 4.6: The effect of drying time on dielectric properties a) Mass of LMO-ST composite changing over drying time. b) Relative permittivity and dielectric losses as a function of drying time.

In Figure 4.6 a), it was shown that a constant mass was reached after 3 h of drying, which indicates that the drying time could be optimized to 3 h. This is beneficial in terms of time and energy consumption for the RTF process. However, it was also found that a shorter drying time at 110 °C could have a detrimental effect on the relative permittivity, as shown in Figure 4.6 b). The dielectric properties of samples dried for 3, 6, 10, and 20 h are shown in Figure 4.6 b). Dielectric measurements showed that the relative permittivity of samples dried for 3, 6, 10, and 20 h increased slightly with increasing drying time, although the weight of the pellets remained constant. The slight increase in relative permittivity presumably emerges from the higher crystallinity of the LMO binding phase, achieved with a longer drying time. As reported in the study [103] and further verified during my experimental work, the same properties are obtained when the ceramic is dried in a desiccator for longer than 48 h.

### 4.1.7 The Effect of Pressure and Pressing Time on Dielectric Properties of LMO-ST Composites

The main driving force of consolidation and densification during RTF of LMO-ST composites is the difference in chemical potential of the LMO solution and the applied pressure. This enables the rearrangement and subsequent binding of the particles, which is facilitated by the presence of LMO in the aqueous phase [46]. In addition, the frictional properties and wetting play an important role in reducing the voids between the ST particles during pressing. Friction may affect filler and binder interaction as it implies the presence of a compressive force normal to the interface. Additionally, the presence of binder in the form of a saturated solution decreases shear forces between the sliding particles, thereby enhancing consolidation. This mainly occurs when the surface is not smooth. Smooth surfaces won't cause friction but will be wetted more easily as it is generally known that surface roughness greatly affects the wetting [153].

To inspect and optimize the RTF process, the pressure was varied from 10 to 60, 130, 250, 380, 500 MPa, and 1 GPa during the compaction of LMO-ST composites. Other operating conditions during RTF were constantly set: 0.5 min of ultrasonic treatment, 5 min of pressing, and 20 h of drying. As expected, higher pressure contributes to the higher

relative density of the LMO-ST composites, ranging from 82 to 87 %, as shown in Figure 4.7 a).

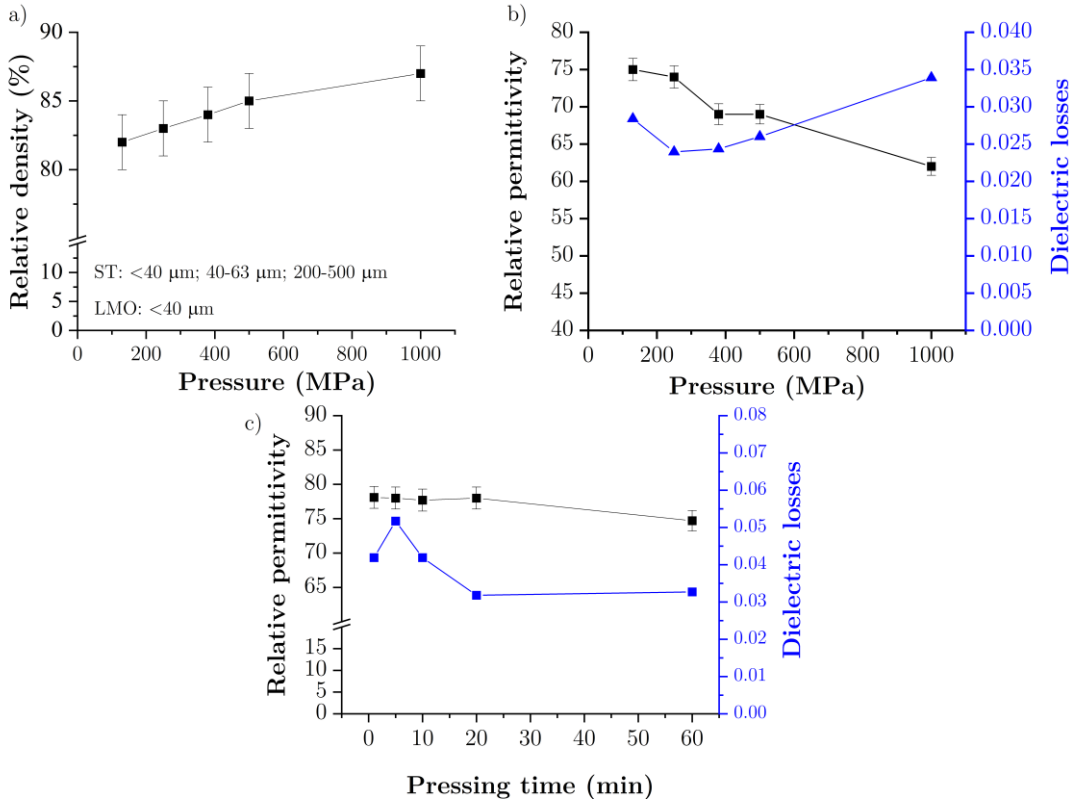


Figure 4.7: The effect of pressure on the relative density (a)) and dielectric properties (b)) of LMO-ST composites. c) The effect of pressing time on relative permittivity and dielectric losses of the LMO-ST composites.

Figure 4.7 b) shows the effect of pressure on the dielectric properties of LMO-ST composites. Pressing at 10 and 60 MPa was unsuccessful, resulting in fracture of the samples, which were thus not characterized for dielectric properties. The pressure was indeed too low to be able to compress the wetted composite mixture. For the samples pressed at higher pressure, the relative permittivity decreases from 75 to 62, with an associated increase in dielectric losses. This behavior could be attributed to the cracks in the larger ST particles formed under higher pressure, leading to higher reflection of the electric field and, consequently, lower dielectric properties. This assumption was confirmed by SEM-EDS analyses of the samples pressed at 130 MPa and 1,000 MPa, as shown in Figures 4.8 a) and b), respectively. However, the cross-sectional area of the pellet pressed at 130 MPa showed almost no cracks. As a result, it was found that 250 MPa was the most optimal pressure for RTF, providing both high relative permittivity and low dielectric losses. In conclusion, a lower pressure for composite processing is advantageous from a fabrication point of view. While inspecting the pressing stage of the RTF process, I also used the cold isostatic pressing of previously RT-pressed wet composite pellets. However, upon removing the sample pellets from the silicone oil and protective cover, the sample pellets were either chipped or completely crushed. Even when using a warm isostatic press at 85°C, the issue persisted as the pellets remained wet, and I encountered the same problems.

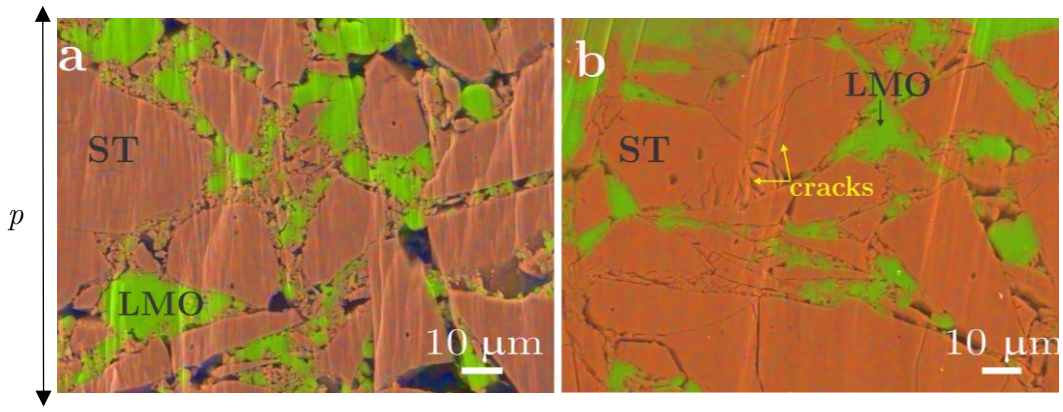


Figure 4.8: SEM micrographs of the LMO-ST composite pressed a) at 130 MPa and b) at 1 GPa. The green color represents the LMO phase, while the orange color corresponds to ST. The black line arrow represents the direction of the pressure.

In the compaction phase at room temperature, the pressing time is a crucial parameter that affects the functional properties of LMO-ST composites. Various pressing times varying from 1, 5, 10, 20, to 60 min were applied at a constant pressure of 250 MPa. The results showed that the measured relative density was constant at 84 for all samples, indicating that it was independent of the pressing time. However, a slight variation of the relative permittivity with the pressing time was observed, which was attributed to the increase in the interaction of the ST filler particles with the LMO binder, as shown in Figure 4.7 c). The dielectric losses increased from 0.042 to 0.052 in the first 5 min but then decreased to 0.020 during the rest of the process. Based on these results, it was concluded that the extended pressing time did not have a beneficial effect on the RTF process. Therefore, the final optimal pressing time was set to 5 min. Although the losses were slightly higher at 5 minutes of pressing, $\varepsilon_r$ was considered a more important parameter for determining the optimal pressing time because $tan\ \delta$ values are highly dependent on various external factors and are not always the best criterion. Furthermore, extending the pressing time by 4 times (~ 20 min, see Figure 4.7 c)) would significantly prolong the entire RTF process of the sample synthesis without contributing much to improving the dielectric properties.

## 4.2 Conclusions

The optimization of the RTF process for LMO-ST composites was the subject of this chapter. More precisely, the influence of various processing parameters on the final dielectric performance of LMO-ST composites has been investigated. The figures above demonstrate data as a function of the varied processing parameters, including relative permittivity and dielectric losses, which varied between 46 to 78 and 0.002 to 0.05 at 1 MHz, respectively. These results indicate that the RTF process can produce dense LMO-ST ceramic composites with excellent dielectric properties without the need for additional sintering steps at high temperatures. The high content of ST filler contributes to an increased relative permittivity. At the same time, the LMO binder in the solid and aqueous phases facilitates densification during pressing, resulting in a higher packing density of 84 %. The SEM-EDS analysis of the composites confirmed that the LMO is distributed between the ST particles, which physically binds them together and reduces the overall porosity of the composites. An improvement in the dielectric properties of the LMO-ST composites was achieved by selecting the larger ST particles (200–500 µm), which were combined with smaller ST fractions below 63 µm. Moreover, ultrasonic treatment as a

processing step is shown to positively affect the dielectric losses of the upside-down LMO-ST composites. However, the important influence of ambient humidity on the dielectric properties has been confirmed, so careful control of the operating conditions is inevitable. Moreover, dielectric measurements must be performed in a moisture-free atmosphere. As a drying step of the RTF was studied, a constant mass was obtained after 3 h. Moreover, a shorter drying time has a minor effect on the dielectric properties. As expected, increasing pressure contributes to a higher relative density of the LMO-ST composites and a lower relative permittivity. However, the dielectric properties decrease with increasing pressure, probably due to the cracks generated by the strong mechanical stress. Therefore, 0.5 min of ultrasonic treatment, 5 min of pressing at 250 MPa, and a drying time of 3–6 h are the optimal processing parameters proposed in this study. When the RTF of LMO-ST composites is compared to the solid-state sintering of ST ceramics, it is clear that a lower relative density was achieved with RTF. The relative density of sintered LMO and ST, as well as LMO-ST composites, are generally >97% (section 9.1.1). Those results are hardly comparable with cold sintering processing as no research has been conducted on LMO-ST composites. The closest comparison of RTF to CS is a study on $Li_2MoO_4$-$Al_2O_3$ composites cold-sintered at 200 MPa pressure and 150 ℃ which resulted in higher MW properties ($\varepsilon_r$ of 6.67, $Q \times f \sim$ 17,846 GHz, $\tau_f \sim -105 \times 10^{-6}$/K when 40 % of $Al_2O_3$ was used; [160]) compared to LMO-ST (section 8.1.3). Cold sintering of pure ST at 180 °C and 750 MPa required a post-annealing step at 950 °C and resulted in $\rho \sim 97$ % and $\varepsilon_r$ of 100 at 1 MHz [95].

The presented results show that the RTF of upside-down ceramics paves the way for novel processing of electroceramics without significant degradation of their functionality and enables further integration possibilities in various electronic devices.

# Chapter 5

# Dielectric Performance of LMO-ST Composites as a Function of Varied Composition

In this chapter, I investigated the correlation between composition, microstructure, and dielectric properties when composition in LMO-ST composites was varied. The results showed that increasing the LMO binder content resulted in a higher relative density (up to 93%) but a lower dielectric constant in the range of 75 to 5. Experimental results of relative permittivity were further compared with the calculated results using Rules of mixtures (ROM). Among them, the most suitable was the Lichtenecker mixing rule, modified for a three-phase composite system. Modeling further explained the detrimental effects of porosity on the dielectric properties.

Results presented in this chapter appear as a section within a published manuscript entitled "Room Temperature Fabrication and Post-impregnation of LMO-ST Composites: Engineering and Modeling of Dielectric Properties."

**Published in the journal** Open Ceramics, October 17, 2023, https://doi.org/10.1016/j.oceram.2023.100495

## 5.1 Results and Discussion

### 5.1.1 The effect of composition on densification and microstructure

As described previously in the Materials and Methods section (3.1), Room temperature densification of composites is based on the combination of a functional ceramic filler with a corresponding binder in solid and aqueous solution form. The composite system in which the weight fraction of solid LMO was varied in the range from 1, 6.5, 10, 20, 30, 40, 50, 60, 80 to 100 wt % (5, 15, 19, 33, 44, 54, 65, 87, 100 vol %) was investigated. Results showed that the binder-filler proportion, the interactions, and the remaining porosity significantly affect the final functional properties. SEM-EDS analysis was performed on LMO-ST cross-sections of specimens with 1, 20, 30, and 50 wt % LMO (Figure 5.1).

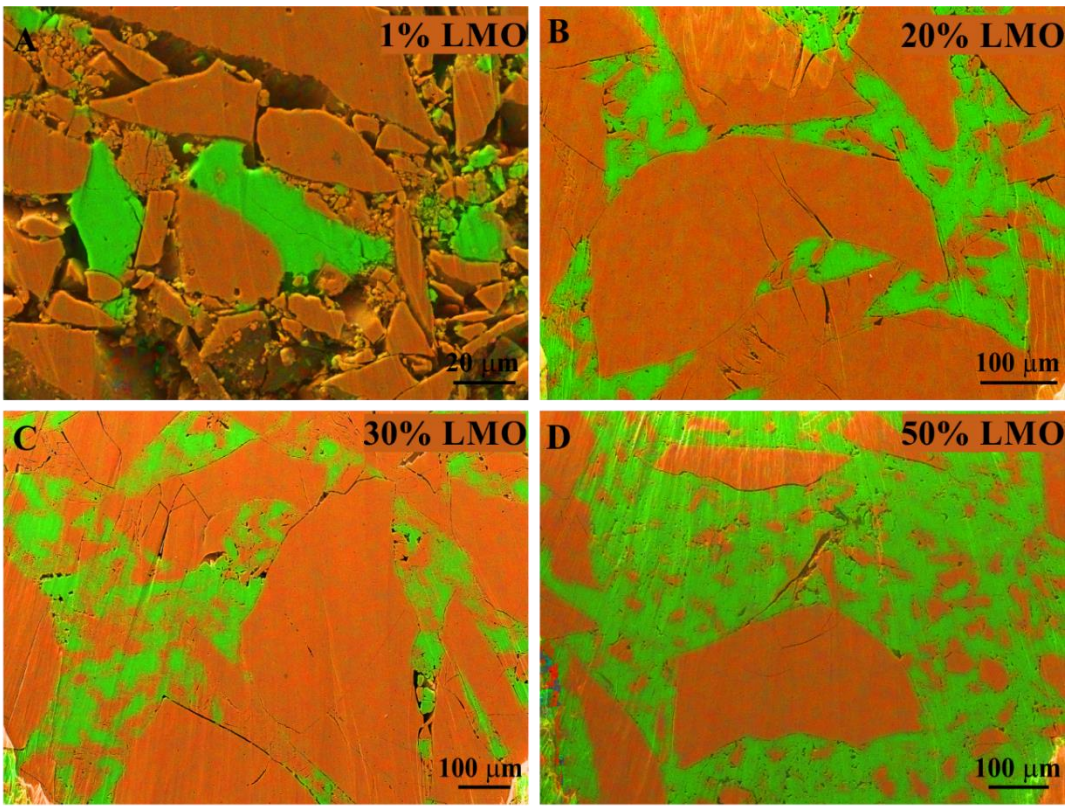


Figure 5.1: EDS mappings of LMO-ST composites as a function of varied LMO content.

The microstructures exhibited an even distribution of larger ST particles, positioned closely together and surrounded by the LMO phase. Micrographs of four representative sample compositions demonstrate a trend toward reduced porosity as the LMO content increases. This is consistent with the results of relative density measurements on as-prepared samples (Figure 5.2). A good contact between ST and LMO can be observed, which becomes even more evident with increased LMO content. Some cracks on larger ST grains are observed in micrographs and can be attributed to the pressing of pellets. No additional phase that could be formed during the preparation processes was observed in the analyzed microstructures. Figure 5.2 illustrates that a higher amount of LMO increased relative density from 81 % to 93 %. The highest relative density, reaching 93 %, was obtained at the composition of 50 wt % of LMO. However, a slight decrease in relative density was observed above 50 % LMO addition, which falls within the margin of measurement error.

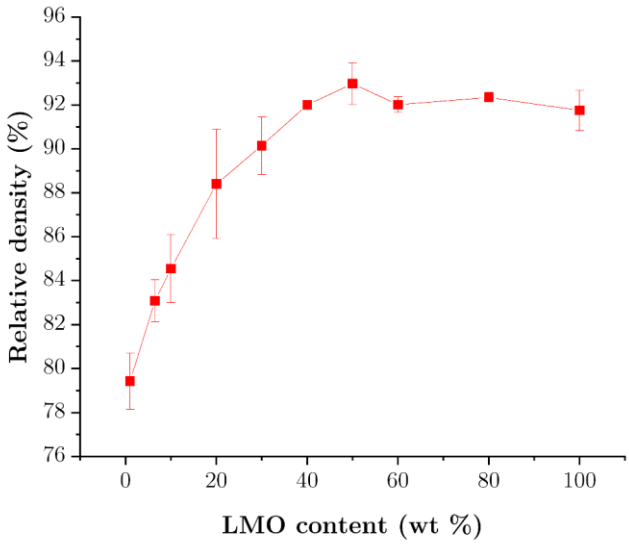


Figure 5.2: Relative density of LMO-ST composites with varied composition (1–100 wt % of LMO).

### 5.1.2 Dielectric properties of LMO-ST composites with varied composition

Dielectric properties as a function of LMO content measured at 1 MHz are shown in Figure 5.3 and indicate that both the relative permittivity and dielectric losses decrease with increasing LMO content. The binder-filler proportion was varied from 1, 6.5, 10, 20, 30, 40, 50, 60, 80 to 100 wt % of LMO binder. When up to 20 % LMO was added, the relative permittivity ranged from 75 to 42. Increasing the LMO concentration in the 30 wt %–80 wt % range resulted in a decrease in the relative permittivity of more than 60 %. This indicates that when the LMO-ST proportion reaches a certain threshold, the connectivity of the LMO phase is established, which reverts the upside-down structure into a 0–3 composite structure.The relative permittivity in the LMO-ST system gradually decreases with increasing LMO content until it reaches the relative permittivity of 5 and dielectric losses *tan* δ of 0.0005 at 1 MHz attributed to the pure LMO. On the other hand, classically sintered ST has a relative permittivity of 296 and dielectric losses of 0.0015 at 1 MHz [161]. The difference in relative permittivity of the two constituents is significant and directs the trend of dielectric performance as the LMO binder content is varied. As shown in Figure 5.2, a lower LMO content corresponds to a lower relative density of the composite samples. However, the highest relative permittivity at 1 wt % LMO is attributed to the highest volume fraction of ST, which significantly increases the relative permittivity. As noted, increased LMO content aids the densification process, leading to an increase in relative density from 80 % to 93 % (Figure 5.2). As indicated in Figure 5.3, the dielectric losses fluctuated from 0.0009 to 0.0087, with the highest value at 20 wt % LMO content. In general, dielectric losses are influenced by various factors, such as porosity, ambient humidity, particle and grain size, defects, frequency, concentration of dipoles and charge carriers, and their mobility [157]. Based on these results, it is evident that the functional properties can be tailored by changing the composition and, as such, enable use for various applications from high-speed electronic components to low-k satellite communication devices [157], [162].

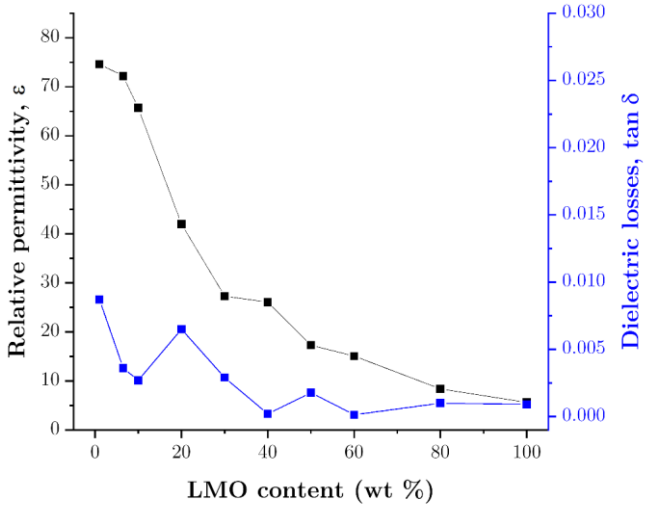


Figure 5.3: Dielectric properties of LMO-ST composites, as a function of varied LMO content (1-100 wt%) measured at 1 MHz.

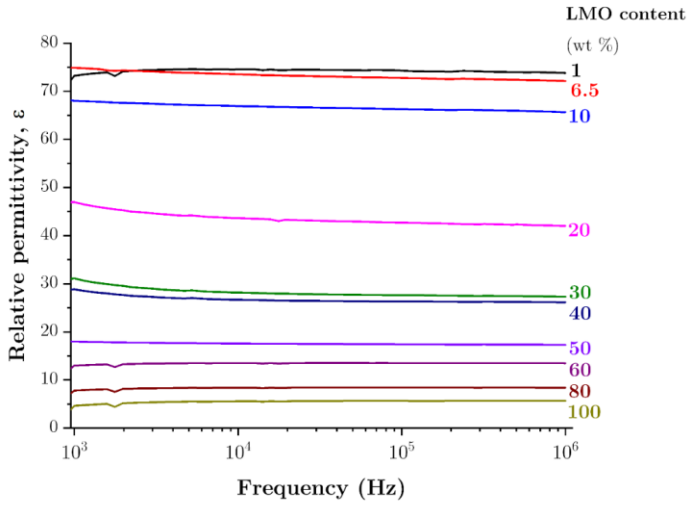


Figure 5.4: Relative permittivity of LMO-ST composites with varied composition measured in a frequency range from 1 kHz to 1 MHz.

The relative permittivity and the dielectric losses measured between 1 kHz and 1 MHz decreased only slightly with the increasing frequency for the compositions from 1 to 100 wt % of LMO (Figure 5.4). The most significant difference is observed in the sample containing 1 wt % LMO, where the relative permittivity experiences a 20 % decline from 1 kHz to 1 MHz. This appears to be more pronounced at lower LMO concentrations, primarily due to increased porosity and the build-up of electric charges at particle interfaces, resulting in polarization within the composite [103]. Dielectric losses of pure sintered ST amount to 0.0015 at 1 MHz, whereas pure RTF-LMO exhibits losses of 0.0005 at the same frequency [161]. As demonstrated in Figure 5.4, no dielectric relaxation peaks appear as the frequency increases.

### 5.1.3 Prediction of dielectric properties with mathematical rules of mixtures – correlation to experimental values

As described in the Introduction (section 1.8), rules of mixtures can serve as a useful tool to calculate and theoretically predict functional properties, i.e., the relative permittivity of composite materials. In general, the relative permittivity of a mixture should be somewhere in between the relative permittivity of each of the constituents. According to the law of mixtures, the overall relative permittivity of a composite is strongly related to the volume ratio of the individual phases. In our study, the relative permittivity was predicted as a function of varied LMO-ST composition. The relative permittivity predicted using Lichtenecker and Maxwell-Garnett (MG) rules of mixture for a three-phase system was compared with experimental data.

Table 1.1 (Chapter 1, section 1.8) lists all equations used. Rules of mixtures for engineering materials for electronic applications can serve as useful tools for predicting functional properties and further understanding experimentally observed phenomena.

Many studies, especially those focusing on polymer-ceramic composite systems, have used the conventional models of Lichtenecker as well as MG to predict functional properties or correlate them with experimental data [30]. When used for such a two-phase composite system, the contribution of air has usually been neglected [42,44–46]. Lichtenecker's formulas refer to the relative permittivity $\varepsilon_r$ of a mixture of $n$ phases, where $\varepsilon_i$ and $f_i$ denote the relative permittivity and the volume fraction of constituent $i$, respectively, leading to the model Equation (1.4). Lichtenecker described the effective dielectric function of a two-phase composite in Equation (1.5). The parameter $k$ represents the anisotropy at the boundary conditions and ranges from − 1 and 1 [40]. For the limiting case where $k$ is 0, the function has the form of Equation (1.6). Three-phase systems were first considered in geologic mixtures to correlate the measured electrical permittivity of soil (s) with its water (w) and air (a) content [29]. The soil was considered a mixture of solid particles, water, and air. In Equations (1.7) and (1.8), $p$ represents the porosity of the soil and is equal to the sum of the volume fractions of air and water. Therefore, the divergence between the porosity and the volume fraction of water is used to determine the volume fraction of air. In this study, the highest agreement of the experimental values with Lichtenecker (Equations (1.7) and (1.8).) was reported when the parameter $k$ was set to 0.5 [41]. Considering this, we have rewritten (1.8) as Equation (1.9) because it is more accurate for ceramic composite systems. As reported previously for $Li_2MoO_4$–$TiO_2$ composite ceramics, conventional Lichtenecker (Equation (1.6)) was only applicable when anywhere from 80 to 100 % of LMO was added [20]. When applying the conventional Lichtenecker equation for the LMO-ST composite system (Equation (1.6)), in which the presence of air is neglected, the predicted permittivity values for up to 40 % of LMO concentrations deviate substantially from the experimental data (circle-shaped blue line in Figure 5.5 a)). When the air fraction was considered, an excellent fit to the experimental data was obtained, which can be clearly seen in Figure 5.5 a) (comparison between the blue and the magenta curve). We also obtained a $k$ value of 0.04 for the system LMO-ST by fitting the function to the experimental results of relative permittivity. The function used is represented in Equation (1.10). Beyond the 40 % of LMO addition, the Lichtenecker model (Equation (1.6)) and experimental results (black curve) diverge due to an increase in porosity. While using Lichtenecker's equation (Equation (1.9)) for a three-phase system showed a good agreement with measured relative permittivity, Figure 5.5 a) shows that the contribution of air has a significant effect on the dielectric constant, especially at low LMO additions where porosity is higher. This can be due to the fact that gases generally have the lowest dielectric constant [11]. Understanding the important relationship between porosity and

dielectric properties is critical for further improving the dielectric properties of LMO-ST composites with, i.e., impregnation, as first elucidated in this study (see section 3.3.2).

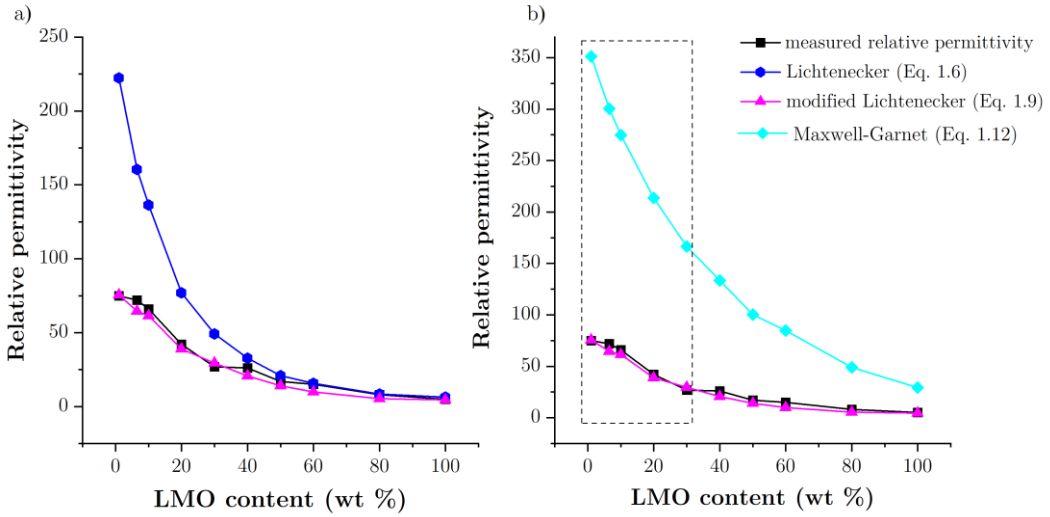


Figure 5.5: Predicted relative permittivity as a function of composition compared to experimental values a) different formulations of Lichtenecker (Equations (1.6, 1.9), b) comparison between experimental values, Lichtenecker, and MG models (Equation (1.12)).

Further, I compared the experimental relative permittivity values with the MG mixing rule (Equation (1.11)), where index 1 represents the matrix and index 2 is filler material. In this approximation, one of the constituents is considered a continuous host in which inclusions of the other constituent are embedded. In this study, the MG rule was modified for a three-phase composite system (ST – LMO – air), as shown in Equation (1.12). The predicted data (turquoise diamond curve, Figure 5.5 b)) differed greatly from the experimentally determined values of relative permittivity as a function of different compositions, as can be seen from Figure 5.5 b)). When the MG rule was extended to include air Equations (1.12), (1.13), (1.14) as a third constituent, an even greater deviation from the experimental data was observed. The closest to the experimental values of the relative permittivity was the conventional MG rule adopted from reference [42], Equation (1.11). This suggests that the MG rule may not be the most accurate for our composite system. On the other hand, it was previously reported [43] that using the MG rule to predict the properties of pure LMO samples resulted in very good agreement with the experimental values when the porosity effect ($P$) was considered, Equation (1.14) [43]. Applying this model to our system did not result in a good agreement with the experimental data, as shown in Figure 5.5 b)). To sum up, these results confirm that the modified Lichtenecker mixing rule can be successfully used to predict the dielectric properties in the LMO-ST system. Further studies aim to evaluate the dielectric properties of impregnated samples using the rules of mixture.

## 5.2 Conclusions

The results of this chapter show that increasing the weight fraction of the LMO binder in the LMO-ST composites prepared by the RTF method results in a higher relative density and lower relative permittivity. The relative permittivity of LMO-ST composites is almost frequency-independent, below 1 MHz for the whole compositional range, which is highly desired for many microelectronic applications. Calculated data using rules of mixtures was compared with experimentally measured values. The Lichtenecker rule, reformulated for a three-phase composite system, showed the best agreement with the experimental data. Considering the air content to be equally important as other functional constituents in LMO-ST composites is indeed very important in obtaining reliable simulated data of relative permittivity. Additionally, based on calculations, the negative influence of porosity was confirmed. For applications requiring high relative permittivity, the samples must primarily consist of a high fraction of ceramic filler ST. On the other hand, pure LMO acts as a promising candidate for low-$\varepsilon_r$ applications, especially in the MW frequency range.

# Chapter 6

# OOF Simulations — From Microstructure to Functional Properties

The work within this chapter was conducted in collaboration with David Fabijan from the Advanced Materials Department, who provided help with the OOF2 software adjustments, SEM image reconstruction, and simulation experiments. All data presented are intended to be published in a joint publication, which is currently in the submission process.

Creating a pre-experimental roadmap and predicting the functional properties can be extremely important prior to experimental work. The object-oriented finite element method, OOF2, is a useful and versatile numerical instrument complementing experimental work. It can further explain experimentally observed phenomena, compare obtained results with the modeled data, and simulate and predict dielectric properties for further experiments. OOF2 is a public domain software created by the Centre for Computational and Theoretical Materials Science (CTCMS) at the US National Institute of Standards and Technology (NIST, Gaithersburg, USA) to examine the functional properties of materials microstructure. In recent years, this approach has been utilized to simulate the mechanical and thermal properties of composite materials numerically.

The OOF2 tool has two main benefits: it can assist in interpreting experimental data and forecast the outcome of planned experiments. Section 6.1.1 introduces the OOF method. In sections 6.1.2-6.1.4, OOF2 is used to explain the experimental data (compositional changes, LMO-ST proportion), while in 6.1.4-6.1.5, OOF is used mostly for predictions of future experiments (coating media, coating thickness, Ag additions).

## 6.1 Results and Discussion

### 6.1.1 Simulation of dielectric properties of LMO-ST composites with OOF2– verification against/towards theoretical models

The functionality and the limit cases of the OOF2 system were tested with the most fundamental theoretical models. The simple reference, series, and parallel verification models were used for this purpose, and they are illustrated in Figure 6.1. The presented models can be expressed as two extreme modes of the Lichtenecker model (Equations ((1.4)-(1.6)); Table 1.1) when $k$ is either –1 (series) or 1 (parallel), which correspond to the Wiener boundary values [8]. The $k$ value represents a composite's micro geometry or topology and may be interpreted as a transition from anisotropy at $k$=–1 to anisotropy at $k$=1 [163]. As shown in Chapter 5, it was found that Lichtenecker's rule with $k \sim 0.04$ most accurately fits the experimental results of LMO-ST composites.

The expected permittivity of such a model can be easily derived from the equations for capacitors connected in series/parallel; with Equations (6.1) for series and (6.2) for the parallel verification models:

$$\frac{1}{\varepsilon_m} = \frac{f_1}{\varepsilon_1} + \frac{f_2}{\varepsilon_2} \tag{6.1}$$

$$\varepsilon_m = f_1\varepsilon_1 + f_2\varepsilon_2 \tag{6.2}$$

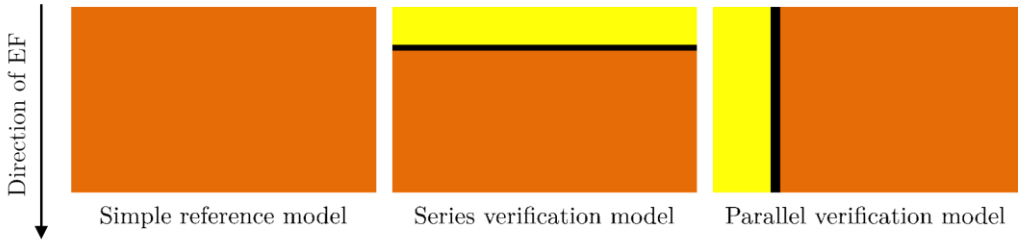


Figure 6.1: Illustration of the simple reference model (left), series verification model (middle), and parallel verification model (right). The black line represents an air interface.

A simple reference model represented pure ST with the $\varepsilon_r$ of 296 at 1 MHz, while parallel and series models included volume fractions of air (black band) and LMO (yellow band) with properties as $\varepsilon_{r,air}$=1, $\varepsilon_{r,LMO}$=5 at 1 MHz. In the following figures in this chapter, LMO is highlighted in yellow, and ST is highlighted in orange. Exact relative permittivity values simulated for each model type are compared with expected theoretical models in Table 6.1. It can be observed that the orientation of the low-dielectric material phase affects the final relative permittivity values. In the series verification model, polarization is blocked with the low-permittivity (low-$\varepsilon_r$) materials as air and LMO over the whole x-axis. These low-$\varepsilon_r$ interfaces disrupt the continuity of high-permittivity material and, therefore, hinder the penetration of the electric field (EF). This consequently results in the reduction of the observed relative permittivity. The permittivity of the pure LMO is very similar to the permittivity of air. So, the presence of LMO causes a similar reducing effect on the overall polarization as porosity.

Table 6.1: Simulated data for different types of models.

| **Model type** | **ST fraction (%)** | **LMO+air fraction (%)** | **Relative permittivity, $\varepsilon_r$ (OOF2)** | **Expected theoretical values (ROM)** |
|---|---|---|---|---|
| Simple reference | 100 | 0 | 296.0 | 296.0 |
| Series verification | 78 | 19+3 | 13.4 | 14.2 |
| Parallel verification | 78 | 19+3 | 231.8 | 231.9 |

### 6.1.2 Experimental data compared to OOF2 and modified Lichtenecker model

The relative permittivity changes with respect to the varying LMO-ST proportion (shown in Chapter 5, Figure 5.3).

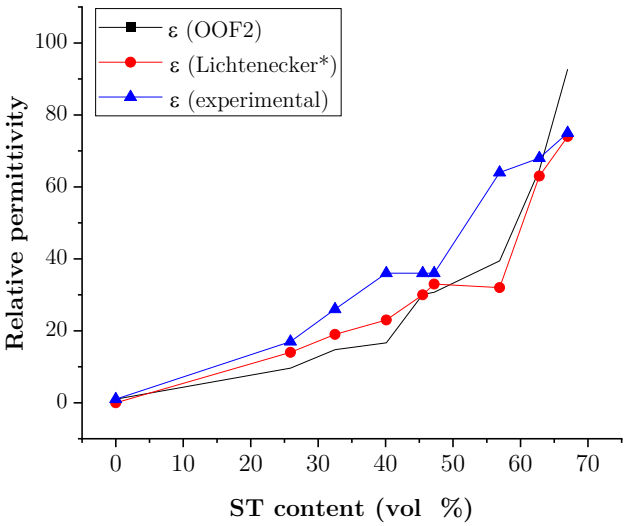


Figure 6.2: Relative permittivity as a function of changing ST content measured experimentally, simulated with OOF2, and calculated with modified Lichtenecker.

Application of the modified Lichtenecker for a three-phase system (Lichtenecker*, Equation (1.9)) showed the best agreement with experimental data among various ROMs. Indeed, such mathematical calculations supported the experimental data and explained to some extent the effect of air on the total relative permittivity. However, running OOF2 simulations can help to understand and visualize the critical issues that reduce the relative permittivity when such compositional changes occur. The OOF2-simulated relative permittivity values closely resemble those predicted by the Lichtenecker* ROM (Figure 6.2). While experimentally measured relative permittivity values exhibit slight variations. This might be due to the fact that the air content varies within the batch of experimental

samples and cannot be precisely controlled even when the initial LMO-ST proportion is maintained.

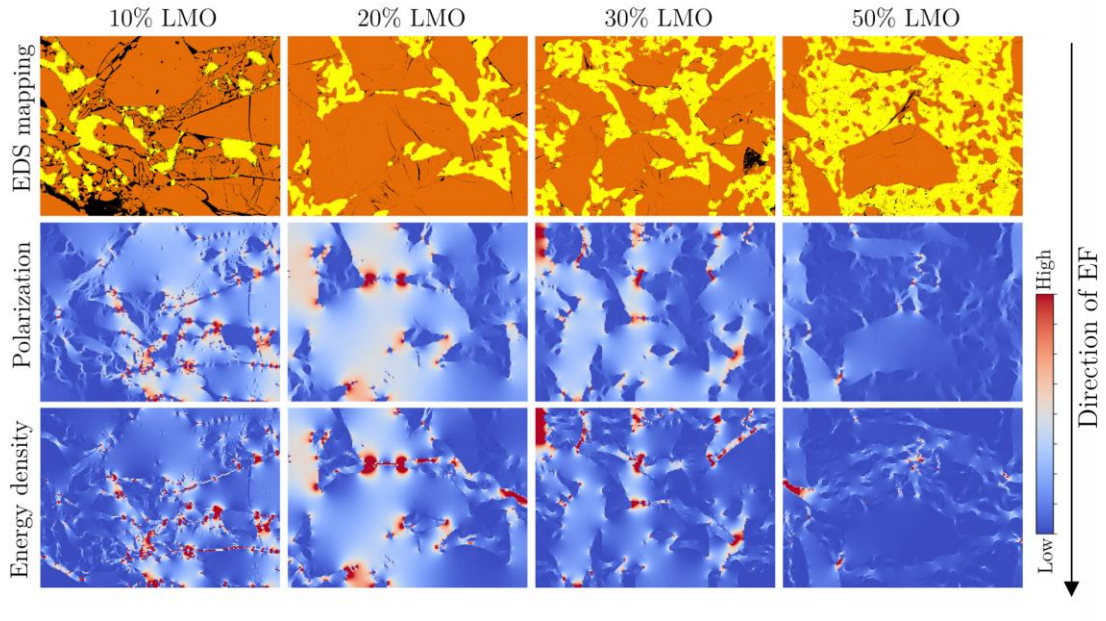


Figure 6.3: Polarization magnitude and energy density of electric field simulated with OOF2 for LMO-ST composites, where the LMO fraction varies from 10, 20, 30, and 50 wt%.

Figure 6.3 demonstrates that the highest level of polarization and energy density of the electric field was detected at the direct ST-ST contacts (highlighted in red and white). At the same time, the large areas of the LMO phase and air (blue-colored areas) significantly decreased the local polarization and energy density. On the contrary, larger ST grains present in the composite system imply fever unfavorable low-$\varepsilon_r$ phase boundaries. This further clarifies the effect of particle size on dielectric properties, which was observed earlier (Chapter 4, section 4.1.3).

As the LMO content in LMO-ST composites increased, the polarization, energy density, and relative permittivity decreased noticeably. The OOF2-predicted relative permittivity values decreased significantly from 102 to 30 in correspondence with the Lichtenecker model for the three-phase system and experimental data, as shown in Figure 6.2.

The difference between OOF2 and experimental values for relative permittivity can be ascribed to different factors, such as the inherent 2D limitation of the OOF2 technique, repeatability of experimental samples, and the limited number of input micrographs for 2D simulations. We should keep in mind that relative permittivity is a 3D property of materials, which may not be fully estimated by the 2D nature of the OOF2 method. Another limitation is that the area of the investigated (polished) microstructure of the LMO-ST composite considered in OOF2 simulations is smaller than the entire sample; however, the samples are assumed to be homogeneous in the microstructure.

Figure 6.4, showing the local polarization vectors, further supports the correlation between the particle size distribution and contacts with dielectric properties. Enhanced polarization vectors are observed in the ST areas, while there is minimal polarization in the LMO and air sections.

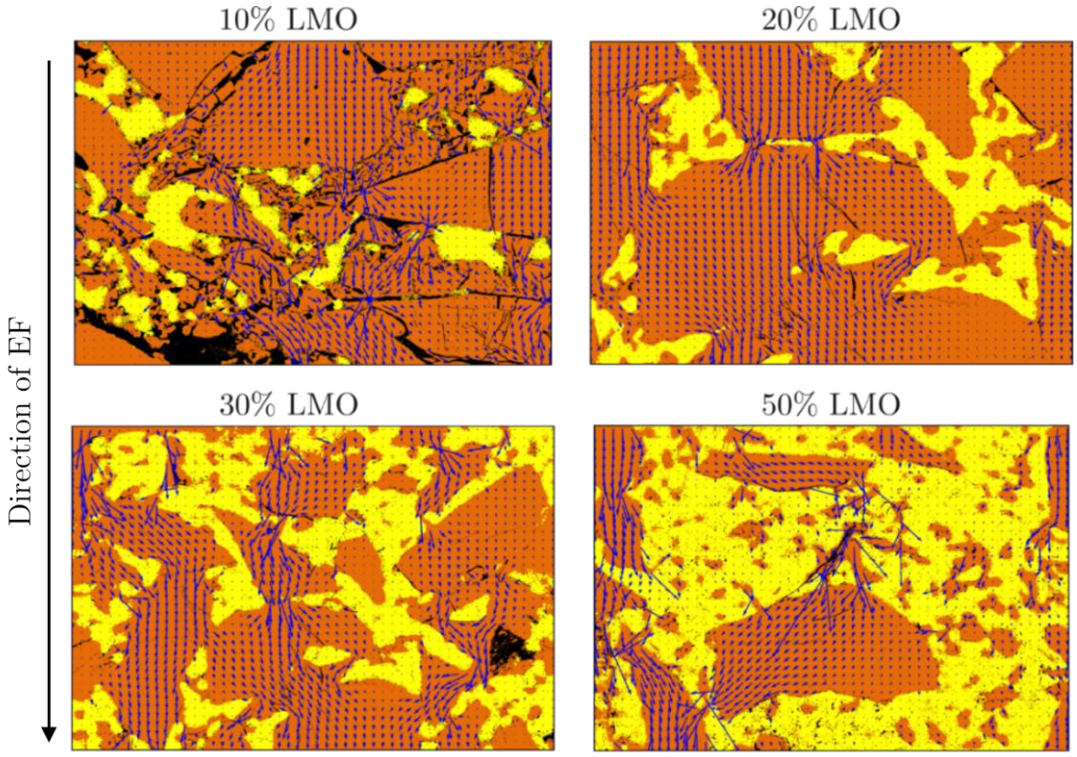


Figure 6.4: Polarization vectors in LMO-ST composites with varied LMO content from 10, 20, 30 to 50 %.

Yellow LMO regions show almost no polarization. On the contrary, polarization vectors are more pronounced in the large ST particles or when the direct path through the ST is enabled from top to bottom of the OOF Microstructure. In the 50 % LMO Microstructure, it is also shown that a polarization gradient is present when low-$\varepsilon_r$ material surrounds the larger ST particle from one side. So, the EF will always try to transmit through the direct ST-ST contacts.

### 6.1.3 The effect of cracks and their orientation in the microstructure

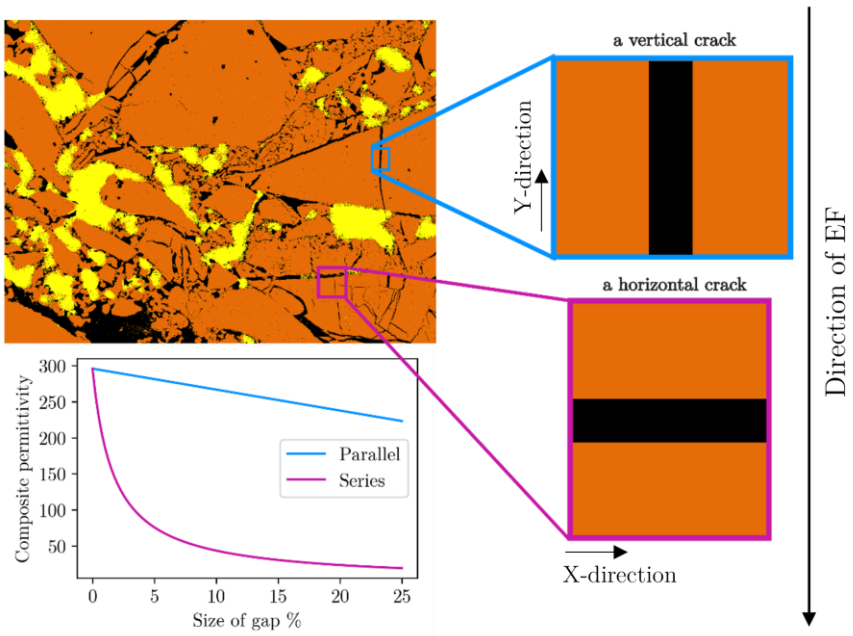


Figure 6.5: Composite permittivity as a function of crack size and orientation.

Further, the effect of the pores (air gaps) and cracks differ in their shape and size. Enlarged regions (blue and purple rectangles) in Figure 6.5 represent the cracks that emerged in the original LMO-ST microstructure during RTF. These cracks may be oriented in any direction relative to the applied voltage. Horizontal and vertical directions represent the extreme cases. Such orientations can be directly compared to a simple series (horizontal) and parallel (vertical) model. As shown in Figure 6.5, in the series model, the composite permittivity changed significantly with the gap size; in contrast, the effect is more subtle in the parallel model. This can be explained again as the low-$\varepsilon_r$ materials block the polarization through the whole x-direction of the Microstructure. In the real microstructure of a composite dielectric system consisting of multiple dielectrics, a combination of parallel, series, and intermediate situations occurs, and the actual distribution of the electric field is complex. According to the literature, a triple-joint effect can also appear at the points where three different media are in contact [164].

### 6.1.4 OOF2 simulations of coating thickness and media varied on relative permittivity of LMO-ST composites compared with experimental results

In terms of better densification of LMO-ST composites, coating ST particles with LMO was also studied. The results of coating with LMO on PZT particles were used for a reference [103].

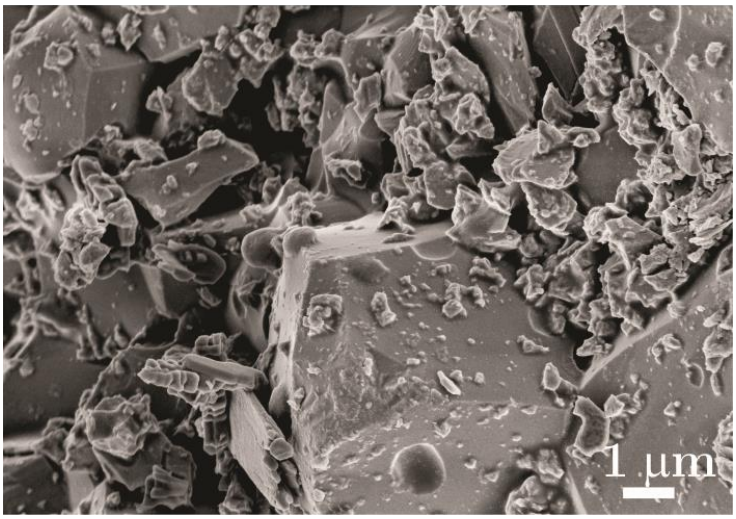


Figure 6.6: LMO-coated surface of ST particles.

Experimental samples consisting of LMO-coated ST particles were prepared with RTF. Then, OOF2 simulations on constructed equivalent microstructures were conducted to better understand and explain the changed dielectric properties after the coating was applied. The measured average values of relative density, relative permittivity, and dielectric losses are presented in Table 6.2.

Based on SEM analysis, the coating of LMO on ST was not confirmed. Smaller isolated LMO particles were deposited on the surface of ST filler particles (see Figure 6.6). The results on the real LMO coating aligned closely with the simulated perforated coating on ST particles. This coating allows the layer of soluble salt (LMO solid layer) to come into direct contact with the LMO saturated solution during the pressing of the composite mixture, leading to better redistribution and densification of the particles. The layer of supersaturated coating material in between the ST particles is expected to fill in the voids and result in higher packing density overall.

Table 6.2: Dielectric properties of experimentally produced LMO-ST samples consisting of coated or uncoated ST particles. The composition, 93.5 wt % (85 vol %) ST/6.5 wt % (15 vol %) LMO, was kept constant.

| LMO-ST composites | **Relative density, ρ (%)** | **Relative permittivity, $\varepsilon_r$** at 1 MHz | **dielectric losses, *tan* δ** at 1 MHz |
|---|---|---|---|
| **Coated ST with LMO** | 84 | 64 | 0.0034 |
| **Uncoated ST** | 84 | 72 | 0.0054 |

Based on experimental results on the relative density, it was not possible to determine the impact of coating on the densification process, as the values fell within the range of the error margin. As mentioned in a previous study on LMO-PZT composites [94], a significant drop in relative permittivity was observed and attributed to high local dielectric variation in the composite. Coating particles with a layer of low-$\varepsilon_r$ material reduces the polarization and energy density of the material in an applied electric field, especially at higher frequencies. This occurs as charges accumulate at interfaces and lead to a drop in the overall relative permittivity of a composite [103]. As can be seen from Table 6.2, our results

showed that coating does not enhance the relative density nor relative permittivity of LMO-ST composites.

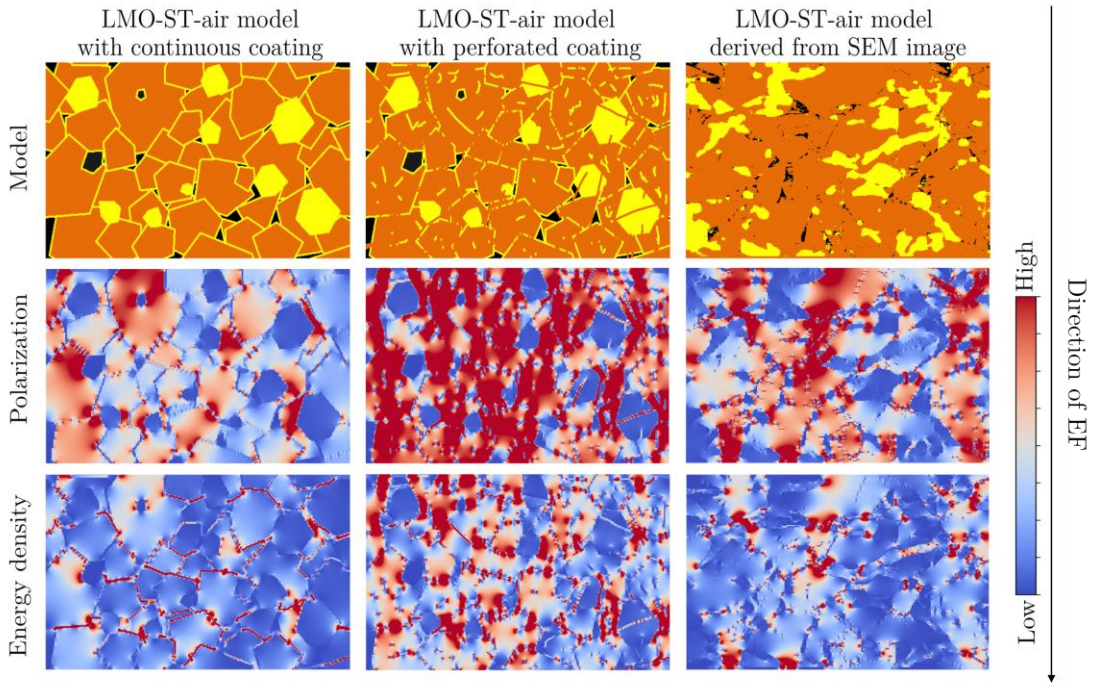


Figure 6.7: OOF2 simulation of polarization magnitude and energy density on the realistic LMO-ST-air model with coated ST particles (left column), LMO-ST-air model with contacting ST particles (middle column), and LMO-ST-air model derived from the original SEM image.

The utilization of the OOF2 coating simulation proved to be highly beneficial in providing further insights into the experimentally observed drop in overall relative permittivity when ST particles were coated with LMO. The impact of the coating was simulated using two distinct models (Figure 6.7), one representing a perfect coating surrounding the ST particles (Figure 6.7 a)) and the other incorporating perforations, allowing for direct interaction between the ST particles (Figure 6.7 b)). The microstructures were constructed using GIMP software. The LMO: ST: air proportions of the constructed models were matched to the proportions of an actual microstructure cross-section (presented in Figure 6.7 c)).

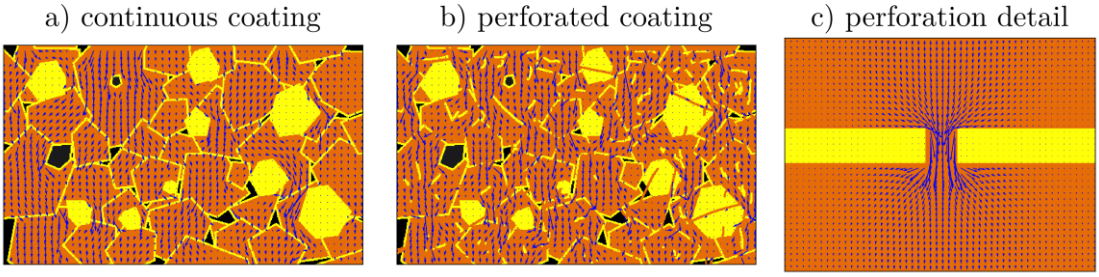


Figure 6.8: Polarization vectors in coated ST (a), contacting ST particles (b). A hole/channel between two phase materials (c).

Moreover, OOF2 has the potential to serve as a valuable tool for predicting the outcomes of future experimental work. Using OOF2, various coating media and their thickness's effect on the ceramic-ceramic composite's overall relative permittivity were explored. The thickness of the simulated coating on the ST particles in the OOF2 Microstructure is represented in pixels. Figure 6.9 displays the relationship between the relative permittivity of the binder-ST-air composite system and the relative permittivity or thickness of the coating medium.

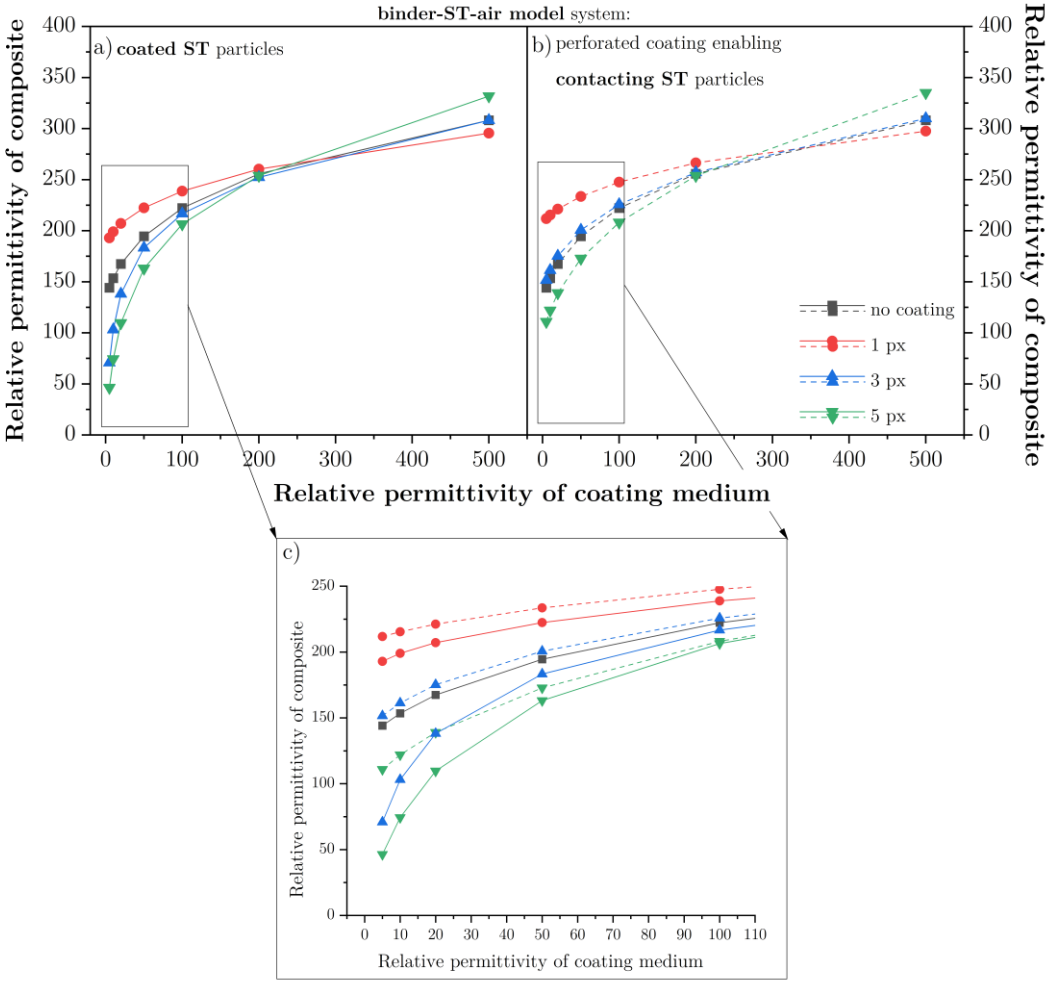


Figure 6.9: The comparison of two models used to simulate the effect of coating media and its thickness on the binder-ST-air composite system. Coated ST particles (a)); Perforated coating of ST particles (b)); close-up in the lower permittivity region (c)).

Ideally, the coating should have higher relative permittivity than the binder and hence increase the polarization in the composite. Here, different thicknesses and relative permittivities of the coating were simulated for the binder-ST-air system. Part a) of Figure 6.9 shows the ideally coated ST particles (no holes), while part b) displays the perforated binder coating on ST particles. As the relative permittivity of the coating increases, the overall relative permittivity of LMO-ST composites also increases, which can be seen in Figure 6.7 and Figure 6.8. In Figure 6.7, the red areas indicate high polarization and are most intensely observed with middle-column simulated images with perforated contacts. In addition, polarization vectors are much more pronounced in the middle column image

in Figure 6.8, where the direct ST-ST contacts are enabled. The perfect coating (no holes) isolating the ST-ceramic particles would only benefit the overall permittivity in the composite if the relative permittivity of the coating would be larger than that of ST (or any other filler) itself. Part (c) shows a zoomed-in simulation of how the electric field concentrates at the hole or an ST-ST channel. The OOF2 simulations provide further evidence that charge is accumulated at the interfaces in the composite, which can result in reduced polarization. The challenge lies in experimentally controlling coating thickness and identifying a suitable medium with higher relative permittivity.

The most significant difference, as the coating thickness differs, can be observed when a low-permittivity material with $\varepsilon_r$~(1-100) was simulated as a coating medium. Indeed, the effect of the perforated coating is more pronounced when the coating medium has a low permittivity (i.e., 5 in the case of LMO). This is presented as the difference between the dashed and solid blue lines. On the other hand, when the relative permittivity of the coating medium was similar to that of ST ceramic filler ($\varepsilon_r$~300), the overall relative permittivity of as-prepared composites tended to limit towards the permittivity of pure ST. In OOF2 simulations, the coating thickness on ST varied between 1, 3, and 5 pixels (px).

### 6.1.5 OOF2 simulations of Ag addition in LMO-ST composites: densification and dielectric performance

The objective here was to investigate the potential of Ag, a metallic powder, in improving the dielectric properties of LMO-ST composites. The concept was tackled in two ways: experimentally by making the LMO-ST-Ag samples and by simulating the addition of Ag to the existing microstructural images of LMO-ST composites. The correlation between polarization/energy and the Ag content was inspected using OOF2.

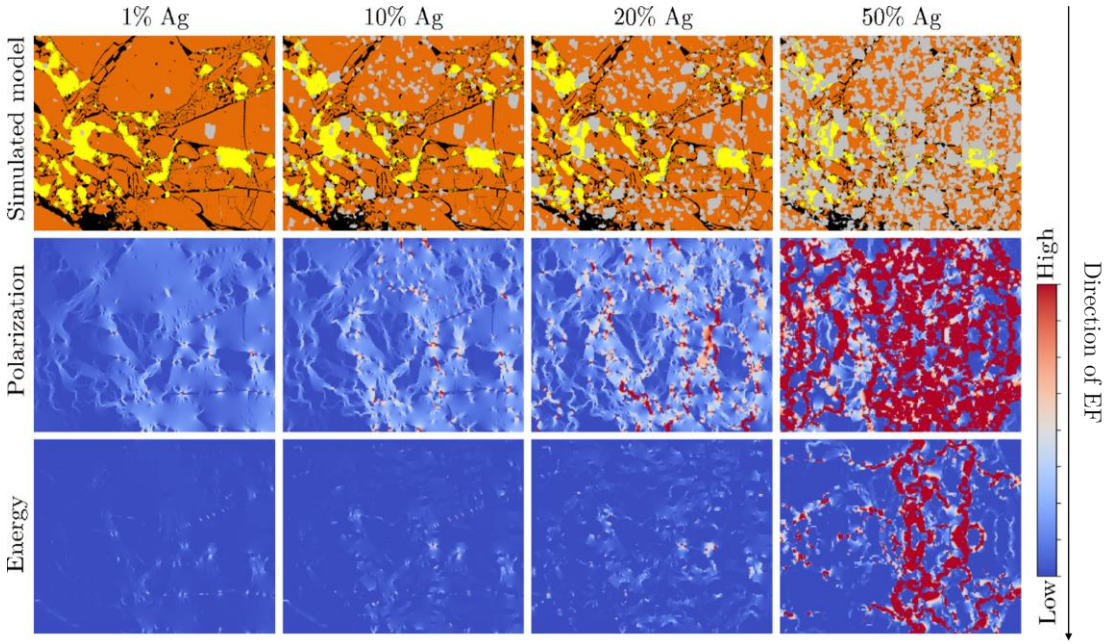


Figure 6.10: Polarization and energy as a function of Ag addition ranging from 1, 10, 20, to 50 %.

The LMO and ST fractions were adjusted according to the Ag weight fraction, whose values were 1, 5, 10, 20, 30, and 50 %, respectively. The simulated models of LMO-ST-Ag

composites are demonstrated in Figure 6.10. The real microstructures of LMO-ST composites were modified by adding Ag. However, SEM imaging of the LMO-ST-Ag cross sections has not been conducted. From the OOF2 simulations, it is clear that relative permittivity increases exponentially until the 30 wt % Ag loading level, where it then dramatically increases and the simulated composite sample becomes conductive.

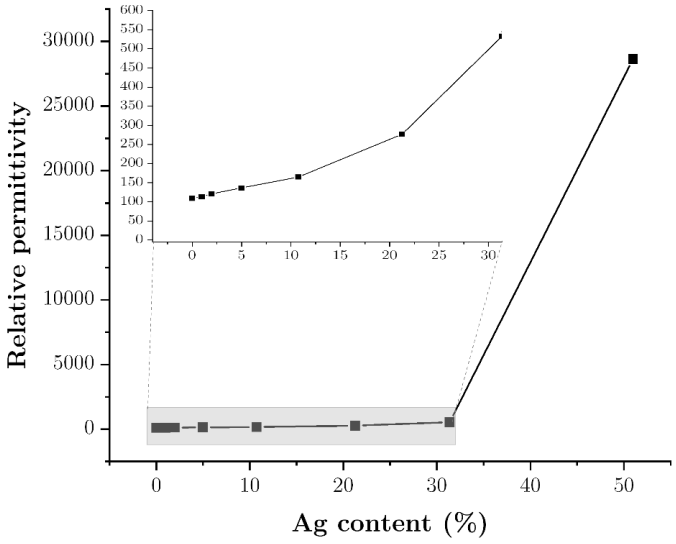


Figure 6.11: OOF2 simulations: Relative permittivity vs. Ag content (%).

This critical concentration of added Ag corresponds to the percolation threshold, where, for the first time, the electrical current runs from one edge to the other. In composites, the dielectric response is related to the geometric arrangement of the constituent phases, including the geometry of the respective interfaces [165].

Table 6.3: Density and dielectric properties of experimentally obtained LMO-ST-Ag composites.

| ST-LMO-Ag composites (prepared by RTF) | | | |
|---|---|---|---|
| **Ag content** | **Relative density, ρ** | **Relative permittivity, $\varepsilon_r$** at 1 MHz | **Dielectric losses, *tan* δ** at 1 MHz |
| (wt %) | % | | |
| 1 | 76.3 | 75.8 | 0.0028 |
| 5 | 80.6 | 79.8 | 0.0011 |
| 10 | 81.3 | 121.8 | 0.0153 |
| ≥20 | | conductive – not measured | |

As can be seen from Figures 6.10 and 6.11, polarization (relative permittivity) increases with the increasing Ag content. The Ag particles act as conductors in this system. Ag was modeled in OOF2 as a material with an extremely high permittivity > $10^6$. The red color in Figure 6.10 depicts high-polarization/high-energy areas, and dark blue areas represent low-polarization/low-energy areas. As seen in Figures 6.10 and 6.11, the percolation level is reached with increasing Ag content. According to OOF2 simulations, this occurs when

30 % of Ag is added. The physical origin of the increased permittivity occurs due to the electric charges accumulated at the conductor-insulator interface, which further leads to the development of the interfacial charge polarization within the bulk material and increases the relative permittivity [166]. Figure 6.12 b) shows that silver conducting particles have a higher polarization field.

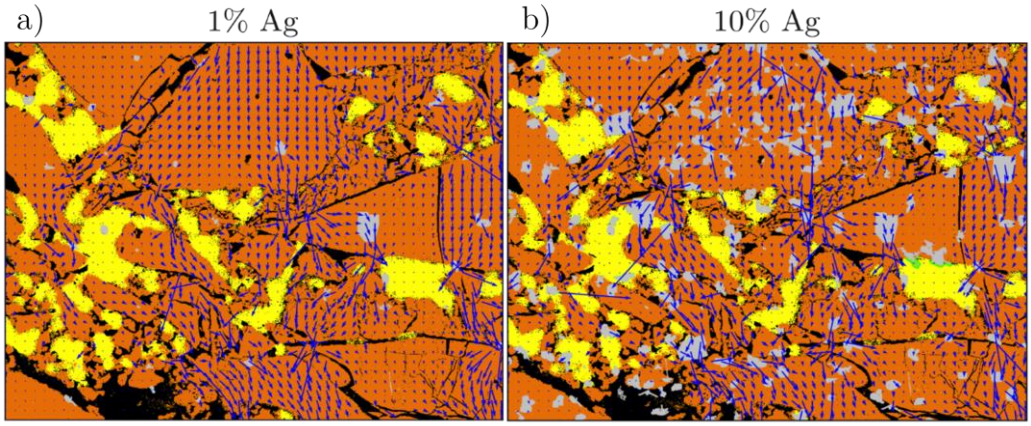


Figure 6.12: Polarization vectors in LMO-ST-Ag composites with 1 % of Ag (a) and 10 % of Ag (b).

Based on the results presented in Figure 6.10, it can be observed that adding a certain amount of silver leads to the formation of conductive paths through the microstructure from top to bottom in the y-direction (as shown in images 20 % and 50 % Ag). The results of experimentally prepared LMO-ST-Ag samples are presented in Table 6.3. It is important to note that the distribution of Ag particles in the experimental LMO-ST-Ag samples may be significantly different from the simulated images, which may explain the difference in the measured ($e_{10\%Ag,\ experimental}$ =121.8 at 1 MHz) and calculated ($e_{10\%Ag,\ OOF2}$ =164.9 at 1 MHz) relative permittivity values. Relative density increased with the higher Ag content.

## 6.2 Conclusions

The impact of microstructure on the estimation of dielectric properties of LMO-ST composites with remaining porosity and cracks has been investigated using object-oriented finite element modeling in two dimensions. To the best of my knowledge, this is the first investigation of dielectric properties of LMO-ST composites using OOF2, which complements experimental results. The experimentally measured relative permittivity values differ only slightly from OOF2 at specific LMO-ST compositions, confirming the simulation's ability to consider the impact of real microstructural characteristics accurately. I observed very similar results of OOF2 simulations and calculations using modified Lichtenecker's ROM. In addition, this analysis sheds light on the varying effects of ST content on permittivity and helps in understanding the underlying physics of the system. The effect of cracking in the composites was also tackled with OOF2 simulations. In line with previous experimental results (Chapter 4, section 4.1.7), increased pressure led to cracking, resulting in reduced relative permittivity. A different effect depending on the orientation of the crack in the microstructure was shown. It was also shown that coating of ST filler particles is beneficial when the relative permittivity of the coating medium is higher than that of ST. Perforated coating (when coating media has $\varepsilon_r < \varepsilon_{r,\ filler(ST)}$), which allows for direct ST-ST contacts, results in slightly better properties. The addition of Ag to the LMO-ST composite may improve the overall relative permittivity by 1.7-fold until

conductive Ag connections are formed in the sample. However, I have not considered the effect of Ag addition on the dielectric losses of such composites.

# Chapter 7

# Impregnation of Upside-Down LMO-ST Composites

In this chapter, I present the results of relative density and dielectric properties of LMO-ST composites after impregnation with Titanium(IV) isopropoxide (TTIP). The impregnated samples were analyzed using FTIR, TG-MS, and SEM-EDS. After 3 cycles of impregnation, the relative density and dielectric properties were measured. Impregnating with TTIP was found to reduce overall porosity and enhance relative permittivity from 72 to 99 at 1 MHz.

The idea of the impregnation process with TTIP was discovered by Mikko Nelo in Oulu. Experiments were partially performed during my second visit to the Microelectronics research unit.

The results of this chapter are published as a part of the manuscript entitled: "Room Temperature Fabrication and Post-impregnation of LMO-ST Composites: Engineering and Modeling of Dielectric Properties".

**Published in the journal** Open Ceramics, October 17, 2023; https://doi.org/10.1016/j.oceram.2023.100495.

## 7.1 Results and Discussion

### 7.1.1 Impregnation of LMO-ST samples with TTIP to partially compensate residual porosity

As mentioned in Section 1.8, composites can contain porosity, which can be intentionally designed or undesired [8]. In most cases, reducing porosity is preferable for improved dielectric or mechanical properties. This was additionally confirmed with ROM calculations (section 5.1.3). After pressing the upside-down LMO-ST composites, a certain amount of water remains in the sample, which comes from the saturated solution of the LMO binder. This water evaporates during drying, and as a result, some porosity appears in the final composite.

Table 7.1: Density and porosity of LMO-ST composites (6.5 wt % LMO) fabricated at room temperature.

| | **Density** | **Open porosity** | **Fraction of open porosity** |
|---|---|---|---|
| | ($g/cm^{-3}$) | (%) | (%) |
| Geometrical ($\rho_{geo}$) | 4.1 | N/A | N/A |
| Theoretical ($\rho_{th}$) | 4.9 | N/A | N/A |
| He- pycnometer ($\rho_{py}$) | 4.8 | 14.6 | 89.6 |

As shown in Table 7.1, a significant portion of the porosity is open, which has led to experimental testing of the filling of the open pores with an impregnating agent. To the best of our knowledge, impregnation as a solution for addressing residual porosity in multiphase ceramic composites has not been extensively studied. In the present study, TTIP was a suitable candidate for the impregnation of the LMO-ST system with a composition of 6.5 wt % LMO (equal to 15 vol %). TTIP is commonly used as a precursor for synthesizing $TiO_2$ nanoparticles through the sol-gel method [167]. The presence of water caused hydrolysis of TTIP (Figure 2.4), which led to the formation of intermediate titanium (IV) hydroxide $Ti(OH)_4$. As reported previously[168], $Ti(OH)_4$ undergoes a condensation reaction at elevated temperatures, resulting in crystalline $TiO_2$ and water. After successful four impregnation steps, TTIP fills the open pores and precipitates to a solid Ti-based phase after hydrolysis [149]. This is depicted in Figure 3.3. Depending on the annealing temperature range and precipitation conditions, anatase, rutile, or brookite crystal structure of polymorphic $TiO_2$ may form [167], [169]. In reality, however, impregnation is often limited by the nature of the porosity and the change in surface energy that occurs upon wetting. The impregnating agent may have difficulty penetrating the composite system despite the increased external pressure [170].

### 7.1.2 Microstructural features and porosity determination in impregnated ST-LMO composites

The SEM analysis of polished cross-sections coupled with EDS mapping showed that TTIP fills the pores in a composite at least 150 µm deep. In Figure 7.1, the green color represents

LMO, the orange color represents ST, and the blue color represents hydrolyzed TTIP. In contrast, the light green at the top is the silver paste applied after impregnation for electrical measurements. In Figure 7.1, it is evident that the impregnating agent mostly covered the surface of the LMO-ST composite pellet (indicated by the black rectangle). This was expected, as the top and bottom surfaces of the pellets are the largest areas exposed to the impregnating agent. From the EDS analysis of the impregnated phase (marked with yellow dots), it is clear that Ti and O are the main elements present, which suggests that the analyzed phase was formed by hydrolysis of TTIP. Based on the SEM-EDS analysis, I concluded that the impregnation was partially successful and resulted in hydrolyzed TTIP phase in the pores. The content of hydrolyzed TTIP produced after three impregnation cycles was estimated to be 2.5% based on graphical analysis of SEM-EDS image and relative density results.

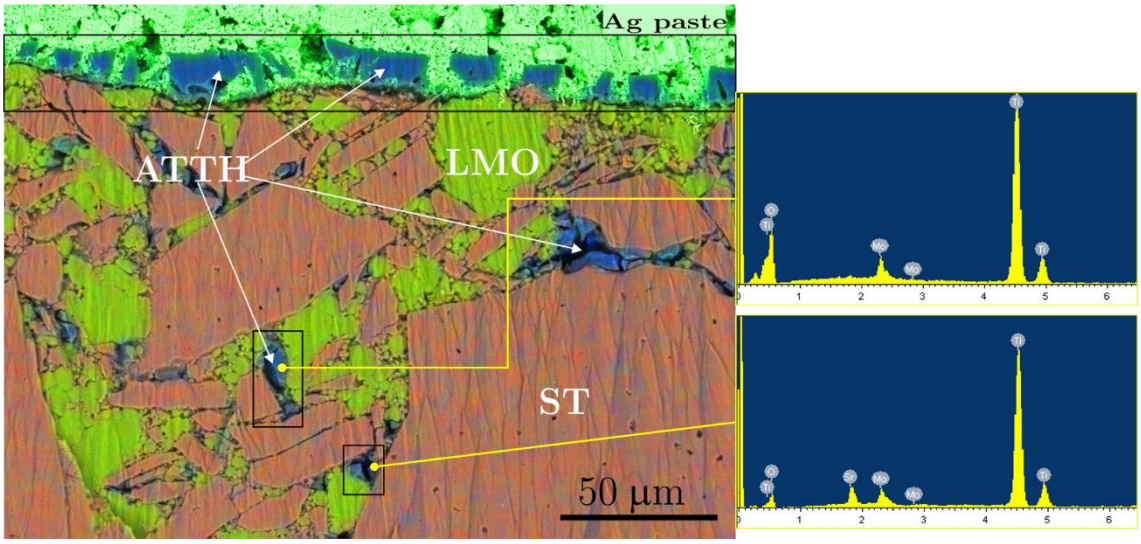


Figure 7.1: EDS mapping polished cross-section of 3x-impregnated LMO-ST composite complemented with point compositional analysis.

Porosity in the LMO-ST was determined based on two different density measurements (geometrically and using a helium pycnometer). Note that the geometric density considers all pores, while the pycnometric density accounts for closed pores only. Total porosity in the LMO-ST upside-down composites with 6.5 wt %/15 vol % of LMO was determined to be 16.3 vol %. The results confirmed the presence of up to 14.6 % open porosity, which corresponds to the fraction of open porosity of 89.6 % (Table 7.1).

Pores that remain open can be closed by further impregnation to improve the overall density of LMO-ST composites. For this purpose, I impregnated the LMO-ST composite samples three times. After each impregnation cycle, the relative density was estimated and found to increase by ~1 % per cycle. Figure 7.2 demonstrates the average relative density of the LMO-ST composite samples before and after three impregnation cycles. An increase in relative density from 83 % to 86 % after three cycles was achieved. For both as-prepared and LMO-ST samples impregnated three times, there is a trend of a slight decrease in relative density with an increase in post-treatment temperature (Figure 7.2). Furthermore, the highest relative density (87 %) was achieved by drying LMO-ST composite samples in a vacuum at RT.

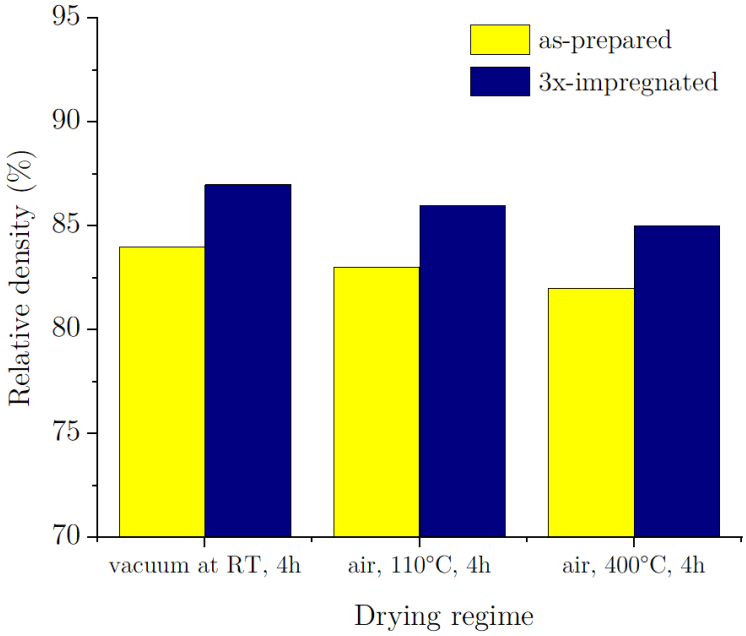


Figure 7.2: Average relative density of LMO-ST composite samples before and after 3x-impregnation, dried 4 h under different conditions (vacuum, RT; air, 110°C; air, 400°C).

### 7.1.3 XRD, TG, and FTIR analysis

Chemical analyses, including XRD, TG, and FTIR, were performed on the as-prepared and three-times-impregnated LMO-ST composite samples.

To understand the ongoing processes in impregnated LMO-ST samples, hydrolysis of TTIP was studied separately, and these results served as a reference. According to the XRD analysis, hydrolysis of TTIP led to the precipitation of a solid amorphous Ti-based product when heat-treated at 110 °C (Figure 7.3). The results of the TG measurement, coupled with mass spectroscopy, showed that the water released from the hydrolyzed TTIP up to 800 °C contributed to a total mass loss of 9.3 wt % (Figure 7.4 a)), which suggests that the hydrolyzed TTIP is not pure $Ti(OH)_4$, but a mixture of amorphous titania and titanium tetrahydroxide (going forth named ATTH). If all of the $Ti(OH)_4$ would be converted into $TiO_2$, a 31 % mass loss would be expected. TG results suggest that $TiO_2$ prevailed in the Ti-containing phase along $Ti(OH)_4$.

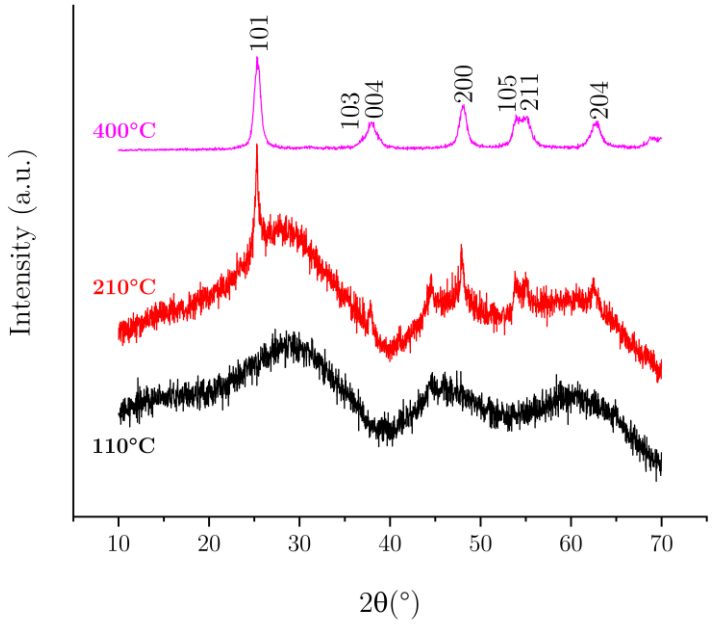


Figure 7.3: XRD analysis of hydrolyzed TTIP heated at different temperatures for 4 h.

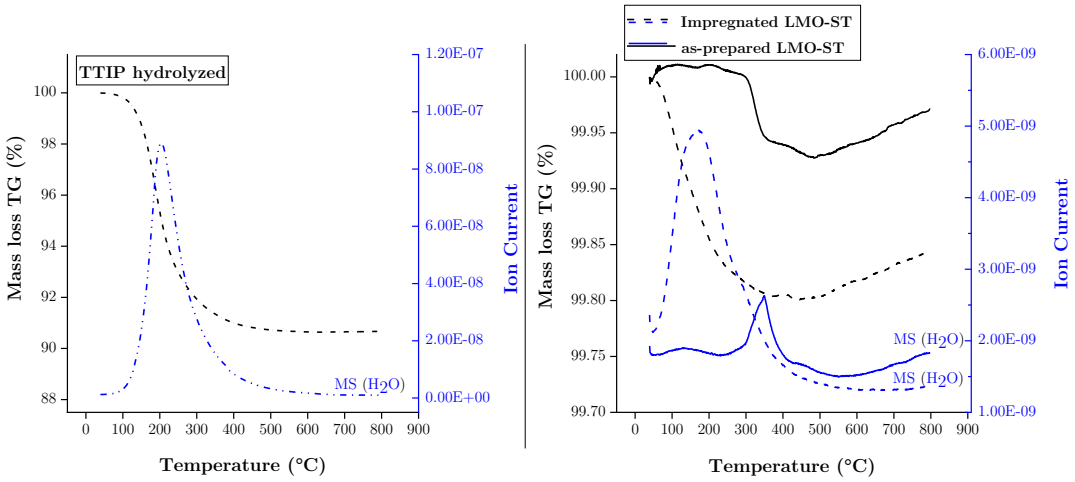


Figure 7.4: TG-MS analysis. a) hydrolyzed TTIP: TG and mass spectrum for $H_2O$; b) as-prepared and three times impregnated LMO-ST composite: TG and mass spectrum for $H_2O$.XRD analysis of ATTH dried at 110 °C, 210 °C, and 400 °C is presented in Figure 7.3. The XRD diffractogram of ATTH after heat treatment at 210 °C shows a slight tendency to crystallize into anatase, whereas, at 400 °C, the XRD reflections typical for anatase were observed [171]. It is clear from the XRD analysis that at temperatures below 200-400 °C, phases containing Ti (ATTH) are present in an amorphous state.

Figure 7.4 b) shows the clear difference between the as-prepared and the three times impregnated sample, as the mass loss in the as-prepared LMO-ST sample is about 0.02 %, while in the case of the impregnated sample, it is 0.2 %. When comparing the TG analysis results of hydrolyzed TTIP to the impregnated sample, it's evident that the mass spectrum for water exhibits a very similar trend.

Figure 7.5 shows the FTIR spectra for the as-prepared LMO-ST, the once and three times impregnated- LMO-ST, and the hydrolyzed TTIP. The spectra display certain bands characteristic of LMO and ST in the spectrum of the LMO-ST composite.

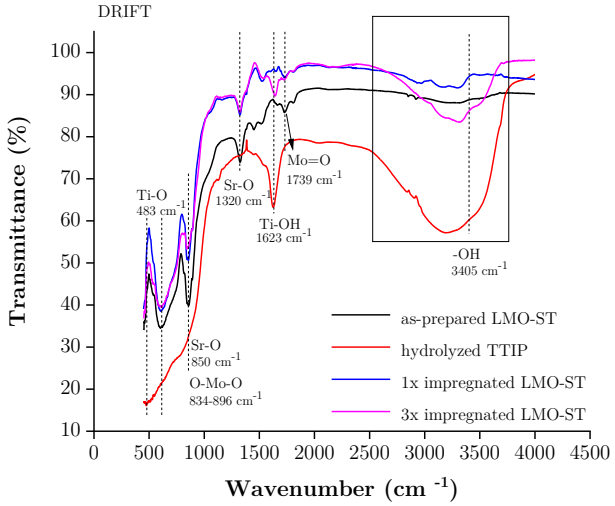


Figure 7.5: FTIR-DRIFT analysis of as-prepared and 3x-impregnated LMO-ST composite and hydrolyzed TTIP.A band at 557 $cm^{-1}$ corresponds to the stretching vibration of the SrTi-O bond [172]. Also typical of ST particles is the broad absorption band at around 625 $cm^{-1}$, corresponding to $TiO_6$ octahedron bending and stretching vibration [173]. In addition, the FTIR spectra of the impregnated LMO-ST composites were compared with the FTIR spectrum of the pure hydrolyzed TTIP. Figure 7.5 shows bands in the 2800–3800 $cm^{-1}$ range corresponding to the vibrations of water molecules. A trend of increasing intensity in the –OH vibrational band is visible for once-impregnated, three times impregnated, and pure hydrolyzed TTIP. The formation of Ti-OH bonds is partially visible after single impregnation but is evident in the case of the three times impregnated LMO-ST composite.

### 7.1.4 Dielectric properties of impregnated LMO-ST composites

Results showed that impregnation, combined with the additional thermal treatment of LMO-ST samples, improves dielectric properties. Figure 7.6 illustrates dielectric properties versus frequency for the as-prepared and the three times impregnated LMO-ST composites. Different drying regimes were investigated to optimize the post-heating process. As demonstrated in Figure 7.6, relative permittivity and dielectric losses for both sets of as-prepared and three-times-impregnated samples decrease with increased frequency. The relative permittivity of three times impregnated LMO-ST samples, dried for 4 h in a vacuum at RT, was notably the highest, measuring 207 at 1 kHz and 117 at 1 MHz. As expected, the same samples also exhibited the highest dielectric losses, especially at low frequencies (with $tan\ \delta > 0.25$ at 1 kHz and $tan\ \delta$ of 0.059 at 1 MHz), which can be attributed to OH groups in ATTH. After subjecting the three times impregnated samples to a 20-h drying period at 110 °C, a relative permittivity of 112 at 1 kHz and 92 at 1 MHz and dielectric losses of 0.106 at 1 kHz and 0.0096 at 1 MHz were determined. This suggests that a longer drying time reduces the content of –OH groups in ATTH. For comparison, the as-prepared LMO-ST samples exhibit a relative permittivity of 69.7 at 1 MHz with dielectric losses of 0.0026, as seen in Figure 7.6 a), b). Another drying regime of heating the impregnated LMO-ST samples at 400 °C resulted in a relative permittivity of 114 at kHz and 99 at 1 MHz and dielectric losses of 0.075 at 1 kHz and 0.0097 at 1 MHz. Reduced

dielectric losses, particularly at lower frequencies, were observed in three times impregnated samples when fired at 400 °C. This indicates that the bound water and –OH groups were removed at heating. Partial crystallization of ATTH to anatase occurred (Figure 7.3). When drying in a vacuum at room temperature was carried out on impregnated samples, it resulted in extra lossy behavior ($tan\ \delta > 0.25$) in the low-frequency range, which indicated that condensation reactions were incomplete. From an application perspective, short-term vacuum drying at room temperature may not be suitable for drying three times impregnated samples.

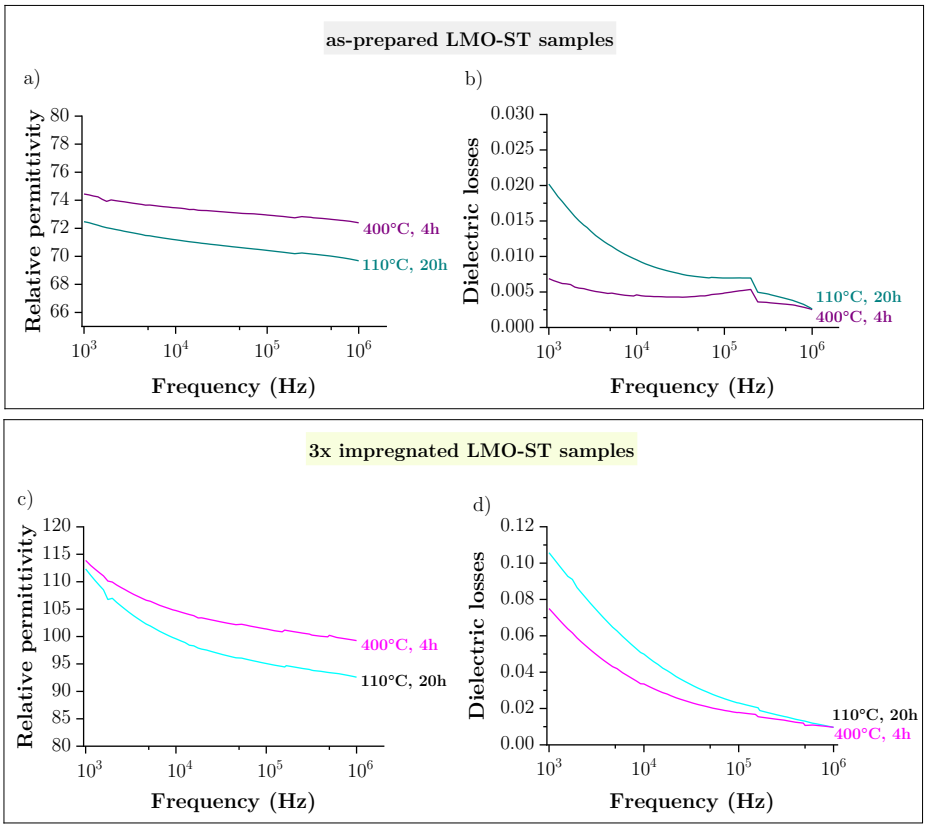


Figure 7.6: Average values of dielectric properties of a), b) as-prepared LMO-ST samples (6.5 wt % LMO) compared to the c), d) three times impregnated LMO-ST composites (6.5 wt % LMO) that were dried under two different conditions (20 h in an oven-air atmosphere at 110 °C and 4 h in a furnace at 400 °C).

## 7.2 Conclusions

Impregnation was used as a post-treatment step that can positively affect the overall densification by approximately 1 % per impregnation cycle. TTIP was successfully used as an impregnating agent and showed an increase in relative permittivity (at 1 MHz) of 43 % after three cycles. As shown, impregnation caused slightly increased dielectric losses, presumably due to the -OH groups and the remaining bound water. This was further investigated by changing the drying procedure after impregnation. SEM-EDS analysis confirmed the presence of a Ti-containing phase at the surface and deeper in the composites. Further, TG showed that only 9.3% of the total mass occurred during the hydrolysis of TTIP. This means that the Ti-containing phase present in the composites after impregnation is mostly amorphous $TiO_2$, and to some extent, $Ti(OH)_4$. Two significant phenomena occurred when the impregnated samples were heated to 400 °C: crystallization TTIP to anatase and removing the remaining -OH groups and bound water. Moreover, the impregnating agent can be substituted if it further improves density and dielectric properties. The three times impregnated LMO-ST samples remained intact and stable after the impregnation process. In addition, their mechanical stability increased after the impregnation process.

It is, however, important to tackle porosity in our future research on RTF, as the relative density of the binder-ST is still low when compared to the sintered ceramics. Extensive research was conducted by Smith et al. [174], which optimized the RTF process by pressing the composite mixture at higher pressure (650 MPa) in a vacuum-assisted die and subsequently exposing the die to sonification repeatedly. They studied the effect of increased pressure, sonification repetitions, and exposure to vacuum on the relative density by considering each treatment separately and all of them together. Their innovative approach is reported to increase relative density up to 96.9 % in the case of LMO-BST (x=0.5 or 0.45) and up to 95.1 % in the case of LMO-PZT (y=0.5) composites prepared at RT. Based on that, the previously used fabrication method presented in this study can be advanced to reconsider the densification in binder-ST composites and further decrease the porosity.

# Chapter 8

# New Inorganic Binders and Fillers alternative to LMO-ST upside-down RTF Composites

In previous research in the thesis, I employed LMO as the sole binding phase and exclusively ST as a filler phase in the RTF binder-filler composites. However, my objective was to introduce potential binding materials that can cure at RT, yield a dense structure upon drying, and exhibit adequate or enhanced dielectric and mechanical properties.

In the following chapter, I present new binders as alternatives to the previously extensively studied LMO binder using the RTF method. The inorganic compounds $Na_2MoO_4$ (NMO), $Na_2WO_4$ (NWO), $Na_2SiO_3$ (NSiO), and $MgSO_4$ (MSO) were utilized as binding phases (15 vol %) in RT-fabricated binder–$SrTiO_3$ (ST) composite systems. This resulted in pellets with relative density ($\rho$=83-88 %) and dielectric properties applicable in radio and microwave (MW) frequency ranges. The relative permittivity of as-prepared binder-ST composites varied from 68 to 124 at 1 MHz and between 67 and 129 in the MW frequency range. The dielectric losses exhibited a range of 0.0029 and 0.0142 at 1 MHz, corresponding $Q \times f$ values between 689 and 1335 GHz. In addition, BT was employed as a substitute for ST filler and BT-ST in combination, aiming to broaden the spectrum of dielectric properties.

The binding potentials, microstructure, and stabilities of the prepared binders in the binder–ST composites were investigated using SEM coupled with EDS, XRD, and TG-MS. Furthermore, RT-pressing of binder-filler composites was compared with heat-assisted (HA) pressing at 110 °C (Appendix, A.4).

This chapter provides valuable insights into using alternative binders to fabricate binder-ST composite systems. Owing to their enhanced properties, these systems could have significant implications in various fields, including electronics and telecommunications. Part of the experimental results presented in this chapter was reported in the form of a research paper entitled: “New Inorganic Binders for Room Temperature Fabrication of Upside-down $SrTiO_3$-based Ceramic Composites”

**Published in the journal** Ceramics International, June 12, 2024, https://doi.org/10.1016/j.ceramint.2024.06.129.

## 8.1 Results and Discussion

Alternative binders to LMO in RTF of upside-down binder-ST composites were combined in the proportion of 85 vol % ST and 15 vol % of the corresponding binder, which has previously been shown to result in effective properties. The constant volume percentage was used in all binder-ST and binder-BT systems due to the difference in the inherent density of the binders. The proportion of solid binder powder was combined with a mixture of ST particles of varying sizes and further moistened with an aqueous phase for each composite sample. A saturated solution was utilized in NMO-, NWO-, and NSiO-ST composites, whereas in MSO-ST composites, distilled water was implemented.

### 8.1.1 Microstructural analysis of binder-ST composites

As shown in SEM micrographs (Figure 8.1), the ST particles and binder phase mainly formed good contacts. The smaller binder phase is closely packed with smaller filler ST particles; however, some larger pores can be observed near the larger particles. A wide-size particle distribution in composites was confirmed with SEM-EDS imaging.

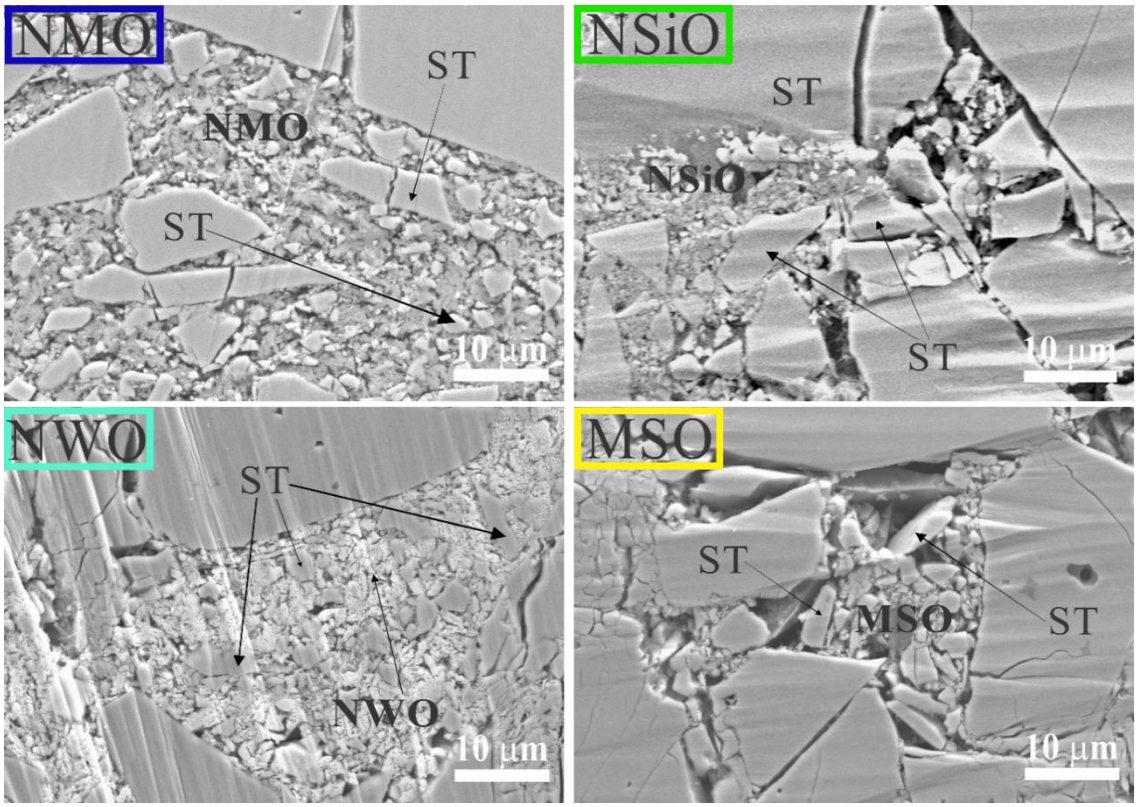


Figure 8.1: SEM micrographs of binder-ST composites.

The present phases in the binder-ST composites were confirmed by EDS analysis (Figure 8.2). EDS mappings show that the binder phase incorporates smaller ST particles. Therefore, the binder connects the all-sized ST particles. In the EDS mapping of the NSiO-ST composite sample, the binder phase is less noticeable due to the overlap of the silicon K alpha peak (1.739 keV) with strontium L alpha (1.81 keV). Consequently, sodium was used to identify the NSiO binder. In NWO, the tungsten M alpha peak (1.774 keV) overlaps with the strontium L alpha signal. Thus, Na was used again to identify sodium tungstate.

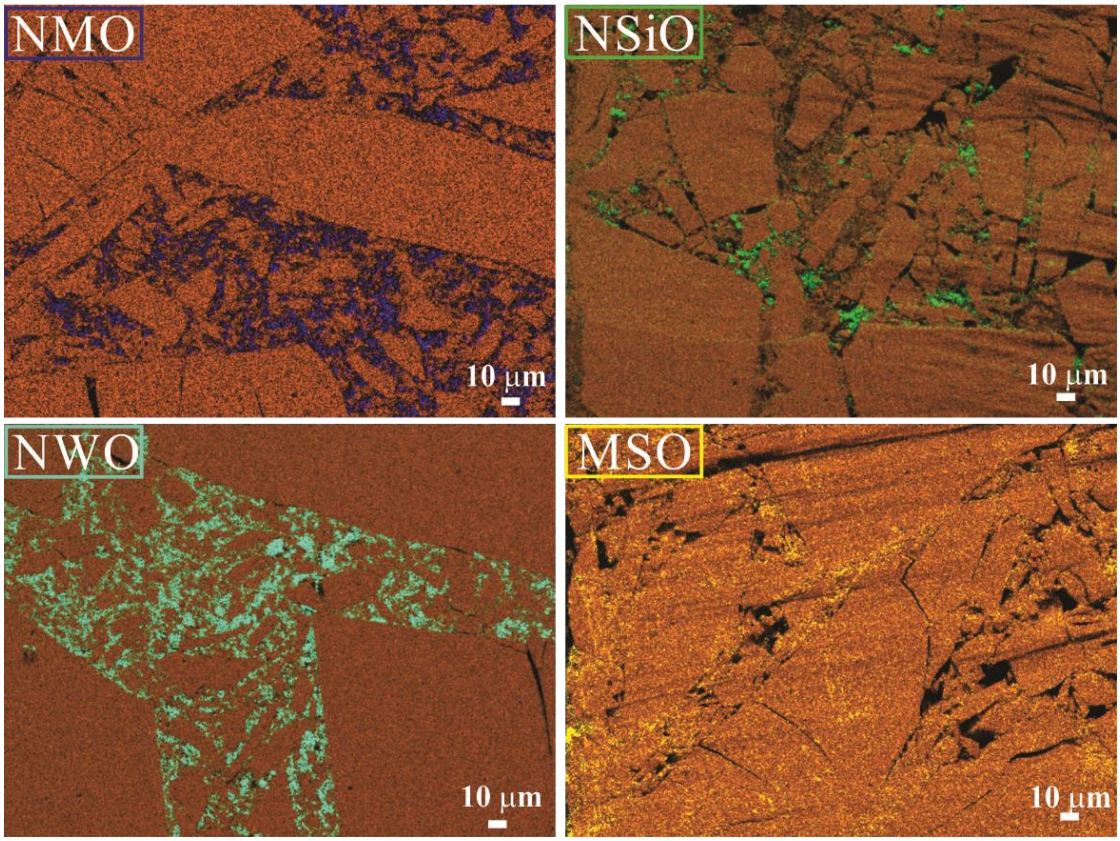


Figure 8.2: EDS mapping analysis of binder-ST composites. The ST phase is orange, while the binders are in their respective colors: NMO (purple), NSiO (green), NWO (turquoise), and MSO (yellow).

### 8.1.2 XRD, TG, and FTIR analysis

The results of the XRD analysis performed on the binders NMO, NWO, NSiO, MSO, and binder-ST composites are shown in Figure 8.3 a) and b). The NMO, NWO, and NSiO binders were successfully prepared through solid-state synthesis, as indicated by the results. The XRD patterns of pure binders matched the XRD standard patterns of ICDD files No. 12-0773 (NMO), 12-0772 (NWO), 16-0818 (NSiO), 24-0719 (MSO).

The XRD patterns of binder-ST composites exhibit reflections of ST and the corresponding binder in proportion to their respective fraction. The XRD patterns of binder-ST composites show very low-intensity reflections of binders due to the low binder volume fraction. No new reflections were observed, indicating no chemical reaction between the binders and ST. This observation is consistent with the LMO-ST XRD analysis (Chapter 4).

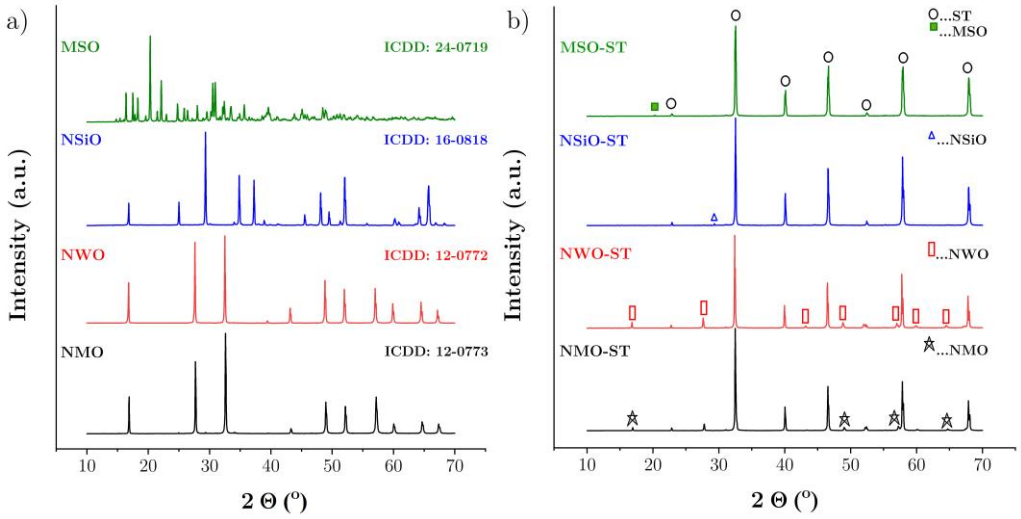


Figure 8.3: XRD patterns of the a) binders, b) binder-ST composites prepared at RT, dried at 110°C, and stored in a desiccator.

Thermogravimetry–mass spectroscopy (TG-MS) was used to analyze the phase transitions, different stages of dehydration, and released gases while heating the pure NMO,

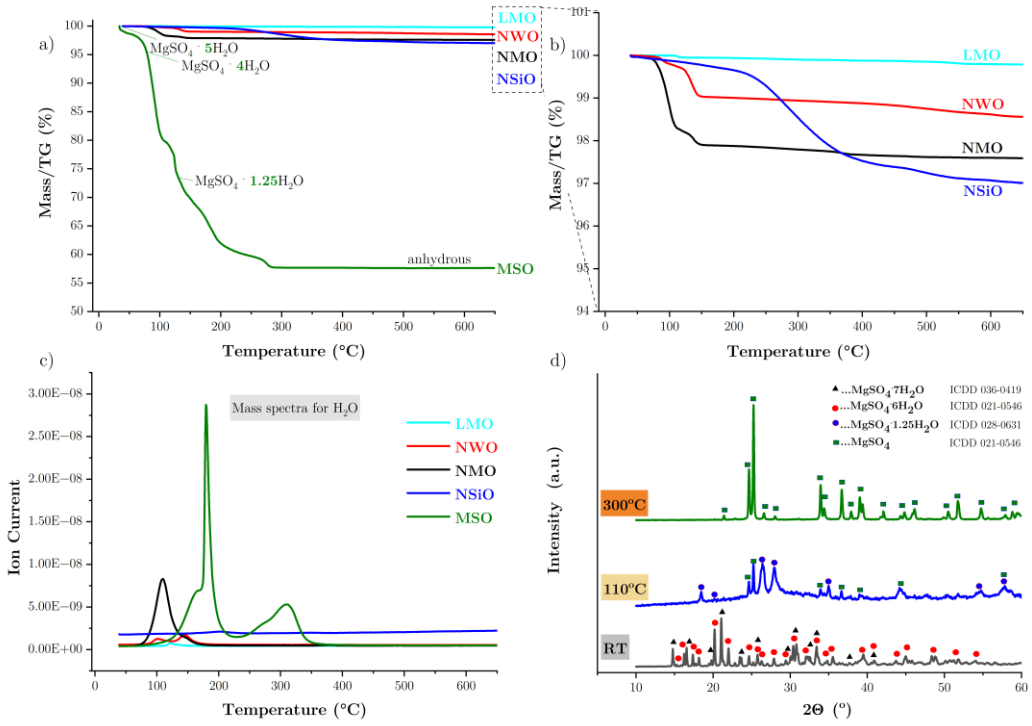


Figure 8.4: TG-MS analysis of a), b) binders, whereas b) shows a zoomed region of low-mass loss in figure a); c) MS spectra for $H_2O$ for all binders, d) XRD of MSO dried at RT, 110°C and 300°C (4 h).

NWO, NSiO, and MSO binder powders. The TG-MS spectrum for LMO is also included for comparison. Figure 8.4 illustrates the results of thermogravimetric analysis of the binders. The thermal behavior of binders is strongly related to their chemical nature and

differs among them. TG-MS of NMO and NWO confirmed that the mass loss, observed below 300 °C, is primarily due to the presence of physically adsorbed water molecules. This conclusion is supported by the presence of ions at 18 m/z ($H_2O$ fragments), as shown in Figure 8.4 c). NWO and NMO exhibit a low mass loss of 1-2.1 % up to 150 °C and 2.5 % above 350 °C, presumably due to physically adsorbed water, which agrees with the literature [57]. NSiO showed a minor loss of 0.25 % up to 150 °C, which increased to 2 % above 350 °C. The weight loss of MSO started at 22 °C; however, above 350 °C, the residual weight fraction was stabilized at 57.7 %. The experimentally obtained TG data for MSO indicated that crystal-bound water was released upon heating to 300 °C, which aligns closely with the information found in the literature [175]. The total 42.3 % mass loss confirmed that MSO was present as pentahydrate ($MgSO_4 \cdot 5H_2O$) at the onset of TG measurement. According to the XRD, at RT, MSO exists in both heptahydrate ($MgSO_4 \cdot 7H_2O$) and hexahydrate ($MgSO_4 \cdot 6H_2O$). $MgSO_4 \cdot 7H_2O$ starts transforming to $MgSO_4 \cdot 6H_2O$ already from 25 °C to 34 °C [176]–[178]. It was not possible to confirm the presence of $MgSO_4 \cdot 7H_2O$ and $MgSO_4 \cdot 6H_2O$ from TG analysis due to limitations of the TG-MS instrument and the influence of ambient humidity. $MgSO_4 \cdot 5H_2O$ is dehydrated to tetrahydrate ($MgSO_4 \cdot 4H_2O$) at 77 °C, consistent with the existing literature [178]. Further mass loss indicates the presence of $MgSO_4 \cdot 1.25H_2O$ at 130 °C. As seen in 8.4 c), The MS spectrum for water shows two distinct peaks, up to 180°C, where 37.7 %of mass loss is detected, and an additional 9.6 % upon heating to 300 °C [177]. Dehydration of MSO is a combination of deliquescence, partial dissolution, and recrystallization from the saturated solution that forms during heating [77].

Additionally, different forms of the $MgSO_4$ hydrates were identified by XRD, i.e., $MgSO_4 \cdot 7H_2O$ and $MgSO_4 \cdot 6H_2O$ at RT. By heating the MSO powder to 110°C for 4 h, the $MgSO_4 \cdot 7H_2O$ was converted to $MgSO_4 \cdot 1.25H_2O$ and partially to anhydrous MSO according to the XRD analysis. However, the complete removal of crystal-bound water was observed by further heating to 300 °C (Figure 8.4 d)).

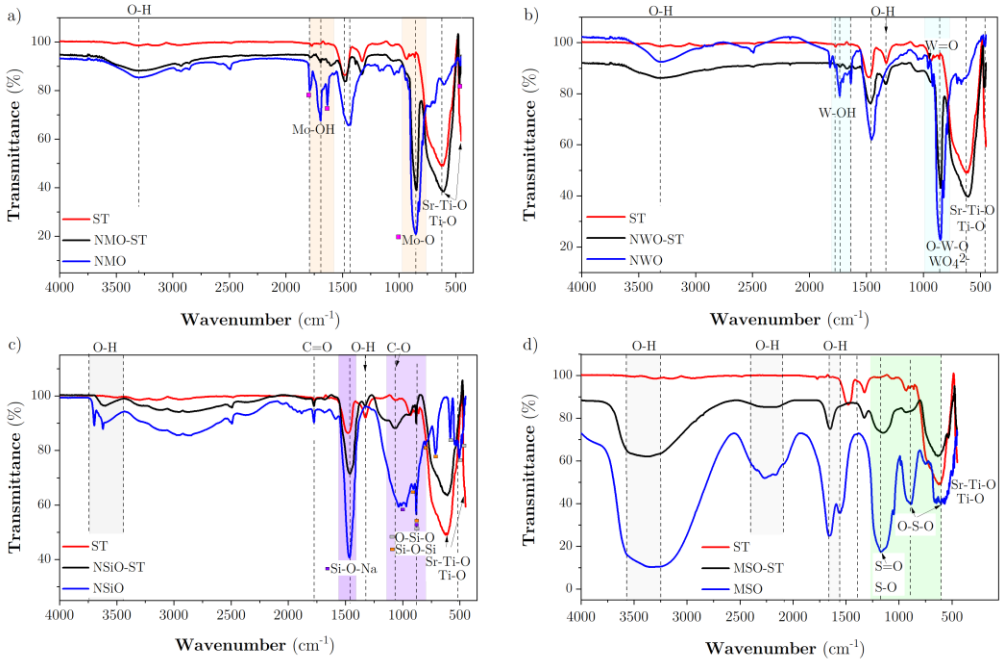


Figure 8.5: FTIR analysis of binder-ST composites a) NMO-ST; b) NWO-ST; c) NSiO-ST; d) MSO-ST compared to ST and particular binders.

Furthermore, FTIR-DRIFT analysis of the samples was conducted. The resulting spectra (Figure 8.5) consist of bonding vibrations of the binder-ST composites, which were compared to those of sintered ST and the binders NMO, NWO, NSiO, and MSO. No new bands were observed from the spectra of all binder-ST composites, indicating that the FTIR measurements confirmed no chemical reaction between the binder and filler phase during RTF.

The next section describes a more detailed description of FTIR spectra. Characteristic bands for ST were observed near 460, at 610 and 625, 1326 and 1480 $cm^{-1}$. Absorption bands between 460 and 625 $cm^{-1}$ correspond to the $TiO_6$ octahedron bending and stretching vibration [173], [179]. The absorption bands at 1640-1688 and 3300 $cm^{-1}$ originate from the samples' O–H bending and stretching vibrations of the residual water [180], [181]. OH absorption band characterizing free water is generally observed at 3600-3700 $cm^{-1}$. Absorption bands appearing at 1788, 1694, and 855 $cm^{-1}$ are the typical molybdate bands. The characteristic band for NMO near 860 $cm^{-1}$ corresponds to the vibration of the $MoO_4$ units. Other bands at 1040, 1170, 1430, 2490, and near 2900 were also observed in the reported IR spectrum for NMO. NWO shows characteristic IR bands at 460, 670, 700, 790, 850, 920, 960, 1454, 1638, and 1735 $cm^{-1}$, which partially aligns with the existing literature [182], [183]. The distinctive vibrations of the O determine the ($WO_4$) groups' frequencies – W–O bridge and $WO_4^{2-}$ groups. The stretching vibration of the $WO_4^{2-}$ tetrahedron is present in the range 650–800 $cm^{-1}$. The strong absorption band at 850 $cm^{-1}$ can be ascribed to the O–W–O stretches of the $WO_4$ tetrahedron [180]. In the NSiO- IR spectrum, the bands at 480, 505-580, 715, and 880 $cm^{-1}$ were ascribed to the different forms of the stretching vibration of O-Si-O. Bands observed between 505 and 590 $cm^{-1}$ represent (Na)O-Si-O(Na) and (Si)O-Si-O(Si) vibrations. New Si-O-Si stretching bands appeared at about 715 and 880 $cm^{-1}$, corresponding to Si-O- symmetric stretching vibration. The 715 $cm^{-1}$ appears when oxygen is bound to Si and 880 $cm^{-1}$ when oxygen and $Na^+$ are adjacent. The absorption band around 800 $cm^{-1}$ corresponds to the Si-O-Si stretching vibration of bridging oxide or inter-tetrahedral, and the absorption band around 950 $cm^{-1}$ is known to be due to Si-OH [184]. The IR band corresponding to Si-O-Si asymmetric stretching vibration corresponds to 1035, 970, and 960 $cm^{-1}$. Si-O-Na stretching vibration was observed at about 1000 $cm^{-1}$. The absorption band around 1040 $cm^{-1}$ is due to the asymmetric stretching vibration of Si-O(Na).

### 8.1.3 Dielectric and Microwave properties of binder-ST composites

Tables 8.1-8.3 present the dielectric properties of the pure binder pellets and the binder-ST composites. Dielectric characterization was performed across radio and microwave frequency ranges to investigate broader application possibilities.

Table 8.1: Dielectric properties of pure binders measured in radio- (1 MHz) and MW ranges (5 GHz). Samples were prepared at RT.

| binders | relative density, $\rho$ (%) | relative permittivity, $\varepsilon_r$ at 1 MHz | relative permittivity, $\varepsilon_r$ at 5 GHz |
|---|---|---|---|
| **NMO** | 75 | 2.5 | 2.6 |
| **NWO** | 78 | 3.6 | 3.1 |
| **NSiO** | 68 | 4.5 | 3.8 |
| **MSO** | 72 | 4.6 | 4.5 |

Dielectric measurements for the pure binders were conducted from 20 Hz to 1 MHz and from 1 GHz to 20 GHz; the values presented in Table 8.1 show the results at frequencies of 1 MHz and 5 GHz. The relative permittivity values of all binder-type samples remained constant throughout the MW-frequency range of 1–20 GHz. Dielectric properties of new binders were compared to LMO, which was previously reported in the literature ($\varepsilon_r = 5.0$ and $tan\ \delta = 0.0005$ at 1 MHz; $\varepsilon_r = 5.1$ and $tan\ \delta = 0.0004$ at 9.6 GHz) [185]. MSO and NSiO exhibit similar relative permittivity as LMO in the whole frequency range ($\varepsilon_r = 4.5$-5.0 at 1 MHz, $\varepsilon_r = 4.3$-4.8 at resonant frequencies). Relative permittivity values of NMO and NWO in the microwave frequency range align well with the literature, where properties such as $\varepsilon_{rNMO}$ of 4.1, $\rho_{NMO}$ of 90 %, and $\varepsilon_{rNWO}$ of 5.8, $\rho_{NWO}$ of 96 % were reported [54],[59], [60] Among them, LMO exhibits the highest relative density of 93 %. NMO binder shows an average relative density of 75 %, slightly lower than cold-sintered pure NMO ($\rho$=83.2 %) prepared at similar conditions (cold sintering at 100 °C, 350 MPa) [186]. Among the binders, it is evident that LMO exhibits the highest relative density of 93 %.

Table 8.2: Relative density and dielectric properties of RT-fabricated binder-ST composites, including additional drying at 110 °C (measured in radio-frequency range at 1 MHz.

| Filler | | **ST** | | | | |
|---|---|---|---|---|---|---|
| Binders | | **LMO** | **NMO** | **NWO** | **NSiO** | **MSO** |
| relative density, $\rho$ | % | 83 | 82 | 83 | 83 | 83 |
| relative permittivity, $\varepsilon_r$ | 1 MHz | 70 | 80 | 68 | 113 | 124 |
| dielectric losses, *tan* $\delta$ | | 0.0029 | 0.0054 | 0.0066 | 0.0062 | 0.0011 |
| binder solubility | (g/mL $H_2O$) | 0.795 | 0.653 | 0.682 | 0.374 | 0.351 |

As indicated in Table 8.2, using NMO and NWO binders in ST-composites results in similar values of relative permittivity when compared to LMO binder ($\varepsilon_{r,\,LMO\text{-}ST} = 70$, $\varepsilon_{rNMO\text{-}ST} = 80$, $\varepsilon_{r,\,NWO\text{-}ST} = 68$) at 1 MHz. On the contrary, MSO and NSiO binders outperform NMO, NWO, and LMO, resulting in $\varepsilon_r$ values of 113 for NSiO-ST and 124 for MSO-ST composites at 1 MHz. The dielectric losses measured at 1 MHz for the MSO binder (~0.0011) were lower than those for the LMO binder (~0.0029), whereas slightly higher losses were observed for NMO, NSiO, and NWO (~0.0054-0.0066). The experimentally obtained solubility values for each binder are listed in Table 8.2.

The average relative density values of alternative binder-ST composites prepared by RTF ($\rho$~83 %) are comparable to that of LMO-ST composites ($\rho$=83 %).

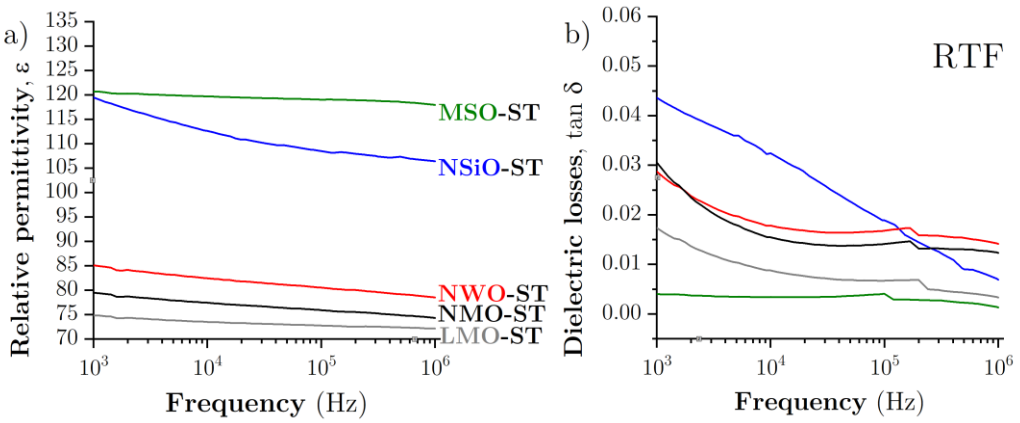


Figure 8.6: Dielectric properties of binder-ST composites prepared by RTF vs. frequency (1 kHz-1 MHz): a) relative permittivity and b) dielectric losses.

Figure 8.6 displays the relative permittivity, $\varepsilon_r$, and dielectric losses, *tan* $\delta$, for binder-ST composites prepared by RTF across a frequency range ranging from 1 kHz to 1 MHz. In fact, relative permittivity values of MSO-, NWO-, NMO-, and LMO-ST composites were relatively constant across the whole frequency range. However, the highest variation in the dielectric behavior was noticed in NSiO-ST composites, $\varepsilon_r$ ranging from 120 (1 kHz) to 106.5 (1 MHz) and *tan* $\delta$ from 0.0436 to 0.0070.

Table 8.3 lists the dielectric properties of the binder–ST composites measured in the MW-frequency range. Relative permittivity values were calculated by the method presented by Krupka [15]. This could also be obtained by using the ErCalc program [187]. The comparison between both methods is available in Appendix (A.5.2). The loaded $Q_L$ factor was measured in reflection mode. Unloaded $Q$ ($Q_u$) values were calculated from the $Q_L$ by considering the multiplication factor, as described in the Introduction (1.2). Smith charts for each binder-ST composition and details on the calculations are available in Appendix (A.5.1). NMO and NWO outperform LMO binder ($\varepsilon_{r,\,NMO–ST} = 92$, $\varepsilon_{r,\,NWO–ST} = 89$, $\varepsilon_{r,\,LMO–ST} = 67$) when used in binder–ST composites. The $Q_u \times f$ values of the LMO–ST and NWO–ST samples were comparable. The MSO–ST composites retained the highest relative permittivity in the MW- frequency range, whereas the NSiO–ST composites showed the highest $Q_u \times f$ values. When comparing the properties of the samples prepared for measuring the RF and MW dielectric properties, I noticed a higher relative density with the MW samples. This difference may be due to the different pellet dimensions ($d_{MW\text{-}composites}$=6 mm, $h_{MW\text{-}composites}$=3.5 mm vs. $d_{RF\text{-}composites}$=10 mm, $h_{RF\text{-}composites}$=2 mm) and the higher pressure gradient in the MW samples, leading to greater densification.

Table 8.3: Relative density and dielectric properties of RT-fabricated binder-ST composites, including additional drying at 110°C (measured in the microwave range).

| Filler | **ST** | | | | |
|---|---|---|---|---|---|
| Binders | **LMO** | **NMO** | **NWO** | **NSiO** | **MSO** |
| relative density, ρ (%) | 83 | 87 | 88 | 81 | 87 |
| relative permittivity, $\varepsilon_r$ | 67 | 92 | 89 | 104 | 120 |
| $Q_u \times f$ (GHz) | 883 | 960 | 849 | 1335 | 689 |
| $f$ (GHz) | 5.9 | 5.2 | 5.3 | 4.7 | 4.6 |

#### 8.1.3.1 The temperature coefficient of resonant frequency for the binder-ST composites

The average temperature coefficient of resonant frequency ($\tau_f$ or $TCF$) is reported in Table 8.4. TCF was determined by the following Equation (8.1):

$$TCF\ (\tau_f) = \frac{1}{f} \times \frac{df}{dT} \tag{8.1}$$

Additionally, further methods for determining the TCF values were explored. More details are available in Appendix (A.5.1).

Table 8.4: The temperature coefficient of resonant frequency for all binder-ST composites. Samples were prepared at RT.

| Composite sample type | frequency at 27.5 °C | frequency at 65 °C | $TCF_{average}$ |
|---|---|---|---|
| | GHz | GHz | ppm/°C |
| **LMO-ST** | 5.49 | 5.74 | 1123 |
| **NMO-ST** | 5.66 | 6.00 | 1495 |
| **NWO-ST** | 5.55 | 5.82 | 1221 |
| **NSiO-ST** | 5.87 | 6.42 | 793 |
| **MSO-ST** | 4.53 | 4.76 | 1283 |

The results indicate that the NSiO-ST composites have a significantly lower average temperature coefficient of frequency (TCF) than the other binder-ST composites. The results align with the reported TCF values for sintered ST ceramics (> 1100 ppm/°C) [179].

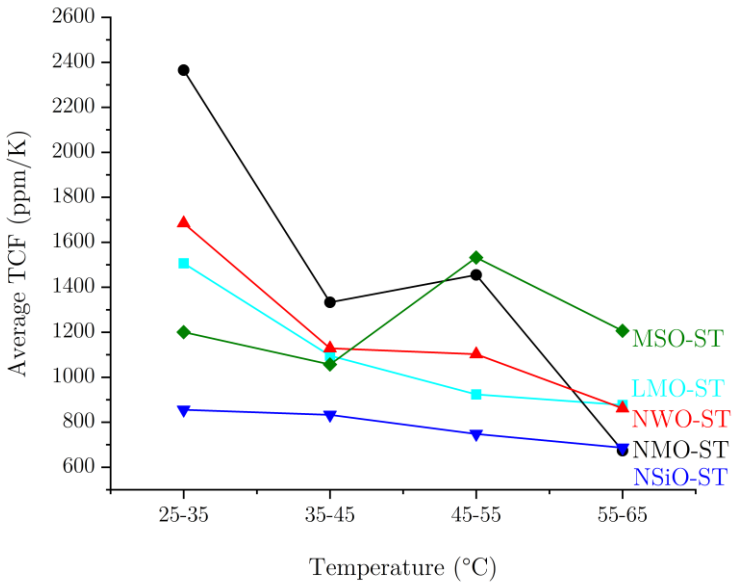


Figure 8.7: Average values of TCF for all binder-ST composites in the entire temperature range, with a step of 10 °C.

As shown in Figure 8.7, the TCF for NMO-ST, NWO-ST, and MSO-ST varies significantly across the entire temperature range, while the TCF for LMO-ST and NSiO-ST tends to remain constant. Average values for TCF per 2-3 samples are reported.

As an alternative to ST, BT was also used as a ceramic filler in binder-filler composites with the same compositional proportion of 85 vol % of filler /15 vol % of the binder. Table 8.5 shows the relative density and dielectric properties of binder-BT composites. The observed trend with binder-BT composites remains the same as with binder-ST composites. As the ST was substituted with BT, relative permittivity increased up to 3 times. The average relative permittivity of conventionally sintered BT was measured to be 1328 at 1 MHz with corresponding dielectric losses of 0.0768. The highest relative permittivity of binder-BT composites was achieved with NSiO ($\varepsilon_r = 271$) and MSO ($\varepsilon_r = 320$) as a binder. Concurrently, dielectric losses in binder-BT composites increased substantially compared to binder-ST composites (for ~ 2-10x). Since BT is ferroelectric, we did not perform electrical measurements in the MW range.

Table 8.5: Relative density and dielectric properties of binder-BT composites measured in the RF frequency range.Samples were prepared at RT.

| Filler (85 vol %) | | **BT** | | | | |
|---|---|---|---|---|---|---|
| Binders (15 vol %) | | **LMO** | **NMO** | **NWO** | **NSiO** | **MSO** |
| relative density, ρ | % | 83 | 81 | 84 | 82 | 84 |
| relative permittivity, $\varepsilon_r$ | 1 MHz | 122 | 133 | 136 | 271 | 320 |
| dielectric losses, *tan* δ | | 0.0273 | 0.0279 | 0.0190 | 0.0251 | 0.0080 |

Further, composites of binder-BT-ST were prepared by mixing BT and ST in a 1:1 ratio, making up 85 % of the total volume of a composite. The binder volume fraction was kept constant. Results of dielectric properties and density are reported in Table 8.6. Introducing BT to a binder-ST composite enhanced relative permittivity and increased dielectric losses. The highest relative permittivity was observed with NSiO-BT-ST and MSO-BT-ST composites.

Table 8.6: Relative density and dielectric properties of binder-BT-ST composites measured in the RF frequency range. Samples were prepared at RT.

| Fillers (85 vol %) | | **BT-ST=1:1** | | | | |
|---|---|---|---|---|---|---|
| Binders (15 vol %) | | **LMO** | **NMO** | **NWO** | **NSiO** | **MSO** |
| relative density, ρ | % | 86 | 85 | 83 | 88 | 86 |
| relative permittivity, $\varepsilon_r$ | 1 MHz | 98 | 105 | 107 | 190 | 179 |
| dielectric losses, *tan* δ | | 0.0245 | 0.0214 | 0.0187 | 0.0184 | 0.0059 |

## 8.2 Conclusions

Room temperature fabrication has previously demonstrated that ceramic composites can be produced at 110 °C, resulting in properties that are approximately one-third of those achieved through solid-state sintering, which, of course, is dependent on the composition [46], [148],[103]. For instance, sintered ST exhibits a relative permittivity of 296 (at 1 MHz), while RT-fabricated binder-ST composites exhibit $\varepsilon_r$ up to 124 at 1 MHz. In this chapter, different inorganic binders such as NMO, NWO, NSiO, and MSO were, for the first time, successfully utilized as alternatives to LMO in binder-ST composites fabricated at RT. The new binders yielded comparable relative densities ($\rho \sim 83$ %) and similar or improved dielectric performance $\varepsilon_{r,\text{ binder-ST-composites}} = 68\text{-}124$; $tan\ \delta = 0.011\text{-}0.0066$ at 1 MHz; $Q_u \times f$ values between 689 and 1335 at 5 GHz). The absence of a chemical reaction between salts and ST particles was verified through X-ray diffraction. Regarding dielectric properties in radio- and microwave-frequency ranges, NSiO- and MSO-ST composites exhibit higher relative permittivity of 100 -130 at 1 MHz. Furthermore, the binder-ST composites underwent heat-assisted pressing for comparison. Relevant data can be found in the Appendix (A.1.4.1). Using the HA-pressing method with binder-ST samples, I obtained slightly higher relative density ($\rho$ from ~93 % to ~98 % of LMO- and NMO-binder-ST composites) and improved dielectric properties of binder-ST composites $\varepsilon_{r,\text{ HA-binder-ST-composites}} = 88\text{-}134$; $tan\ \delta = 0.0023$ at 1 MHz. Considering that we need to maintain constant heating at 110 °C during HA-pressing and that the compression process takes longer (~ 30 min), we have not made enough improvements in the properties to justify using HA-pressing in the regular composites processing.

In addition, a potential limitation to the application of MSO and other environmentally sensitive salts is the ease with which dehydration/rehydration transformations occur in the $MgSO_4 \cdot nH_2O$ system relative to humidity and temperature.

In this chapter, filler ST was replaced or partially substituted with BT to inspect the effect on dielectric performance. The dielectric properties of binder-ST composites were compared to those of binder-BT and binder-BT-ST composites. The single-phase BT exhibits higher relative permittivity compared to ST $\varepsilon_{r,\text{ BT ceramics}} = 1328$, $tan\ \delta = 0.0768$; $\varepsilon_{r,\text{ ST ceramics}} = 296$, $tan\ \delta = 0.0015$ at 1 MHz, so it increases the dielectric properties of composites $\varepsilon_{r,\text{ binder-BT-composites}} = 122\text{-}320$ at 1 MHz. Combining BT and ST as a filler leads to properties in between $\varepsilon_{r,\text{ binder-BT-ST-composites}} = 98\text{-}190$ at 1 MHz.

The choice of binder and its physicochemical properties can strongly affect the final dielectric performance It was shown that different binder or filler phases in the upside-down ceramic composites prepared by RTF lead to a very broad range of dielectric properties, enabling various applications.

# Chapter 9

# Mechanical Properties of ST- and LMO-, NSiO- Ceramics and LMO-ST, NSiO-ST Ceramic Composites

Mechanical characterization was performed in collaboration with Abdullah Jabr and Prof. Dr. Raul Bermejo from the Materials Science department, Montanuniversität Leoben, Austria. LMO-ST and NSiO-ST composites and their corresponding single-phase materials (LMO, NSiO, and ST ceramics) were investigated. For the precise statistical analysis, 10-30 samples of each type of material were prepared for the ball-on-three-ball (B3B) testing. Mechanical testing was partially conducted during my working visit to Leoben in March 2023.

This chapter explores the effect of the binder phase on the mechanical strength of RT-fabricated ST-based ceramic composites. Among all the proposed binder-ST compositions, I decided to perform mechanical testing on NSiO-ST, which showed the best and most stable electrical properties, and additionally on LMO-ST samples for reference. However, the remaining compositions with other binders will be tested in the future. A comparison with single-phase high-temperature sintered counterparts was also conducted to see how much the fabrication process affects the final mechanical strength, going from high to low temperatures and from single phase to composites.

The results of B3B measurements showed that the biaxial strength of RTF NSiO-ST was seven times higher than that of LMO-ST composites (i.e., 77 MPa to 11 MPa), resulting in approximately 40 % of the strength of single-phase ST sintered at high temperature (i.e., ~200 MPa). The relatively high strength of RTF NSiO-ST is related to the polycondensation of $(SiO_4)^{4-}$ monomers in $Na_2SiO_3$ aqueous solution. Such a process yields stronger bonding of NSiO with ST particles, as evidenced by wettability tests supported by spectroscopy and fractographic analyses. Understanding the impact of the binder phase on the densification of ceramics fabricated at room temperature may result in enhanced structural integrity of ceramic composites.

This chapter's content resulted in a joint **manuscript** entitled: “Towards high strength $SrTiO_3$-based composites fabricated at room temperature”, which was **published in** Journal of European Ceramic Society, July 2024, https://doi.org/10.1016/j.jeurceramsoc.2024.116782.

## 9.1 Results and Discussion

The mechanical stability of ceramic materials should be addressed before using them in electronics and subjecting them to operational loads. This chapter presents the results of the mechanical characterization of conventionally sintered ST ceramics, binder LMO, and NSiO ceramics compared to the RTF-prepared binders LMO and NSiO, as well as binder-filler composites. In addition, I focused on identifying a binder phase that may enhance the mechanical strength of the composite and further understanding the chemical interactions between the binder phase and the filler material, as they dictate the cohesion strength. In addition, SEM, XRD, FTIR, and wetting angle analyses were conducted to inspect the crystal structure, microstructure, bonding, and wetting properties of ceramics and ceramic composites. Sample preparation conditions are summarized in Table 9.1.

Table 9.1: Processing conditions of ceramic and ceramic-ST composites obtained by different consolidation methods.

| Sample type | ID | **Consolidation** | **Temperature (°C)** | **Dwell time (h)** |
|---|---|---|---|---|
| **ST** | **(S)** | Solid-state sintering | 1400 | 12 |
| **LMO** | **(S)** | Solid-state sintering | 660 | 3 |
| **LMO** | **(R)** | RTF | RT + 110 | 6 |
| **LMO-ST** | **(R)** | RTF | RT + 110 | 6 |
| **NSiO** | **(S)** | Solid-state sintering | 950 | 3 |
| **NSiO** | **(R)** | RTF | RT + 110 | 6 |
| **NSiO-ST** | **(R)** | RTF | RT + 110 | 6 |

### 9.1.1 Relative density of ST- and LMO, NSiO-ceramics and LMO-ST and NSiO-ST composites

The relative density was determined geometrically from the mass and size of samples after the preparation process concerning the theoretical density of the corresponding phase (details can be found in Chapter 3, section 3.2 ). The average relative densities of sintered and RT-fabricated samples are presented in Figure 9.1. As expected, the conventionally sintered ST (S) and LMO (S) ceramics exhibit the highest relative densities of 98.4 % and 96.9 %, respectively. As shown in Chapter 5, different LMO content can significantly affect the relative density of RT-fabricated LMO-ST (R) composites. The relative densities ranged from 84.9 % to 92.8 % as the LMO proportion was adjusted across 15, 30, 45, and 75 vol %. In the case of pure LMO and NSiO binder, two approaches, solid-state sintering for 3 h at 660 °C/950 °C and room temperature fabrication, were utilized to obtain dense pellets. As shown in Figure 9.1, increasing the consolidation temperature from RT to 660 °C slightly enhances the relative density of LMO samples, increasing from 94.5 % (RTF) to 96.9 % (sintered). In contrast, sintered NSiO (S) exhibited a significantly higher relative density of 84.2 %, representing a ~20 % overall increase in relative density compared to NSiO (R) samples prepared by RTF. However, 15 vol % NSiO- ST (R) composite samples exhibit a relatively high relative density of 82.0 %, almost resembling the density of NSiO (S). LMO (R) has a significantly higher average relative density than NSiO (R) ceramics, which was also confirmed by SEM analysis.

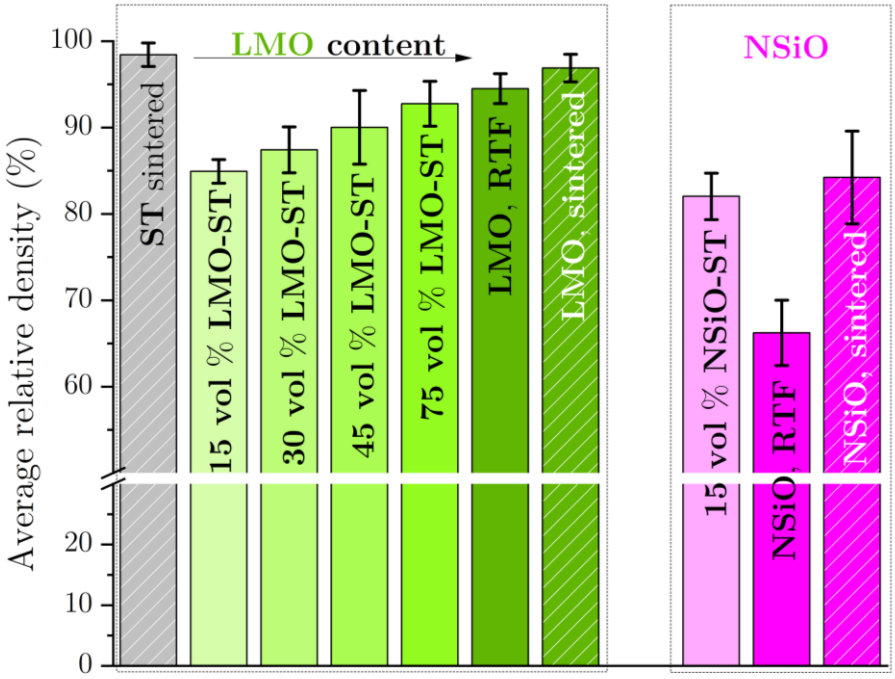


Figure 9.1: Average relative density of sintered ST, sintered and RT-fabricated binders (LMO and NSiO), and composite samples (NSiO-ST and LMO-ST). Error bars represent one standard deviation.

### 9.1.2 Microstructural analysis

Figure 9.2 represents the microstructure of polished cross-sections of RT-fabricated LMO- and NSiO-ST composites, cross-sections of RT-fabricated binders LMO and NSiO, as well as sintered ceramics (LMO, NSiO, ST). Sintered ST shows a dense microstructure with

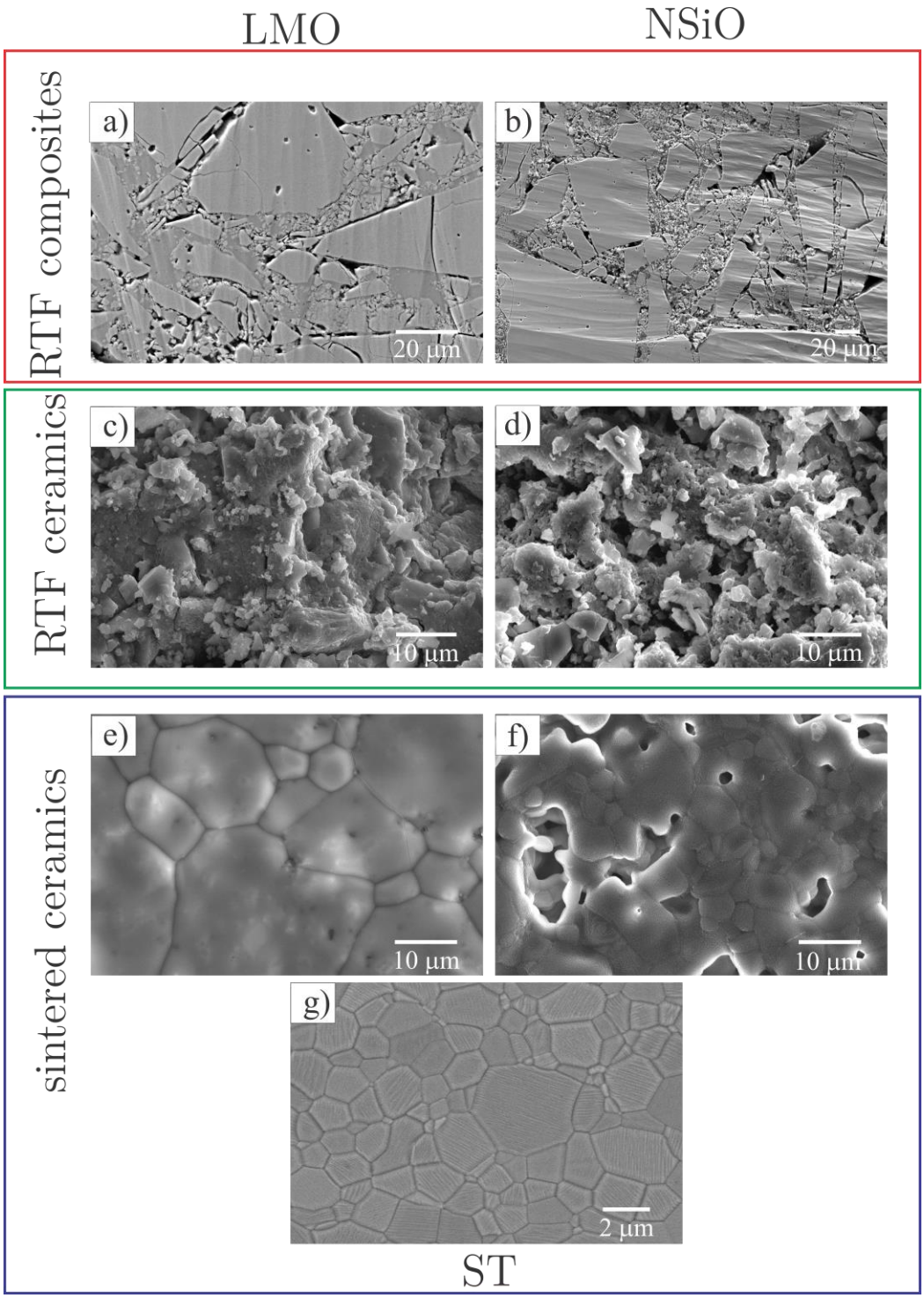


Figure 9.2: SEM micrographs of microstructures a) LMO-ST, b) NSiO-ST composites; RT- fabricated binder phases: c) surface of LMO, and d) NSiO; sintered binder phases: e) LMO, f) NSiO; and sintered g) ST ceramics.

equiaxed grains with an average size of 1.5 µm. In the case of LMO and NSiO sintered ceramics, the mean grain size is larger, being ~14 µm and ~7 µm, respectively. Larger inherent porosity was observed with NSiO samples, which may be associated with the prominent covalent character of Si-O bonds. ST-composites consisting of either LMO or

NSiO binder show homogeneous particle distribution, good contact between binder and filler particles, and residual porosity. SEM analysis of a cross-section of RT-fabricated LMO and NSiO reveals that LMO has a greater density than NSiO.

### 9.1.3 XRD analysis

The XRD analysis was conducted and described here to complement the mechanical characterization results. Figure 9.3 shows XRD patterns for single-phase materials, LMO and NSiO, along with their corresponding composite systems of ST.

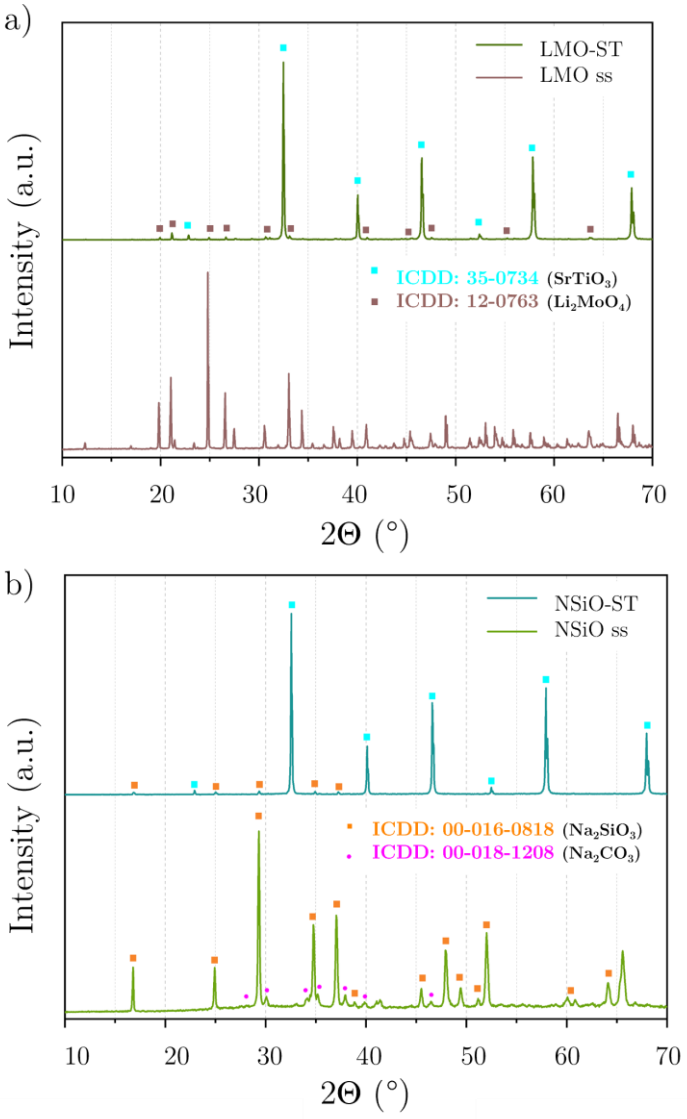


Figure 9.3: XRD spectra of a) LMO-ST composite and LMO dried from saturated solution (LMO ss); b) NSiO-ST composite and NSiO dried from saturated solution (NSiO ss).

Identification of phases was based on standard XRD patterns of the ICDD using the following patterns: 12-0763 ($Li_2MoO_4$), 16-0818 ($Na_2SiO_3$), and 18-1208 ($Na_2CO_3$). No secondary phase formation or reaction occurred during the drying process of LMO, as evidenced by the XRD pattern in Figure 9.2 a), resembling that of the standard XRD pattern of LMO. The LMO-ST composite pattern shows the standard reflections of LMO

and ST, indicating no degradation of ST or secondary phase formation. In the case of NSiO, drying from the saturated solution results in the formation of a small amount of $Na_2CO_3$. This can be seen in the XRD pattern in Figure 9.3 b), showing $Na_2CO_3$ reflections in addition to the standard reflections of NSiO.

Hence, NSiO in an aqueous solution, exposed to the ambient atmosphere partially reacts with $CO_2$. In the NSiO-ST composite pattern, reflections specific for $Na_2CO_3$ were not observed, as the amount of NSiO is much lower than that of ST, resulting in a lower intensity of NSiO reflections in comparison to pure NSiO dried from a saturated solution. Moreover, the increased background indicates the presence of an amorphous phase. In general, crystalline silicates, such as sodium metasilicate $Na_2SiO_3$, are easily soluble in water due to the ionic nature of the $Na^+$ and $(O\text{-}Si)^-$ ion pair bonds. The solubility of a substance in water is affected by the pH of the solution. In the LMO solution, the pH was experimentally measured to be 8. On the other hand, NSiO saturated solution exhibits a pH of 11. Dissolution of crystalline NSiO results in a mixture of primarily monomeric tetrahedral $(SiO_4)^{4-}$ ions; however, oligomeric linear or cyclic silicate ions and polysilicate ions are also expected. The pH value decreases after exposure of such an aqueous system to an ambient atmosphere containing $CO_2$ (424.6 ppm, February 2024, Mauna Loa Observatory) [188]. This causes spontaneous gelation due to the polycondensation of basic silicate units, which results in a firmly bonded amorphous network. A part of $Na^+$ ions that are not ionically bonded to Si-O form $Na_2CO_3$ with environmental $CO_2$ [189], [190]. The XRD pattern of the received NSiO did not show any reflections of carbonate nor a higher-intensity background. This explains the $Na_2CO_3$ reflections and the increased background detected in the dried solution. The XRD pattern of NSiO-ST shows only reflections associated with NSiO and ST, indicating no secondary phase formation (Figure 9.3 b)). The high pH of the NSiO solution did not result in any degradation of the ST phase. Retaining the initial phases of the materials without secondary phase formation is a clear advantage of the low fabrication temperature of RTF.

## 9.1.4 Cohesion analysis of ST and binders

### 9.1.4.1 Contact angle measurements

Contact angle measurements provide experimental means of predicting the wetting behavior of different materials. It is generally recognized that a good wetting of the binder phase in composite materials is required to ensure adequate spreading, adhesion, and uniform density of the composite. Previous studies reported a significant effect of the wetting properties of the binder on the mechanical properties of composite materials [191].

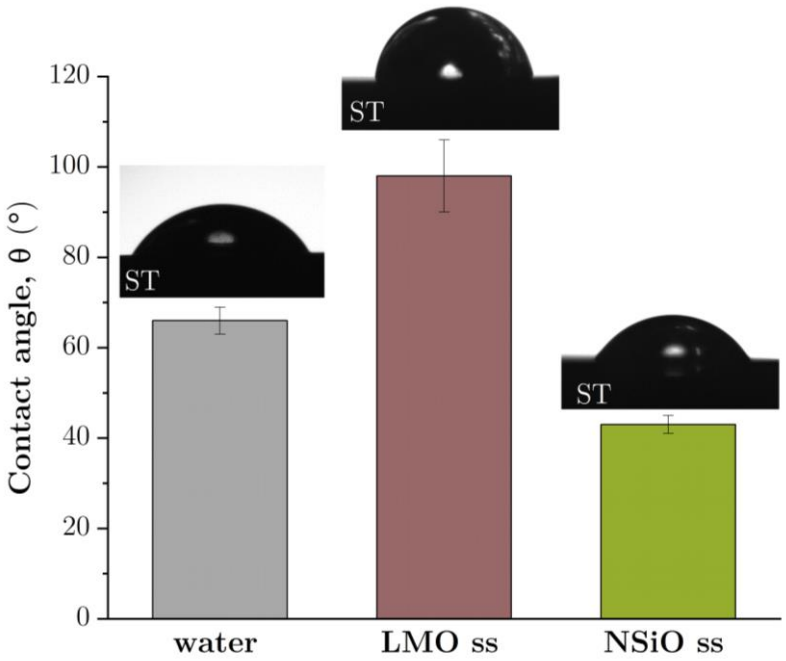


Figure 9.4: Wettability of polished ST surface with different media: deionized water, LMO saturated solution, and NSiO saturated solution.

Figure 9.4 represents the contact angle of LMO and NSiO saturated solutions compared to deionized water deposited on the ST surface. As a reference, water wets ST at an angle of ~ 65°. NSiO saturated solution exhibits a much lower contact angle of ~45°, compared to ~100° measured for LMO saturated solution with ST. The much lower contact angle of NSiO saturated solution indicates higher wettability and affinity of NSiO and ST. This results in better spreading and adhesion behavior of NSiO on ST particles, enhancing the interphase cohesion of the composite. Contact angle measurements of other binder (NMO and NWO) saturated solutions show values similar to those of LMO and are reported in Appendix (A.1).

#### 9.1.4.2 FTIR analysis

To reveal the formation of new chemical bonds between the phases during RTF, FTIR spectroscopy was performed on single-phase binders (LMO and NSiO) and the respective composite systems, i.e., LMO-ST and NSiO-ST. The IR spectra of the binders were collected after drying their saturated solutions to reveal chemical interactions arising from the drying process during RTF.

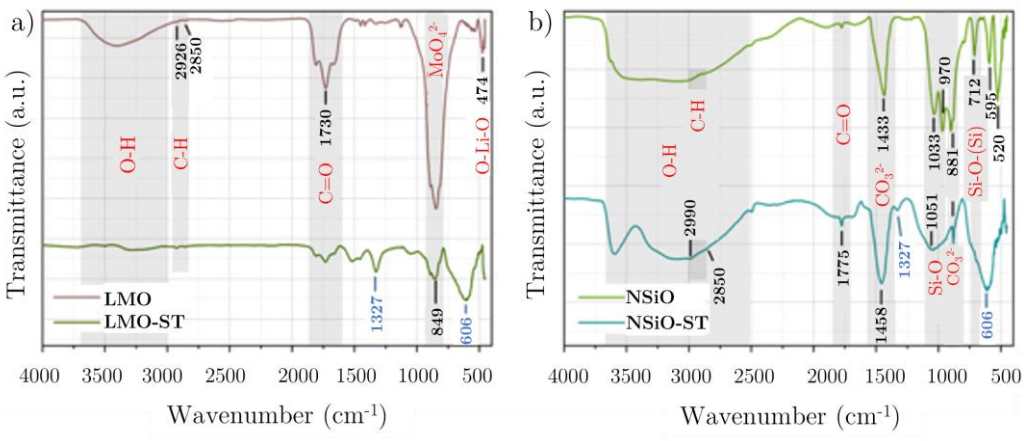


Figure 9.5: FTIR analysis of a) LMO-ST composite and LMO dried from saturated solution (LMO ss); b) NSiO-ST composite and NSiO dried from saturated solution (NSiO ss). The grey-shaded bands are common bands between the binder and the composite.

Both LMO and NSiO binders are hygroscopic. Therefore, the spectra show a broad band at 2500–3700 $cm^{-1}$, characteristic of O–H stretching mode due to adsorbed water and free surface OH group, especially in the case of NSiO-ST composites. In the IR spectrum of LMO (Figure 9.5 a)), the bands appearing at 800–900 are related to the stretching vibrations of Mo–O within $MoO_4^{2-}$ [192]–[194]. The band at 474 $cm^{-1}$ corresponds to the stretching vibration of Li–O [195]. The band at 1730 $cm^{-1}$ is characteristic of C=O stretching vibration arising from the carbonyl group [196]. This is likely associated with the formation of lithium carbonate or lithium bicarbonate species due to the reaction of LMO with atmospheric $CO_2$. The Spectrum of the LMO-ST composite represents a superposition of both spectra of LMO and ST without any additional peaks (Figure 9.5 a)). No newly formed bonds can be detected, indicating the absence of a chemical reaction between both materials. The wide band extending from 500–800 $cm^{-1}$ with a peak at 606 $cm^{-1}$ is assigned for $SrTiO_3$ stretching vibrations [179], [197]. The IR spectrum of NSiO (Figure 9.5 b) shows bands associated with $Na_2SiO_3$ and $Na_2CO_3$. The bands at 881 and 1433 $cm^{-1}$ are ascribed to $CO_3^{2-}$ bending and stretching vibrations [196]. The band at 1775 $cm^{-1}$ is due to the C=O stretching vibration [179], [196]. The sharp peaks at 712, 970, and 1033 $cm^{-1}$ are within the vibration frequency of various symmetric and asymmetric Si–O stretching and are related to the silicate phase [196], [198], [199]. The peaks at 520 and 595 $cm^{-1}$ are related to the asymmetric deformation vibration of O–Si–O [184], [200], [201]. Therefore, the FTIR analysis of NSiO agrees with the XRD measurements, confirming the presence of $Na_2SiO_3$ and the formation of $Na_2CO_3$ due to reaction with atmospheric $CO_2$. In the NSiO-ST composite, the NSiO peaks overlap with those of ST. Significant changes occurred with respect to peak broadening, specifically around 1050 $cm^{-1}$, which is a typical vibration frequency of Si–O stretching. Such broadening has been observed in previous works and is caused by a change in the phase from crystalline to a less ordered amorphous structure [196], [199]. This demonstrates the polycondensation of $(SiO_4)^{4-}$ into an amorphous network, as discussed in section 9.1.2.

### 9.1.5 Mechanical strength ST- and LMO, NSiO-ceramics and LMO-ST and NSiO-ST composites

To investigate the strength of brittle ceramics, a significant number of tested specimens must be provided to obtain a statistically reliable result. The characteristic also depends significantly on the size of the tested specimen, which is corroborated by Equation (1). This is simply solved by setting the range of standard thickness and diameter of specimens for each fixture separately. The number of tested samples of each sample type is marked with N. The state-of-the-art and the exact procedure of the ball on three balls biaxial testing (B3B) is described in sections 1.10 and 2.11. It is important to note that the B3B test results are often affected by the environment, test conditions, test rates, subcritical cracks, and other flaws.

The failure stress, $\sigma_{max,}$ for all ceramic samples was calculated using Equation (1.25) (described in section 1.10. The factor f was determined by taking the Poisson's ratio for ST (0.24), LMO(0.35), and NSiO (0.27) based on the literature [202],[203],[204]. For composite systems, the Poisson's ratio was calculated according to the mixing law (Equation (9.1)), where $\nu_c$ is the composite Poisson's ratio, $f_b$ is the volume fraction of the binder phase, $\nu_b$ and $\nu_{ST}$ are the Poisson's ratio of the binder phase and ST, respectively.

$$\nu_c = f_b \cdot \nu_b + (1 - f_b) \cdot \nu_{ST} \tag{9.1}$$

Table 9.2: Summary of characteristic mechanical strength and Weibull Modulus values for all ceramic samples.

| Sample type | ID/ label | Number of tested samples $N$ | Characteristic strength $\sigma_0$ (MPa) | Weibull Modulus, $m$ (/) |
|---|---|---|---|---|
| **ST** | **(S)** | 25 | 202 [189—215] | 6 [4—7] |
| **LMO** | **(S)** | 18 | 30 [29–32] | 9 [6–11] |
| **LMO** | **(R)** | 18 | 25 [25–26] | 13 [9-17] |
| **LMO-ST** | **(R)** | 18 | 11 [10–12] | 4 [3–5] |
| **NSiO** | **(S)** | 20 | 105 [95–115] | 5 [3-6] |
| **NSiO** | **(R)** | 9 | 42 [38–47] | 7 [4–9] |
| **NSiO-ST** | **(R)** | 18 | 77 [74–81] | 10 [6–12] |

#### 9.1.5.1 Strength distribution of ST

Weibull diagrams plotted failure stress against the probability of failure for sintered ST-ceramics, NSiO-, and LMO-binder phases (Figure 9.6). The characteristic strength, $\sigma_0$, is the failure stress at which the probability of failure is ~63 %. The best fit of the strength data was calculated according to the maximum likelihood method and is represented by a full line whose slope corresponds to the Weibull modulus, m. The failure stress values adhere to a Weibull distribution, which is linked to the defect distribution in the material. The statistical analysis of the distribution resulted in a characteristic strength of sintered ST ceramics, $\sigma_0$ of 202 [189-215] MPa and $m$= 6 [4-7], respectively. The bracketed values correspond to the 90 % confidence intervals. The mechanical strength of ST has not been investigated in the literature, but the current results fall within the anticipated strength

range of similar electroceramics (e.g., $BaTiO_3$) of comparable tested volumes [205], [206]. The Weibull modulus is relatively low, $m$=6, which implies a wide defect size distribution in the material.

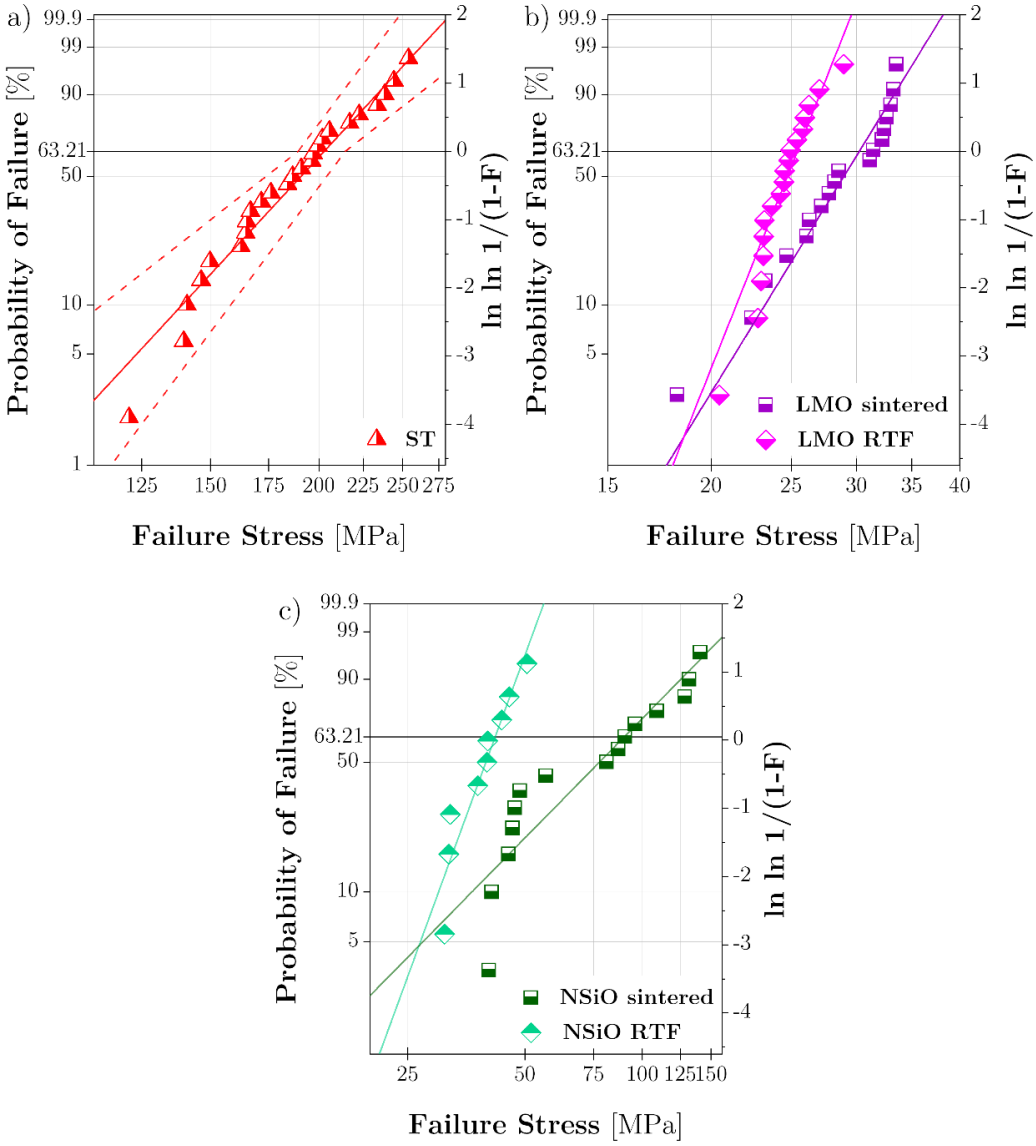


Figure 9.6: Weibull diagrams (Probability of failure as a function of Failure Stress) for a) high-temperature sintered ST-ceramics; b) LMO-ceramics sintered vs. RTF; c) NSiO-ceramics sintered vs. RTF. The solid line in all diagrams equals the best fit calculated by the maximum likelihood method, whereas the dashed lines show 90 % confidence intervals. The Weibull parameters ($\sigma_0$ and $m$) and the number of tested samples ($N$) are inserted.

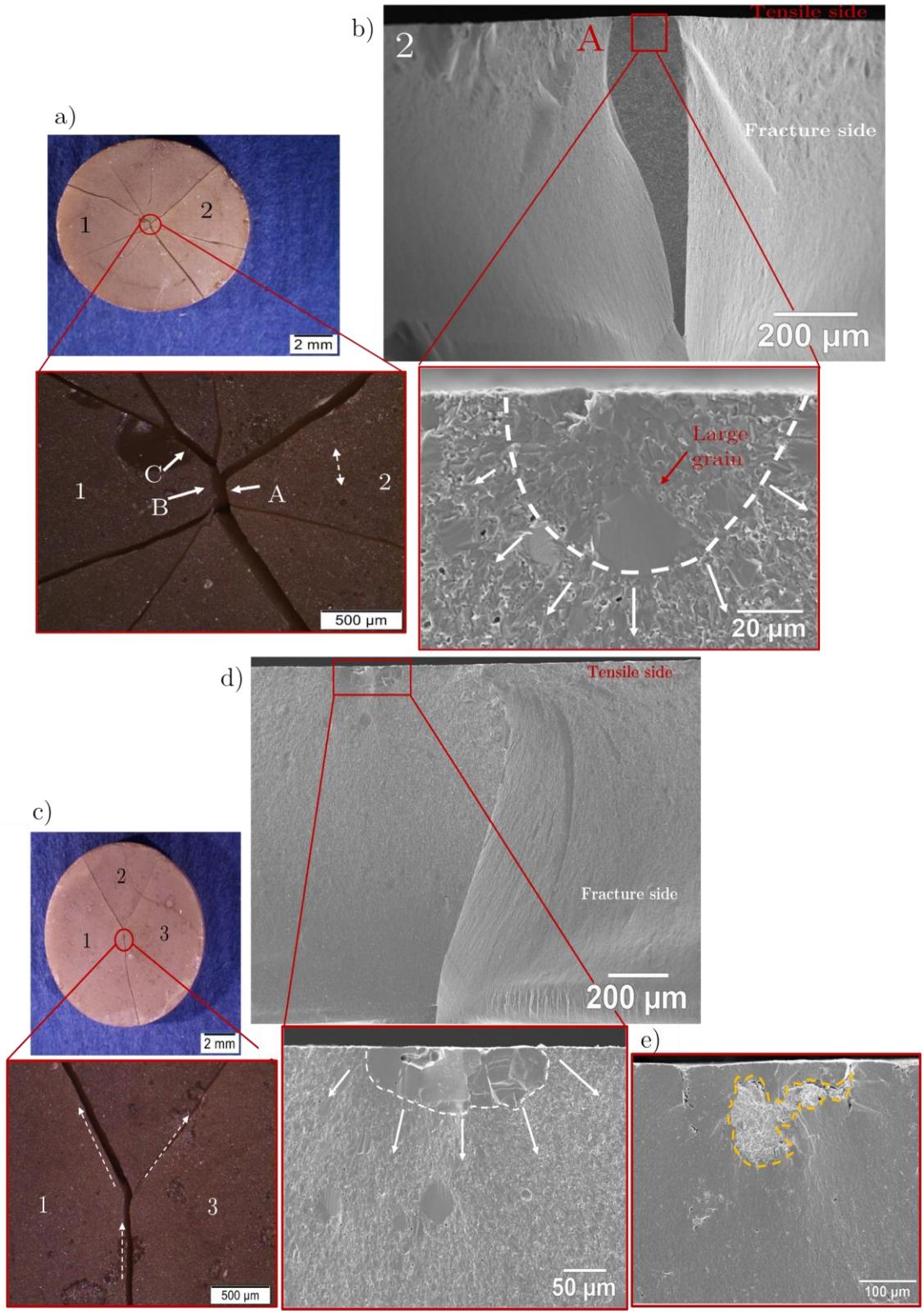


Figure 9.7: SEM images of the fracture surface of ST specimens fractured under B3B test: a) crushed sintered ST pellet, which was reassembled to identify the fracture origin, where numbers identify the fragments ordered and the direction of crack propagation; b) large grain at the surface which caused the fracture; c) crushed sintered ST pellet reassembled to identify the direction of cracks; d) large grain fracture origin (highlighted by white

dashed line). White arrows indicate hackle lines. The failure occurred at ~ 240 MPa. e) an agglomerate fracture origin (highlighted by orange dashed line) in a specimen fractured at ~140 MPa. The top surface is the tensile-loaded surface in both images.

Fractography is used to determine the fracture origins in ceramics and, to some extent, ceramic composites. In addition, it serves as a valuable tool for further explanation of the difference in the strength of samples (additional description in section 1.11). Examining the tested ceramic pellet under the optical microscope is the first step in identifying what causes the particular fracture behavior in specific samples. Next, the fractured part of the material where the fracture is thought to have started is subjected to SEM analysis to identify the microscopic flaw that caused the fracture.

In general, sintered ST ceramics are more homogeneous in microstructure and exhibit a different type of fracture origin compared to composites and binder phases. Figure 9.7 shows typical defects found at the fracture surface of the tested samples. Large grains associated with abnormal grain growth were frequently found as failure-initiating defects (Figure 9.7 b), d)). The fractured ST specimen was first reassembled after testing and analyzed by optical microscope. Figure 9.7 a), c) shows the fracture origin, where numbers identify the ordered fragments and the crack propagation direction. The fracture origins in both ST samples are identified by flaws located near the surface, a large grain, and an irregular pore, respectively. The white dashed line and arrows feature the fractured mirror, mist region, and Hackle lines. Abnormal grain growth is a well-known phenomenon in perovskite materials and has been frequently reported in the literature for ST [207]–[209]. Another type of identified strength-limiting defects in ST were agglomerates, as seen in Figure 9.7 e). A distinctive fractographic feature of agglomerates is the shell-like crack around the agglomerated region due to the differential sintering rate, causing agglomerates to sinter away from the rest of the matrix [210]. The occurrence of agglomerates may be reduced by optimizing the powder preparation process (e.g., addition of binders, granulation, etc.), yet it is out of the scope of this work.

#### 9.1.5.2 Strength distributions of LMO and NSiO binder phases

The binder phase in the RTF process serves as a medium holding the functional particles (ST in this study) together. It is anticipated that the structural integrity of upside-down composites is primarily due to the cohesion strength of the binder and filler material (ST). Consequently, the mechanical strength of two different single-phase binder phases, namely LMO and NSiO, was investigated to understand their respective impact on the overall strength of the composite materials. Figure 9.8 compares the strength distribution of LMO produced at room temperatures against high-temperature sintered LMO in a Weibull diagram. The calculated Weibull parameters are presented in Table 9.2. The average inherent strength of LMO prepared by RTF, $\sigma_0$, coincides with a value of 25 [25-26], only slightly lower than conventionally sintered LMO (i.e. 25 MPa vs 30 MPa). This difference (ca. 20 %) can be attributed to the higher porosity in LMO (R), being ~94.5 % dense compared to the ~ 97 % relative density in high-temperature LMO (S). Additionally, the LMO (R) shows a slightly higher Weibull modulus of 13 [9–17], indicating a narrower distribution of the defect sizes, likely related to the higher porosity in LMO (R). The narrow confidence interval of characteristic strength for LMO (R) suggests high sample consistency. These results show that RTF of LMO can result in samples with comparable mechanical strength as LMO (S) without the need for a firing step, which agrees with previous results showing retained functional performance in LMO (R) [211]. This has a significant advantage, as preparing LMO (R) is more energetically favorable.

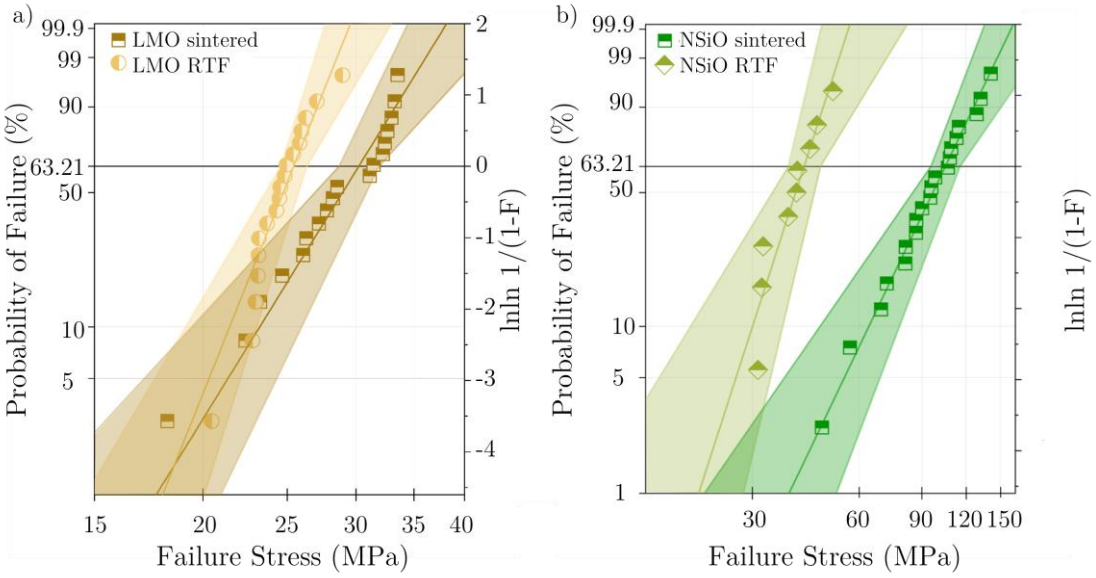


Figure 9.8: Weibull plot showing the probability of failure of a) conventionally sintered LMO vs room temperature fabricated LMO as a function of failure stress; b) conventionally sintered NSiO vs room temperature fabricated NSiO as a function of failure stress. The solid lines represent the best fit of the strength values according to the maximum likelihood method. The shaded area represents the respective 90 % confidence interval of each set.

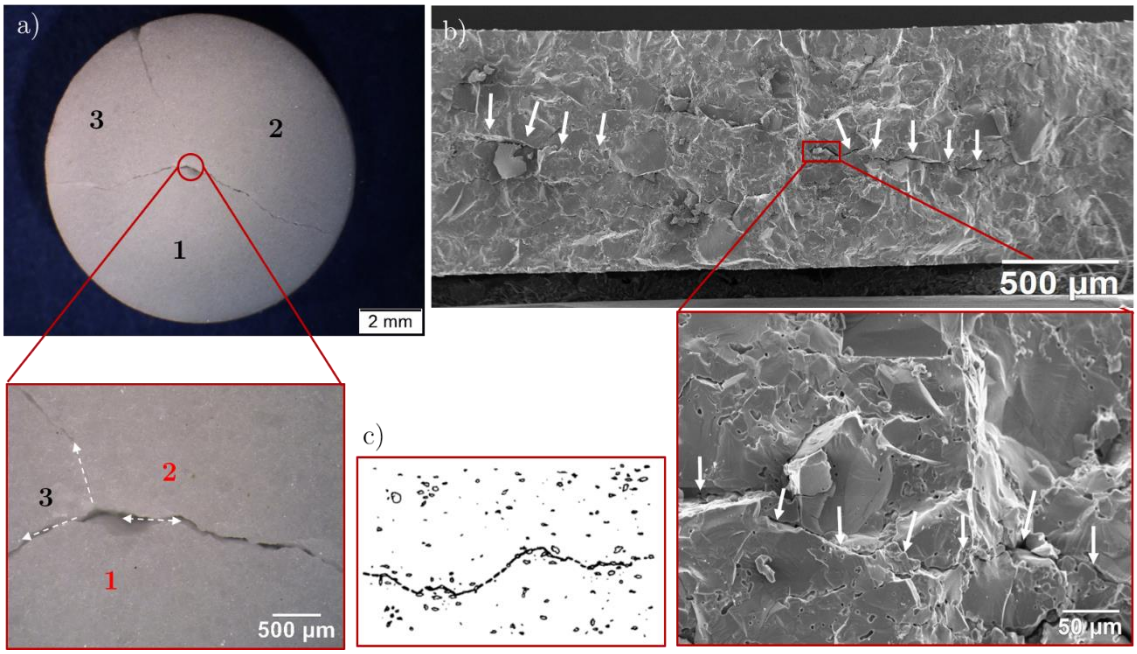


Figure 9.9: Fracture surfaces and fracture origins in the sintered LMO ceramics; a) fractured LMO (S) specimen analyzed by optical microscope, where numbers identify the fragments ordered and the direction of crack propagation; b) SEM investigation of the fracture surface of LMO (S) sample. c) The fracture origins in LMO(S) samples are identified by microcracking at the grain boundaries, highlighted by white arrows.

Figure 9.9 shows representative fracture surfaces of sintered LMO samples after testing in the B3B. In LMO (S) ceramics, so-called “microfault pockets” were observed over the whole microstructure, especially at the grain boundaries (Figure 9.9 b)), and presumably

caused the fracture. "Microfault pockets" are a collection of tiny microstructural faults attributed to microcracking (see Figure 9.9 c)) [132]. Microcracking can also originate from microporosity, which is evident from the SEM image and confirmed by relative density calculations in both LMO(S) and LMO(R) samples.

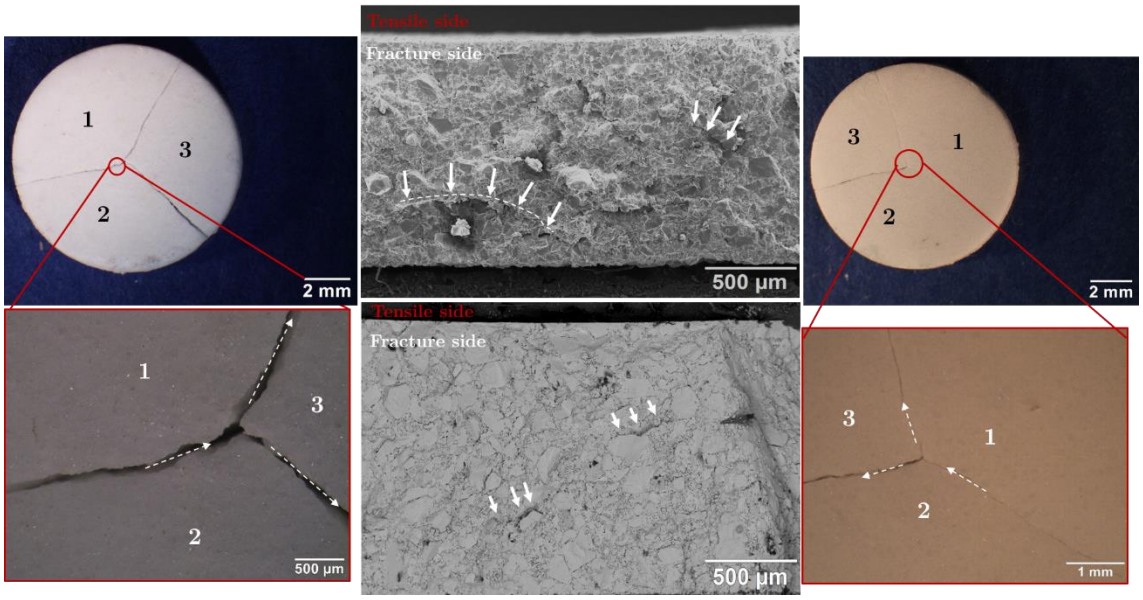


Figure 9.10: Fracture surfaces and fracture origins in the LMO ceramics prepared by RTF; a) fractured LMO (R) specimen analyzed by optical microscope, where numbers identify the fragments ordered and the direction of crack propagation; b) SEM investigation of the fracture surface of LMO (R) sample. c) The fracture origins in LMO (R) samples are identified by microcracking at the particle contacts, highlighted by white arrows.

Figure 9.8 b) shows the effect of the processing method on the mechanical strength of NSiO, represented in a Weibull diagram. The Weibull parameters are given in Table 9.2. NSiO (R) shows a 60 % lower strength than NSiO (S), i.e., $\sigma_0$~42 MPa vs $\sigma_0$~ 105 MPa. The higher strength in the latter may be linked to its relatively higher density of ~82 % compared to NSiO (R), only ~ 66 %. However, due to the large confidence interval for NSiO (S), the Weibull modulus, $m$ of 3 [2–4]) is the lowest among all. A higher Weibull modulus and a narrower probability curve of the strength distribution directly translate to higher material consistency, which means that the flaws are evenly distributed throughout the entire volume [212].

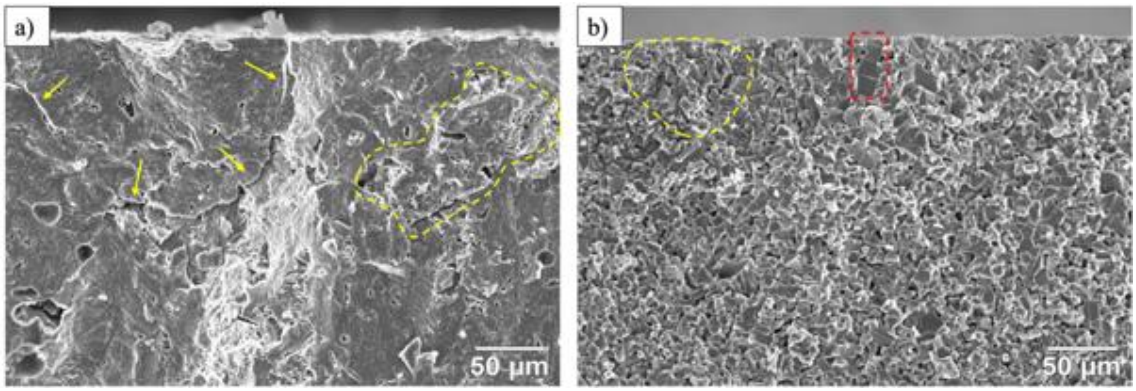


Figure 9.11: Representative fracture surface of (a) NSiO (R) and (b) NSiO (S). The yellow dashed line in (a) marks a near-surface pore network, which may be the failure-initiating defect. The yellow arrows indicate microcracking. The yellow dashed line marks a group of large grains. The top surface is the tensile-loaded side in both images.

Examples of fracture surfaces of NSiO (S) and NSiO (R) samples are shown in Figure 9.11. In NSiO (R), the fracture surface exhibits inter-agglomerate porosity and abundant cracks (Figure 9.11 a)). Hence, it's challenging to determine the precise origin of the fracture. In the case of NSiO (S), the fracture origin may be related to a pore network or group of large grains at the surface, as indicated in Figure 9.11 b). Fractography could not identify exact fracture origins due to the high porosity and weak intrinsic strength of both materials. Furthermore, NSiO (S) exhibits larger grains due to grain growth, which may act as fracture origin if located at or near the surface.

#### 9.1.5.3 Strength distribution of LMO-ST and NSiO-ST composites

A high filling ratio of the functional ceramic phase (85 vol %) in a composite system is generally preferred, as it facilitates improved electrical performance but is usually restricted due to structural integrity reasons. As mentioned, upside-down ST-based composites are defined by an inverse filling ratio, where the active (functional) ceramic phase dominates, and the binder phase represents only a minor part of the entire system. The mechanical strength results of LMO-ST and NSiO-ST are presented in this section. Also, results for characteristic strength and Weibull modulus are demonstrated in Table 9.2.

Figure 9.12 a) shows the average strength results of LMO-ST. The Weibull parameters are reported in Table 9.2. As can be seen, the strength of LMO-ST (i.e., $\sigma_0$=11 MPa) is much lower than the strength of the constituent single-phase materials, being $\sigma_0$=200 MPa and 25 MPa for conventionally sintered ST and LMO (R), respectively. Since ST particles are connected only by the LMO phase, it is expected that the load-bearing capability will be governed by the strength of the interfacial bonding between ST and the binder phase or by the strength of the binder phase. The lower strength of LMO-ST compared to LMO (R) can be attributed to (i) the higher porosity in the composite compared to the single-phase LMO (relative density of 85 % vs. 95 %), likely related to incomplete coverage of ST particles, hence resulting in reduced load distribution and bonding of ST particles; (ii) weak interfacial bonding between LMO and ST.

In correspondence with the study of dielectric properties of LMO-ST composites with varied compositions (Chapter 5), the LMO-ST composites with 15, 30, 45 vol %, and 75 vol % of LMO binder were tested mechanically.

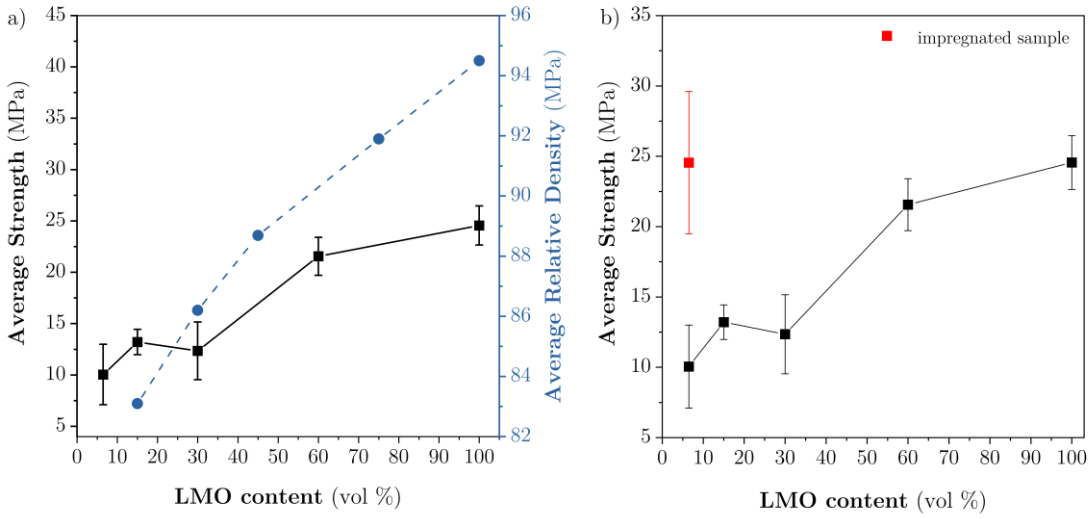


Figure 9.12: a) Average Strength and average relative density of LMO-ST composites as a function of LMO to ST proportion; b) Average strength of impregnated samples vs. Untreated LMO-ST composites.

Figure 9.12 shows the effect of increasing LMO content on the strength and density of LMO-ST. As can be seen, the density and $\sigma_0$ improve with increasing LMO content and eventually coincides with the $\sigma_0$ value for the LMO (R). The strength remains constant (between 10 MPa and 12 MPa) up to an LMO content of 30 vol %, which corresponds to relative density values below 90 % in that range. At 30 vol % LMO content, the high amount of porosity reduces the bonding area of ST particles with LMO due to incomplete coverage, which decreases the strength of the composite. Above 30 vol % LMO content, the strength increases to 22 MPa, similar to the strength value of LMO (R). The increase in the strength above a relative density of 90 %, which is the value at which the material exhibits only closed porosity, explains the lower strength of LMO-ST compared to LMO (R). At relative densities >90 %, the strength of the composite becomes less affected by the porosity and is ultimately limited by the strength of the binder phase. From these results, it can be concluded that a higher binder content can increase the strength of the composite but at the expense of reduced electrical performance. In Chapter 5, a significant effect of composition (binder-filler proportion) on the final dielectric performance of the electroceramic composites was shown. As the binder content varied from 5 to 88 vol %, the relative density ranged from 81 % to 93 %, and the relative permittivity from 75 to 42 at 1 MHz, along with dielectric losses ranging from 0.0009 to 0.0087 at 1 MHz. It was previously shown that reducing the filler content can cause up to a 60 % decrease in relative permittivity. Mechanical strength is enhanced with increased relative density at the expense of adding an LMO binder to the LMO-ST composite system. This further indicates that the mean strength of LMO-ST is mainly dominated by the weak binding (LMO) phase. In the light of comparison, three times impregnated (with TTIP, see Chapter 7), LMO-ST composites (15 vol %) were subjected to B3B biaxial testing to estimate the effect of impregnation on mechanical strength. As illustrated in Figure 9.12 b), impregnation improves characteristic strength twofold. After impregnation, LMO-ST exhibits the $\sigma_0$ of 24 [18-29], similar to the LMO values (R). Hence, it can be concluded that impregnation improves both dielectric performance and mechanical stability.

The effect of the binder phase on the strength of ST composites is shown in Figure 9.13, which compares the strength of LMO-ST and NSiO-ST. Values of Weibull modulus and

characteristic strength for both types of binder-ST composites are reported in Table 9.2. In Chapter 8, it was shown that the choice of binder can significantly impact the overall dielectric performance. Regarding mechanical stability, NSiO-ST has seven times higher strength compared to LMO-ST, i.e., 77 MPa vs 11 MPa, and and twice for the Weibull modulus (m = 10 [6–12] vs m = 4 [3–5]). As discussed above, the strength of the composite is mainly controlled by the strength of the binder phase. Therefore, the higher strength in NSiO-ST is given by the strength of single-phase NSiO (R). Interestingly, the strength of NSiO-ST exceeds that of NSiO (R), 77 vs 42 MPa. This may be related to the higher density of the composite (~20 % increase). Nevertheless, the notable higher strength of NSiO-ST compared to LMO-ST cannot be attributed only to density, as both systems show similar density values. It may be explained by the polycondensation of the NSiO saturated liquid phase, which firmly connects functional ST ceramic and binder NSiO particles. In addition, the much better wetting of NSiO aqueous phase on ST, as confirmed by contact angle measurements, results in enhanced spreading of NSiO and better coverage of the ST particles. This increases the cohesion of the composite due to uniform stress distribution across the phases. On the contrary, LMO only deposits and crystallizes locally on ST particles and hence does not effectively spread on the particles as NSiO, which may lead to more stress concentration sites. Furthermore, NSiO is known to harden concrete through geopolymerization [211], [213]. The NSiO-ST composites behave remarkably, as their strength values are almost identical to those of NSiO(S) prepared at 950°C. The Weibull modulus for NSiO-ST(R) outperformed the Weibull modulus for NSiO(S). Based on these mechanical properties results, it can be easily understood that high-temperature sintering may not always benefit fracture toughness and energy consumption. The aim is to provide a compromise between the most optimal dielectric and mechanical properties.

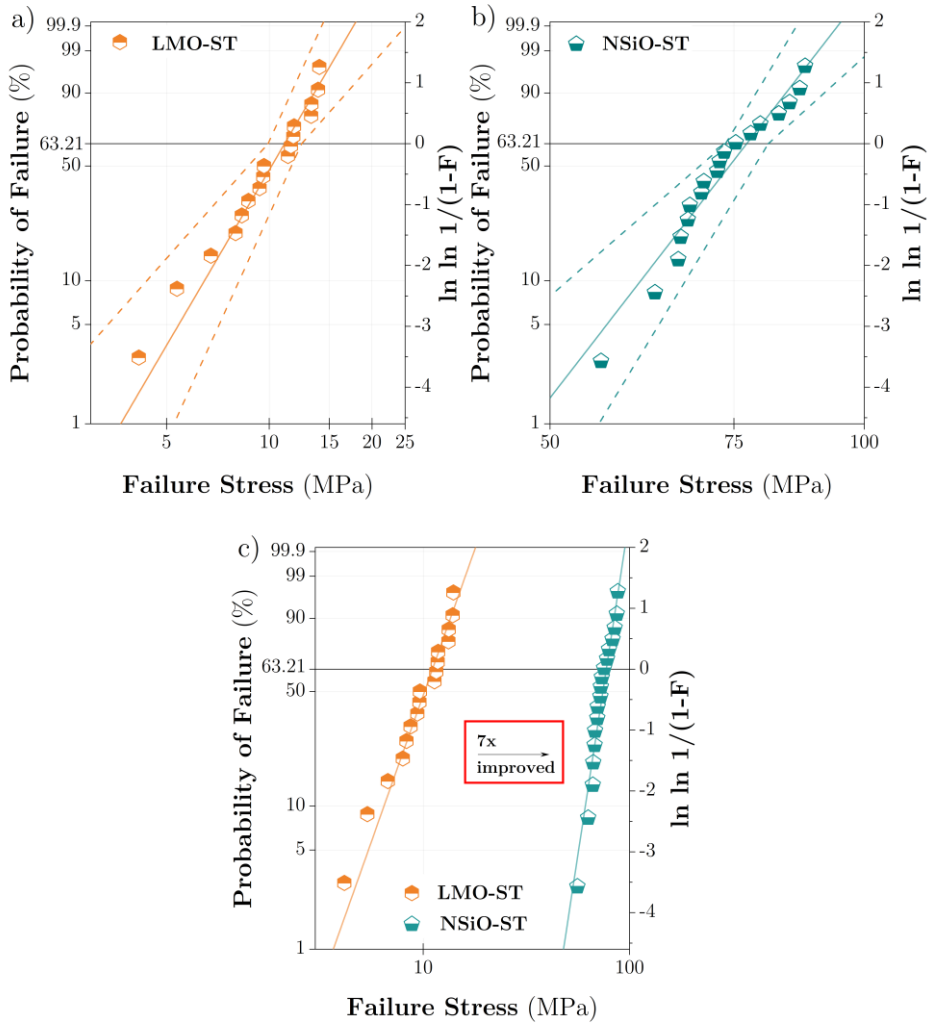


Figure 9.13: a-c) Weibull plot of failure probability vs. Failure stress for LMO-ST and NSiO-ST.

A fractographic analysis of both composite systems is shown in Figure 9.14. Exact fracture origins cannot be discerned due to the rough fracture surfaces. In both systems, fracture occurs along the ST particles through the binder phase. However, the NSiO binder in NSiO-ST seems to show stronger bonding to the ST particles, as seen from its attachment to ST particles after fracture (Figure 9.14 a)). This confirms that fracture occurred within the binder phase. In the case of LMO-ST, the separation of ST particles along the binder phase can be seen at the fracture surface. In contrast to NSiO-ST, the separation of the ST particles occurred along the interphase between ST and LMO, as can be seen in Figure 9.14 b). This is evident from the flattened morphology of the LMO particles, suggesting the location of a pre-existing ST particle and indicating weak adhesion between LMO and ST. These fractographic features may account for the higher strength of NSiO-ST compared to LMO-ST, as they are related to stronger interphase bonding in the former.

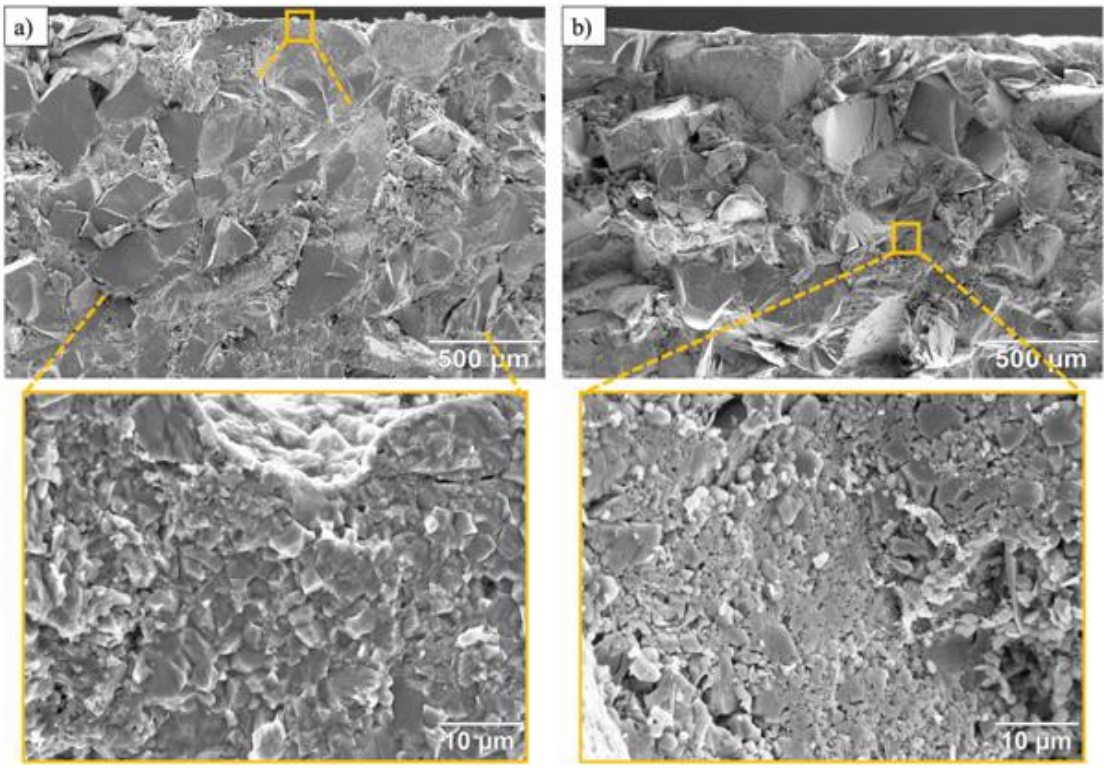


Figure 9.14: Fracture surface of (a)) NSiO-ST and (b)) LMO-ST. The yellow marked areas represent a higher magnification of the corresponding positions. The morphological difference of the binder phase between (a)) and b)) visualizes separation within the binder phase and along the interphase, respectively.

In addition, LMO(R), LMO(S), and LMO-ST(R) samples are slightly hygroscopic, and exposing samples to ambient humidity during testing can induce slow crack growth, which may occur as a consequence of water adsorption [132]. There is no intergranular cracking observed in LMO(R) and LMO-ST(R) samples (Figs. 9.10, 9.14 b)), which might be attributed to the weak bonding in such materials compared to ST(S). The force-displacement curve (reported in Appendix, Figure A.8.1) also showed untypical behavior for ceramics -"bumps," which may indicate the microcracking in LMO-ST composite when exposed to mechanical load.

## 9.2 Conclusions

In the B3B testing setup, a sample is symmetrically supported by the three-point contacts, making this method well-suited for uneven specimens, i.e., In service, ceramic components are often biaxially loaded, which additionally explains the practical applicability of the B3B test. However, the appropriate thickness of B3B testing specimens must be selected for the test to be considered valid. The breaking forces are high, and the middle loading ball can initiate contact cone cracks, which propagate to the tensile side and ultimately lead to unintended fracture [132]. In addition, for the analysis to be statistically evaluated by Weibull theory, a significant number of samples must be tested.

In this chapter, the mechanical properties of binder NSiO and LMO-filler ST composites and their corresponding single-phase ceramic materials fabricated at room temperature have been characterized for the first time. Such materials were compared with single-phase

conventionally sintered ST ($\sigma_0$ = 202 MPa). It was observed that the pure LMO prepared with RTF or sintering had comparable density (~95 % vs 97 %) and mechanical strength ($\sigma_0$ = 25 MPa vs. 30 MPa). It was shown that using NSiO as a binder in RTF composite systems increases its strength seven times compared to LMO-ST composites. On the contrary, the strength of RT-fabricated NSiO exhibited significantly lower mechanical strength than conventional sintered NSiO single-phase samples ($\sigma_0$ = 40 MPa vs. 100 MPa), which may be attributed to the low densification achieved by RTF. However, NSiO samples, both sintered and prepared by RTF, outperform the mean strength of LMO and the strength of LMO-ST composites. Additionally, it was shown that increasing the LMO content or utilizing the impregnation with TTIP can improve the mechanical strength of LMO-ST composites twofold.

The strength of the composite materials varied significantly based on the type of binder phase used. Using NSiO binder in the ST-based composite system resulted in seven times higher mechanical strength compared to LMO-ST composites ($\sigma_0$ = 77 MPa vs 11 MPa) due to the strong bonding of NSiO with ST particles. NSiO showed the formation of sodium carbonate as well as an amorphous phase due to polycondensation and further reaction to the ambient atmosphere and humidity. The saturated solution of NSiO exhibited better wettability on the polished ST surface than the LMO saturated solution. The improved wettability and partial polycondensation of monomeric tetrahedral $(SiO_4)^{4-}$ groups led to enhanced mechanical strength in the NSiO-ST composites. A lower contact angle of NSiO indicates higher surface tension, which means the surface is more reactive to other surfaces and/or ST and binder particles. In the RTF process, a saturated solution is added to a dry composite mixture to wet the surface of ST particles and, ideally, form a thin film on them. From experimental work, I found that this process is very specific for each individual binder.

Fractography analysis in this chapter provided valuable insight into the fracture behavior of ST, LMO, NSiO ceramics, and ceramics composites. ST ceramics fractured due to irregular large grains and surface defects. In addition, fracture surface analysis confirmed that LMO and LMO-ST samples fabricated by RTF are prone to internal cracking. However, comparing ceramic LMO-ST, NSiO-ST composites, and RTF-prepared LMO- and NSiO- ceramics with conventionally sintered ST, LMO-, NSiO- ceramics is challenging, as RTF materials fracture intergranularly due to the weak interface bonding. Nevertheless, according to the results, the NSiO-ST composite samples were fabricated by RTF fracture at the weak phase boundaries.

My future research will center on the new room-temperature composite systems, focusing on the synergy between optimal electrical and mechanical properties for potential benefits in electronic and energy storage applications.

# Chapter 10

# Conclusions

Obtained experimental results lead to the following conclusions.

The RTF method surpasses conventional electroceramics sintering techniques by lowering the processing temperature and reducing energy consumption. An improvement in the dielectric properties of the $Li_2MoO_4$ (LMO)-$SrTiO_3$ (ST) composites was achieved by optimizing the processing parameters. Selecting the larger ST particles (200–500 µm) and combining them with smaller ST fractions below 63 µm lead to increased relative density and improved relative permittivity. Moreover, ultrasonic treatment has positively affected the dielectric losses of the upside-down LMO-ST composites. However, the critical influence of ambient humidity on the dielectric properties has been detected and confirmed, so careful storage of samples in a desiccator or application of commercial protective coating is necessary. The effect of changing pressure and pressing time was further investigated. Increasing pressure contributes to a higher relative density of the LMO-ST composites and a lower relative permittivity resulting from the cracks generated by the strong mechanical stress. The effect of cracking was additionally confirmed with OOF2 simulations. The optimum conditions for the RTF process were set to 0.5 min of ultrasonic treatment, 5 min of pressing at 250 MPa, and a drying time of 3–6 h at 110 °C.
Next, the effect of changing the LMO-ST proportion was investigated. I showed that increasing the fraction of the LMO binder in the LMO-ST composites results in a higher relative density and lower relative permittivity. It was shown that the relative permittivity of LMO-ST composites is almost frequency-independent, below 1 MHz for the whole compositional range, which is highly desired for many microelectronic applications. Experimentally measured relative permittivity values were further compared with the calculated data using rules of mixtures. The Lichtenecker rule, reformulated for a three-phase composite system, showed the best agreement with the experimental data. Based on calculations, the negative influence of porosity was confirmed. This was further studied with OOF simulations. Impregnation was used as a post-treatment step that can positively affect the overall densification by approximately 1 % per impregnation cycle. TTIP was successfully used as an impregnating agent and showed an increase in relative permittivity (at 1 MHz) of 43 % after three cycles. However, this causes slightly increased dielectric losses, presumably due to the OH groups and the remaining bound water. It is essential to know that the impregnating agent can be substituted if it further improves density and dielectric properties. Despite the water vapor treatment (hydrolysis step) of the three times impregnated LMO-ST samples, they remained undamaged and stable after the impregnation process. Furthermore, after performing mechanical characterization, this was confirmed as the characteristic strength doubled. Impregnating RT-fabricated pellets with

TTIP can be easily performed on multiple samples simultaneously, providing a viable advantage.

Although impregnation has proven to be a partially successful method for compensating porosity, there are still many research opportunities in this area of RTF. For instance, if we look back to the processing steps, using vacuum-assisted pressing coupled with increased pressure and sonification could further optimize the densification process, as shown for LMO-BST and LMO-PZT by Smith et al. [174]. Therefore, it is important to reduce the remaining porosity in future experiments.

Object-oriented finite element modeling (OOF2) not only complemented the experimental data but also enabled the study and prediction of the effect of the coating media and its thickness, as well as simulate the change in relative permittivity when the highly conductive phase is added to a binder-ST system. It was also shown that low-$\varepsilon_r$ phase surrounding ST ceramics particles reduces overall polarization through the composite. Hence, direct ST-ST contacts are desired to enable higher dielectric performance.

LMO binder was successfully substituted with $Na_2MoO_4$ (NMO), $Na_2WO_4$ (NWO), $Na_2SiO_3$ (NSiO), and $MgSO_4$ (MSO). The use of various binder-ST systems resulted in relative density ($\rho$=83-88%) and enabled a wide dielectric property range, i.e., $\varepsilon_r$ from 68 to 124 at 1 MHz and between 67 and 129 in the MW frequency range. The dielectric losses exhibited a range of 0.0029 and 0.0142 at 1 MHz, corresponding $Q_u \times f$ values between 689 and 1335 GHz. Results on various binders presented in the thesis are expected to expand the general understanding of the densification RTF mechanism and broaden the applicability of such ceramic composites.

The strength of the composite materials varied significantly based on the type of binder phase used. Using NSiO binder in the ST-based composite system resulted in seven times higher mechanical strength compared to LMO-ST composites ($\sigma_0$ = 77 MPa vs 11 MPa) due to the strong bonding of NSiO with ST particles. NSiO showed the formation of sodium carbonate as well as an amorphous phase due to polycondensation and further reaction to the ambient atmosphere and humidity. The saturated solution of NSiO exhibited better wettability on the polished ST surface than the LMO saturated solution. The improved wettability and polycondensation reaction mechanism led to enhanced mechanical strength in the NSiO-ST composites. I assumed the relation between wetting and surface tension as that: the lower the contact angle, the higher the surface tension on the ST surface, which makes it more reactive towards other ST and binder particles. However, additional research in the field of surface and interfacial energies is required. Understanding how the effects of composite densification and its mechanical properties can lead to the engineering of novel binder-ceramic composite systems. So far, there have been limited studies on the mechanical properties of composites, making the findings from this doctoral thesis significant. The knowledge gained can be used to enhance the functional properties of future RTF ceramic composites.

In this thesis, I studied various aspects and challenges of the room temperature fabrication (RTF) method, which enables the production of functional electronic components with a wide range of properties. Each new binder-filler composite system opens up a new set of unsolved questions, which can undoubtedly be approached more easily based on the knowledge I have acquired through my studies. In future research, the relation between wetting, surface energy, functionalization of ceramics, and bonding in composites should be a priority. Understanding these factors could enhance the functionality and increase the applicability of electroceramic materials produced with RTF in the electronic industry.

# Appendix

# Additional Information for the Experimental Results

## A.1 Wetting Angle Studies

The interaction of the liquid solvent (LMO saturated solution and water) and the ST ceramic surface, under different conditions, was further inspected. A measuring setup for wetting angle studies is shown in Figure A.1. Table A.1. shows the results of the contact angle of distilled water ($dH_2O$) and LMO saturated solution deposited on polished ST surfaces that were treated in three different ways ( exposed to 100 % humidity overnight, left 1 day at ambient temperature and humidity, dried for 1 h at 110 °C)

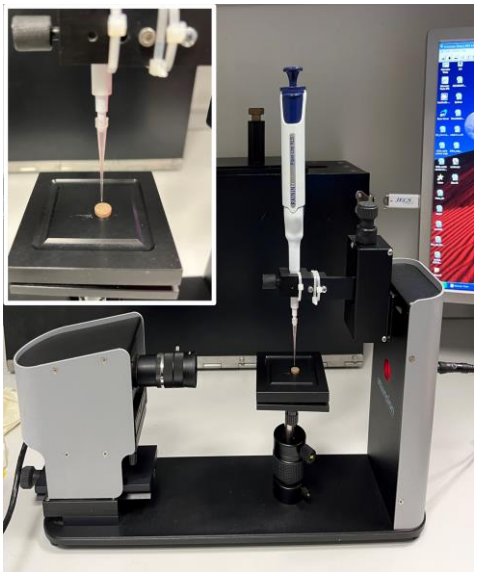

Figure A.1: Surface wettability was investigated using a contact angle meter, Theta Lite (Biolin Scientific, Gothenburg, Sweden).

Table A.1: Wetting angle studies: Water and LMO-saturated solution were deposited on the polished ST surface, which was exposed to three different conditions (100 % RH, ambient RH, drying at 110 °C).

| **Sample surface** | **Contact angle, θ(°)** | | **Images of contact angle** | |
|---|---|---|---|---|
| **ST** | **LMO** saturated solution | **$dH_2O$** | **LMO** saturated solution | **$dH_2O$** |
| **ST** exposed to **100 % humidity** overnight | 100 | 85 | 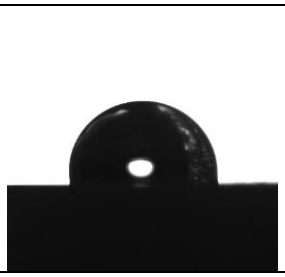 | 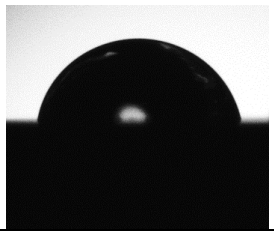 |
| **ST** left 1 day at **ambient T** and **humidity** | 96 | 71 | 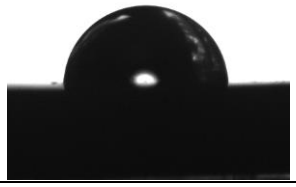 | 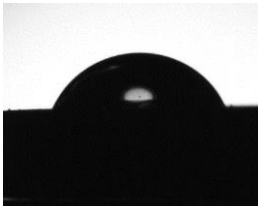 |
| **ST dried** for 1h at 110°C | 90 | 67 | 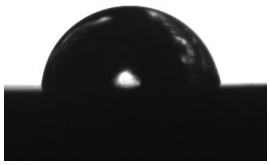 | 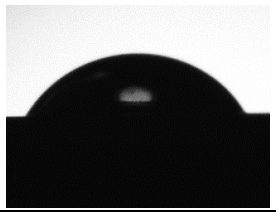 |

Table A.2: NMO, NWO, and NSiO saturated solution deposited on the polished ST surface, which was dried at 110 °C.

| Sample surface | Contact angle, θ (°) | | |
|---|---|---|---|
| **ST** | **NMO** saturated solution | **NWO** saturated solution | **NSiO** saturated solution |
| **ST dried** for 1h at 110 °C | 90 | 87 | 43 |
| Images of contact angle | 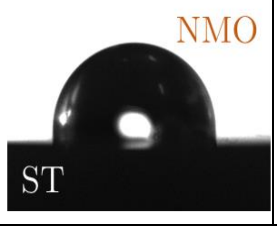 | 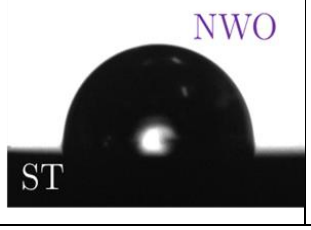 | 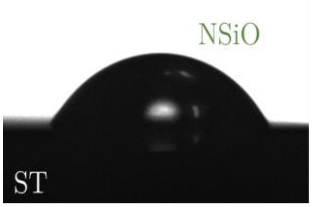 |

In the case of ST surfaces exposed to 100 % humidity or ambient humidity, the contact angle was larger compared to the one at the dried ST surface. Surprisingly, I observed from the results that a layer of physically adsorbed water on the ST surface increases its hydrophobicity.

As depicted in Table A.2, the NSiO-saturated solution shows the best wetting properties among all binder-saturated solutions. NMO and NWO exhibit values similar to those of an LMO-saturated solution. This further complements wetting studies and mechanical characterization of binder-ST samples, shown in Chapter 9. Here, all ST surfaces were dried for 1 h at 110°C prior to wetting angle studies.

## A.2 Crystallization of LMO

The crystallization process of the LMO aqueous solution deposited on the surface of the sintered ST pellet was examined through XRD analysis. The XRD spectra were compared to the standard spectra for LMO and ST (the pink dotted symbol represents LMO, and the black dotted symbol represents ST). The results presented in Figure A.2 show that drying the sample in an oven at 110 °C, as opposed to slow drying in a desiccator, resulted in more pronounced reflections of LMO that were also higher in intensity. Slow drying of LMO-saturated solution leads to oriented (preferential) crystal growth, while equiaxed crystals from the saturated solution during fast drying. These results might explain slightly higher density when samples are heated to 110 °C. The sample, dried in a desiccator, shows broader reflections due to the lower crystallinity of LMO on the ST surface. This presumably appeared because of the incomplete removal of water at RT in the LMO film.

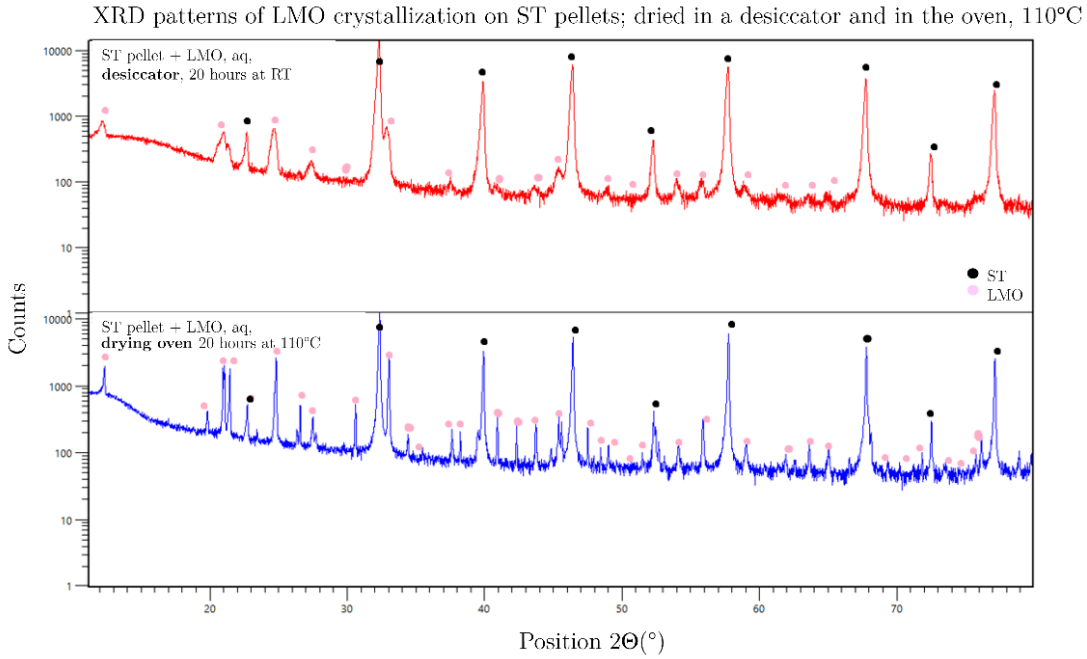


Figure A.2: XRD spectra of the thin film of LMO that crystallized from the aqueous solution deposited on ST pellet when it was dried in a desiccator for 20 h, RT (top), or in a drying oven for 20 h, 110°C (bottom).

## A.3 TEM Analysis of the LMO-ST Sample

Prof. Dr. Nina Daneu conducted a TEM analysis of LMO-ST samples using Jeol JEM-2100 (JED 2300 EDS, GATAN CCD Orious camera). Our goal was to observe the interaction between LMO and ST phases and confirm the presence of a possible preferential orientation of LMO on ST.

We observed that ST particles have higher hardness, while LMO is much softer. Both phases are crystalline, and there is no epitaxial relationship (Figure A.3 b) SAED). A very tight contact between ST and LMO (Figure A.3 c), d); Figure A.4 a), b)). ST is embedded into the LMO phase, as was previously observed with SEM. Complementary to SEM imaging, EDS analyses confirmed the presence of ST and LMO (Figure A.3 e)). Many dislocations were observed in ST, which appeared due to the crushing of ST particles prior to RTF. (Figure A.4).

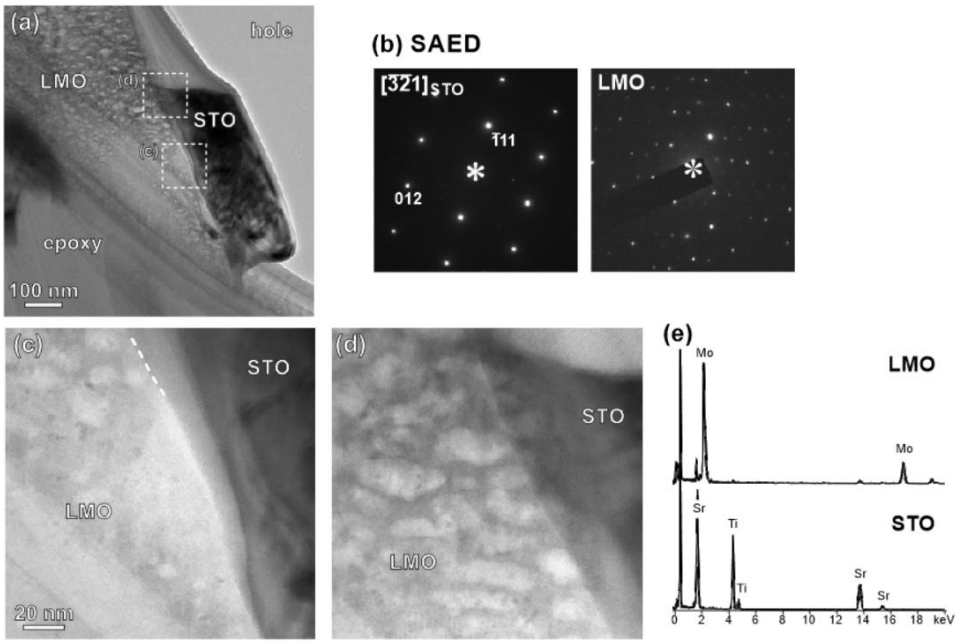


Figure A.3: TEM analysis of LMO-ST composite: a) thicker ST particles with higher hardness and thinner LMO phase; b) crystallinic nature of both phases (SAED); c), d) a tight contact between ST and LMO; ST embedded in LMO; e) EDS analyses of ST and LMO.

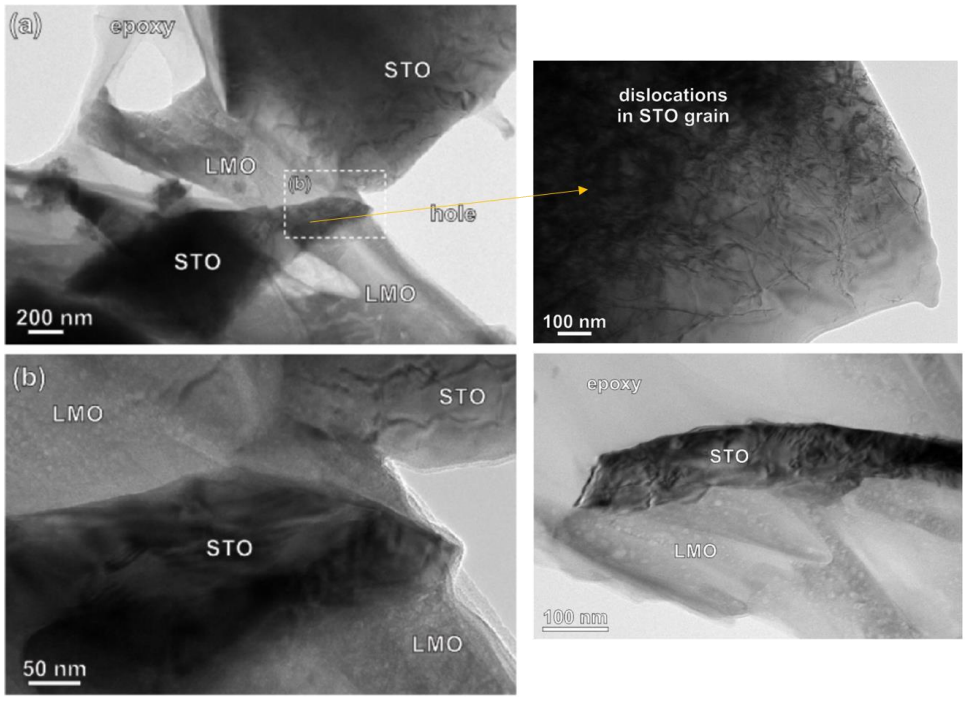


Figure A.4: TEM analysis of LMO-ST composite: a), b) the interface between LMO and ST phases; dislocations in ST particles.

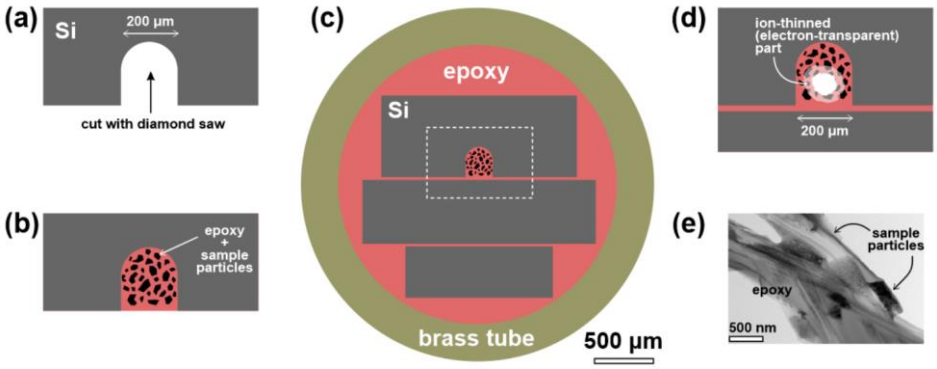


Figure A.5: TEM sample preparation; a) crushing of LMO-ST pellet; b) mixed with epoxy; c) cut into the Si-substrate; d) Ar ion-thinning; e) TEM image.

However, due to the nature of the LMO-ST composite sample, TEM sample preparation (Figure A.5) was very challenging. We first crushed the LMO-ST sample and inserted the powder mixture into a cut on the Si substrate. We embedded the particles in epoxy resin inside the cut. In the final stage of preparation, we did Ar ion-thinning to achieve electron transparency. Other binder-ST samples have not yet been analyzed with TEM.

## A.4 Heat-assisted Pressing of Binder-ST Composites

Table A.3 presents the dielectric properties and relative density values of binder-ST composites prepared by heat-assisted (HA-) pressing at 110 °C.

Table A.3: Relative density and dielectric properties of heat-assisted pressed binder-ST composites.

| Filler | | ST | | | | |
|---|---|---|---|---|---|---|
| Binders | | $Li_2MoO_4$ | $Na_2MoO_4$ | $Na_2WO_4$ | $Na_2SiO_3$ | $MgSO_4$ |
| relative density($\rho$) | % | 89 | 87 | 83 | 84 | 83 |
| relative permittivity($\varepsilon_r$) | 1 MHz | 88 | 90 | 89 | 134 | 72 |
| dielectric losses($tan\ \delta$) | | 0.0032 | 0.0132 | 0.0137 | 0.0048 | 0.0023 |

Table A.4: Comparison of RTF vs. HA-pressing applied on $MgSO_4$-ST composites (Relative density and dielectric properties; measured in radio-frequency range at 1 MHz).

| MSO - ST | temperature (T) | relative density ($\rho$) | relative permittivity ($\varepsilon_r$) | dielectric losses (tan $\delta$) |
|---|---|---|---|---|
| | (°C) | (%) | | |
| RTF | RT + 110 | 82 | 120 | 0.0029 |
| HA-pressing | 110 | 83 | 101 | 0.0026 |
| | 130 | 84 | 74 | 0.0028 |
| | 300 | 86 | 72 | 0.0026 |

As expected, HA-pressing of the binder-ST composites resulted in slightly improved relative density in the case of LMO and NMO samples (83%< $\rho_{LMO}$ <89%; 82%< $\rho_{NMO}$ <87%). The highest increase in relative density occurred following the HA-pressing of LMO-ST composites. Furthermore, HA-pressing contributed to a subsequent rise in the relative permittivity of most binder-ST composites (Table A.3). However, the relative permittivity of MSO-ST hot-pressed composites decreases with temperature, as is shown in Table A.4. This might be attributed to the decrease in MSO salt polarizability with increasing temperature [214]. The difference in $\varepsilon_r$ of MSO-ST either pressed 5min at RT and additionally dried for 6 h at 110°C or HA-pressed at 110°C for 30 min is around 20 %, which can be further explained by the fact that bound water increases overall relative permittivity and is released at higher temperatures. The temperature of HA-pressing of MSO was adjusted according to the TG-MS spectra. Since a significant mass loss was detected when heating to 300°C, the same conditions were set for preparing MSO-ST samples intended for electrical characterization. In addition, the local temperatures applied to the sample mixture may be higher since the thermocouple regulates the pressing temperature. This makes the process more consistent and accurate than heating samples in a drying oven at the same temperature. However, HA-pressing for 30 min at an elevated temperature of 110 °C still represents a less favorable production method for energy consumption than cold pressing and drying at room temperature (RTF).

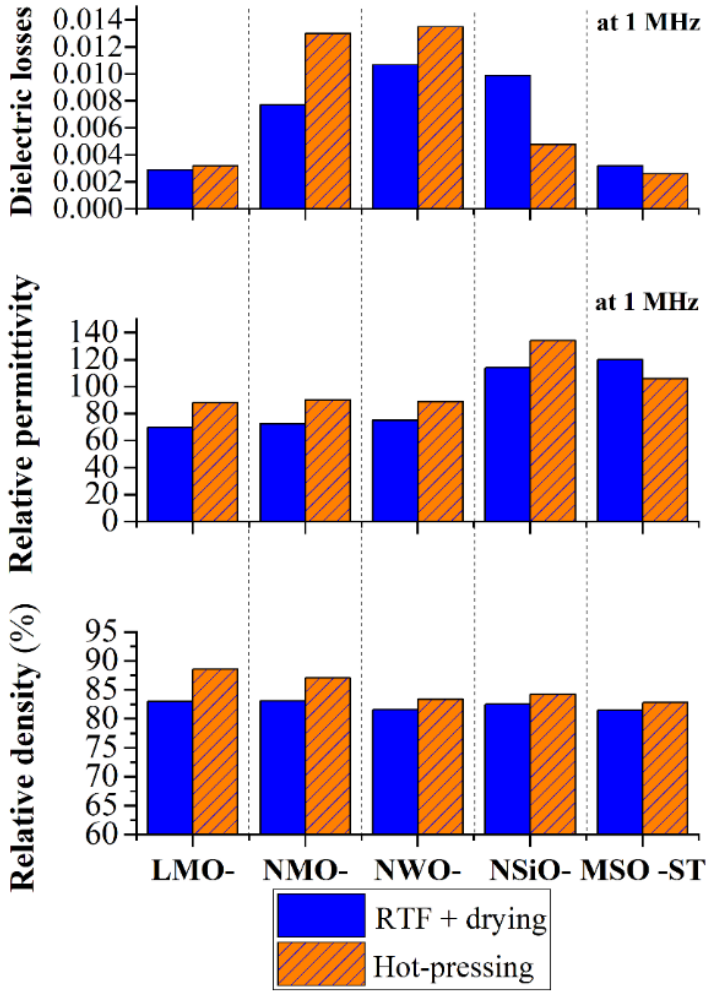


Figure 11.6: Relative density and dielectric properties for all binder-ST composites prepared by RTF + drying or HA-pressing.

Relevant data are presented in Figure A.6. to provide a brief overview and comparison of the relative density and dielectric properties of various binder-ST composites. Below is a more comprehensive depiction of the results and corresponding discussion.

This was supported by temperature-dependent measurements of dielectric properties of MSO-ST samples at 1MHz. Figure A.7 shows the change in relative permittivity and dielectric losses as the temperature was varied from RT to 150 °C and frequency was constant at 1 MHz. As a result, the $\varepsilon_r$ of the MSO-ST composite ranged from 130 to 102 at the temperature from 25 °C to 150 °C. Increasing the temperature leads to the removal of the free and bound water. However, an increase of tan $\delta$ from 0.0019 to 0.0034 was observed due to the temperature rise. The relative density of MSO-ST composites increased with increasing pressing temperature (82.8 %$<\rho<$85.9 %, 110°C$<$T$<$300 °C). This can be attributed to the dehydration of bound water, which was compensated by maintaining the pressure constant at 250 MPa. Dielectric losses of HA-pressed MSO-ST samples are increasing with temperature.

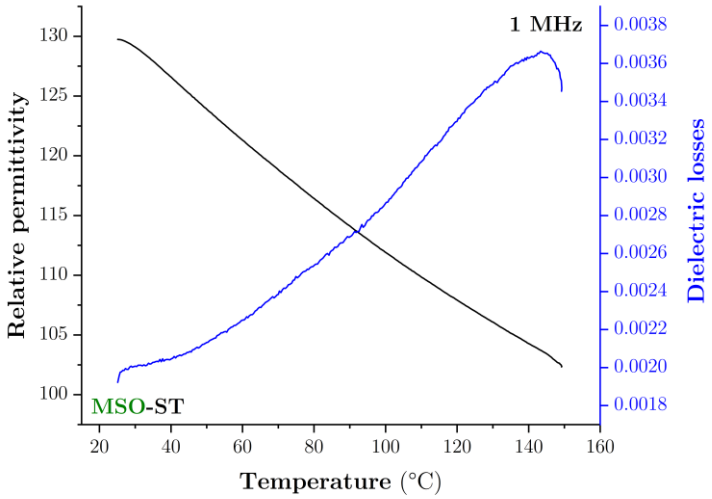


Figure 11.7: Temperature dependence of relative permittivity and dielectric losses for a 15 vol % MSO-ST composite. The frequency during measurement was set at 1MHz.

Presumably, HA-pressing could facilitate the removal of additional free water, which might otherwise be retained within the closed pores when the MSO-ST sample is pressed at RT and subsequently dried at 110 °C for 6 h.

## A.5 Microwave measurements and fitting of TCF

### A.5.1 Calculation of unloaded Q from loaded Q for all binder-ST composites

Unloaded $Q$ was calculated from the loaded $Q$ multiplied by the multiplication factor, which was precisely calculated from the $d$ values obtained from Smith charts represented in Figure A.8 for each binder-ST composition. $d$ values, which usually range between $0.1<d<1$, are displayed in Table A.5.

Table A.5: Parameters to calculate $Q_u$ from the measured $f$.

| Composite sample type | $d$ (units) | Coupling factor, β | Multiplication factor (1+β) |
|---|---|---|---|
| LMO-ST | 0.904 | 0.825 | 1.825 |
| NMO-ST | 0.820 | 0.695 | 1.695 |
| NWO-ST | 0.868 | 0.767 | 1.767 |
| NSiO-ST | 0.926 | 0.862 | 1.862 |
| MSO-ST | 0.76 | 0.613 | 1.613 |

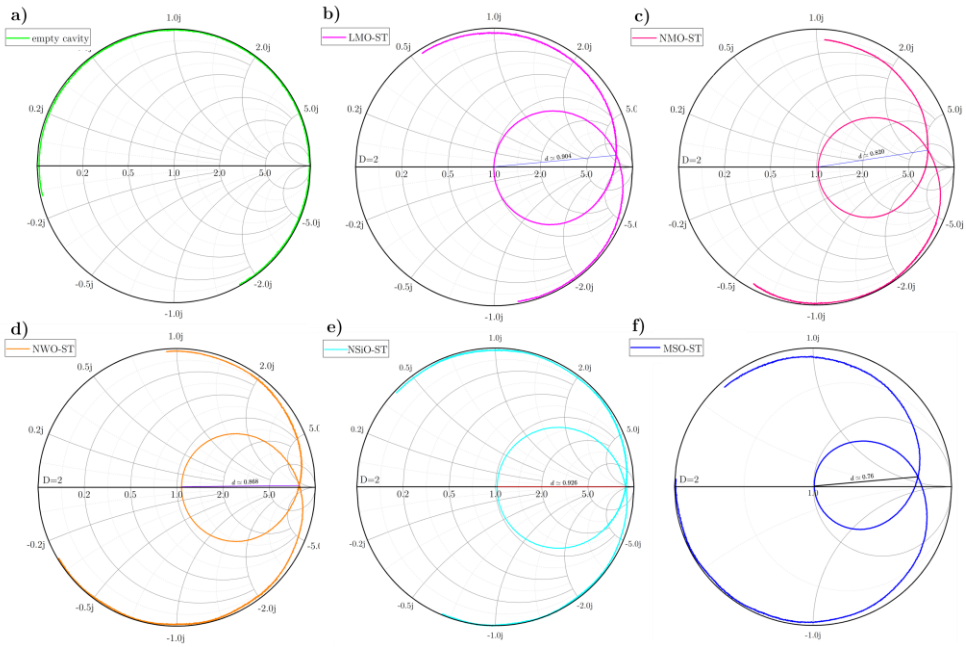


Figure A.8: Polar Smith charts for composite binder-ST samples: a)empty cavity; b) LMO-ST; c) NMO-ST; d) NWO-ST; e) NSiO-ST; f) MSO-ST with the corresponding parameters marked.

### A.5.2 Comparative analysis of the Krupka Method and ErCalc program relative permittivity calculations in the microwave range

The relative permittivity values for all binder-ST composites in the MW range were calculated using two different approaches (Krupka [15] and ErCalc [187]) based on the experimental values for the resonant frequency, dimension of the sample pellet, and cavity features. Results are presented in Figure A.9. It is important to mention that the ErCalc program could not compute for all samples, especially with the NSiO-ST composite sample type. Relative permeability values calculated by ErCalc are reported to have a typical error of ~ +15 % [187]. From the results shown in Figure A.9, it can be seen that both methods gave similar values of $\varepsilon r$ in all binder-ST composite mixtures, except for NSiO-ST, where comparison was not possible.

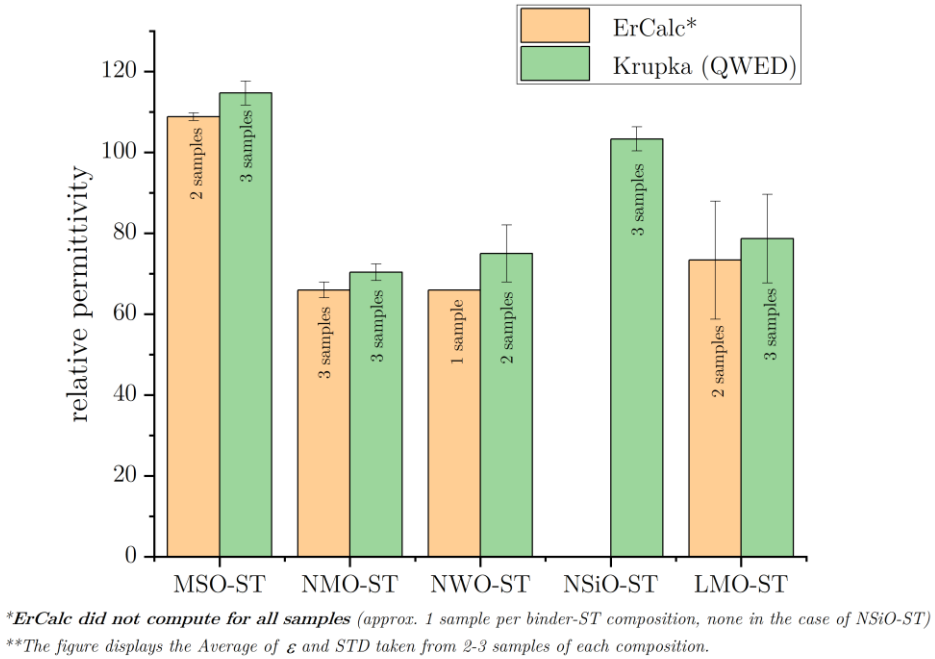


Figure A.9: Comparison between relative permittivity values calculated by the Krupka method and ErCalc program.

### A.5.3 Fitting the TCF values using different calculation methods

Here, I present various fitting methods that can be used to calculate TCF factors from measured temperature and frequency values.
As previously mentioned, the temperature coefficient of resonant frequency for all binder-ST composites was experimentally obtained by measuring a frequency change between 27.5°C and 65°C, with a step of 10°C. The measured data were originally fitted by using Method 1(earlier represented in Equation 8.1):

$$TCF\ (\tau_f) = \frac{1}{f_{27.5}} \cdot \frac{\Delta f}{\Delta T} = \frac{1}{f_{27.5}} \cdot \frac{f_{65} - f_{27.5}}{65°C - 27.5°C} \tag{A.1}$$

For comparison, I conducted fitting according to the previous work by Li, et al. [215] (Method 2).

$$TCF\ (\tau_f) = \frac{(f_{27.5} + f_{65})}{2} \cdot \frac{\Delta f}{\Delta T} = \frac{(f_{27.5} + f_{65})}{2} \cdot \frac{f_{65} - f_{27.5}}{65°C - 27.5°C} \tag{A.2}$$

In both methods, only the start and end values of the temperature range were used, and the $\Delta f$ was calculated accordingly. The only difference between methods 1 and 2 is that $\Delta f$ is taken over the whole temperature range instead of f at 27.5°C. The Comparison of both fitting methods is represented in Figure A.10.

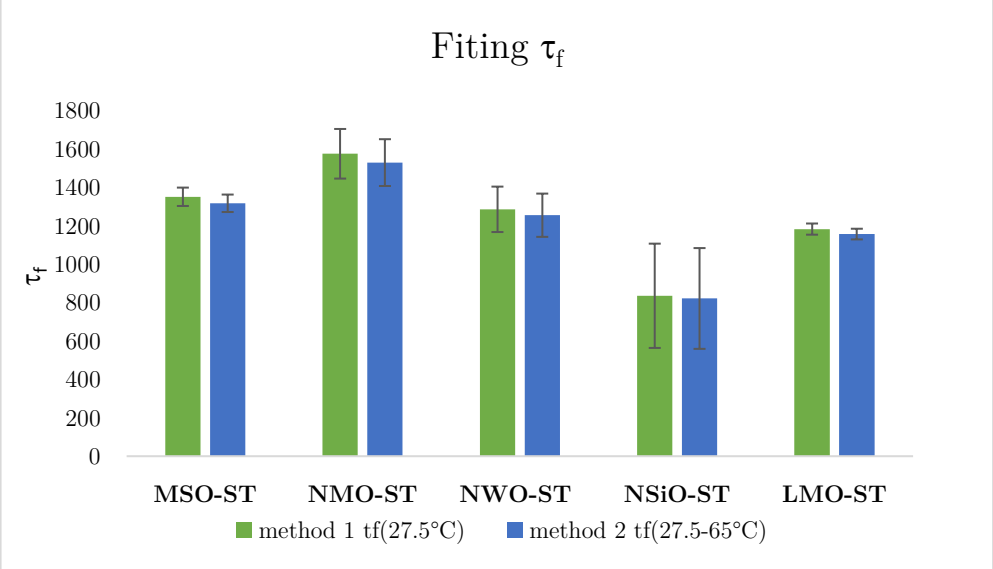


Figure A.10: Average f values calculated by methods 1 and 2 for all binder-ST compositions. Error bars are represented for 3 parallel samples of each composition.

In the method 3, resonant frequency values were fitted to the Equation (A.3) with the least square regression method. The fitting was performed using the Excel LINEST function. The values of $\tau_f$ were calculated using Equation (A.5) with the parameters $k$ and $f_0$ acquired from the fit.

$$f(\mathrm{T}) = k \cdot \mathrm{T} + f_0 \tag{A.3}$$

$$k = \frac{\partial f}{\partial T} \tag{A.4}$$

$$\tau_f(\mathrm{T}) = \frac{k}{k \cdot T + f_0} \tag{A.5}$$

Lastly, I used a similar approach by fitting the measured data to a quadratic equation (Equation A.6, method 4) and using Equation (A.8) for the $f_0$ vs $T$ results based on the procedure explained by Li *et al.*[215]. The benefit of the methods 3 and 4 is that the $\tau_f$ can be calculated at any temperature within the experimental range.

$$f_0 = aT^2 + bT + c \tag{A.6}$$

$$\frac{df_0}{dT} = 2aT + b \tag{A.7}$$

$$TCF\ (\tau_f) = \frac{1}{f_0}(2aT + b) = \frac{2aT + b}{aT^2 + bT + c} \tag{A.8}$$

As suggested in the paper by Li et al., the minimum T should be taken below the room temperature to ensure good fitting, which, unfortunately, our measuring setup does not allow for. The comparison between method 3 and method 4 is presented in the Figure A.9.

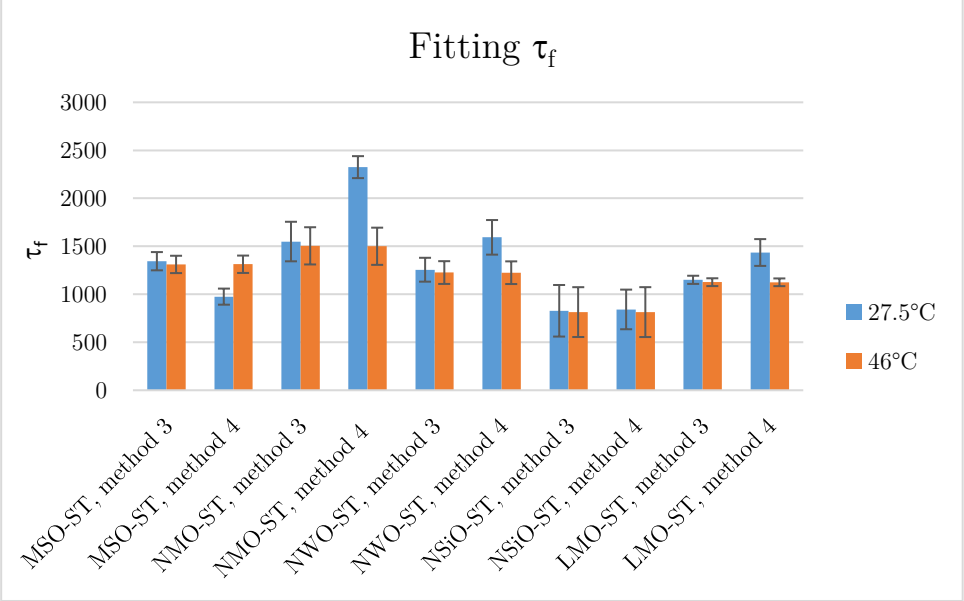


Figure A.11: Average  f values fitted by methods 3 and 4 for all binder-ST compositions. Error bars are represented for 3 parallel samples of each composition. The blue column represents data at T= 27.5 °C, while the orange column is data at the average T in the experimental temperature range.

Looking at the results, it is evident that the least square method (Method 3) matches well with method 1, which was originally used (at T=27.5, blue columns). Besides, it matches well with method 1 when we take T=46 °C (orange columns). Whereas the quadratic method matches well for T=46 °C ((27.5°C+65°C)/2) with both other methods (1 and 2), it is a poor match for T=27.5 °C (with method 1). This is because there is not enough data for a quality quadratic fit. It would be better to have more measurements, especially at temperatures lower than room temperature. Since room temperature is the limit of experimental data, I obtain overfitting artifacts for these values. Due to the limitations of our measurement system for microwave properties that do not enable cooling below RT, the measurements were performed at a minimum T of 27.5°C.

It is also clear that the originally chosen fitting method (Method 1) is somewhat limiting, but it gives the value for $f$ at 27°C. Given that there is more experimental data available, the linear least square method (Method 3) is a valuable improvement. The lack of lower temperature data, however, makes the quadratic method (Method 4) unreliable. The difference between the methods is not substantial, as can be seen in Figure A.11. Above all, it is smaller than the deviations between different repetitions of the same sample, which is a limitation of this processing approach. To sum up, the calculated $\tau_f$ is obviously quite large for such materials and, to some extent, inconsistent between replicates of the same composition, regardless of the details of the fitting method.

## A.6 Organotitanate-ST Composites

The experimental research presented in this section was conducted during the second working visit at the Microelectronic Research Unit, University of Oulu, where I was supervised by Prof. Dr. Heli Jantunen and Dr. Mikko Nelo. I focused on the preparation of all ceramic composites. In addition, I tested the compatibility between new binder

compounds and ST as the main functional ceramic material. The fabrication approach of all the so-called ceramic composites was a combination of soft-solution processing, heat-assisted pressing, and an upside-down composite approach. A gel-like $TiO_x$ precursor was used as a binder in this set of experiments. The particle size of ST-powder was varied from <63 µm to 500 µm. ST particles were mixed with organotitanate gel precursor in the ratio of 80/20 wt %. The sample mixture was pressed at 250 MPa and simultaneously heated to 160 and 340 °C. A more detailed description of the fabrication process is shown in Figure A.8.

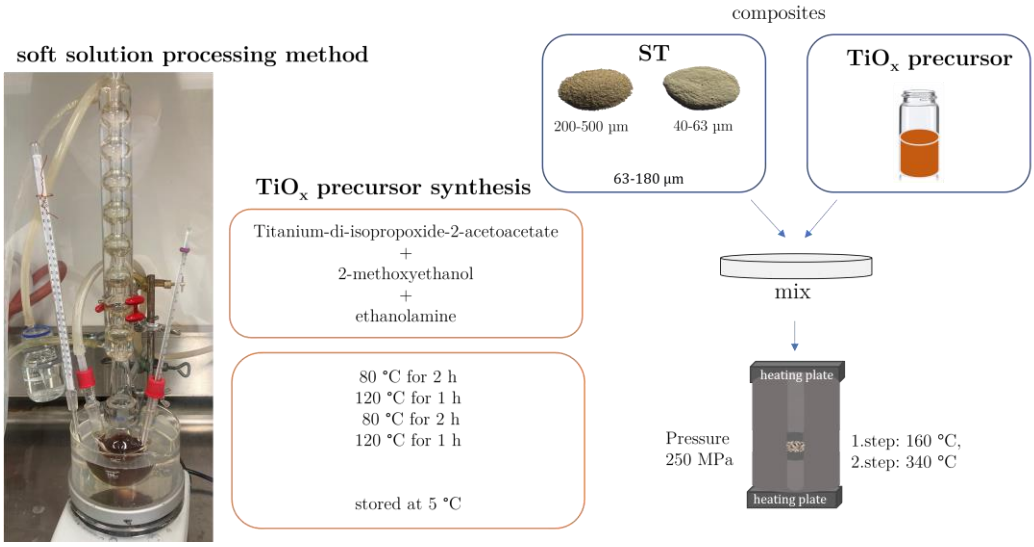


Figure A.12: Schematics of the processing of ST-TiOx sample.

The heating was adjusted according to the TG-MS analysis. Based on that, it was expected that the mixture would react to $TiO_2$ and form a connected structure at 340 °C. Dielectric properties of such ST-$TiO_x$ were investigated as a function of ST particle size. The relative permittivity of as-prepared ST-$TiO_x$ samples was measured in the range from 61-111 at 1 MHz, whereas dielectric loss values ranged between 0.0032 to 0.0163 at 1 MHz. ST-$TiO_x$ samples exhibited relative density from 76 to 89 %. In order to achieve better mechanical stability, samples were additionally treated with a four-step impregnation process (Figure A.8). Impregnated samples resulted in higher dielectric losses.

Table A.6: Functional properties of ST-TiOx composites.

| **ST particle size** | **Estimated wt % of $TiO_x$ precursor after the process** | **Relative density, ρ** | **Relative permittivity, $\varepsilon_r$** | **Dielectric losses, tan δ** | **Post-treatment** |
|---|---|---|---|---|---|
| | (wt %) | (%) | | | |
| 40-63 µm | 5 | 81 | 76 | 0.0070 | impregnated |
| | | 85 | 70 | 0.0070 | x |
| 63-180 µm | | 84 | 117 | 0.0104 | impregnated |
| | | 86 | 67 | 0.0053 | x |
| 200-500 µm | | 87 | 114 | 0.0166 | impregnated |
| | | 76 | 73 | 0.0069 | x |
| 75 % 200-500 µm + 25 % 40-63 µm | | 86 | 99 | 0.0151 | impregnated |
| | | 89 | 81 | 0.0107 | |
| | | 80 | 94 | 0.0107 | |
| | | 87 | 86 | 0.0058 | x |
| | | 89 | 82 | 0.0057 | |
| | | 86 | 85 | 0.0035 | |
| | | 86 | 80 | 0.0082 | |

According to the relative density values and measured dielectric properties (Table A.5), I confirmed that the most suitable particle size distribution is the mixture of large particles (200-500 µm) and smaller particles (<63 µm) in a ratio of 75/25. This resulted in improved properties, such as a relative density of 80-86 % and relative permittivity of 83, with corresponding dielectric losses of 0.0058 at 1 MHz. The impregnation of such ST-$TiO_x$ composites further improved properties, with a relative density of 85 % and a relative permittivity of 91, with correspondingly higher dielectric losses of 0.0122 at 1 MHz, respectively. SEM images of untreated and impregnated ST-$TiO_x$ samples are depicted in Figures A.9 and A.10.

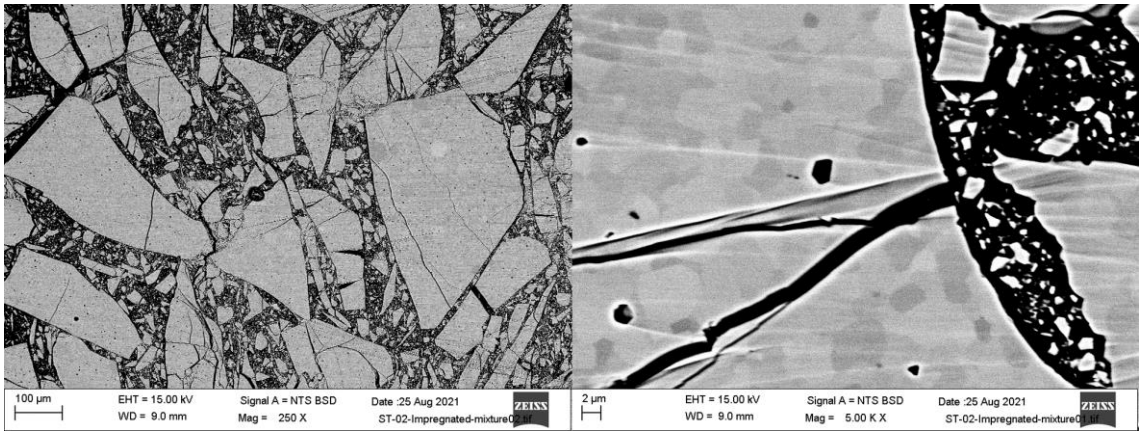


Figure A.13: SEM analysis of the impregnated ST-TiOx sample.

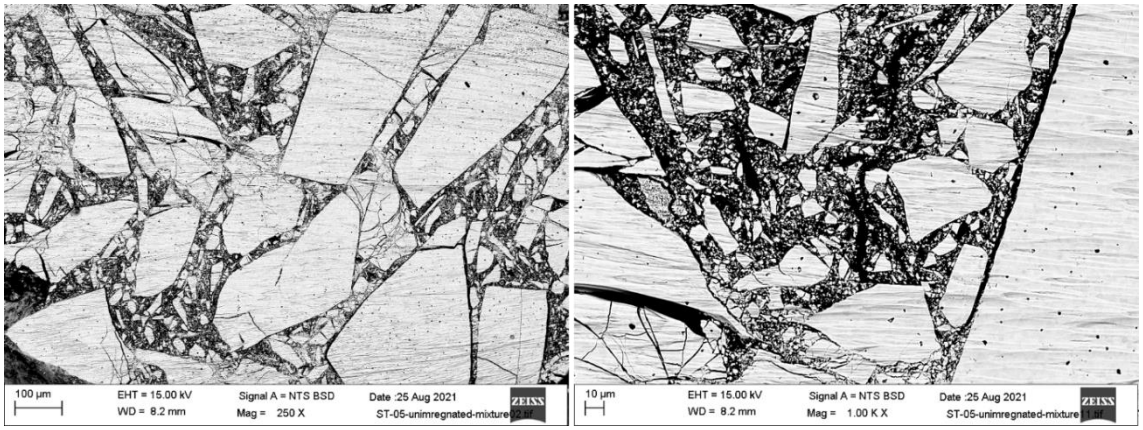


Figure A.14: SEM analysis of the unimpregnated ST-TiOx sample.

From those results, I concluded that using such a new approach and organotitanate binder did not substantially improve relative density and dielectric properties.

## A.7 PVDF-ST Composites

For comparison, I prepared ST-polymer composites with the same composition, 93.5 wt % of ST and 6.5 wt % of PVDF. PVDF was chosen due to its relatively high relative permittivity compared to other polymers ($\varepsilon_r$= 12.88 at 100 kHz) [216]. Table A.6 shows the relative density and dielectric properties of PVDF-ST composites. Experimentally obtained results using a polymeric binder were lower compared to inorganic salts.

Table A.7: The relative density and dielectric properties of PVDF-ST composites.

| ST-filler | | | | |
|---|---|---|---|---|
| | **Binder content** | **Relative density, ρ** | **Relative permittivity, $\varepsilon_r$** | **Dielectric losses, tan δ** |
| | (wt %) | % | | |
| PVDF binder | 6.5 | 76 | 47.9 | 0.0252 |

## A.8 Mechanical Characterization with B3B Testing

The force-displacement curve (Figure A.11) showed diverse behavior of samples under exposed load. The curve for LMO-ST samples differs substantially and exhibits "bumps", which indicate that multiple cracks occurred.

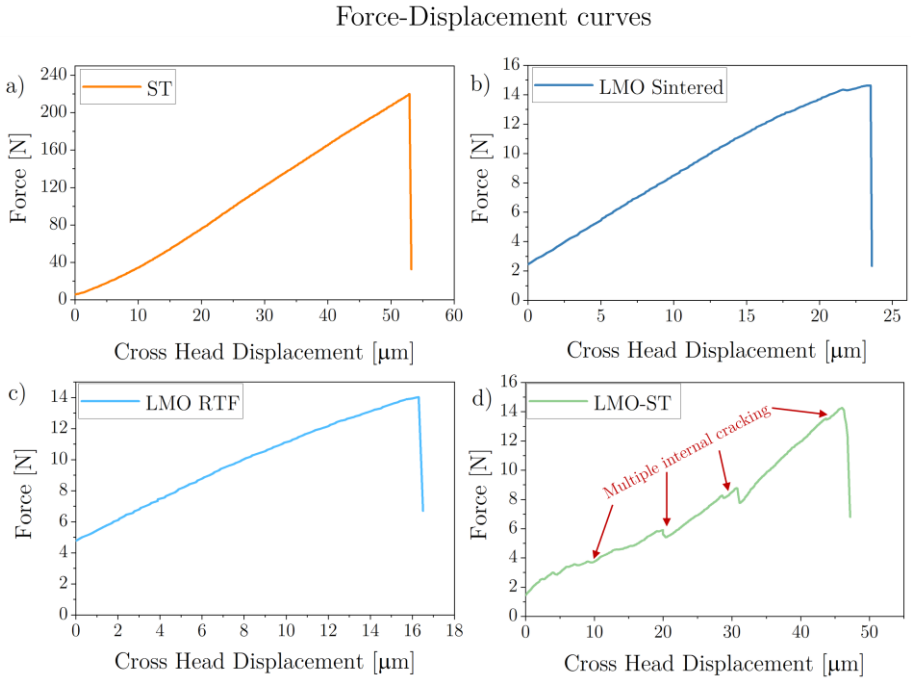


Figure A.15: Force-Displacement curves for ST; LMO (R) and LMO (S); LMO-ST composites.

# References


[1] Q. Zhang *et al.*, "Emerging Technologies for Green Energy Conversion and Storage," *Adv. Sustain. Syst.*, vol. 5, no. 3, p. 2000152, Mar. 2021, doi: https://doi.org/10.1002/adsu.202000152.

[2] G. Wang *et al.*, "Electroceramics for high-energy density capacitors: current status and future perspectives," *Chem. Rev.*, vol. 121, no. 10, pp. 6124–6172, 2021.

[3] P. Sharma and T. S. Bhatti, "A review on electrochemical double-layer capacitors," *Energy Convers. Manag.*, vol. 51, no. 12, pp. 2901–2912, 2010, doi: https://doi.org/10.1016/j.enconman.2010.06.031.

[4] J. Ho, T. R. Jow, and S. Boggs, "Historical introduction to capacitor technology," *IEEE Electr. Insul. Mag.*, vol. 26, no. 1, pp. 20–25, 2010.

[5] N. Setter and R. Waser, "Electroceramic materials," *Acta Mater.*, vol. 48, no. 1, pp. 151–178, 2000, doi: https://doi.org/10.1016/S1359-6454(99)00293-1.

[6] J. F. Scott, "Applications of modern ferroelectrics," *Science (80-. ).*, vol. 315, no. 5814, pp. 954–959, 2007, doi: 10.1126/science.1129564.

[7] W. D. Callister and D. G. Rethwisch, *Materials Science and Engineering*. Wiley, 2014. [Online]. Available: https://books.google.si/books?id=99UeMAEACAAJ

[8] M. Tuhkala, M. Teirikangas, and J. Juuti, "Modeling of Microwave Dielectric Properties of Composites," in *Microwave Materials and Applications 2V Set*, John Wiley & Sons, Ltd Chichester, UK, 2017, pp. 53–80. doi: https://doi.org/10.1002/9781119208549.ch2.

[9] M. T. Sebastian, R. Ubic, and H. Jantunen, *Microwave Materials and Applications, 2 volume set*. John Wiley & Sons, 2017.

[10] M. A. M. Albreem, "5G wireless communication systems: Vision and challenges," in *2015 International Conference on Computer, Communications, and Control Technology (I4CT)*, IEEE, 2015, pp. 493–497.

[11] M. B. Krishna and J. L. Mauri, "Advances in mobile computing and communications: perspectives and emerging trends in 5G networks," 2016.

[12] Z. Qadir, K. N. Le, N. Saeed, and H. S. Munawar, "Towards 6G Internet of Things: Recent advances, use cases, and open challenges," *ICT Express*, vol. 9, no. 3, pp. 296–312, 2023, doi: https://doi.org/10.1016/j.icte.2022.06.006.

[13] A. P. Gregory, "Q-factor measurement by using a Vector Network Analyser," 2021.

[14] J. Krupka, "Frequency domain complex permittivity measurements at microwave frequencies," *Meas. Sci. Technol.*, vol. 17, no. 6, p. R55, 2006.

[15] J. Krupka, K. Derzakowski, B. Riddle, and J. Baker-Jarvis, "A dielectric resonator for measurements of complex permittivity of low loss dielectric materials as a function of temperature," *Meas. Sci. Technol.*, vol. 9, no. 10, p. 1751, 1998.

[16] S. B. Narang and S. Bahel, "Low loss dielectric ceramics for microwave applications: a review," *J. Ceram. Process. Res.*, vol. 11, no. 3, pp. 316–321, 2010.

[17] I. M. Reaney and D. Iddles, "Microwave Dielectric Ceramics for Resonators and Filters in Mobile Phone Networks," *J. Am. Ceram. Soc.*, vol. 89, no. 7, pp. 2063–

2072, Jul. 2006, doi: https://doi.org/10.1111/j.1551-2916.2006.01025.x.

[18] D. Zhou, T. Zhou, Y. Tian, X. Zhu, and Y. Tu, "Perovskite-Based Solar Cells: Materials, Methods, and Future Perspectives," *J. Nanomater.*, vol. 2018, p. 8148072, 2018, doi: 10.1155/2018/8148072.

[19] N.-G. Park, "Perovskite solar cells: an emerging photovoltaic technology," *Mater. Today*, vol. 18, no. 2, pp. 65–72, 2015, doi: https://doi.org/10.1016/j.mattod.2014.07.007.

[20] C. N. R. Rao, "Perovskites," R. A. B. T.-E. of P. S. and T. (Third E. Meyers, Ed., New York: Academic Press, 2003, pp. 707–714. doi: https://doi.org/10.1016/B0-12-227410-5/00554-8.

[21] J. L. Clabel Huaman and V. A. Garcia Rivera, Eds., *Perovskite Ceramics Recent Advances and Emerging Applications*, 1st ed. Elsevier, 2022. [Online]. Available: https://shop.elsevier.com/books/perovskite-ceramics/huaman/978-0-323-90586-2

[22] A. R. West, *Basic solid state chemistry*. John Wiley & Sons Incorporated, 1999.

[23] M. W. Lufaso and P. M. Woodward, "Prediction of the crystal structures of perovskites using the software program SPuDS," *Acta Crystallogr. Sect. B Struct. Sci.*, vol. 57, no. 6, pp. 725–738, 2001.

[24] R. Ubic *et al.*, "Lattice-constant prediction and effect of vacancies in aliovalently doped perovskites," *J. Alloys Compd.*, vol. 644, pp. 982–995, 2015.

[25] R. D. t Shannon and C. T. Prewitt, "Revised values of effective ionic radii," *Acta Crystallogr. Sect. B Struct. Crystallogr. Cryst. Chem.*, vol. 26, no. 7, pp. 1046–1048, 1970.

[26] Z. Li, M. Yang, J.-S. Park, S.-H. Wei, J. J. Berry, and K. Zhu, "Stabilizing Perovskite Structures by Tuning Tolerance Factor: Formation of Formamidinium and Cesium Lead Iodide Solid-State Alloys," *Chem. Mater.*, vol. 28, no. 1, pp. 284–292, Jan. 2016, doi: 10.1021/acs.chemmater.5b04107.

[27] A. R. West, *Solid state chemistry and its applications*. John Wiley & Sons, 2022.

[28] D. W. Richerson, "Modern ceramic engineering : properties, processing, and use in design." 2018. [Online]. Available: https://search.ebscohost.com/login.aspx?direct=true&scope=site&db=nlebk&db=nlabk&AN=1802218

[29] G. G. Raju, *Dielectrics in electric fields: Tables, Atoms, and Molecules*. CRC press, 2017.

[30] M. G. Cain, *Characterisation of ferroelectric bulk materials and thin films*, vol. 2. Springer, 2014.

[31] S. Kwon, W. Hackenberger, E. Alberta, E. Furman, and M. Lanagan, "Nonlinear dielectric ceramics and their applications to capacitors and tunable dielectrics," *IEEE Electr. Insul. Mag.*, vol. 27, no. 2, pp. 43–55, 2011.

[32] G. H. Kwei, A. C. Lawson, S. J. L. Billinge, and S. W. Cheong, "Structures of the ferroelectric phases of barium titanate," *J. Phys. Chem.*, vol. 97, no. 10, pp. 2368–2377, 1993.

[33] O. E. Kvyatkovskii, "Quantum effects in incipient and low-temperature ferroelectrics (a review)," *Phys. Solid State*, vol. 43, no. 8, pp. 1401–1419, 2001, doi: 10.1134/1.1395075.

[34] Y. Koyama, T. Moriyasu, E. Okamura, Y. Yamada, K. Tanaka, and T. Kohmoto, "Doping-induced ferroelectric phase transition in strontium titanate: Observation of birefringence and coherent phonons under ultraviolet illumination," *Phys. Rev. B*, vol. 81, no. 2, p. 24104, Jan. 2010, doi: 10.1103/PhysRevB.81.024104.

[35] T. Mitsui and W. B. Westphal, "Dielectric and X-Ray Studies of Ca x Ba 1− x Ti O 3 and Ca x Sr 1− x Ti O 3," *Phys. Rev.*, vol. 124, no. 5, p. 1354, 1961.

[36] H. Uwe and T. Sakudo, "Stress-induced ferroelectricity and soft phonon modes in $SrTiO_3$," *Phys. Rev. B*, vol. 13, no. 1, pp. 271–286, Jan. 1976, doi: 10.1103/PhysRevB.13.271.

[37] K. A. Müller, W. Berlinger, M. Capizzi, and H. Gränicher, "Monodomain strontium titanate," *Solid State Commun.*, vol. 8, no. 7, pp. 549–553, 1970, doi: https://doi.org/10.1016/0038-1098(70)90302-9.

[38] V. V Lemanov, "Phase transitions in SrTiO 3-based solid solutions," *Phys. Solid State*, vol. 39, pp. 1468–1473, 1997.

[39] M. Itoh, R. Wang, Y. Inaguma, T. Yamaguchi, Y. J. Shan, and T. Nakamura, "Ferroelectricity induced by oxygen isotope exchange in strontium titanate perovskite," *Phys. Rev. Lett.*, vol. 82, no. 17, p. 3540, 1999.

[40] T. Sakudo and H. Unoki, "Dielectric properties of SrTi O 3 at low temperatures," *Phys. Rev. Lett.*, vol. 26, no. 14, p. 851, 1971.

[41] A. Manan and I. Qazi, "Dielectric properties of ceramics for microwave and millimeter wave applications," in *2013 International Conference on Aerospace Science & Engineering (ICASE)*, IEEE, 2013, pp. 1–7.

[42] J. Pelleg and J. Pelleg, "Defects in Materials," *Diffus. Ceram.*, pp. 21–30, 2016.

[43] B. Liu, V. R. Cooper, H. Xu, H. Xiao, Y. Zhang, and W. J. Weber, "Composition dependent intrinsic defect structures in SrTiO 3," *Phys. Chem. Chem. Phys.*, vol. 16, no. 29, pp. 15590–15596, 2014.

[44] R. E. Newnham, D. P. Skinner, and L. E. Cross, "Connectivity and piezoelectric-pyroelectric composites," *Mater. Res. Bull.*, vol. 13, no. 5, pp. 525–536, 1978, doi: https://doi.org/10.1016/0025-5408(78)90161-7.

[45] L. Zhang, P. Bass, and Z. Y. Cheng, "Physical aspects of 0-3 dielectric composites," *J. Adv. Dielectr.*, vol. 5, no. 2, 2015, doi: 10.1142/S2010135X15500125.

[46] M. Nelo, J. Peräntie, T. Siponkoski, J. Juuti, and H. Jantunen, "Upside-down composites: Electroceramics without sintering," *Appl. Mater. Today*, vol. 15, pp. 83–86, 2019, doi: https://doi.org/10.1016/j.apmt.2018.12.021.

[47] T. W. S. Yip, E. J. Cussen, and C. Wilson, "Spontaneous formation of crystalline lithium molybdate from solid reagents at room temperature," *Dalt. Trans.*, vol. 39, no. 2, pp. 411–417, 2010.

[48] P. Patnaik, *Handbook of inorganic chemicals*, vol. 529. McGraw-Hill New York, 2003.

[49] E. Sarmiento, J. G. González-Rodriguez, A. M. Ramirez-Arteaga, and J. Uruchurtu, "Corrosion inhibition of 316L stainless steel in LiBr+ Etileneglycol+ H2O By using inorganic inhibitors," *Int. J. Electrochem. Sci*, vol. 8, no. 12, pp. 12417–12433, 2013.

[50] F. Stavale, N. Nilius, and H.-J. Freund, "Lithium-molybdate nanostructures grown on the Mo(001) surface," *Surf. Sci.*, vol. 609, pp. 78–84, 2013, doi:

https://doi.org/10.1016/j.susc.2012.11.007.

[51] J. Wang *et al.*, "Lithium molybdate composited with carbon nanofibers as a high-capacity and stable anode material for lithium-ion batteries," *Energy Mater*, vol. 2, p. 200026, 2022.

[52] H. Zhang *et al.*, "Preparation of Li2MoO4 using aqueous solution method and microwave dielectric properties after sintering," *J. Mater. Sci. Mater. Electron.*, vol. 27, no. 5, pp. 5422–5426, 2016, doi: 10.1007/s10854-016-4444-2.

[53] S. S. Faouri *et al.*, "High quality factor cold sintered Li2MoO4BaFe12O19 composites for microwave applications," *Acta Mater.*, vol. 166, pp. 202–207, 2019.

[54] G. Zhang, H. Wang, J. Guo, L. He, D. Wei, and Q. Yuan, "Ultra-low Sintering Temperature Microwave Dielectric Ceramics Based on Na2O-MoO3 Binary System," *J. Am. Ceram. Soc.*, vol. 98, no. 2, pp. 528–533, Feb. 2015, doi: https://doi.org/10.1111/jace.13297.

[55] H. M. Reisenauer, "Relative Efficiency of Seed-and-Soil-Applied Molybdenum Fertilizer1," *Agron. J.*, vol. 55, no. 5, pp. 459–460, Sep. 1963, doi: https://doi.org/10.2134/agronj1963.00021962005500050015x.

[56] W. Zhang *et al.*, "Laminarin and sodium molybdate as efficient sustainable inhibitor for Q235 steel in sodium chloride solution," *Colloids Surfaces A Physicochem. Eng. Asp.*, vol. 637, p. 128199, 2022, doi: https://doi.org/10.1016/j.colsurfa.2021.128199.

[57] S. Nakagaki *et al.*, "Use of anhydrous sodium molybdate as an efficient heterogeneous catalyst for soybean oil methanolysis," *Appl. Catal. A Gen.*, vol. 351, no. 2, pp. 267–274, 2008, doi: https://doi.org/10.1016/j.apcata.2008.09.026.

[58] A. Ndayishimiye, Z. Fan, J. Mena-Garcia, J. M. Anderson, and C. A. Randall, "Coalescence in cold sintering: A study on sodium molybdate," *Open Ceram.*, vol. 11, p. 100293, 2022, doi: https://doi.org/10.1016/j.oceram.2022.100293.

[59] J. Hao *et al.*, "Grain size effect on microwave dielectric properties of Na2WO4 ceramics prepared by cold sintering process," *Ceram. Int.*, vol. 46, no. 17, pp. 27193–27198, 2020, doi: https://doi.org/10.1016/j.ceramint.2020.07.200.

[60] J. Hao *et al.*, "Cold sintering of Na2WO4 ceramics using a Na2WO4-2H2O chemistry," *J. Eur. Ceram. Soc.*, vol. 41, no. 12, pp. 6029–6034, 2021.

[61] H. L. Dong, C. X. Hu, W. J. Wang, H. P. Bao, W. J. Liu, and B. Yang, "Novel Low-Permittivity, Low-Sintering-Temperature Na2WO4 Microwave Dielectric Ceramics for LTCC Applications," *J. Ceram. Sci. Technol.*, vol. 9, no. 4, pp. 471–475, 2018.

[62] S. A. Abbas *et al.*, "Spinel-type $Na_2MoO_4$ and $Na_2WO_4$ as promising optoelectronic materials: First-principle DFT calculations," *Chem. Phys.*, vol. 538, p. 110902, 2020.

[63] H. H. Weldes and K. R. Lange, "Properties of soluble silicates," *Ind. Eng. Chem.*, vol. 61, no. 4, pp. 29–44, 1969.

[64] R. C. Merrill, "Chemistry of the soluble silicates.," *J. Chem. Educ.*, vol. 24, no. 6, p. 262, 1947.

[65] V. Kahlenberg, "Structural Chemistry of Anhydrous Sodium Silicates – A Review," *Chimia (Aarau).*, vol. 64, no. 10 SE-Scientific Articles, p. 716, Oct. 2010, doi: 10.2533/chimia.2010.716.

[66] S. Chakraborty, "Frequency-dependent electrical behaviour of Na2SiO3: a brief

report," *Bull. Mater. Sci.*, vol. 43, no. 1, p. 238, 2020, doi: 10.1007/s12034-020-02184-6.

[67] C. H. Hurley and T. H. Thornburn, *Sodium silicate stabilization of soils: A review of the literature*. Soil Mechanics Laboratory, Department of Civil Engineering, Engineering …, 1971.

[68] L. Lehrman and H. L. Shuldener, "Action of sodium silicate as a corrosion inhibitor in water piping," *Ind. Eng. Chem.*, vol. 44, no. 8, pp. 1765–1769, 1952.

[69] "Final Report on the Safety Assessment of Potassium Silicate, Sodium Metasilicate, and Sodium Silicate1," *Int. J. Toxicol.*, vol. 24, no. 1_suppl, pp. 103–117, Jan. 2005, doi: 10.1080/10915810590918643.

[70] S. Chakraborty, "Analysis of Dielectric Relaxation in Sodium Silicate (Na2SiO3) using Complex Impedance Spectroscopy," *J. Inst. Eng. Ser. D*, vol. 104, no. 1, pp. 45–50, 2023, doi: 10.1007/s40033-022-00383-5.

[71] V. Colson, M. Bourebrab, M. Dalmais, O. Jadeau, and C. Lanos, "Formulation of novel fire retardant additives for biobased insulation material," *Acad. J. Civ. Eng.*, vol. 37, no. 2, pp. 134–141, 2019.

[72] J. Hoffmann, M. Kaniewski, D. Nieweś, and K. Hoffmann, "Selected magnesium compounds as possible inhibitors of ammonium nitrate decomposition," *Polish J. Chem. Technol.*, vol. 22, no. 2, pp. 1–8, 2020, doi: doi:10.2478/pjct-2020-0011.

[73] K. E. N'Tsoukpoe, T. Schmidt, H. U. Rammelberg, B. A. Watts, and W. K. L. Ruck, "A systematic multi-step screening of numerous salt hydrates for low temperature thermochemical energy storage," *Appl. Energy*, vol. 124, pp. 1–16, 2014, doi: https://doi.org/10.1016/j.apenergy.2014.02.053.

[74] S. J. Chipera and D. T. Vaniman, "Experimental stability of magnesium sulfate hydrates that may be present on Mars," *Geochim. Cosmochim. Acta*, vol. 71, no. 1, pp. 241–250, 2007.

[75] D. T. Vaniman, D. L. Bish, S. J. Chipera, C. I. Fialips, J. William Carey, and W. C. Feldman, "Magnesium sulphate salts and the history of water on Mars," *Nature*, vol. 431, no. 7009, pp. 663–665, 2004, doi: 10.1038/nature02973.

[76] S. Karan and S. P. Sen Gupta, "Vickers microhardness studies on solution-grown single crystals of magnesium sulphate hepta-hydrate," *Mater. Sci. Eng. A*, vol. 398, no. 1, pp. 198–203, 2005, doi: https://doi.org/10.1016/j.msea.2005.03.016.

[77] P. A. J. Donkers, S. Beckert, L. Pel, F. Stallmach, M. Steiger, and O. C. G. Adan, "Water Transport in MgSO4 · 7H2O During Dehydration in View of Thermal Storage," *J. Phys. Chem. C*, vol. 119, no. 52, pp. 28711–28720, Dec. 2015, doi: 10.1021/acs.jpcc.5b08730.

[78] J. Peng, Y. Zhao, L. Jiao, W. Zheng, and L. Zeng, "CO2 emission calculation and reduction options in ceramic tile manufacture-the Foshan case," *Energy Procedia*, vol. 16, pp. 467–476, 2012.

[79] D. W. Richerson and W. E. Lee, *Modern ceramic Engineering Properties, processing, and Use in design*, vol. 53, no. 9. 2018. doi: 10.1017/CBO9781107415324.004.

[80] W. D. Kingery, "Introduction to ceramics," *JohnWiley Sons Publ.*, 1976.

[81] M. N. Rahaman, *Ceramic processing and sintering*, vol. 1. CRC press, 2017.

[82] R. C. Rossi and R. M. Fulrath, "Final Stage Densification in Vacuum Hot-Pressing of Alumina," *J. Am. Ceram. Soc.*, vol. 48, no. 11, pp. 558–564, 1965.

[83] M. H. Bocanegra-Bernal, "Hot Isostatic Pressing (HIP) technology and its applications to metals and ceramics," *J. Mater. Sci.*, vol. 39, no. 21, pp. 6399–6420, 2004, doi: 10.1023/B:JMSC.0000044878.11441.90.

[84] N. Yamasaki, K. Yanagisawa, M. Nishioka, and S. Kanahara, "A hydrothermal hot-pressing method: apparatus and application," *Hydrothermal React. Mater. Sci. Eng. An Overv. Res. Japan*, pp. 423–424, 1989.

[85] J. Monroe, "Physical Geology Exploring The Earth," 2004.

[86] J. Andrews, D. Button, and I. M. Reaney, "Advances in cold sintering: Improving energy consumption and unlocking new potential in component manufacturing," *Johnson Matthey Technol. Rev.*, vol. 64, no. 2, pp. 219–232, 2020, doi: https://doi.org/10.1595/205651320X15814150061554.

[87] D. S. B. Heidary, M. Lanagan, and C. A. Randall, "Contrasting energy efficiency in various ceramic sintering processes," *J. Eur. Ceram. Soc.*, vol. 38, no. 4, pp. 1018–1029, 2018.

[88] F. Fei, L. He, B. Zhou, Z. Xu, and X. Song, "Hydrothermal-Assisted Transient Binder Jetting of Ceramics for Achieving High Green Density," *JOM*, vol. 72, no. 3, pp. 1307–1313, 2020, doi: 10.1007/s11837-019-03962-2.

[89] A. Ndayishimiye, S. H. Bang, C. J. Spiers, and C. A. Randall, "Reassessing cold sintering in the framework of pressure solution theory," *J. Eur. Ceram. Soc.*, vol. 43, no. 1, pp. 1–13, 2023, doi: https://doi.org/10.1016/j.jeurceramsoc.2022.09.053.

[90] C. A. Randall, J. Guo, A. Baker, M. Lanagan, and H. Guo, "(12) Patent Application Publication (10) Pub. No.: US 2017/0088471 A1," 2017

[91] K. R. McCLAY, "Pressure solution and Coble creep in rocks and minerals: a review," *J. Geol. Soc. London.*, vol. 134, no. 1, pp. 57–70, Oct. 1977, doi: 10.1144/gsjgs.134.1.0057.

[92] F. Bouville and A. R. Studart, "Geologically-inspired strong bulk ceramics made with water at room temperature," *Nat. Commun.*, vol. 8, no. 1, pp. 1–8, 2017.

[93] H. Guo, A. Baker, J. Guo, and C. A. Randall, "Cold Sintering Process: A Novel Technique for Low-Temperature Ceramic Processing of Ferroelectrics," *J. Am. Ceram. Soc.*, vol. 99, no. 11, pp. 3489–3507, 2016, doi: 10.1111/jace.14554.

[94] Y. Huang *et al.*, "Influence of incongruent dissolution-precipitation on 8YSZ ceramics during cold sintering process," *J. Eur. Ceram. Soc.*, vol. 42, no. 5, pp. 2362–2369, 2022, doi: https://doi.org/10.1016/j.jeurceramsoc.2021.12.072.

[95] R. Boston, J. Guo, S. Funahashi, A. L. Baker, I. M. Reaney, and C. A. Randall, "Reactive intermediate phase cold sintering in strontium titanate," *RSC Adv.*, vol. 8, no. 36, pp. 20372–20378, 2018.

[96] D. Wang *et al.*, "Cold sintered CaTiO3-K2MoO4 microwave dielectric ceramics for integrated microstrip patch antennas," *Appl. Mater. Today*, vol. 18, p. 100519, 2020, doi: https://doi.org/10.1016/j.apmt.2019.100519.

[97] N. Santha, M. Rakhi, and G. Subodh, "Fabrication of high quality factor cold sintered MgTiO3–NaCl microwave ceramic composites," *Mater. Chem. Phys.*, vol. 255, p. 123636, 2020, doi: https://doi.org/10.1016/j.matchemphys.2020.123636.

[98] M. Biesuz, S. Grasso, and V. M. Sglavo, "What's new in ceramics sintering? A short report on the latest trends and future prospects," *Curr. Opin. Solid State Mater. Sci.*, vol. 24, no. 5, p. 100868, 2020, doi: https://doi.org/10.1016/j.cossms.2020.100868.

[99] S. Vinoth and S.-F. Wang, "Cold Sintering Process for a BaTiO3/Poly(vinylidene difluoride) Ceramic–Polymer Composite: Evaluation of the Structural and Microwave Dielectric Properties," *Inorg. Chem.*, vol. 62, no. 21, pp. 8326–8333, May 2023, doi: 10.1021/acs.inorgchem.3c00838.

[100] T. Yu, J. Cheng, L. Li, B. Sun, X. Bao, and H. Zhang, "Current understanding and applications of the cold sintering process," *Front. Chem. Sci. Eng.*, vol. 13, no. 4, pp. 654–664, 2019, doi: 10.1007/s11705-019-1832-1.

[101] H. Kähäri, M. Teirikangas, J. Juuti, and H. Jantunen, "Dielectric properties of lithium molybdate ceramic fabricated at room temperature," *J. Am. Ceram. Soc.*, vol. 97, no. 11, pp. 3378–3379, 2014.

[102] H. C. Sorby, "II. The Bakerian lecture.— On the direct correlation of mechanical and chemical forces," *Proc. R. Soc. London*, vol. 12, pp. 538–550, Jan. 1997, doi: 10.1098/rspl.1862.0117.

[103] M. Nelo, T. Siponkoski, H. Kähäri, K. Kordas, J. Juuti, and H. Jantunen, "Upside - down composites: Fabricating piezoceramics at room temperature," *J. Eur. Ceram. Soc.*, vol. 39, no. 11, pp. 3301–3306, 2019, doi: 10.1016/j.jeurceramsoc.2019.04.052.

[104] A. Mormeneo-Segarra, S. Ferrer-Nicomedes, N. Vicente-Agut, and A. Barba-Juan, "The role of the LATP particle size as a cornerstone of the cold sintering process," *J. Eur. Ceram. Soc.*, vol. 44, no. 8, pp. 5105–5114, 2024, doi: https://doi.org/10.1016/j.jeurceramsoc.2024.02.028.

[105] C. S. Grove Jr, R. V Jelinek, and H. M. Schoen, "Crystallization from solution," in *Advances in chemical engineering*, vol. 3, Elsevier, 1962, pp. 1–60.

[106] G. Bánhegyi, "Comparison of electrical mixture rules for composites," *Colloid Polym. Sci.*, vol. 264, no. 12, pp. 1030–1050, 1986, doi: 10.1007/BF01410321.

[107] M. Tuhkala, J. Juuti, M. Teirikangas, and H. Jantunen, "Polymer-ceramic composite filler selection using mixing rules," *J. Appl. Phys.*, vol. 117, no. 6, p. 64103, 2015.

[108] V. A. Markel, "Introduction to the Maxwell Garnett approximation: tutorial," *JOSA A*, vol. 33, no. 7, pp. 1244–1256, 2016, doi: 10.1364/JOSAA.33.001244.

[109] H. Fricke, "The Maxwell-Wagner dispersion in a suspension of ellipsoids," *J. Phys. Chem.*, vol. 57, no. 9, pp. 934–937, 1953.

[110] R. W. Sillars, "The properties of a dielectric containing semiconducting particles of various shapes," *J. Inst. Electr. Eng.*, vol. 80, no. 484, pp. 378–394, 1937.

[111] S. Rajesh, K. P. Murali, K. V. Rajani, and R. Ratheesh, "SrTiO3-Filled PTFE Composite Laminates for Microwave Substrate Applications," *Int. J. Appl. Ceram. Technol.*, vol. 6, no. 5, pp. 553–561, Sep. 2009, doi: https://doi.org/10.1111/j.1744-7402.2009.02389.x.

[112] K.-T. Wu, Y. Yuan, S.-R. Zhang, X.-Y. Yan, and Y.-R. Cui, "ZrTi 2 O 6 filled PTFE composites for microwave substrate applications," *J. Polym. Res.*, vol. 20, pp. 1–6, 2013.

[113] L. Ramajo, M. Reboredo, and M. Castro, "Dielectric response and relaxation phenomena in composites of epoxy resin with BaTiO3 particles," *Compos. Part A Appl. Sci. Manuf.*, vol. 36, no. 9, pp. 1267–1274, 2005.

[114] S. Lee, J.-G. Hyun, H. Park, J. Kim, and K.-W. Paik, "Frequency behavior of embedded epoxy/SrTiO3 composite capacitor materials," in *Proceedings Electronic Components and Technology, 2005. ECTC '05.*, 2005, pp. 1222–1227. doi: 10.1109/ECTC.2005.1441426.

[115] D. S. McLachlan, A. Priou, I. Chenerie, E. Issac, and F. Henry, "Modeling the permittivity of composite materials with a general effective medium equation," *J. Electromagn. Waves Appl.*, vol. 6, no. 9, pp. 1099–1131, 1992.

[116] A. V. Goncharenko, V. Z. Lozovski, and E. F. Venger, "Lichtenecker's equation: applicability and limitations," *Opt. Commun.*, vol. 174, no. 1–4, pp. 19–32, 2000, doi: 10.1016/S0030-4018(99)00695-1.

[117] T. Zakri, J.-P. Laurent, and M. Vauclin, "Theoretical evidence for Lichtenecker's mixture formulae' based on the effective medium theory," *J. Phys. D. Appl. Phys.*, vol. 31, no. 13, p. 1589, 1998, doi: 10.1088/0022-3727/31/13/013.

[118] N. Kuzmić, S. D. Škapin, M. Nelo, H. Jantunen, and M. Spreitzer, "Room temperature fabrication and post-impregnation of LMO-ST composites: Engineering and modeling of dielectric properties," *Open Ceram.*, vol. 16, p. 100495, 2023, doi: https://doi.org/10.1016/j.oceram.2023.100495.

[119] D. Manaila-Maximean, "Effective permittivity of a multi-phase system: nanoparticle-doped polymer-dispersed liquid crystal films," *Molecules*, vol. 26, no. 5, p. 1441, 2021, doi: https://doi.org/10.3390/molecules26051441.

[120] M. Väätäjä, H. Kähäri, K. Ohenoja, M. Sobocinski, J. Juuti, and H. Jantunen, "3D printed dielectric ceramic without a sintering stage," *Sci. Rep.*, vol. 8, no. 1, pp. 1–8, 2018, doi: OI:10.1038/s41598-018-34408-5.

[121] S. George and M. T. Sebastian, "Three-phase polymer–ceramic–metal composite for embedded capacitor applications," *Compos. Sci. Technol.*, vol. 69, no. 7–8, pp. 1298–1302, 2009, doi: https://doi.org/10.1016/j.compscitech.2009.03.003.

[122] A. Reid, S. Langer, and S. Keshavarz, "OOF: Flexible finite element modeling for materials science," in *2nd International Workshop on Software Solutions for ICME. http://congress. cimne. com/icme2016/frontal/default. asp. Accessed March*, 2018.

[123] S. A. Langer, E. R. Fuller, and W. C. Carter, "OOF: an image-based finite-element analysis of material microstructures," *Comput. Sci. Eng.*, vol. 3, no. 3, pp. 15–23, 2001.

[124] A. C. E. Reid, R. C. Lua, R. E. García, V. R. Coffman, and S. A. Langer, "Modelling microstructures with OOF2," *Int. J. Mater. Prod. Technol.*, vol. 35, no. 3–4, pp. 361–373, 2009.

[125] S. A. Langer, A. C. E. Reid, S. I. Haan, R. E. Garcia, R. C. Lua, and V. R. Coffman, "The OOF2 manual," *NIST, US*, 2008.

[126] V. R. Coffman, A. C. E. Reid, S. A. Langer, and G. Dogan, "OOF3D: An image-based finite element solver for materials science," *Math. Comput. Simul.*, vol. 82, no. 12, pp. 2951–2961, 2012.

[127] C. Waters, M. Salih, and S. Ajinola, "Porosity comparative analysis of porous copper

and OOF modelling," *J. Porous Mater.*, vol. 22, no. 4, pp. 989–995, 2015, doi: 10.1007/s10934-015-9973-1.

[128] A. Börger, P. Supancic, and R. Danzer, "The ball on three balls test for strength testing of brittle discs: stress distribution in the disc," *J. Eur. Ceram. Soc.*, vol. 22, no. 9, pp. 1425–1436, 2002, doi: https://doi.org/10.1016/S0955-2219(01)00458-7.

[129] A. Börger, P. Supancic, and R. Danzer, "The ball on three balls test for strength testing of brittle discs: Part II: analysis of possible errors in the strength determination," *J. Eur. Ceram. Soc.*, vol. 24, no. 10, pp. 2917–2928, 2004, doi: https://doi.org/10.1016/j.jeurceramsoc.2003.10.035.

[130] R. Morrell, N. J. McCormick, J. Bevan, M. Lodeiro, and J. Margetson, "Biaxial disc flexure – modulus and strength testing," *Br. Ceram. Trans.*, vol. 98, no. 5, pp. 234–240, May 1999, doi: 10.1179/096797899680507.

[131] R. DANZER, P. SUPANCIC, and W. HARRER, "Biaxial Tensile Strength Test for Brittle Rectangular Plates," *J. Ceram. Soc. Japan*, vol. 114, no. 1335, pp. 1054–1060, 2006, doi: 10.2109/jcersj.114.1054.

[132] G. D. Quinn and G. D. Quinn, *Fractography of ceramics and glasses*, vol. 960. National Institute of Standards and Technology Washington, DC, 2007.

[133] W. Harrer, R. Danzer, P. Supancic, and T. Lube, *The Ball on Three Balls Test: Strength Testing of Specimens of Different Sizes and Geometries*. 2008.

[134] J. Pelleg, *Mechanical properties of ceramics*, vol. 213. Springer Science & Business, 2014.

[135] G. N. Greaves, A. L. Greer, R. S. Lakes, and T. Rouxel, "Poisson's ratio and modern materials," *Nat. Mater.*, vol. 10, no. 11, pp. 823–837, 2011, doi: 10.1038/nmat3134.

[136] W. Weibull, "A statistical theory of strength of materials," *IVB-Handl.*, 1939.

[137] W. Weibull, "A statistical distribution function of wide applicability," *J. Appl. Mech.*, 1951.

[138] B. Bergman, "On the estimation of the Weibull modulus," *J. Mater. Sci. Lett.*, vol. 3, no. 8, pp. 689–692, 1984.

[139] 4FT Pierce, "Tensile tests for cotton yarns. v.-'the weakest link', theorems on the strength of long composite specimens," *J. Text. Inst*, vol. 17, pp. T355-368, 1926.

[140] M. Tiryakioğlu and J. Campbell, "Weibull Analysis of Mechanical Data for Castings: A Guide to the Interpretation of Probability Plots," *Metall. Mater. Trans. A*, vol. 41, no. 12, pp. 3121–3129, 2010, doi: 10.1007/s11661-010-0364-6.

[141] R. Danzer, W. Harrer, P. Supancic, T. Lube, Z. Wang, and A. Börger, "The ball on three balls test—Strength and failure analysis of different materials," *J. Eur. Ceram. Soc.*, vol. 27, no. 2, pp. 1481–1485, 2007, doi: https://doi.org/10.1016/j.jeurceramsoc.2006.05.034.

[142] R. Danzer, "Some notes on the correlation between fracture and defect statistics: Are Weibull statistics valid for very small specimens?," *J. Eur. Ceram. Soc.*, vol. 26, no. 15, pp. 3043–3049, 2006, doi: https://doi.org/10.1016/j.jeurceramsoc.2005.08.021.

[143] B. Cantor, *The equations of materials*. Oxford University Press, 2020.

[144] F. Zok, F. F. Lange, and J. R. Porter, "Packing density of composite powder mixtures," *J. Am. Ceram. Soc.*, vol. 74, no. 8, pp. 1880–1885, 1991.

[145] J. E. Brewe and J. J. Myers, "Particle size optimization for reduced cement high strength concrete," *Proc. PCI-NBC Bridg. Life*, 2005.

[146] C. C. Furnas, "The relations between specific volume, voids, and size composition in Systems of Broken Solids of mixed sized, Department of Commerce, Bureau of Mines," *Reports Investig.*, pp. 1–10, 1928.

[147] J. E. Funk and D. R. Dinger, *Predictive process control of crowded particulate suspensions: applied to ceramic manufacturing*. Springer Science & Business Media, 2013.

[148] M. Väätäjä, H. Kähäri, J. Juuti, and H. Jantunen, "Li2MoO4-based composite ceramics fabricated from temperature-and atmosphere-sensitive MnZn ferrite at room temperature," *J. Am. Ceram. Soc.*, vol. 100, no. 8, pp. 3626–3635, 2017, doi: https://doi.org/10.1111/jace.14914.

[149] U. of O. Nelo, Mikko (Microelectronics research unit, "Patent FI 20215914: Impregnation of ceramic composite material," 2022

[150] R. Viana, P. Lunkenheimer, J. Hemberger, R. Böhmer, and A. Loidl, "Dielectric spectroscopy in SrTiO3," *Phys. Rev. B*, vol. 50, no. 1, pp. 601–604, Jul. 1994, doi: 10.1103/PhysRevB.50.601.

[151] N. F. Muhamad, R. A. M. Osman, M. S. Idris, and M. N. M. Yasin, "Physical and electrical properties of SrTiO3 and SrZrO3," in *EPJ Web of Conferences*, EDP Sciences, 2017, p. 1052.

[152] J. Zheng, W. B. Carlson, and J. S. Reed, "The packing density of binary powder mixtures," *J. Eur. Ceram. Soc.*, vol. 15, no. 5, pp. 479–483, 1995, doi: https://doi.org/10.1016/0955-2219(95)00001-B.

[153] A. V Shenoy, "Steady shear viscous properties," in *Rheology of Filled Polymer Systems*, Springer, 1999, pp. 243–311.

[154] R. Cabiscol *et al.*, "Effect of particle size on powder compaction and tablet strength using limestone," *Adv. Powder Technol.*, vol. 31, no. 3, pp. 1280–1289, 2020, doi: https://doi.org/10.1016/j.apt.2019.12.033.

[155] L. H. Thompson and L. K. Doraiswamy, "The rate enhancing effect of ultrasound by inducing supersaturation in a solid–liquid system," *Chem. Eng. Sci.*, vol. 55, no. 16, pp. 3085–3090, 2000, doi: https://doi.org/10.1016/S0009-2509(99)00481-9.

[156] H. Li, H. Li, Z. Guo, and Y. Liu, "The application of power ultrasound to reaction crystallization," *Ultrason. Sonochem.*, vol. 13, no. 4, pp. 359–363, 2006.

[157] M. T. Sebastian, R. Ubic, and H. Jantunen, "Low-loss dielectric ceramic materials and their properties," *Int. Mater. Rev.*, vol. 60, no. 7, pp. 392–412, 2015, doi: https://doi.org/10.1179/1743280415Y.0000000007.

[158] H. Kähäri, P. Ramachandran, J. Juuti, and H. Jantunen, "Room-temperature-densified Li2MoO4 ceramic patch antenna and the effect of humidity," *Int. J. Appl. Ceram. Technol.*, vol. 14, no. 1, pp. 50–55, Jan. 2017, doi: https://doi.org/10.1111/ijac.12615.

[159] C. G. Malmberg and A. A. Maryott, "Dielectric Constant of Water from 00 to 1000 C," *J. Res. Natl. Bur. Stand. (1934).*, vol. 56, no. 1, pp. 1–8, 1956.

[160] N. Chen *et al.*, "Structure, thermal and microwave dielectric properties of cold-sintered Li2MoO4-Al2O3 ceramic," *J. Mater.*, p. 100940, 2024, doi:

https://doi.org/10.1016/j.jmat.2024.100940.

[161] N. Kuzmić, S. D. Škapin, M. Nelo, H. Jantunen, and M. Spreitzer, "Dielectric Properties of Upside-Down SrTiO3/Li2MoO4 Composites Fabricated at Room Temperature," *Front. Mater.*, vol. 8, p. 121, 2021, doi: 10.3389/fmats.2021.669421.

[162] M. R. Baklanov and K. Maex, "Porous low dielectric constant materials for microelectronics," *Philos. Trans. R. Soc. A Math. Phys. Eng. Sci.*, vol. 364, no. 1838, pp. 201–215, 2006.

[163] A. V Goncharenko, V. Z. Lozovski, and E. F. Venger, "Lichtenecker's equation: applicability and limitations," *Opt. Commun.*, vol. 174, no. 1–4, pp. 19–32, 2000.

[164] T. Takuma and B. Techaumnat, *Electric fields in composite dielectrics and their applications*. Springer Science & Business Media, 2010.

[165] A. Bunde and W. Dieterich, "Percolation in composites," *J. electroceramics*, vol. 5, pp. 81–92, 2000.

[166] Z. Jiang, "Technology assessment and market analysis of solid state ultracapacitors." Massachusetts Institute of Technology, 2007.

[167] A. Wypych *et al.*, "Dielectric properties and characterisation of titanium dioxide obtained by different chemistry methods," *J. Nanomater.*, vol. 2014, pp. 1–9, 2014, doi: https://doi.org/10.1155/2014/124814.

[168] S. Mahshid, M. Askari, and M. S. Ghamsari, "Synthesis of TiO2 nanoparticles by hydrolysis and peptization of titanium isopropoxide solution," *J. Mater. Process. Technol.*, vol. 189, no. 1, pp. 296–300, 2007, doi: https://doi.org/10.1016/j.jmatprotec.2007.01.040.

[169] A. Cenovar, P. Paunovic, A. Grozdanov, P. Makreski, and E. Fidanccevska, "Preparation of nano-crystalline TiO2 by Sol-gel method using titanium tetraisopropoxide (TTIP) as a precursor," *Adv. Nat. Sci. Theory Appl.*, 2012, [Online]. Available: http://hdl.handle.net/20.500.12188/429

[170] A. G. Gibson and J.-A. Månson, "Impregnation technology for thermoplastic matrix composites," *Compos. Manuf.*, vol. 3, no. 4, pp. 223–233, 1992, doi: https://doi.org/10.1016/0956-7143(92)90110-G.

[171] K. M. S. Khalil and M. I. Zaki, "Synthesis of high surface area titania powders via basic hydrolysis of titanium(IV) isopropoxide," *Powder Technol.*, vol. 92, no. 3, pp. 233–239, 1997, doi: https://doi.org/10.1016/S0032-5910(97)03250-6.

[172] T. Xie, Y. Wang, C. Liu, and L. Xu, "New insights into sensitization mechanism of the doped Ce (IV) into strontium titanate," *Materials (Basel).*, vol. 11, no. 4, p. 646, 2018.

[173] T. Xian, H. Yang, L. Di, J. Ma, H. Zhang, and J. Dai, "Photocatalytic reduction synthesis of SrTiO3-graphene nanocomposites and their enhanced photocatalytic activity," *Nanoscale Res. Lett.*, vol. 9, no. 1, p. 327, 2014, doi: 10.1186/1556-276X-9-327.

[174] E. Smith, A. Block, and R. Ubic, "A novel room-temperature synthesis technique for producing high-density Ba1-xSrxTiO3 and PbZryTi1-yO3 composites," *J. Eur. Ceram. Soc.*, vol. 42, no. 10, pp. 4212–4220, 2022, doi: https://doi.org/10.1016/j.jeurceramsoc.2022.04.002.

[175] M. N. Scheidema and P. Taskinen, "Decomposition Thermodynamics of Magnesium

Sulfate," *Ind. Eng. Chem. Res.*, vol. 50, no. 16, pp. 9550–9556, Aug. 2011, doi: 10.1021/ie102554f.

[176] C. J. Ferchaud, H. A. Zondag, J. B. J. Veldhuis, and R. De Boer, "Study of the reversible water vapour sorption process of MgSO4. 7H2O and MgCl2. 6H2O under the conditions of seasonal solar heat storage," in *Journal of Physics: Conference Series*, IOP Publishing, 2012, p. 12069.

[177] S. E. D. Hamad, "An experimental study of the salt hydrate MgSO4 · 7H2O," *Thermochim. Acta*, vol. 13, no. 4, pp. 409–418, 1975.

[178] H. L. Robson, "The system MgSO4-H2O from 68 to 240," *J. Am. Chem. Soc.*, vol. 49, no. 11, pp. 2772–2783, 1927.

[179] E. Rocha-Rangel *et al.*, "Synthesis of SrTiO3 by the calcination of SrCO3 and TiO2 mixtures intensively ground by means of high energy milling," *Arch. Metall. Mater.*, vol. 65, no. 2, pp. 621–626, 2020.

[180] F. Dkhilalli *et al.*, "Characterizations and morphology of sodium tungstate particles," *R. Soc. Open Sci.*, vol. 5, no. 8, p. 172214, Aug. 2018, doi: 10.1098/rsos.172214.

[181] A. Narayana and L. S V, "Enhanced Photocatalytic Activity of Perovskite SrTiO3 nanorods," *Solid State Technol.*, vol. 63, pp. 1913–1920, Jul. 2020.

[182] A. K. Panda, S. P. Moulik, B. B. Bhowmik, and A. R. Das, "Dispersed Molecular Aggregates: II. Synthesis and Characterization of Nanoparticles of Tungstic Acid in H2O/(TX-100+Alkanol)/n-Heptane W/O Microemulsion Media," *J. Colloid Interface Sci.*, vol. 235, no. 2, pp. 218–226, 2001, doi: https://doi.org/10.1006/jcis.2000.7323.

[183] Y. V Matveichuk, "Ftir-spectroscopic investigation of sodium tungstate and sodium molybdate solutions in wide range of pH," 2017.

[184] Y. B. Ryu and M. S. Lee, "Infrared spectra and thermal properties of sodium silicate solutions," *Korean J. Met. Mater.*, vol. 56, no. 1, pp. 72–78, 2018.

[185] H. Kähäri, M. Teirikangas, J. Juuti, and H. Jantunen, "Improvements and Modifications to Room-Temperature Fabrication Method for Dielectric Li 2 MoO 4 Ceramics," *J. Am. Ceram. Soc.*, vol. 98, no. 3, pp. 687–689, 2015.

[186] A. Ndayishimiye *et al.*, "Roadmap for densification in cold sintering: Chemical pathways," *Open Ceram.*, vol. 2, p. 100019, 2020, doi: https://doi.org/10.1016/j.oceram.2020.100019.

[187] R. Ubic, "Software for Calculating Permittivity of Resonators: HakCol & ErCalc," *Adv. Multifunct. Mater. Syst. II Ceram. Trans. Vol. 245*, pp. 65–75, 2014.

[188] P. S. Singh, M. Trigg, I. Burgar, and T. Bastow, "Geopolymer formation processes at room temperature studied by 29Si and 27Al MAS-NMR," *Mater. Sci. Eng. A*, vol. 396, no. 1–2, pp. 392–402, 2005.

[189] U. Hribar, M. B. Østergaard, N. Iversen, M. Spreitzer, and J. König, "The mechanism of glass foaming with water glass," *J. Non. Cryst. Solids*, vol. 600, p. 122025, 2023, doi: https://doi.org/10.1016/j.jnoncrysol.2022.122025.

[190] D. Dimas, I. Giannopoulou, and D. Panias, "Polymerization in sodium silicate solutions: a fundamental process in geopolymerization technology," *J. Mater. Sci.*, vol. 44, pp. 3719–3730, 2009.

[191] M. Malaki, A. Fadaei Tehrani, B. Niroumand, and M. Gupta, "Wettability in metal matrix composites," *Metals (Basel).*, vol. 11, no. 7, p. 1034, 2021.

[192] S. Vilminot, G. André, M. Richard-Plouet, F. Bourée-Vigneron, and M. Kurmoo, "Magnetic structure and magnetic properties of synthetic lindgrenite, Cu3 (OH) 2 (MoO4) 2," *Inorg. Chem.*, vol. 45, no. 26, pp. 10938–10946, 2006.

[193] O. Barinova, S. Kirsanova, A. Sadovskiy, and I. Avetissov, "Properties of Li2MoO4 single crystals grown by Czochralski technique," *J. Cryst. Growth*, vol. 401, pp. 853–856, 2014, doi: https://doi.org/10.1016/j.jcrysgro.2013.10.051.

[194] G. Harichandran, S. Radha, J. Yesuraj, and B. Muthuraaman, "Facile Synthesis and Characterization of Cu3 (MoO4) 2 (OH) 2 Nanorods for High Performance Supercapacitor Electrode Application," *ChemistrySelect*, vol. 5, no. 35, pp. 11037–11047, 2020.

[195] X. Wang and L. Andrews, "Infrared spectra, structure and bonding in the LiO2, LiO2Li, LiO and Li2O molecules in solid neon," *Mol. Phys.*, vol. 107, no. 8–12, pp. 739–748, 2009.

[196] P. Larkin, *Infrared and Raman spectroscopy: principles and spectral interpretation.* Elsevier, 2017.

[197] A. M. Youssef, H. K. Farag, A. El-Kheshen, and F. F. Hammad, "Synthesis of nano-structured strontium titanate by sol-gel and solid state routes," *Silicon*, vol. 10, pp. 1225–1230, 2018.

[198] P. A. Bhat and N. C. Debnath, "Study of structures and properties of silica-based clusters and its application to modeling of nanostructures of cement paste by DFT methods," in *IOP Conference Series: Materials Science and Engineering*, IOP Publishing, 2013, p. 12001.

[199] A. Oufakir, L. Khouchaf, M. Elaatmani, A. Zegzouti, G. Louarn, and A. Ben Fraj, "Study of structural short order and surface changes of SiO2 compounds," in *MATEC Web of Conferences*, EDP Sciences, 2018, p. 1041.

[200] B. Li *et al.*, "Calcined sodium silicate as an efficient and benign heterogeneous catalyst for the transesterification of natural lecithin to L-α-glycerophosphocholine," vol. 8, no. 1, pp. 78–84, 2019, doi: doi:10.1515/gps-2017-0190.

[201] I. Halasz, M. Agarwal, R. Li, and N. Miller, "Vibrational spectra and dissociation of aqueous Na 2 SiO 3 solutions," *Catal. Letters*, vol. 117, pp. 34–42, 2007.

[202] A. Hachemi, H. Hachemi, A. Ferhat-Hamida, and L. Louail, "Elasticity of SrTiO3 perovskite under high pressure in cubic, tetragonal and orthorhombic phases," *Phys. Scr.*, vol. 82, no. 2, p. 25602, 2010.

[203] R. Zosiamliana, B. Chettri, G. Abdurakhmanov, M. P. Ghimire, and D. P. Rai, "Electronic, mechanical, optical and piezoelectric properties of glass-like sodium silicate (Na 2 SiO 3) under compressive pressure," *RSC Adv.*, vol. 12, no. 20, pp. 12453–12462, 2022.

[204] D. Belmonte, C. Gatti, G. Ottonello, P. Richet, and M. Vetuschi Zuccolini, "Ab Initio Thermodynamic and Thermophysical Properties of Sodium Metasilicate, Na2SiO3, and Their Electron-Density and Electron-Pair-Density Counterparts," *J. Phys. Chem. A*, vol. 120, no. 44, pp. 8881–8895, Nov. 2016, doi: 10.1021/acs.jpca.6b08676.

[205] C. R. Koripella, "Mechanical behavior of ceramic capacitors," *IEEE Trans. Components Hybrids Manuf. Technol.*, vol. 14, no. 4, pp. 718–724, 1991.

[206] E. Sharova, "Bestimmung bruchmechanischer Eigenschaften als Funktion der Temperatur am Beispiel eines PTC-Werkstoffes," 2013.

[207] M. Bäurer, S.-J. Shih, C. Bishop, M. P. Harmer, D. Cockayne, and M. J. Hoffmann, "Abnormal grain growth in undoped strontium and barium titanate," *Acta Mater.*, vol. 58, no. 1, pp. 290–300, 2010.

[208] B.-K. Lee, S.-Y. Chung, and S.-J. L. Kang, "Grain boundary faceting and abnormal grain growth in BaTiO3," *Acta Mater.*, vol. 48, no. 7, pp. 1575–1580, 2000.

[209] L. Amaral, A. M. R. Senos, and P. M. Vilarinho, "Sintering kinetic studies in nonstoichiometric strontium titanate ceramics," *Mater. Res. Bull.*, vol. 44, no. 2, pp. 263–270, 2009.

[210] G. Quinn, "A NIST recommended practice guide: fractography of ceramics and glasses. Special publication960–16e2. Washington, DC: National Institute of Standardsand Technology." 2016.

[211] J. Sivasubramanian and Y. Gino, "Effect of sodium silicate on hardening property of concrete," *Int. J. Civ. Eng. Tech*, vol. 10, pp. 642–650, 2019.

[212] K. Sankar, P. Stynoski, G. K. Al-Chaar, and W. M. Kriven, "Sodium silicate activated slag-fly ash binders: Part I–Processing, microstructure, and mechanical properties," *J. Am. Ceram. Soc.*, vol. 101, no. 6, pp. 2228–2244, 2018.

[213] X. Pan, C. Shi, J. Zhang, L. Jia, and L. Chong, "Effect of inorganic surface treatment on surface hardness and carbonation of cement-based materials," *Cem. Concr. Compos.*, vol. 90, pp. 218–224, 2018.

[214] M. Li, B. Zhuang, Y. Lu, Z.-G. Wang, and L. An, "Accurate Determination of Ion Polarizabilities in Aqueous Solutions," *J. Phys. Chem. B*, vol. 121, no. 26, pp. 6416–6424, Jul. 2017, doi: 10.1021/acs.jpcb.7b04111.

[215] L. Li, R. Ubic, and X. M. Chen, "On the τf measurement of microwave dielectric ceramics," *Mater. Res. Bull.*, vol. 178, p. 112920, 2024, doi: https://doi.org/10.1016/j.materresbull.2024.112920.

[216] S. El-Sayed, T. A. Abdel-Baset, and A. Hassen, "Dielectric properties of PVDF thin films doped with 3 wt.% of RCl3 (R = Gd or Er)," *AIP Adv.*, vol. 4, no. 3, p. 37114, Mar. 2014, doi: 10.1063/1.4869093.

# Bibliography

## Publications Related to the Thesis

### Journal Articles

N. Kuzmić, S. D. Škapin, M. Nelo, H. Jantunen, and M. Spreitzer, “Dielectric Properties of Upside-Down $SrTiO_3/Li_2MoO_4$ Composites Fabricated at Room Temperature,” Front. Mater., vol. 8, p. 121, 2021, doi: 10.3389/fmats.2021.669421, [COBISS.SI-ID 67912963].

N. Kuzmić, S. D. Škapin, M. Nelo, H. Jantunen, and M. Spreitzer, “Room temperature fabrication and post-impregnation of LMO-ST composites: Engineering and modeling of dielectric properties,” Open Ceram., vol. 16, p. 100495, 2023, doi: https://doi.org/10.1016/j.oceram.2023.100495 ,[COBISS.SI-ID 169829891].

N. Kuzmić, E. Terbovšek, S. D. Škapin, M. Nelo, H. Jantunen, and M. Spreitzer, “New Inorganic Binders for Room Temperature Fabrication of Upside-down $SrTiO_3$-based Ceramic Composites,” Ceram. Int., 2024, doi: https://doi.org/10.1016/j.ceramint.2024.06.129, [COBISS.SI-ID 205732611].

A. Jabr#. N. Kuzmić#, S. D. Škapin, H. Jantunen, M. Nelo, M. Spreitzer, R. Bermejo, “Towards high strength $SrTiO_3$-based composites fabricated at room temperature,” J. Eur. Ceram. Soc., vol. 44, no. 15, p. 116782, 2024, doi: https://doi.org/10.1016/j.jeurceramsoc.2024.116782
# equally contributed (1st authors)

### Conference Abstracts

N. Kuzmić, E. Terbovšek, A. Jabr, M. Nelo, S. D. Škapin, H. Jantunen, and M. Spreitzer, . “Room temperature fabrication of ceramic composites for electronic applications”, 12th International Conference on Microwave Materials and Their Applications, book of abstracts, page. 1, electronic source, 2023, Available: https://converia.unimainz.de/frontend/index.php?page_id=3294&v=List&do=15&day=all&ses=2440#, [COBISS.SI-ID 190881027].

N. Kuzmić, D. Fabijan, M. Nelo, S. D. Škapin, H. Jantunen, and M. Spreitzer, “Tailoring the Dielectric Properties of Binder-ST Composites: RTF Experiments vs. OOF2 Modeling”, Polymers 2024, Composites 2024 and 3BS Materials 2024 International Joint Conference, book of abstracts, page. 97, electronic source, 2024, Available: https://setcor.org/userfiles/files/2024/Seville/Polymers-Composites-3BsMaterials-2024-Joint-Conferences-Book-of-Abstracts.pdf. . COBISS.SI-ID 190277891

N. Kuzmić, M. Nelo, S. D. Škapin, H. Jantunen, and M. Spreitzer. “How can we fabricate passive electronic components in a greener way?”. In: N. Kuzmić (editor.), et al. 14. študentska konferenca Mednarodne podiplomske šole Jožefa Stefana = 14th Jožef Stefan International Postgraduate School Students' Conference: knjiga povzetkov = book of abstracts: 1. - 3. junij 2022, Kamnik, Slovenia = 1st - 3rd June, 2022, Kamnik, Slovenia. .

Ljubljana: Jožef Stefan Institute: Jožef Stefan International Postgraduate School, 2022. p. 72, ilustr. http://ipssc.mps.si/Book_of_Abstracts.pdf. [COBISS.SI-ID 139157251]

N. Kuzmić, M. Nelo, S. D. Škapin, H. Jantunen, and M. Spreitzer. "Ceramic upside-down composites for future electronics". In: V. Srdić (editor), A. Kocjan (editor), M. Canillas Perez (editor). 14th ECerS Conference for Young Scientists in Ceramics : program and book of abstracts : October 20-23, 2021, Novi Sad, Serbia. Novi Sad: Faculty of Technology, 2021. Str. 98. ISBN 978-86-6253-136-0. [COBISS.SI-ID 83943683]

N. Kuzmić, M. Nelo, S. D. Škapin, H. Jantunen, and M. Spreitzer. "Ceramic upside-down composites for energy-storage applications". In: M. Horvat Zagorec (editor), et al. Cutting Edge 2021 : scientific conference for young researchers : independent in science : Thursday, 16. 09. 21, virtual conference: book of abstracts. Ljubljana: Fakulteta za kemijo in kemijsko tehnologijo, 2021. p. 90, . ISBN 978-961-7078-21-3. [COBISS.SI-ID 83928835]

N. Kuzmić, M. Nelo, S. D. Škapin, H. Jantunen, and M. Spreitzer. "Room temperature fabricated ceramic composites as future capacitors". In: K. Žagar (editor), et al. Throughout knowledge towards a green new world: 13. Študentska konferenca Mednarodne podiplomske šole Jožefa Stefana in 15. dan mladih raziskovalcev (Konferenca KMBO), 27-28 maj 2021, Ljubljana, Slovenija : knjiga povzetkov = 13th Jožef Stefan International Postgraduate School Students' Conference and 15th Young Researchers' Day of Chemistry, material science, biochemistry and environment, (CMBE day), 27th-28th May 2021, online : book of abstracts. Ljubljana: Mednarodna podiplomska šola Jožefa Stefana: = Jožef Stefan International Postgraduate School: Inštitut Jožef Stefan: = Jožef Stefan Institute, 2021. Str. 62-63. http://ipssc.mps.si/bookOfAbstracts/Book_of_abstracts_v04.pdf. [COBISS.SI-ID 67917827]

## Other Publications

A.C. Barros Lobato (editor); A. Pavlovič (editor); A. Hrepić (editor); A. Tesovnik (editor); A. Vozelj (editor); B. Gec (editor); B. Pavlovič (editor); C. Terro (editor); I. Konjević (editor); L. Gašparič (editor); M. Rubio (editor); M. Zver (editor); M. Žabčić (editor); M. Lachhab (editor); N. F. Nolte (editor); N. Kuzmić (editor); R. Sorrentino (editor); S. Podgornik (editor); S. Mežnar (editor); U. Živič (editor); V. Regis de Moraes (editor); Ž. Gostenčnik (editor) 16th Jožef Stefan International Postgraduate School Students' Conference, 29th – 31st May, Piran, Slovenia [electronic source] : Book of abstracts; Two decades of discovery: advancing science and solutions. 2024, http://ipssc.mps.si/auxiliary_material/IPSSC24_BoA.pdf. [COBISS.SI-ID 198759171].

N. Kuzmić (editor), A.Čontala (editor), A. C. Barros Lobato, (editor), A. Oberlintner(editor), A. Pavlovič (editor), A. Hrepić (editor), B. Repič (editor), B. Gec (editor), C. Terro (editor), D. Božič (editor), G. Noveski (editor), M. Caf (editor), M. Zver (editor), P.Borštnar (editor), R. Novak (editor), S. Mežnar (editor), S. Salmanov (editor), T. Černič (editor), U. Hribar (editor), Ž.Gostenčnik (editor), M. Šadl (editor), "15th Jožef Stefan International Postgraduate School Students' Conference", 31st May - 2nd June 2023, Kamnik, Slovenia: Book of abstracts. Ljubljana: Jožef Stefan Institute: Jožef Stefan International Postgraduate School, 2023. 1 electronic source. http://ipssc.mps.si/auxiliary_material/BoA%20IPSSC%202023.pdf. [COBISS.SI-ID 156276995]

R. Novak(editor), A. Čontala (editor), A.C. Barros Lobato (editor), B. Evkoski (editor), C. Terro (editor), E. Andreasidou (editor), D. Božič (editor), G. Noveski (editor), K. Žagar (editor), M. Zver (editor), M. Novak (editor), M. Šadl (editor), N. Rehman (editor), N. Kuzmić (editor), Ž. Gostenčnik (editor), 14. študentska konferenca Mednarodne podiplomske šole Jožefa Stefana, 1. - 3. junij 2022, Kamnik, Slovenia = 14th Jožef Stefan International Postgraduate School Students' Conference, 1st - 3rd June, 2022, Kamnik, Slovenia. Knjiga povzetkov = book of Ljubljana: Jožef Stefan Institute: Jožef Stefan International Postgraduate School, 2022. 1 electronic source http://ipssc.mps.si/2022/Book_of_Abstracts.pdf. [COBISS.SI-ID 113677315]

M. Spreitzer, N. Kuzmić, S.D. Poročilo za opravljeni analizi šobe z batom : poročilo za opravljeni analizi v sklopu sodelovanja med Institut "Jožef Stefan" Jamova 39 1000 Ljubljana Slovenia in Trimo d.o.o. Prijateljeva cesta 12 8210 Trebnje, Slovenija. 2021. IJS delovno poročilo, 13590, zaupno. [COBISS.SI-ID 73712387]

D. Nabergoj, N. Kuzmić , B. Drakslar , A. Podgornik . “Effect of dilution rate on productivity of continuous bacteriophage production in cellstat”. Applied microbiology and biotechnology. 2018, vol. 102, iss. 8, pp. 3649-3661, ISSN 0175-7598. https://link.springer.com/article/10.1007%2Fs00253-018-8893-9, DOI: 10.1007/s00253-018-8893-9.[COBISS.SI-ID1537731779]

N. Kuzmić, D. Nabergoj . “Spreminjanje produktivnosti pridobivanja bakteriofagov v kontinuirnem sistemu” = “Effect of dilution rate on productivity of continuous production of bacteriophages”. In: Zbornik znanstvenih radova. XXII. Međunarodna Tehnologijada, Trogir, 7. - 13. svibnja 2018. Zagreb: Fakultet kemijskog inženjerstva i tehnologije, 2018. pp. 13. [COBISS.SI-ID 1537796035], nagrada: 3. mesto v znanstvenem delu tekmovanja Tehnologijada 2018

D. Nabergoj, N. Kuzmić, A. Podgornik. “Effect of dilution rate on productivity of continuous production of bacteriophages”. In: KLJUN, Jakob (editor), GABER, Aljaž (editor). Book of abstracts. Scientific Conference for Young Researchers, 19. 9. 2017. Ljubljana: Fakulteta za kemijo in kemijsko tehnologijo, 2017. pp. 89,. ISBN 978-961-6756-83-9. [COBISS.SI-ID 1537523395]

A.Podgornik, D. Nabergoj, P. Modic, N. Kuzmić, B. Drakslar. “ Continuous production of bacteriophages in cellstat” : [oral presentation]. In: ESBES 2018: book of abstracts. [S. l.: s. n.], 2018. p. 45. https://esbes2018.org/Programme/_/2018-09-04%20-%20ESBES%20-20Book%20of%20Abstracts.pdf.[COBISS.SI-ID1537900227]

# Biography

The following information is about Nina Kuzmić, the author of a thesis. Nina was born on February 12, 1995, in Ljubljana, Slovenia. In 2013, she enrolled in the Chemical Engineering Bachelor program at the Faculty of Chemistry and Chemical Technology at the University of Ljubljana. In 2016, Nina graduated and enrolled in the Master's program in Chemical engineering at the same institution. During her Master's studies, she completed two Erasmus+ program exchanges, gaining valuable study and practical experience. First, Nina attended a study exchange at Friedrich-Alexander-Universität, Erlangen, Germany (5 months), and second, she attended an Erasmus+ traineeship at the University of Beira, Covilhã, Portugal (5 months). In August 2019, Nina graduated from the Master's program at the Faculty of Chemistry and Chemical Technology at the University of Ljubljana. She received the faculty Prešeren's award for her Master's thesis.

In October 2019, she started her doctoral studies at the Jožef Stefan International Postgraduate School. As a doctoral student in the Advanced Materials Department, she focused on researching the low-temperature fabrication of ceramic composites for energy storage and electronic devices. Her work focused on providing a better understanding of the densification mechanisms, binder-filler interactions, and the effect of processing parameters on the fabrication process, which could result in optimized dielectric and mechanical properties. In addition, she focused on designing new possible binder-filler composite systems that can be fabricated at room temperature and further applied in passive electronic devices. During her doctoral studies, she took part in three working visits, the first (November-December 2019, 3 weeks) and second JECS TRUST founded (August-October 2021, 2 months) at the Microelectronic research unit at the University of Oulu, and the third short visit at the Montanuniversität Leoben, Austria (March 2023, 1 week). In 2023 and 2024, the candidate received a certificate twice for outstanding contribution to the development of extracurricular activities at IPS due to her exceptional dedication and work in the Student Council and IPS Student Conference organizing committee.